Universidad Autónoma de Madrid

PhD Thesis

Optical manipulation of quantum fluids in semiconductor microcavities

Author:
Guilherme Tosi

Supervisor:
Prof. Luis Viña

Madrid, January 14, 2013

To my family.

"...And it is of course not true that we have to follow the truth.
Human life is guided by many ideas. Truth is one of them.
Freedom and mental independence are others.
If Truth, as conceived by some ideologists,
conflicts with freedom, then we have a choice.
We may abandon freedom. But we may also abandon Truth."

Paul Feyerabend

Acknowledgements

All the achievements described in this PhD thesis would not have been possible without the help of people to whom I am greatly indebted. I would like to first acknowledge my advisor, Prof. Luis Viña, for all the efforts done along these years in providing all the available tools for carrying out our research in the best possible way, and specially for a careful reading and detailed correction of this manuscript.

I was benefited during these years from positive interactions with the highly qualified SEMICUAM research team at the Universidad Autónoma de Madrid. When performing the experiments, I had the pleasure to share the workplace with Prof. José Manuel Calleja, Matthias Baudisch, Cristoph Lingg, Lukas Langer and Carlos Antón, who nowadays keeps the research quality in our lab at the highest level. The success of our group work is also greatly due to the theoretical support provided by Prof. Carlos Tejedor and Dr. Francesca Marchetti, along with help and fruitful discussions with Andrei Berceanu and Alejandro González. Last but not least, thanks goes to Dr. Marzena Szymańska at the University of Warwick for collaborating with simulations and fruitful discussions.

Special thanks goes to Dr. Daniele Sanvitto who trusted in my potential and opened the doors to a new life in Spain, not only for introducing me to the world of polaritons with clever and exciting ideas, but also for constant advise and support in personal matters.

I also greatly acknowledge the friendly and stimulating work environment found during my stay in the Nanophotonics group at the University of Cambridge, where the constant enlightenment from Prof. Jeremy Baumberg, the support and help from Dr. Gabriel Christmann, and the theoretical support from Dr. Natalia Berloff culminated in so many fascinating results in a very short time. And of course the days in the lab were much more interesting with stimulating discussions on physics and musical advising from Peter Cristofolini.

The fact that polaritons emerged as a hot topic in the last years strongly resides on the high-quality samples grown in Molecular Beam Epitaxy systems. I must acknowledge Dr. Aristide Lemaître and Prof. Jacqueline Bloch at the Laboratoire de Photonique et de Nanostructures (CNRS, Marcoussis, France), Prof. Zacharias Hatzopoulos and Prof. Pavlos Savvidis at the Institute of Electronic Structure and Laser (FORTH, Heraklion, Greece) for providing the last-generation samples used to obtain the results presented on this thesis.

Finally, many funding sources, including Spanish MEC (MAT2008-01555, QOIT-CSD2006-00019) and CAM (S-2009/ESP-1503), British EPSRC (EP/G060649/1) and European CLERMONT4 (235114) and INDEX (289968), allowed for the availability of top-class experimental setups and spreading results in international conferences. I particularly acknowledge an FPI scholarship from the Spanish Ministry of Science and Innovation, which sponsored my work and a 6-months stay at the University of Cambridge.

Quisiera agradecer también a todas las personas que me apoyaron en estos cuatro aos viviendo en Madrid, haciendo que a cada da valiera la pena la distancia de mi hogar. En particular a José Luis, Juancho, Carlos y Jorge por la amistad y buenos momentos compartidos. Y en especial a Cristina por haberme apoyado en tantos momentos de dificultad y sobretodo en los duros das de escritura de esa tesis.

Apesar da distância espacial e temporal, essa tese também não teria sido possível sem o apoio de muitos que fizeram e/ou ainda fazem parte da minha vida no Brasil. Agradeço em particular aos inesquecíveis anos compartilhados com a Gê e sua família; ao Jonas, grande parceiro de festas e ideais; ao Carlos Parra, um grande amigo e conselheiro que, por uma sorte do destino, continua morando ali pertinho, só a duas horas em avião; e à Ju, que de vez em quando aparece com uma caixinha de lembranças.

Não posso deixar de agradecer ao meu antigo orientador, Prof. Paulo Sergio Guimarães, pela excelente iniciação científica e por ter plantado a semente da minha mudança para a Espanha.

Acima de tudo agradeço à minha familia, que desde o princípio me apoiou, me educou e me deu as ferramentas necessárias para meu crecimento e independência pessoal. À minha irmã, Fá, pelo carinho e por ser a filha que é e o filho que não posso ser à distância. E aos meu pais, Ivo e Luci, que sempre tiveram aos filhos como principal razão de ser, pela constante educação, luta, conselhos, apoio e amor.

List of publications

G. Tosi, G. Christmann, N. G. Berloff, P. Tsotsis, T. Gao, Z. Hatzopoulos, P. G. Savvidis and J. J. Baumberg.
"Sculpting oscillators with light within a nonlinear quantum fluid."
Nature Physics 8, 190-194 (2012).
Highlights: Kavokin, A. "Polariton pendulum." Nature Physics 8, 183-184 (2012).
Overton, G. "Semiconductor chip converts laser to visible quantum fluid." Laser Focus World 48, 13-13 (2012).

G. Tosi, G. Christmann, N. G. Berloff, P. Tsotsis, T. Gao, Z. Hatzopoulos, P. G. Savvidis and J. J. Baumberg.
"Geometrically-locked vortex lattices in semiconductor quantum fluids"
Nature Communications. 3:1243 doi: 10.1038/ncomms2255 (2012).

R. Spano, J. Cuadra, G. Tosi, C. Anton, C. A. Lingg, D. Sanvitto, M. D. Martín, L. Viña, P. R. Eastham, M. van der Poel, and J. M. Hvam.
"Coherence properties of exciton polariton OPO condensates in one and two dimensions" (invited)
New Journal of Physics 14, 075018 (2012).

C. Anton, T.C.H. Liew, G. Tosi, M.D. Martin, T. Gao, Z. Hatzopoulos, P.S. Eldridge, P.G. Savvidis and L. Vina.
"Dynamics of a polariton condensate transistor switch"
Applied Physics Letters *101, 261116* (2012)

G. Christmann, G. Tosi, N. Berloff, P. Tsotsis, P. Eldridge, Z. Hatzopoulos, P. G. Savvidis, J. J. Baumberg.
"Polariton ring condensates and sunflower ripples in an expanding quantum liquid."
Physical Review B 85, 235303 (2012).

C. Antón, G. Tosi, M. D. Martín, L. Viña, A. Lemaître, and J. Bloch
"Role of supercurrents on vortices formation in polariton condensates"
Optics Express 20, 16367 (2012).

G. Tosi, F. M. Marchetti, D. Sanvitto, C. Antón, M. H. Szymańska, A. Berceanu, C. Tejedor, L. Marrucci, A. Lemaître, J. Bloch, and L. Viña.
"Onset and Dynamics of Vortex-Antivortex Pairs in Polariton Optical Parametric Oscillator Superfluids."
Physical Review Letters 107, 036401 (2011).

G. Tosi, D. Sanvitto, M. Baudisch, E. Karimi, B. Piccirillo, L. Marrucci, A. Lemaître, J. Bloch and L. Viña.
"Vortex stability and permanent flow in nonequilibrium polariton condensates."
Journal of Applied Physics 109, 102406 (2011);

D. Sanvitto, F. M. Marchetti, M. H. Szymańska, G. Tosi, M. Baudisch, F. P. Laussy, D. N. Krizhanovskii, M. S. Skolnick, L. Marrucci, A. Lemaître, J. Bloch, C. Tejedor and L. Viña.
"Persistent currents and quantized vortices in a polariton superfluid."
Nature Physics 6, 527-533 (2010).

Oral presentations

09-14 Sep 2012 – Cambridge (UK)

POLATOM Network Conference: Cold Atoms, Excitons, Polaritons, Bose-Einstein condensates.

Oral presentation: "Vortex lattices in polariton condensates"

27-31 Aug 2012 – Stanford, California (USA)

ICSCE6 - 6th International Conference on Spontaneous Coherence in Excitonic Systems

Invited talk: "Nonlinear light-matter fluids made to interact: from harmonic oscillations to vortex lattices"

29 Jul - 03 Aug 2012 – Zurich (Switzerland)

ICPS2012 – 31st International Conference of the Physics of Semiconductors

Invited talk: "Optically-induced vortex lattices in a semiconductor quantum fluid"

20-23 Mar 2012 – Rome (Italy)

ESF Exploratory Workshop on Polaritonics: From basic research to device applications

Invited talk: "Spontaneous Harmonics Oscillations and Vortex Lattices in polariton condensates"

25-27 Jan 2012 – Sevilla (Spain)

GEFES2012 - VII Meeting of Grupo Especializado de Física de Estado Sólido

Oral presentation: "Vortex dynamics in polariton Optical Parametric Oscillator superfluids"

07-11 Feb 2011 – Lausanne (Switzerland)

ICSCE5 - 5th International Conference on Spontaneous Coherence in Excitonic Systems

Oral presentation: "Permanent flow and vortex dynamics in superfluid polariton condensates"

15 Dic 2010 – Madrid (Spain)

XIII Young scientists meeting of Instituto de Ciencia de Materiales Nicolás Cabrera

Oral presentation: "Superfluid polariton condensates"

12-16 Apr 2010 – Cuernavaca (Mexico)

PLMCN10 - 11th Physics of Light-Matter Coupling in Nanostructures

Oral Presentation: "Observation of Permanent Flow of Vortices in Superfluid Polariton Condensates"

Contents

Introduction

The transition to the Information Era we are living nowadays relies heavily on the successful use of semiconductor materials, which can store and process a huge amount of data in tiny volumes. Modern growth and lithography techniques have shrank the transistor — the basic logic component — size down to tens of nanometres and increased the processing speed up to Gigahertz. The interconnected world is also dependent on the telecommunications, which links electronically-processed data through the faster information carrier in nature: photons. This electromagnetic signal, after travelling huge distances through optical fibres or using satellites, has to be eventually converted into electric signals, giving rise to a complex field of knowledge known as optoelectronics. Moreover, the need for faster processing speeds and less heat dissipation have motivated to search for fully-optical chips, where non-linearities allow for information to be processed all-optically on the fly. However there are still many problems to be solved before chips based on optical transistors become available [1].

Although Silicon is the semiconductor material *per se* and recently many progress has been made in the direction of Silicon Photonics [2], its indirect band-gap requires high momentum exchanges in optical transitions, hindering efficient optical processes in silicon chips. This is the main reason behind the use of III-V compounds in optoelectronics, and its giant development in the last decades. In fact, the first semiconductor laser, dating back to the 1960s [3], has been built from forward biased $GaAs$ *p-n* junctions. Due to rapid progress of crystal growth technology, complex layered structures of $GaAs$ in combination with aluminium arsenide ($AlAs$) or the alloy $Al_xGa_{1-x}As$ can be grown using molecular beam epitaxy (MBE) or metalorganic vapor phase epitaxy (MOVPE). Because $GaAs$ and $AlAs$ have almost the same lattice constant, the layers have very little induced strain, which allows them to be grown almost arbitrarily thick. The motivation to lower the lasing threshold and to force single mode emission led to the creation of microcavity structures known as VCSELs (Vertical Cavity Surface Emitting Lasers), demonstrated in 1979 [4]. In such structures the laser active medium is surrounded monolithically by many layers of thick semicondutors that form almost perfect mirrors based on interference phenomena — the distributed Bragg reflectors (DBRs). Nowadays, devices based on optical microcavities are already indispensable for a wide range of applications and studies. For example, microcavities made of active III-V semiconductor materials are used to control laser emission spectra enabling long-distance transmission of data over optical fibres; they also ensure narrow spot-size laser read/write beams in CD, DVD and blue-ray players.

The quest for thresholdless lasers improved even further the quality of DBR-microcavities, which are now capable of holding photons inside the cavity for times long enough so that they are absorbed and emitted by excitons in the active media many times before exiting the cavity, giving rise to new quasiparticles called *exciton-polaritons* [5]. Being half-matter, half-light, polaritons have strong dipole-dipole and Coulomb interactions from

its excitonic part and very light mass from its photonic part. The extreme non-linearities originating from Coulomb interactions play a key role in a number of fascinating effects including parametric scattering. Their extremely light mass, of the order 10^{-5} the free electron mass, is responsible for a huge de Broglie wavelength, that becomes comparable to the interparticle distance — in the micrometre scale — at temperatures as high as room temperature. Quantum many-body phenomena can be then investigated in solid-state materials using simple experimental apparatus.

Particles with a bosonic character — for which polaritons are an example — can condense into quantum fluids, where all, or a main part of particles, occupy the same quantum state, behaving like a single macroscopic state [6]. Such rich physical phenomena, known as Bose-Einstein condensation, has been first observed in cold atom gases [7, 8] with proven potential for practical applications as, for example, interferometric devices [9–13].

The polaritons' light mass and the possibility to confine them in natural traps in momentum space have motivated a quest for high-temperature, out-of-equilibrium, Bose-Einstein condensation in semiconductor microcavities, which has been demonstrated by different groups a few years ago [14–16] even at room temperature [17]. By harnessing the photonic component of a polariton condensate through light that escapes out from a microcavity, it is possible to directly visualise in real time its coherent wavefunction on macroscopic length-scales, an impossible task in superconductors or superfluids.

The ability to shape the polariton flow has also allowed to study in great detail its superfluid behaviour [18–20]. Recent progresses augur the appearance of a new generation of opto-electronic devices based on microcavity-polaritons in the next years [21–34].

This PhD thesis is devoted to the study of exciton-polariton condensates in semiconductor microcavities. Here these cold gases made of exciton-photon mixtures are optically excited, both resonantly and non-resonantly, and imaged in both real and momentum spaces through simple optical setups. Coherence and phase properties, together with energy and time resolution, allows for the full characterization of macroscopic wavefunctions, paving the way towards the manipulation of coherent matter waves in a semiconductor chip.

Part I describes the physics background underlying the creation of polariton condensates. The interactions between semiconductor quasiparticles involved in the formation of polaritons are described from a classical, semiclassical and quantum points of view in Chapter 1. Special attention is given to light propagation in microcavities and its interaction with the dipole moment of quantum well excitons that form polaritons. High bosonic densities and liquid Helium temperatures enable polaritons to condense into a single coherent state out of equilibrium, whose basic properties are discussed in Chapter 2 and contrasted with the ones of atomic Bose-Einstein condensates and superfluid Helium. We present in Part II a detailed description of the samples, Chapter 3, and experimental procedures, Chapter 4, used in all the subsequent parts of the thesis.

Part III deals with the occurrence of topological defects in polariton superfluids in the optical parametric oscillator (OPO) regime. Although there are similarities with rotating trapped gases, non-equilibrium systems show a richer phenomenology. Chapter 5 reports the observation of metastable persistent polariton superflows sustaining a quantized angular momentum, $M\hbar$, after applying a 2-ps laser pulse carrying a vortex state [20,35]. A gain response in the condensate lasts for tens of picoseconds during which no dissipation of the circulating currents is detected. Angular momentum can be also transferred directly into the steady state, which acquires permanent rotation for as long as the vortex remains within the condensate. We use two different ways of measuring the circulation

of the condensate and demonstrate that in both cases, polariton condensation in the parametric scattering regime can sustain permanent supercurrents. In Chapter 6, the deterministic behavior of both the onset and dynamics of vortex-antivortex pairs generated by perturbing the system with a pulsed probe is explained in terms of local supercurrents [36]. Simulations elucidate the reason why topological defects form in pairs and can be detected by direct visualizations in multishot OPO experiments. Finally, in Chapter 7, the stability of quantized vortices with topological charge $M = 2$ is studied [20]. The experiments are analysed using a generalized two-component Gross-Pitaevskii equation including photonic disorder, pumping and decay. These results demonstrate the control of metastable persistent currents and show the peculiar superfluid character of non-equilibrium polariton condensates.

Part IV is devoted to polariton condensates created under non-resonant excitation. In Chapter 8, it is shown how a highly dense polariton population, created at a tiny spatial region, condenses into a single energy mode. Such a condensate is expelled from the pumping region due to strong repulsive interactions with the incoherent reservoir [37]. Polaritons thus feel an outward force while preserving the single energy phase-coherent mode, forming and expanding condensate which can propagate over distances two orders of magnitude bigger than the pumping spot. Such an easy, all-optical, control of repulsive potentials and propagation amplitudes allows for the creation of many extended polariton condensates close together and permits studying new phenomena appearing in the region where they overlap. In Chapter 9, polaritons injected at two or more spatially separated pump spots are shown to phase-lock responding to translational symmetries in a new geometrical process. The extremely low disorder of the sample foster the appearance of up to 100 vortices and antivortices distributed in a hexagonal network stable for many minutes [32]. The resultant regular vortex lattices are highly sensitive to the optically-imposed geometry, with 4 pump spots producing bistable square lattices, the optical equivalents to 1D and 2D spin systems with (anti)-ferromagnetic interactions controlled by their symmetry. Modulational instabilities are present in square lattices, where higher polariton densities are responsible for non-linear dynamics of topological defects that move inside guides defined by the geometry. Even more pronounced nonlinearities are discussed in Chapter 10, where the self-repulsion of polaritons is shown to be so nonlinear as to modify its own potential, creating stable archetypal quantum oscillator wavefunctions in real space. More in detail, two dense polariton condensates self-organizes into equally-spaced energy modes in the overlapping region, a solid-state macroscopic version of the simple quantum harmonic oscillator. Interference in time and space reveals that the many condensate modes are intercoherent, generating wavepackets oscillating at tunable THz frequencies. Such systems, which can be reconfigured on the fly, pave the way to widespread applications in the control of quantum fluidic circuits.

Part I

Background

Chapter 1

Semiconductor Microcavities

In this chapter the main physical processes behind light-matter interaction in semiconductor microcavities are described. Special attention is given to $AlGaAs$-based DBR-microcavities, with embedded quantum wells, in the strong coupling regime, which is the physical system underlying all the results obtained in this thesis.

1.1 Semiconductor crystals

A first attempt to physically describe a semiconductor crystal is to write up the Hamiltonian describing all possible interactions between the crystal constituents. As this is clearly impossible to compute, a number of approximations has to be made, according to which phenomena is to be described. The first is to separate electrons into two groups: *core electrons*, the ones in the filled orbitals localized around the nuclei forming the *ion cores*; and the *valence electrons*, the ones in the unfilled orbitals that can move around the crystal.

The next approximation usually invoked is the *Born-Oppenheimer* or *adiabatic approximation*, that assumes that electrons respond almost instantaneously to the movement of the nuclei or, in other words, that to the electrons the ions are essentially stationary. On the other hand, ions cannot follow the motion of the electrons and they see only a time-averaged adiabatic electronic potential. The Hamiltonian of a semiconductor crystal can then be written as:

$$\mathcal{H} = \mathcal{H}_{ions} + \mathcal{H}_e + \mathcal{H}_{e-ions} \tag{1.1}$$

The first term, $\mathcal{H}_{ions}$, describes interaction between atomic nuclei and cores electrons. Its ground state accounts for the crystalline structure. As an example, we describe Gallium Arsenide compounds which are the materials used on the experiments performed in this work. $GaAs$ has a zincblende cubic crystal structure, where each Ga (As) atom is surrounded by four As (Ga) atoms placed at the vertices of a tetrahedron — see Fig.1.1a, where Ga atoms are represented by yellow spheres and As by grey ones. The square box in this figure defines the *unit cell* which, in a perfect crystal, is repeated side-by-side all over the crystal dimensions. In $GaAs$, the unit cell size is $a = 0.565\,nm$.

Before describing the other two terms in Equation 1.1, let us first define a fundamental concept in condensed matter physics: the 1^{st} *Brillouin zone*. Eigenstates of the Hamiltonian 1.1 are usually written in momentum ($\mathbf{k}$) basis, defining a reciprocal space which is related to propagation directions inside the crystal. Periodical potentials implies Bloch-like solutions $\phi(\mathbf{k})$ whose values for any $\mathbf{k}$ are mapped into a small region in

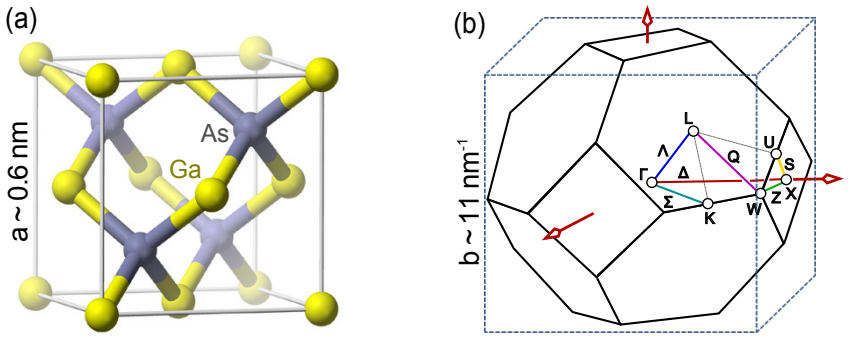

Figure 1.1: *GaAs* crystal structure in real and reciprocal spaces. (a) Zinc-blende unit cell, showing *Ga* and *As* atoms linked together in a tetrahedral structure. a is the unit cell size. (b) 1^{st} Brillouin zone inside a cubic unit cell, with special high-symmetry points denoted by Γ, X, L, K, W and U, while high-symmetry lines joining some of these points are labeled as Λ, Σ, Δ, Q, Z and S. b indicates the typical cell size for *GaAs*.

reciprocal space, the primitive unit cell, called 1^{st} *Brillouin zone*. Fig.1.1b shows the 1^{st} Brillouin zone of a *GaAs* crystal, whose typical size given by $b = 2\pi/a \sim 11nm^{-1}$. Its high-symmetry points and directions are named by Greek and capital letters.

The term $\mathcal{H}_{ions}$ also accounts for crystal collective excitations, such as *phonons* — a *quasiparticle* representing a vibrational excitation of the crystal, characterized by a definite energy and momentum. The phonon dispersion curves in a *GaAs* crystal are shown in Fig.1.2 where, instead of showing the energy as a function of all possible three-dimension k values, the high-symetry directions defined in Fig. 1.1b are chosen. In the diamond- and zincblende- type lattices there are two atoms per primitive unit cell, and hence there are six phonon branches. These are divided into three acoustic–phonon (the three lower energy curves) and three optical–phonon branches (Fig.1.2). Along high-symmetry directions the phonons can be classified as transverse or longitudinal according to whether their displacements are perpendicular or parallel to the propagation direction.

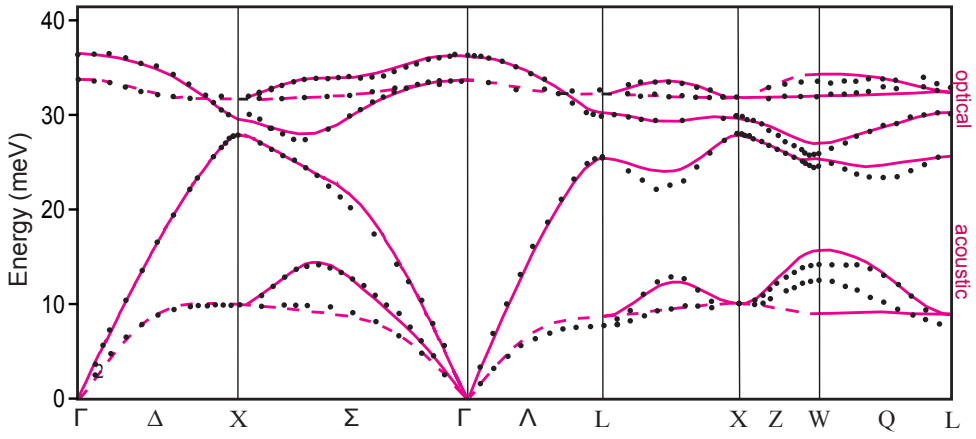

Figure 1.2: *GaAs* phonon dispersion curves along high-symmetry directions of the 1^{st} Brillouin zone, measured by inelastic neutron scattering (dots) and calculated using a rigid-ion model (lines). The x-axis and its dimensions are defined in Fig. 1.1b. The three upper modes are known as optical–phonons and the three lower ones acoustic–phonons. Adapted from [38].

The middle term in Eq. 1.1, $\mathcal{H}_e$, is the Hamiltonian for the *valence electrons* with

the ions frozen in their equilibrium positions. Again, different approximations may be taken: in the *mean-field approximation*, every electron experiences the same averaged potential that includes the nuclei and core electrons. Also, the highly attractive nuclei potentials may be replaced by smoother *ion pseudopotentials* that include core electrons, yielding slowly oscillating valence electron wavefunctions. Such approximations yield to solutions that are determined by the specific chemical nature of each material. These solutions are again given in energy vs momentum basis as a *single electron dispersion*, also known as *band structure*. Fig.1.3 provides the $GaAs$ band structure, calculated by the pseudopotential technique [38], along the main symmetry directions of the 1^{st} Brillouin zone. According to the *Pauli's Exclusion Principle*, each eigenstate can only accommodate up to two electrons of opposite spin. At zero temperature, electron fill up all the *valence band*, defined by the energy states below $0\,eV$. As temperature increases, or any other external excitation is given to electrons, they might acquire enough energy as to start filling also the *conduction band*.

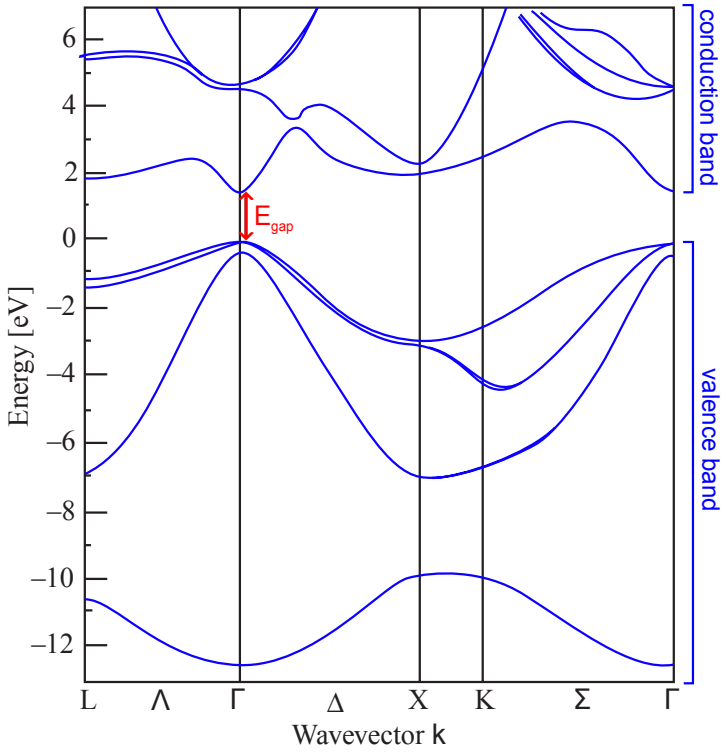

Figure 1.3: GaAs electron dispersion curves, calculated by the pseudopotential technique. The x-axis and its dimensions are defined in Fig. 1.2b. Positive energy branches are named as *conduction band* whereas negative ones as *valence band*. Adapted from [38].

The energy difference between the maximum of the valence band and the minimum of the conduction band is known as *bandgap*, E_{gap}. In $Al_xGa_{1-x}As$ compounds, the bandgap at room-temperature varies between $1.42eV$ ($GaAs$) and $2.16eV$ ($AlAs$). For $x < 0.35$, the bandgap is direct (the minimum of the conduction band and the maximum of the valence band are at the same wavevector $\mathbf{k} = 0$), which makes this material good for optical applications, since transitions of electrons from valence to conduction bands and vice-versa happens without any change in momentum, and so no phonon contributions are needed.

Finally, the last term in Eq. 1.1, $\mathcal{H}_{e-ions}$, describes changes in the electronic energy

as a result of the displacements of the ions from their equilibrium positions. $\mathcal{H}_{e-ions}$ is also known as *electron-phonon interaction*, since under the second quantization picture it accounts for scattering between electron and phonon to final states through momentum and energy exchange. When electrons are excited from their equilibrium state to higher energy ones, $\mathcal{H}_{e-ions}$ accounts for electron thermalisation by loosing energy to lattice phonons. Close to the equilibrium point ($E = E_{gap}$, $\mathbf{k} = 0$), if the excess energy is higher than the lattice optical–phonons energies, relaxation is fast through interactions that exchange high energy and momentum (see Fig. 1.2); when the excess energy becomes smaller than those of optical–phonons, relaxation is only possible through small energy and momentum exchanges, which are slow.

1.2 Excitons

In a semiconductor at zero temperature, the fundamental optical excitation consists on the promotion of an electron from the top of the valence band to the bottom of the conduction band. The state left empty in the valence band can be pictured as a positive charge in an empty band, which is defined as a quasiparticle called *hole*. This enables us to consider the valence band masses[1] as positive in all practical calculations, despite the fact that from the single electron picture they have negative curvature — see Fig. 1.3. The two highest energy branches in the valance band dispersion are called heavy–hole and light–hole branches, according to their curvatures.

The properties of the electron and the hole are both described by the band structure within the one-electron approximation. Negatively charged electrons in the conduction band and positively charged holes in the valence band are subject to Coulomb attraction. This electron-hole interaction gives rise to bound states called *excitons*. In most semiconductors, in particular *GaAs* compounds used in this work, the Coulomb interaction is strongly screened by the valence electrons: the large dielectric constant causes that the electrons and holes are only weakly bound. Such excitons, known as Wannier-Mott excitons, have a typical size of the order of tens of lattices constants and a relatively small binding energy (typically, a few meV).

The *band engineering* in semiconductor structures by means of high-precision growth methods has allowed the creation of a number of electronic and opto-electronic devices including transistors, diodes and lasers. It has also permitted discovery of important fundamental effects including the integer and fractional quantum Hall effects, Coulomb blockade, light-induced ferromagnetism, etc. When epitaxially growing semiconductor materials, the component of thin layers can be varied in order to locally define band structures that are different from the surrounding material. In this way the potential energy of electrons and holes, V_e and V_h, are described for two-dimensional systems, in the growth direction, by quantum wells whose depth and size can be tuned by changing the layer composition and thickness — see insets in Fig. 1.4. The electron and hole ground state energies, E_e and E_h, and wave functions, Φ_e and Φ_h, are tuned accordingly. The large size of Wannier–Mott excitons makes them strongly sensitive to nanometre-scale variations in the quantum well (QW) size — see graph in Fig. 1.4. These QWs are placed inside the microcavities used in this thesis in such a way that the exciton energy

[1] the effective mass is defined as $m^* = \hbar^2 / \left(\frac{\partial^2 E}{\partial k^2}\right)$, where $E(k)$ is the electron dispersion relation. Note that close to the Γ point in Fig. 1.3 the valence band has negative mass whereas the conduction band has positive mass. Note also that the effective mass is inversely proportional to the dispersion curvature.

can be tuned to resonance with the photons confined inside the microcavity, as will be discussed in Section 1.4.

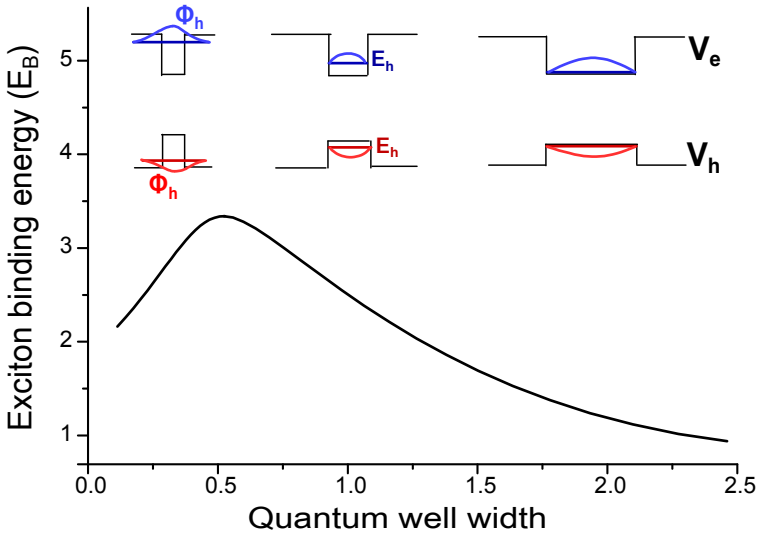

Figure 1.4: Exciton binding energy as a function of the QW width (schema). The insets show the QW potentials, V_e and V_h, and ground state energies, E_e and E_h, and wave functions, Φ_e and Φ_h, of electron (blue) and hole (red), respectively, for different QW widths. Adapted from [39].

The relative electron-hole motion can be found from the Hamiltonian describing the exciton envelope wavefunction [38, 39]. We then add one extra term in the Hamiltonian 1.1 to account for electron–hole coulomb interactions ($\mathcal{H}_{e-h}$):

$$\mathcal{H} = \mathcal{H}_{ions} + \mathcal{H}_e + \mathcal{H}_{e-ions} + \mathcal{H}_{e-h} \tag{1.2}$$

$$\mathcal{H}_{e-h} = -\frac{\hbar^2}{2m_e}\nabla_e^2 - \frac{\hbar^2}{2m_h}\nabla_h^2 + V_e(z) + V_h(z) - \frac{e^2}{4\pi\varepsilon r} \tag{1.3}$$

where $m_{e(h)}$ is the electron (hole) effective mass, z the axis in the confinement direction, e the elementary charge, ε the electric permittivity and r the electron-hole distance.

Without the confining terms, Eq. 1.3 is equivalent to one describing the electron state in a hydrogen atom. For example, the wavefunction of the $1s$ state of a bulk exciton reads:

$$f_{1s} = \frac{e^{-r/a_B}}{\sqrt{\pi a_B^3}} \tag{1.4}$$

with the Bohr radius a_B given as:

$$a_B = \frac{4\pi\hbar^2\varepsilon}{\mu_{eh}e^2} \tag{1.5}$$

with $\mu_{eh} = \frac{m_e m_h}{m_e+m_h}$ the electron-hole reduced effective mass.

The binding energy of the ground exciton state is

$$E_B = \frac{\hbar^2}{2\mu_{eh}a_B^2} \tag{1.6}$$

Table 1.1 presents the exciton parameters in the reduced mass approximation for GaAs, compared to those of the Hydrogen atom.

	GaAs exction	Hydrogen atom
reduced mass μ/m_e	0.058	~ 1
Bohr radius a_B	$15\,nm$	$0.053\,nm$
binding energy E_B	$4.1\,eV$	$13.6\,eV$

Table 1.1: Comparison between GaAs exciton parameters in the reduced mass approximation and those of the Hydrogen atom.

The description we have followed so far used the single electron picture. However, under high densities when both excitons and electron-hole plasma are present, the Coulomb carrier-carrier potential starts to be important, with changes of the dielectric constant ϵ that describes the surrounding media. Thus, the exciton binding energy gets progressively reduced. When dealing with materials with bandgap in the infrared region, *i.e. GaAs*, this corresponds to a shift towards blue frequencies in the electromagnetic spectra, hence the name *blueshift*. If the carrier density is further increased, the excitons eventually dissociate.

1.3 Light propagation inside materials

In this section we explain in detail how electromagnetic-waves propagate inside materials, giving special attention to *DBR-microcavities* — engineered nanostructures that confine and guide light using index of refraction differences in different materials (see Section 1.3.1)

The *electric field*, **E**, and the *magnetic field*, **H**, inside a medium are related spatio-temporally to the *charge density* ρ_e, *current density* **J**, *polarization density* **P**, and *magnetization density* **M**, through the Maxwell equations (SI units) [40]:

$$\nabla \cdot \mathbf{D} = \rho_e \tag{1.7a}$$

$$\nabla \cdot \mathbf{B} = 0 \tag{1.7b}$$

$$\nabla \times \mathbf{E} = -\partial_t \mathbf{B} \tag{1.7c}$$

$$\nabla \times \mathbf{H} = \mathbf{J} + \partial_t \mathbf{D} \tag{1.7d}$$

The *electric flux* **D**, and *magnetic flux* **B**, are defined by:

$$\mathbf{D} = \varepsilon_0 \mathbf{E} + \mathbf{P} = \varepsilon \mathbf{E} \tag{1.8a}$$

$$\mathbf{B} = \mu_0\mathbf{H} + \mathbf{M} = \mu\mathbf{H} \tag{1.8b}$$

Where ε is called *permittivity* and μ, *permeability*.

Considering a medium with neither free charge ($\rho_e = 0$) nor currents ($\mathbf{J} = 0$) and taking the curl of Eq. 1.7c and using Eqs. 1.7d and 1.8, one gets to the following equation for the electric field[2] [41]:

$$\boldsymbol{\nabla^2}\mathbf{E} = \mu\varepsilon\partial_{tt}\mathbf{E} \tag{1.9}$$

which can be identified as a wave equation whose solutions propagate with velocity given by

$$v = \frac{c}{n} = \frac{1}{\sqrt{\mu\varepsilon}} \tag{1.10}$$

where the *refractive index*, n, accounts for the speed reduction of an electromagnetic wave propagating inside a medium. In this section we consider n as a scalar with constant value for each material, however it can be a tensor (accounting for birefringence in anisotropic materials), complex-valued (accounting for absorption) and dependent on the electric field (non–linear electric materials) and on the magnetic field (non–linear magnetic materials).

For a transverse light wave propagating along the z-direction in a medium with wavevector $k = k_0 n$, where k_0 is the wavevector in vacuum, solutions of 1.9 have the general form:

$$E(z) = A^+(z) + A^-(z) = |A^+|e^{ik_0 nz} + |A^-|e^{-ik_0 nz} \tag{1.11a}$$

$$B(z) = \frac{-i}{k_0 c}\partial_z E(z) = \frac{n}{c}|A^+|e^{ik_0 nz} - \frac{n}{c}|A^-|e^{-ik_0 nz} \tag{1.11b}$$

which can also be represented using the positive-, $A^+(z)$, and negative-, $A^-(z)$, propagating electric fields:

$$A^+(z) = \frac{1}{2}(E(z) + \frac{c}{n}B(z)) \tag{1.12a}$$

$$A^-(z) = \frac{1}{2}(E(z) - \frac{c}{n}B(z)) \tag{1.12b}$$

The electromagnetic fields at two different positions along the propagation direction, z and $z + a$, are related through a transfer matrix [39]:

$$\boldsymbol{\Phi}_{z+a} = \mathbf{T}_a\boldsymbol{\Phi}_z \tag{1.13a}$$

$$\boldsymbol{\Phi}_z = \begin{pmatrix} E(z) \\ cB(z) \end{pmatrix} = \begin{pmatrix} E(z) \\ \frac{-i}{k_0}\partial_z E(z) \end{pmatrix} \tag{1.13b}$$

$$\mathbf{T}_a = \begin{pmatrix} \cos k_0 na & \frac{i}{n}\sin k_0 na \\ in\sin k_0 na & \cos k_0 na \end{pmatrix} \tag{1.13c}$$

[2] using the relation $\nabla \times \nabla \times \mathbf{E} = \nabla(\nabla \cdot \mathbf{E}) - \boldsymbol{\nabla^2}\mathbf{E}$ and considering $\nabla \cdot \mathbf{E} = 0$

Such an approach is very useful when solving Maxwell equations in multilayer dielectric structures, where the transfer matrix across m layers is found as:

$$\mathbf{T} = \prod_{\mathbf{i=1}}^{\mathbf{m}} \mathbf{T_i} \tag{1.14}$$

In condensed matter materials, light is guided through differences in refraction indices. When coming from the left side of a boundary between two media with refraction indices n_1(left) and n_2 (right) — see Fig. 1.5a, the matching of the tangential components of electric and magnetic fields gives:

$$A_1^+ + A_1^- = A_2^+ \tag{1.15a}$$

$$(A_1^+ - A_1^-)n_1 = A_2^+ n_2 \tag{1.15b}$$

The *Fresnel amplitude reflection* and *amplitude transmission* coefficients are defined as:

$$r = \frac{A_1^-}{A_1^+} = \frac{n_1 - n_2}{n_1 + n_2} \tag{1.16a}$$

$$t = \frac{A_2^+}{A_1^+} = \frac{2n_1}{n_1 + n_2} \tag{1.16b}$$

The *reflectivity* R (ratio of reflected to incident energy flux) and the *transmittance* T (ratio of transmitted to incident energy flux) are defined as

$$R = |r|^2 \tag{1.17a}$$

$$T = \frac{n_2}{n_1}|t|^2 \tag{1.17b}$$

The factor n_2/n_1 comes from the ratio of light velocities in the two media. If losses are not taken into account, $T = 1 - R$.

Fig. 1.5b shows the reflectivity R between the two media with refraction indices n_1 and n_2 (Eqs. 1.16a and 1.17a). Clearly the amount of reflected wave on an interface between two media is higher for higher index contrasts, but does not depend on which side of the interface has the higher index. On the other hand, it follows from Eq. 1.16a that, when incident on a higher n medium ($n_2 > n_1$), the reflected field has a π-phase shift (r is negative), whereas no shift appears when the field is reflected by a lower n medium ($n_2 < n_1$, r is positive). Moreover, from Eq. 1.16b, t is always positive and so there is no phase-shift on the transmitted field.

The reflectivity can be improved with the use of multiple interfaces that reflect a wave multiple times. The amplitude reflection and transmission coefficients (r_s and t_s) of a structure containing m layers between two semi-infinite media with refractive indices n_{left} and n_{right} before and after the structure, respectively, can be found by solving the system: [39]

$$\mathbf{T}\begin{pmatrix} 1 + r_s \\ n_{left}(1 - r_s) \end{pmatrix} = \begin{pmatrix} t_s \\ n_{right} t_s \end{pmatrix} \tag{1.18}$$

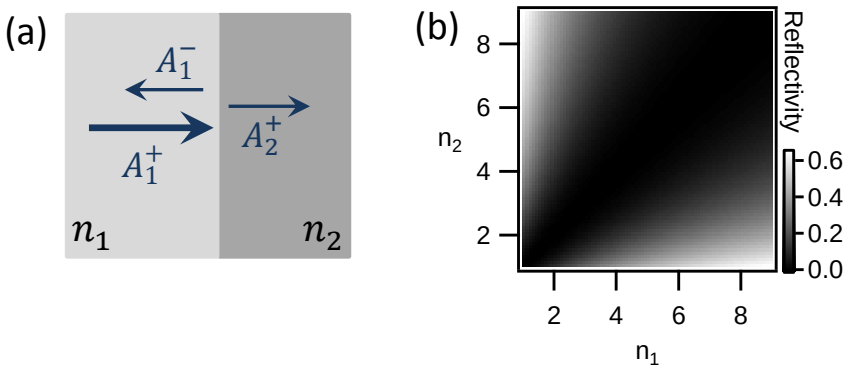

Figure 1.5: (a) Schematic representation of an electromagnetic wave incident perpendicularly on an interface between two media with refractive indices n_1 and n_2. Arrows represent the incoming, A_1^+, the reflected, A_1^-, and the transmitted, A_2^+, amplitudes. (b) Reflectivity between the two media in (a) as a function of n_1 and n_2.

Moreover, if such interfaces are be engineered in such a way that multiple reflections interfere destructively for the transmitted wave, even higher reflectivity can be achieved. This is the main concept behind the high-reflectivity mirrors used in microcavity structures, described in the next Section.

1.3.1 Microcavities

A microcavity is an optical resonator that confines light to small volumes by resonant recirculation. Its dimensions are related to the wavelength of the mode confined inside — micrometer scale for light modes, hence its name. Although geometrical and resonant properties of microcavities are diverse [42], two basic different schemes are used to confine light. In the first, reflection off a single interface is used, for instance from a metallic surface, or from total internal reflection at the boundary between two dielectrics. The second scheme is to use the interference between multiple reflections on microstructures periodically patterned on the scale of the resonant optical wavelength, like *e.g.* in a photonic crystal. Below we describe two devices representative of the second scheme: the Fabry-Perrot interferometer and the DBR-microcavity. We illustrate all the devices with simulations using the Transfer Matrix Method (Eq. 1.13), choosing for that the parameters of a sample investigated on this thesis — described in Section 3.2.

1.3.1.1 Fabry-Perrot interferometer

A Fabry-Perrot (FP) interferometer consists of a transparent plate with two reflecting surfaces. It can be found as a central part of most lasers, forming the cavity resonator, but also has its role on more fundamental physics, *e.g.* circuit quantum electrodynamics [43]

Fig. 1.6 shows a simple version of a FP interferometer, made of a medium with thickness L_c and refractive index $n_c > 1$ surrounded by air. Let us consider only the waves reflected into the air on the left side of the FP. Light with amplitude A_i incident into the left interface is partially reflected with amplitude

$$A_r^1 = -|r|A_i, \tag{1.19}$$

where $r = \frac{1-n_c}{1+n_c}$ and the minus sign accounts for a π-phase jump from reflection by the higher refractive index FP medium. Another part is transmitted into the FP medium,

being partially reflected on the right interface and partially transmitted into air at the left interface with amplitude

$$A_r^2 = A_i t_- |r| t_+ e^{i\delta}, \tag{1.20}$$

where $t_+ = \frac{2}{1+n_c}$ is the transmission coefficient *into* the FP medium, $t_- = \frac{2n_c}{n_c+1}$ the transmission coefficient *out from* the FP medium, and

$$\delta = \frac{2\pi}{\lambda_0} 2n_c L_c = \frac{\omega}{c} 2n_c L_c, \tag{1.21}$$

is the phase acquired by the beam while propagating inside FP medium, with λ_0 the wavelength in air and ω the wave frequency multiplied by 2π.

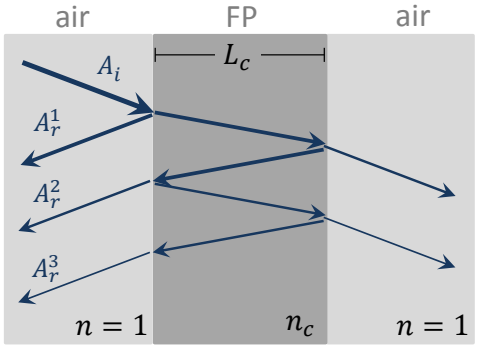

Figure 1.6: Schematic Fabry-Perrot interferometer, showing a L_c-thick medium with refractive index n_c between air ($n = 1$). The incident, transmitted and reflected beams are represented by arrows, with amplitude on the left side labelled by A_i (incident) and A_r^n (reflected), with $n = 1, 2, 3$.

The process described above happens many times with the field on the left side of the FP being then the sum of all the reflected beams:

$$A_r = \sum_{n=1}^{\infty} A_r^n = A_i \left(-|r| + t_- t_+ \sum_{n=2}^{\infty} |r|^{2n-3} e^{i\delta(n-1)} \right) = A_i \left[-|r| + \frac{t_+ t_-}{|r|} \left(\frac{1}{1 - r^2 e^{i\delta}} - 1 \right) \right] \tag{1.22}$$

Note that the relative phase between subsequent reflections is always δ. The amount of reflected light — and hence the reflective character of the FP interferometer — depends on interferences between multiple reflections, and so, from Eq. 1.21 on the wave frequency ω and on the FP parameters n_c and L_c.

Fig. 1.7a shows the electric field profile (simulated using Eq. 1.13) with wavelength in air $\lambda_0 = 800\,nm$ incident on a FP interface with $n_c = 3.4$ and $L_c = \frac{5\lambda_0}{2n_c} \sim 588\,nm$. Putting these values into Eq. 1.21 we have $\delta = 10\pi$, meaning that all the $A_r^{n>2}$ comes out of the mirror with the same phase, which has a π-phase difference with respect to the A_r^1 component. The result is that A_r^1 is destructively interfered by all the $A_r^{n>2}$ components, and the only component on the left side of the structure is A_i, making a flat electric field profile $|E| = |A_i|$. Since no light is reflected, the reflectivity of such a FP is zero at $800nm$ — see the FP reflectivity dependence on wavelength in Fig. 1.7c. Inside the FP medium, the difference in phase between right propagating components and left propagating ones is an integer multiple of 5π, generating a standing wave (Fig. 1.7a).

Following the same logic, if the incident field has a wavelength such that $\delta = 11\pi$ (or any other odd multiple of π), the second and third reflected components will sum up to:

$$A_r^2 + A_r^3 = A_i t_+ t_- (e^{i11\pi} + r^2 e^{i22\pi}) = A_i t_+ t_- (-1 + r^2), \tag{1.23}$$

which is a negative number since $r^2 < 1$. These two components then constructively interfere with the also negative A_r^1 component, the same holding for $A_r^4 + A_r^5$ and so on. The overall reflected field is then greatly enhanced and the FP becomes reflective. This is indeed observed when calculating the electric field profile for $\lambda_0 = \frac{2\pi}{11\pi} 2n_c L_c \sim 727\,nm$ — see Fig. 1.7b, where the reflected field generates an standing wave on the left side of the FP. Accordingly, the reflectivity is maximum at $727\,nm$ — red arrow in Fig. 1.7c.

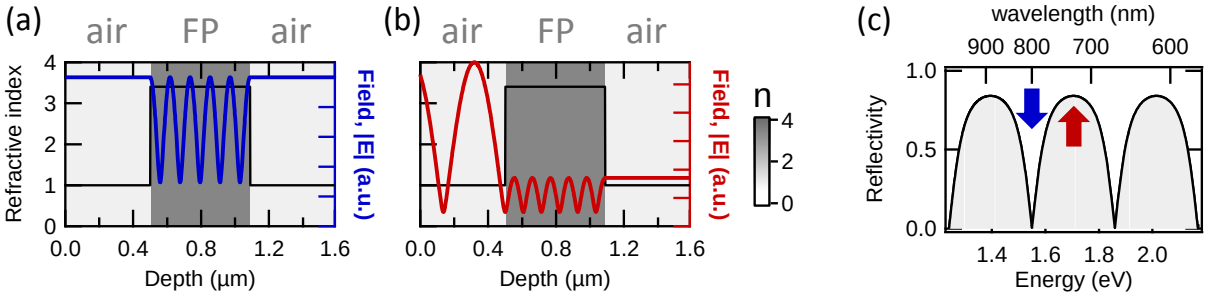

Figure 1.7: Fabry-Perrot interferometer as simulated by the Transfer Matrix Method - Eq. 1.13, using parameters $n_c = 3.4$, $L_c = 588nm$. The field spatial profile is plotted for (a) $\lambda_0 = 800\,nm$ (blue line) and (b) $\lambda_0 = 727\,nm$ (red line). In (a,b) the refractive index is represented by both the black line and the gray colorscale. (c) Reflectivity curve for different incident light frequencies, calculated using Eq. 1.18. The blue arrow marks the wavelength of the field plotted in (a) whereas the red arrow marks the wavelength of the field plotted in (b).

Till now we have considered light impinging perpendicularly incidence to the FP interface. For oblique incidence, the beam should be decomposed **inside the cavity** into its components perpendicular and parallel to the surface, and then apply a similar analysis to that already described for the perpendicular component. The perpendicular wavevectors $k_\perp$ for which the FP reflectivity goes to zero are found when making $\delta = 2\pi q$, with q integer, and $k_\perp = 2\pi n_c/\lambda_0$ on Eq. 1.21:

$$k_\perp = \frac{\pi q}{L_c} \tag{1.24}$$

The modes defined by Eq. 1.24, known as *cavity modes*, have an integral number of half-wavelengths that fit into the microcavity. Their energy E_c are given by:

$$E_c = \hbar c k = \frac{\hbar c}{n_c}\sqrt{{k_\parallel}^2 + {k_\perp}^2} = \hbar c\sqrt{{k_\parallel}^2 + \left(\frac{\pi q}{L_c}\right)^2} \tag{1.25}$$

Equation 1.25 is the dispersion relation of a photon with energy E_c inside the FP cavity. Close to perpendicular incidence ($k_\parallel \ll k_\perp$) it can be approximated to:

$$E_c = E_c^0 + \frac{\hbar^2 k_\parallel^2}{2m_{ph}^*} \tag{1.26}$$

where $E_c^0 = \frac{\hbar\pi qc}{n_c L_c}$ is the mode energy for perpendicular incidence and $m_{ph}^* = \frac{\hbar\pi q n_c}{L_c c}$ is the so called *photon effective mass*.

Another important feature of a Fabry-Perot is its selectivity. It is characterized by the finesse $\mathcal{F}$, which is the ratio between the mode separation (in energy) and the mode full width at half maximum. It can be shown [39] that it depends only on the reflectivity of the FP interfaces:

$$\mathcal{F} = \frac{\pi r}{1 - r^2} \tag{1.27}$$

The higher the reflectivity between interfaces, the higher the photon lifetime inside the cavity. The cavity mode width depends on the reflectivity of each mirror and sets the photon lifetime inside the cavity. High quality samples are those with long photonic lifetimes, and so it is useful to define a *quality factor*, defined as the ratio of a resonant cavity frequency, ω_C, to the linewidth (FWHM) of the cavity mode, $\delta\omega_C$ [39].

$$Q = \frac{\omega_C}{\delta\omega_C} \tag{1.28}$$

The Q-factor is a measure of the rate at which optical energy decays from within the cavity (from absorption, scattering or leakage through the imperfect mirrors) and where Q^{-1} is the fraction of energy lost in a single round-trip around the cavity. Equivalently, the exponentially decaying photon number has a lifetime given by $\tau = Q/\omega_C$.

The best candidates to achieve high quality factors through the use of high reflectivity mirrors are described in next section.

1.3.1.2 DBR-mirror

The ideas based on multiple inferences described in previous sections to achieve high reflectivity mirrors can be further developed by adding more extra layers to the FP scheme in Fig. 1.6. In fact, if all the components reflected by each layer comes out of the structure on the left side with same phase, π-shifted with respect to the incident beam, they will all interfere constructively and reflectivity will be maximum. This can be achieved, *e.g.*, for a given λ_0 to which we want the structure to be reflective, by using for the first layer $n_1 L_1 = \lambda_0/4$, for the second $n_2 L_2 = \lambda_0/4$, with $n_1 > n_2$, and then repeating the first pair layer a number of times. Such multilayer periodic structure is called *Bragg mirror*, also known as *distributed Bragg reflector (DBR)* mirror. The working principle relies on light interference: all the waves propagating on the reflection direction, after multiple reflections on all the interfaces present in the structure, are in phase. Conversely, all the waves propagating in the transmission direction interfere destructively.

Fig. 1.8a shows the electric field profile (simulated using Eq. 1.13) with wavelength in air $\lambda_0 = 800\,nm$ incident on a DBR-mirror made of 32 pairs of layers with $n_1 = 3.5$, $n_2 = 3$, $L_1 \sim 57\,nm$ and $L_2 \sim 67\,nm$. Under these conditions all the layer reflect the field with the same phase, creating a standing wave made of incident and reflected waves on the left side of the structure (air). Note that the standing wave nodes have zero intensity, meaning that the incident and reflected components have the same magnitude, and hence the mirror is $\sim 100\%$ reflective. Differently from a Fabry-Perrot interferometer, a DBR-mirror possess a considerable field penetration on the cavity due to low index contrast.

Fig. 1.8c shows the DBR reflectivity dependence on wavelength. Apart from the maximum expected at $800\,nm$ (blue arrow), the reflectivity is close to 1 for a wide range

of wavelength values centred at $800\,nm$. Such a plateau region of high reflectivity, known as *stop-band*, becomes broader for higher index contrast between layers and higher number of pair layers. The stop-band is surrounded by transmissive energy modes called *Bragg modes*, whose name is due to the fact that the field distribution is mainly concentrated inside the DBR-mirror — see Fig. 1.8b for the field profile corresponding to a wavelength $\lambda_0 = 756\,nm$, marked by a red arrow in Fig. 1.8c.

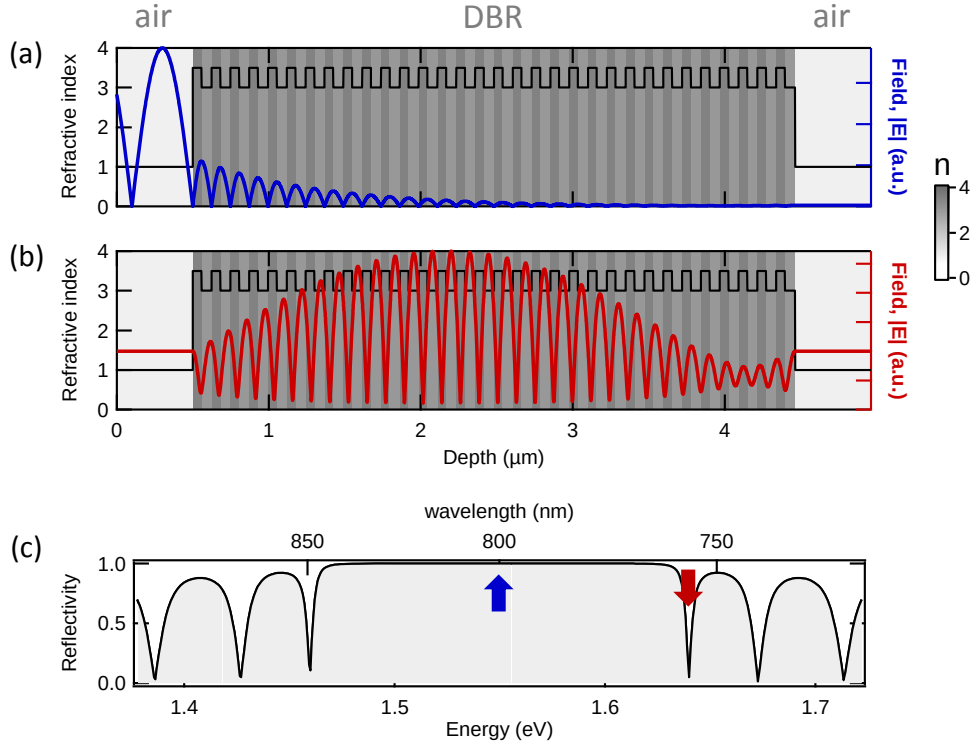

Figure 1.8: Bragg mirror as simulated by the Transfer Matrix Method - Eq. 1.13, using 32 pairs of layers with $n_1 = 3.5$, $n_2 = 3$, $L_1 \sim 57\,nm$ and $L_2 \sim 67\,nm$. The field spatial profile is plotted for (a) $\lambda = 800\,nm$ (blue line) and (b) $\lambda = 756\,nm$ (red line). In (a,b) the refractive index is represented by both the black line and the gray colorscale. (c) Reflectivity curve for different incident light frequency, calculated using Eq. 1.18. The blue arrow marks the wavelength of the field plotted in (a) whereas the red arrow marks the wavelength of the field plotted in (b).

1.3.1.3 DBR-microcavity

A semiconductor microcavity is formed by two DBR mirrors separated by a dielectric layer (the cavity itself), whose thickness determines the cavity mode wavelength, in the same way as in a Fabry-Perrot interferometer.

To illustrate how an electromagnetic field behaves inside a semiconductor microcavity, simulations are performed based on a semiconductor microcavity similar to the one described in Section 3.2: the left DBR is made of 32 pairs of layers with $n_1 = 3.5$, $n_2 = 3$, $L_1 \sim 57\,nm$ and $L_2 \sim 67\,nm$, whereas the right DBR is made of 35 pairs of layers with $n_1 = 3$, $n_2 = 3.5$, $L_1 \sim 67\,nm$ and $L_2 \sim 57\,nm$. Between both mirrors there is a a $5\lambda_0/2$ cavity with $n_c = 3.4$ and $L_c = \frac{5\lambda_0}{2n_c}$.

Fig. 1.9a shows the electric field profile (simulated using Eq. 1.13) with wavelength in air $\lambda_0 = 800\,nm$. Although the mirrors are $\sim 100\%$ reflective under these conditions

interferences with the components reflected by the cavity interfaces makes the whole structure transmissive at this specific wavelength — indicated by a blue arrow in Figs. 1.9c,d. The effect of the cavity on the reflectivity spectra is to open a sharp minima on the DBR stop band. The field is mainly confined inside the cavity, and so photons entering the cavity remain inside for a long time, which is consistent with a extremely sharp energy linewidth (Figs. 1.9d) and high Q-factor. The standing-wave profile with 5 nodes is consistent with the condition $L_c = \frac{5\lambda}{2n_c}$. Inside the cavity, the field have maximum amplitude at four antinodes that can be used to couple photons to exciton in QWs put at such positions, as it will be explained in Section 1.4.

Fig. 1.9c shows the DBR reflectivity spectrum. The mirror stop-band can be again observed, with the transmissive *Bragg modes* (red arrow) having again a field distribution mainly concentrated inside the DBR-mirrors — see Fig. 1.9b for the field profile corresponding to a wavelength marked by a red arrow in Fig. 1.9c.

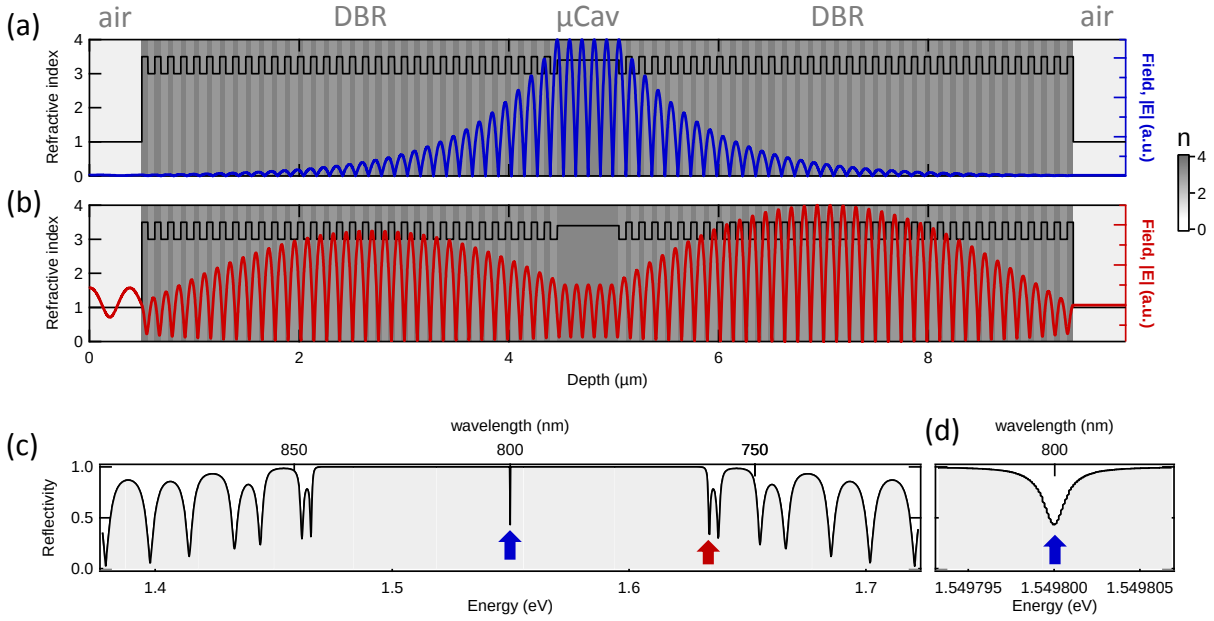

Figure 1.9: Semiconductor microcavity as simulated by the Transfer Matrix Method - Eq. 1.13, using 32 pairs of layers with $n_1 = 3.5$, $n_2 = 3$, $L_1 \sim 57\,nm$ and $L_2 \sim 67\,nm$ for the left DBR, a $5\lambda_0/2$ cavity with $n_c = 3.4$ and $L_c \sim 588\,nm$, and 35 pairs of layers with $n_1 = 3$, $n_2 = 3.5$, $L_1 \sim 67\,nm$ and $L_2 \sim 57\,nm$ for the right DBR. The field spatial profile is plotted for (a) $\lambda_0 = 800\,nm$ (blue line) and (b) $\lambda_0 = 759\,nm$ (red line). In (a,b) the refractive index is represented by both the black line and the gray colorscale. (c) Reflectivity curve for different incident light frequency, calculated using Eq. 1.18. The blue arrow marks the wavelength of the field plotted in (a) whereas the red arrow marks the wavelength of the field plotted in (b). (d) is a zoom of (c) close to the cavity mode ($800\,nm$).

Finally we consider oblique incidence. Reflectivity spectra as a function of incidence angle ϕ_{left} can be calculated by replacing on Eq. 1.18

$$n_{left} \rightarrow n_{left} cos(\phi_{left}), n_{right} \rightarrow n_{right} cos(\phi_{right}) \tag{1.29}$$

Fig. 1.10 shows the transmittance ($T = 1 - R$) dispersion for the microcavity described in Fig. 1.9. As the in-plane momentum $k_{\|}$ increases, the energy of transmissive modes increase, including the weakly transmissive cavity mode.

The dispersion of the cavity mode is expected to be parabolic for a Fabry-Perrot cavity (Eq. 1.26). We calculate the cavity mode energy for perpendicular incidence $E_c^0 = \frac{\hbar\pi 5c}{n_c L_c} = 1.5498eV$ and the photon effective mass $m_{ph}^* = \frac{\hbar\pi 5 n_c}{L_c c} = 2.2276 \times 10^{-34} kg = 2.4454 \times 10^{-4} m_e$, where m_e is the electron mass. The resulting parabolic dispersion is plotted in Fig. 1.10 (dashed blue line). It fits quite well the simulated cavity dispersion, seen as red behind.

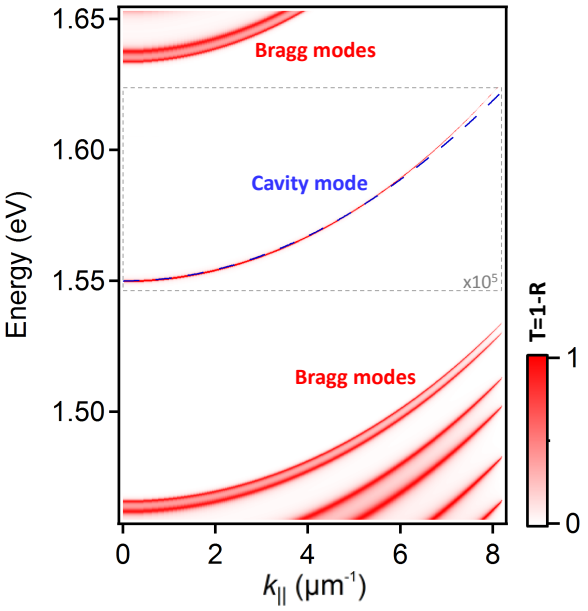

Figure 1.10: Transmittance spectra for the microcavity described in Fig. 1.9, as a function of incident wave energy and k-vector in air, simulated using Eqs. 1.18 and 1.29. High- and low-energy Bragg modes are indicated, as well as the weaker cavity mode. The transmittance of the region inside the dashed gray square has been multiplied by 10^5 to make the cavity mode to appear visible in the colorscale. The cavity mode dispersion, estimated using Eq. 1.26, is plotted as a dashed blue line.

Photons behave then as massive particles while propagating inside a cavity, with an effective mass extremely light if compared to that of an electron. The photon-exciton quasiparticles described in Section 1.4 will also have a very light mass, what is crucial for observing the macroscopic quantum effects described in Chapter 2 at high temperatures.

1.4 Polaritons

When an intrinsic semiconductor crystal is held at cryogenic temperatures, like in all the results presented on this thesis, the thermal energy is not high enough as to promote electrons from the valence to the conduction band, and so the system remains electronically on its ground state. Excitation to higher modes can be done by laser beams, where the energy carried by photons are absorbed by electrons that acquire higher energy.

The photon dispersion relation was computed in section 1.3 when considering the eletromagnetic field propagation inside materials. The cavity mode energy was considered to remain unafected while propagating inside the media. This is equivalent to add a $\mathcal{H}_{ph}$ term to the Hamiltonian 1.2 that accounts for *photonic dispersion*.

In this section we describe how photons drive excitonic-dipole oscillations that changes the energy modes of the system, introducing a last term in Hamiltonian 1.2 called *electron-photon interaction*, $\mathcal{H}_{e-ph}$:

$$\mathcal{H} = \mathcal{H}_{ions} + \mathcal{H}_e + \mathcal{H}_{e-ions} + \mathcal{H}_{e-h} + \mathcal{H}_{ph} + \mathcal{H}_{e-ph} \tag{1.30}$$

1.4.1 Semiclassical light-matter coupling

First we consider light coupling to elementary semiconductor crystal excitations — excitons — and discuss the optical properties of mixed light-matter quasiparticles named exciton-polaritons, which play a decisive role in optical spectra of microcavities. Our considerations are based on the classical Maxwell equations coupled to quantum properties of excitons.

In the semiclassical approximation of light-exciton interaction, electron and hole are bounded together by an harmonic potential $\mu_{eh}\omega_x^2$, $\hbar\omega_x$ being the exciton energy and μ_{eh} its reduced mass, $1/\mu_{eh} = 1/m_e + 1/m_h$. The exciton oscillates when light irradiates the atom, $E(t)$, following [38, 39]:

$$\mu_{eh}\ddot{r_x} + \mu_{eh}2\gamma_x\dot{r_x} + \mu_{eh}\omega_x^2 r_x = eE(t) \tag{1.31}$$

where r_x is the electron-hole distance and γ_x the damping caused by non-radiative processes such as scattering with phonons.

Solutions to Eq. 1.31 give a steady state where the exciton also oscillates harmonically with the frequency of the external field, ω [39]:

$$r_x(t) = \frac{e/\mu_{eh}}{\omega_x^2 - \omega^2 - 2i\omega\gamma_x}E(t) \tag{1.32}$$

Following the approach proposed by Hopfield [44], the excitonic influence on the dielectric constant can be calculated. The polarization density $\mathbf{P}$ created by excitons is taken to be proportional to the amplitude of the harmonic oscillator, which constitutes the so-called *dipole approximation*. Using Eq. 1.32

$$\mathbf{P}(\omega) = \frac{\varepsilon_B 2\omega_x\omega_{LT}}{\omega_x^2 - \omega^2 - 2i\omega\gamma_x}\mathbf{E}(\omega) \approx \frac{\varepsilon_B\omega_{LT}}{\omega_x - \omega - i\gamma_x}\mathbf{E}(\omega) \tag{1.33}$$

where ω_{LT} is the so-called longitudinal-transverse splitting, which is proportional to the exciton *oscillator strength*, and ε_B is the normalized background dielectric constant that does not contain the excitonic contribution, and the approximation has been taken in the vicinity of the resonant frequency.

Equation 1.33 says that the polarization density of an excitonic media depends on the frequency of the electric field. From Eq. 1.8a, the same holds for the permitivity ε, making the wave equation 1.9 a non-linear equation that changes the properties of the propagating field including its frequency.

1.4.1.1 Microcavities containing quantum wells

The frequency-dependent polarization change described by Eq. 1.33 is proportional to the exciton oscillator strength, and so it depends on how well the excitonic wave-function overlaps with the driving electric field. In Section 1.3.1.3 it was shown that the field inside a microcavity is concentrated at the antinodes of a standing wave profile. It is then desirable that excitons are placed at such antinode regions, what can be done by using quantum wells (QWs) inside the microcavity. This also gives a second advantage that the exciton energy, ω_x. can be tuned with the QW width — see Section 1.2

Spatial confinement means that the QW wavefuntions have to be taken into account when the exciton-induced polarization is calculated. According to the non-local dielectric response theory [39], once an exciton is created, the dielectric polarization changes in all points where its wavefunction spreads according to:

$$\mathbf{P}(\omega, z) = \Phi(z) \int \Phi(z') \frac{\varepsilon_B 2\omega_{LT} \pi a_B^3}{\omega_x - \omega - i\gamma_x} \mathbf{E}(\omega, z') dz' \tag{1.34}$$

where $\Phi(z)$ is the exciton wavefunction obtained when solving Eq. 1.3 using a potential well for $V_{e,h}(z_{e,h})$ and a_B is the Bohr radius of exciton in the bulk material (Eq. 1.5).

Introducing Eq. 1.34 into Eqs. 1.8 and 1.9, the latter becomes an integro-differential equation and can be solved exactly using the Greens function method [39]. The reflection and transmission amplitudes can be then calculated using 1.16:

$$r_{QW}(\omega) = \frac{i\Gamma_x}{\omega_x - \omega - i(\Gamma_x + \gamma_x)} \tag{1.35a}$$

$$t_{QW}(\omega) = 1 + r_{QW}(\omega) \tag{1.35b}$$

where Γ_x is the so-called *exciton radiative broadening* which is connected to the exciton radiative lifetime.

A finite exciton radiative lifetime is a peculiarity of confined semiconductor systems. In an infinite bulk crystal, an exciton–polariton can freely propagate in any direction and its lifetime is limited only by non–radiative processes such as scattering with acoustic phonons. On the contrary, in a QW the exciton–polariton can disappear by giving its energy to a photon which escapes the QW plane.

After calculating the transfer matrix of a DBR microcavity containing a QW in the middle of the L_c-thick cavity layer, solving an eigenvalue equation yields [39]:

$$(\omega_x - \omega - i\gamma_x)(\omega_c - \omega - i\gamma_c) = V^2 \tag{1.36a}$$

$$\gamma_c = \frac{c(1 - \sqrt{R})}{n_c \sqrt{R}(L_{DBR} + L_c)} \tag{1.36b}$$

$$V^2 = \frac{c(1 + \sqrt{R})\Gamma_x}{n_c \sqrt{R}(L_{DBR} + L_c)} \tag{1.36c}$$

where R is the DBR reflectivity, γ_c the photon lifetime and $L_{DBR} = \frac{n_1 n_2 \pi c}{\omega_c (n_2 - n_1)}$ is the so called *DBR effective length*.

Equation 1.36a describes a system of two damped harmonic oscillators, namely the exciton resonance and the cavity mode, coupled by a matrix element V. It has two complex solutions:

$$\omega_{+,-} = \frac{1}{2}\left[\omega_x + \omega_c - i(\gamma_x + \gamma_c) \pm \sqrt{4V^2 + (\omega_x - \omega_c - i(\gamma_x - \gamma_c))^2}\right] \tag{1.37}$$

If $\omega_x = \omega_c$, the splitting between the two values is given by the so-called *Rabi splitting* $\Omega_R = \sqrt{4V^2 - (\gamma_x - \gamma_c)^2}$. This changes the normal transmission modes of the electric field on the excitonic media.

The parameter V has the meaning of the coupling strength between the cavity photon mode and the exciton. $2V$ reaches $15\,meV$ in GaAs microcavities, $30\,meV$ in CdTe microcavities, and $50\,meV$ in GaN cavities

If $2V > |\gamma_x - \gamma_c|$, Ω_R is a real number and so $\omega_{+,-}$ are different frequencies from $\omega_{x,c}$, defining new eigeinmodes of the microcavity spectra, called *upper polariton*, ω_+, and *lower polariton*, ω_-. This is the so-called *strong coupling* regime. On the other hand, in the *weak coupling* regime, $2V < |\gamma_x - \gamma_c|$ making Ω_R a pure complex number, and so the eigenfrequencies $\omega_{x,c}$ remain unchanged except from their linewidth. VCSEL lasers operate under the weak coupling regime.

To illustrate better the difference between both regimes we simulate a cavity spectra as the sum of two Gaussians whose peaks and FWHMs are given by the real and imaginary parts, respectively, of $\omega_{+,-}$:

$$T(\omega) = e^{-\frac{(\omega - \mathcal{R}(\omega_+))^2}{2\mathcal{I}(\omega_+)}} + e^{-\frac{(\omega - \mathcal{R}(\omega_-))^2}{2\mathcal{I}(\omega_-)}} \tag{1.38}$$

Fig. 1.11 shows the cavity spectra as a function of the photon energy that crosses the exciton one, using similar parameters to the ones of realistic cavities used in this thesis — see Section 3. In the weak coupling regime (Fig. 1.11a), the bare exciton and photon modes remain the eigenmodes of the system, with slight changes in lifetimes (observed in the width of the lines) at the crossing region. On the other hand, in the strong coupling regime (Fig. 1.11b), a clear distinction between upper and lower polariton branches can be seen, with normal mode splitting given by Ω_R.

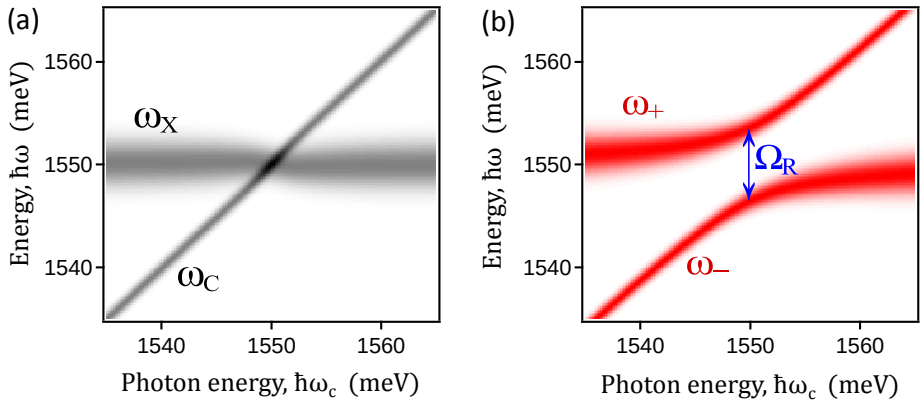

Figure 1.11: Comparison between weak and strong coupling regimes. Panels are solutions of Eqs. 1.38 and 1.37 using parameters $\hbar\gamma_x = 0.4meV$ ($10ps$ exciton lifetime [45]), $\hbar\gamma_c = 4meV$ ($1ps$ photon lifetime), $\hbar\omega_x = 1550meV$ and (a) $2V = 2.4meV < |\gamma_x - \gamma_c| = 3.6meV$ (weak coupling) or (b) $2V = 8meV > |\gamma_x - \gamma_c| = 3.6meV$ (strong coupling). In (a) the coupled modes are practically the same as bare ω_x and ω_c modes, with an decrease of the exciton decay rate at the crossing point. In (b) ω_+ and ω_- modes are separated by $\hbar\Omega_R$ at the anticrossing point.

The conditions for strong coupling are thus high exciton-dipole oscillator strength, good field-exciton overlap and similar, and small, linewidths of the cavity photon (γ_c, controlled by the finesse) and the exciton (γ_x, controlled by the inhomegeneous broadening of the excitons in the sample).

1.4.2 Quantum description of light-matter interaction

In the previous Section, a semiclassical approach to photon-exciton interaction inside a semiconductor microcavity has been shown to change the dielectric constant yielding a normal mode splitting that appears as two new modes. This is in close analogy to the classical two-coupled harmonic oscillator problem [46], where two masses m_A and m_B are attached to springs with constants k_A and k_B and linked together by a third spring with constant κ - see Fig. 1.12a. The eigenfrequencies of the system are given by (damping is ignored):

$$\omega_{\pm}^2 = \frac{1}{2}\left[\omega_A^2 + \omega_B^2 \pm \sqrt{(\omega_A^2 - \omega_B^2)^2 + 4\Gamma^2\omega_A\omega_B}\right] \tag{1.39}$$

where $\omega_A = \sqrt{(k_A + \kappa)(m_A)}$, $\omega_B = \sqrt{(k_B + \kappa)(m_B)}$ and

$$\Gamma = \frac{\kappa}{\sqrt{m_A\omega_A m_B\omega_B}} \tag{1.40}$$

Each eigenmode correspond to both masses oscillating harmonically with a single frequency, for ω_- with the same phase and for ω_+ with a π-phase difference. Any other solution to the problem is a linear superposition of these two eigeinmodes, and will be then characterized by a periodic beating of each mass oscillation. Figure 1.12b shows one of these possible solutions, with $k_A = k_B = 12.5\kappa$. Note the π-phase difference between the beating of each mass, which is responsible for a periodic transfer of energy from one oscillator to the other and vice-versa.

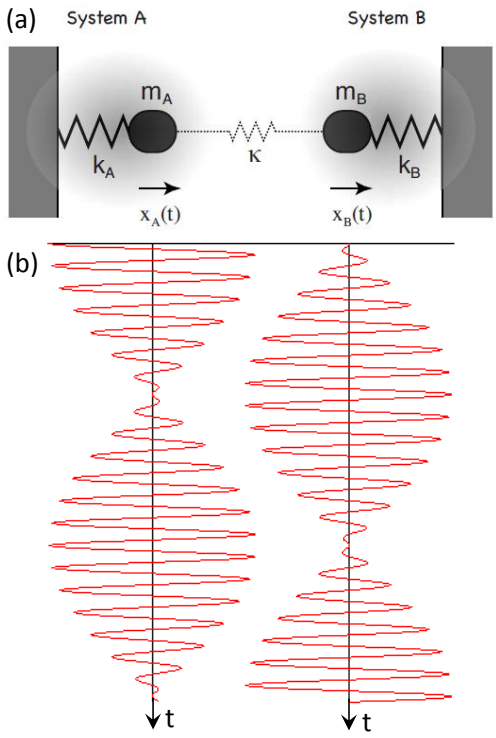

Figure 1.12: Coupled mechanical oscillators. (a) Schematic representation of two harmonic oscillators defined by masses m_A and m_B attached to springs (k_a and k_B) and coupled through a third spring of constant κ. Each mass position, $x_A(t)$ and $x_B(t)$, is displayed as a function of time in (b) for a superposition of the two eigenmodes taking $k_A = k_B = 12.5\kappa$. Adapted from [46].

To illustrate the solutions given by Eq. 1.39 we set $k_A = k_0$, $k_B = k_0 + \Delta k$, and $m_A = m_B = m_0$. Figure 1.13a shows the frequencies of the two oscillators in the absence of coupling ($\kappa = 0$). As Δk is increased from $-k_0$ to $+k_0$, the frequency of oscillator B increases from zero to $\sqrt{2}\omega_0$, while the frequency of oscillator A stays constant. The two curves intersect at $\Delta k = 0$. Once coupling is introduced, the two curves no longer intersect. Instead, as shown in Fig. 1.13b, there is characteristic *anticrossing* with a frequency splitting of Γ.

Equation 1.39 and Figure 1.13 are in full analogy with polariton modes in a microcavity (Equation 1.37 and Fig. 1.11), so one might look for a quantum description of photon-exciton interaction in a microcavity under the coupled oscillators picture. In fact, in the low excitonic density limit, the Hamiltonian describing photons, excitons and their mutual coupling through the dipole moment can be written, in the second quantization picture, as [39]:

$$\mathcal{H}_{e-ph} = \hbar\omega_C \hat{C}^\dagger \hat{C} + \hbar\omega_X \hat{X}^\dagger \hat{X} + \frac{\hbar\Omega_R}{2}(\hat{C}^\dagger \hat{X} + \hat{X}^\dagger \hat{C}) \tag{1.41}$$

where ω_C (ω_x) are the photon (exciton) frequencies and Ω_R the Rabi frequency. The photon (exciton) creation and annihilation operators, $\hat{C}^\dagger$ and $\hat{C}$ ($\hat{X}^\dagger$ and $\hat{X}$), are to be understood, when applied in the uncoupled photon-exciton number basis, as:

$$\hat{C}^\dagger |n_C, n_X\rangle = \sqrt{n_C + 1}\,|n_C + 1, n_X\rangle \tag{1.42a}$$

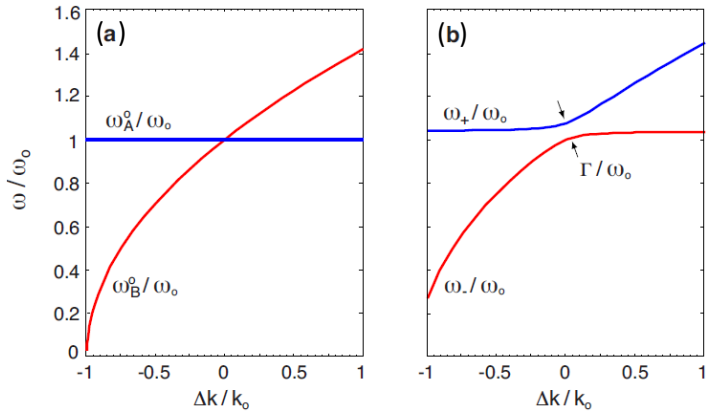

Figure 1.13: Strong coupling regime illustrated by mechanical oscillators. (a) Eigenfrequencies of two uncoupled oscillators ($\kappa = 0$) with equal mass and spring constants k_0 and $k_0 + \Delta k$. (b) Frequency anticrossing due to coupling of strength $\kappa = 0.08k_0$. The coupling of the two oscillators leads to a shift of the eigenfrequencies and a characteristic frequency splitting Γ, which scales linearly with the coupling strength κ. From [46].

$$\hat{C}|n_C, n_X\rangle = \sqrt{n_C}|n_C - 1, n_X\rangle \tag{1.42b}$$

$$\hat{X}^\dagger|n_C, n_X\rangle = \sqrt{n_X + 1}|n_C, n_X + 1\rangle \tag{1.42c}$$

$$\hat{X}|n_C, n_X\rangle = \sqrt{n_X}|n_C, n_X - 1\rangle \tag{1.42d}$$

Given an arbitrary state $|\psi(t)\rangle = c(t)|1,0\rangle + x(t)|0,1\rangle$, its time-evolution can be found when solving the Schrödinger equation, $i\hbar\partial_t|\psi(t)\rangle = \mathcal{H}_{e-ph}|\psi(t)\rangle$:

$$i\hbar\left[\dot{c}(t)|1,0\rangle + \dot{x}(t)|0,1\rangle\right] = \hbar\omega_C c(t)|1,0\rangle + \hbar\omega_X x(t)|0,1\rangle + \frac{\hbar\Omega_R}{2}x(t)|1,0\rangle + \frac{\hbar\Omega_R}{2}c(t)|0,1\rangle \tag{1.43}$$

Equation 1.43 can be written in its matrix from,

$$i\hbar\begin{pmatrix}\dot{c}(t)\\ \dot{x}(t)\end{pmatrix} = \begin{pmatrix}\hbar\omega_C & \frac{\hbar\Omega_R}{2}\\ \frac{\hbar\Omega_R}{2} & \hbar\omega_X\end{pmatrix}\begin{pmatrix}c(t)\\ x(t)\end{pmatrix} \tag{1.44}$$

which is a matrix differential equation that can be easily solved after diagonalization, $i\hbar\partial_t|\psi(t)\rangle = P^{-1}\mathcal{H}_{pol}P|\psi(t)\rangle$ (the column vectors of P, known as Hopfield matrix, are the eigenvectors of the diagonal $\mathcal{H}_{pol}$) giving a pair of uncoupled differential equations:

$$i\hbar\begin{pmatrix}\dot{u}(t)\\ \dot{l}(t)\end{pmatrix} = \begin{pmatrix}\hbar\omega_+ & 0\\ 0 & \hbar\omega_-\end{pmatrix}\begin{pmatrix}u(t)\\ l(t)\end{pmatrix} \tag{1.45}$$

where $\begin{pmatrix}u(t)\\ l(t)\end{pmatrix} = P\begin{pmatrix}c(t)\\ x(t)\end{pmatrix}$. The eigenfrequencies are given by:

$$\omega_\pm = \frac{1}{2}\left(\omega_X + \omega_C \pm \sqrt{\Delta^2 + \Omega_R^2}\right) \tag{1.46}$$

for detuning $\Delta = \omega_C - \omega_X$. Polaritons can then be seen in a simplified, but very accurate model, as the new eigenstates that arise from the coupling of two oscillators, *i.e.*, the photon and the exciton. On resonance, polaritons are half-light, half-matter quasiparticles, with wavefunctions that are superpositions between the excitonic and photonic ones, $\psi = \frac{1}{\sqrt{2}}(\psi_x \pm \psi_c)$.

The corresponding eigenvectors are:

$$\begin{pmatrix} \chi \\ \varsigma \end{pmatrix} and \begin{pmatrix} \varsigma \\ -\chi \end{pmatrix} \tag{1.47}$$

where χ and ς are the Hopfield coefficients [44]:

$$\chi = \left(1 + 4\left(\frac{\omega_- - \omega_X}{\Omega_R}\right)^2\right)^{-2} \tag{1.48a}$$

$$\varsigma = -\left(1 + \frac{1}{4}\left(\frac{\Omega_R}{\omega_- - \omega_X}\right)^2\right)^{-2} \tag{1.48b}$$

This finally yields the time-evolution of $|\psi(t)\rangle$ in the uncoupled photon-exciton basis, $\begin{pmatrix} c(t) \\ x(t) \end{pmatrix} = P^{-1}\begin{pmatrix} u(t) \\ l(t) \end{pmatrix}$. One possible solution is $u(t) = 1/\sqrt{2}e^{-i\omega_+ t}$, $l(t) = 1/\sqrt{2}e^{-i\omega_- t}$, yielding:

$$c(t) \propto \chi e^{-i\omega_+ t} + \varsigma e^{-i\omega_- t} \tag{1.49a}$$

$$x(t) \propto \varsigma e^{-i\omega_+ t} - \chi e^{-i\omega_- t} \tag{1.49b}$$

The coefficients defined by Eq. 1.49 can be used to calculate the probability of having a photon or an exciton at a given time t. Taking the simple case $\omega_C = \omega_X = \omega$, we have $\chi = -\varsigma = \sqrt{2}$ and $\omega_\pm = \omega \pm \Omega_R/2$. Eq. 1.49 yields:

$$|c(t)|^2 = \frac{1}{2}(1 + \cos(\Omega_R t)) \tag{1.50}$$

Equation 1.50 tells us that such a polariton state is seen as a chain process where the exciton annihilates, emitting a photon with the same energy E and momentum k, which is later reabsorbed by the medium, creating a new exciton with the same (E, k). This processes is repeated with a frequency $2\Omega_R$, very similarly to two classically coupled oscillators — see Fig. 1.12b, until the excitation finds its way out of the cavity (resulting in the annihilation of the polariton), or the exciton is scattered.

Other two possible solutions would be the polaritonic eigenmodes, taking $u(t) = 0$ or $l(t) = 0$. The first corresponds to an in-phase harmonic oscillation of the photonic and exciton fields, whereas with a π-relative phase in the second, again in close analogy with the classical coupled oscillators picture.

The dispersion of each polariton mode can be calculated from Eq. 1.46 or 1.37 by taking the momentum dependence of excitonic and photonic modes. Since the exciton mass is much heavier than the photonic one, we assume the excitonic dispersion to be flat and the photonic one to be parabolic. This yield the polariton dispersion for each Hamiltonian eigenvalue, known by the *upper polariton branch* (UPB) and the *lower polariton branch* (LPB) - see Fig. 1.14

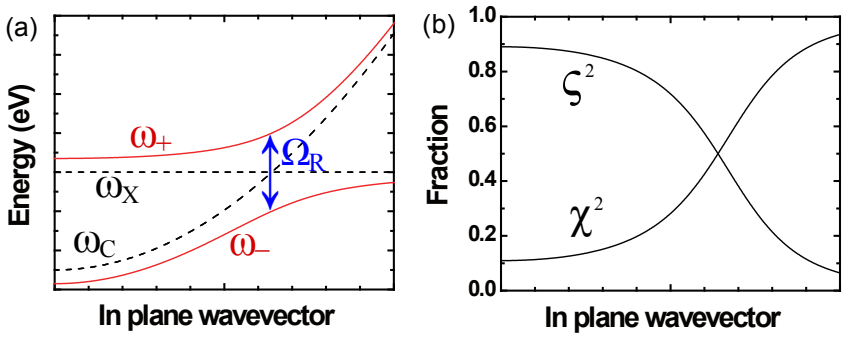

Figure 1.14: (a) Computed dispersions of the upper ω_+ (UPB) and lower ω_- (LPB) polariton branches as a function of in plane wavevector (red lines) along with the uncoupled cavity ω_C and exciton ω_X modes (dashed lines) for negative detuning, showing the Rabi splitting Ω_R where the two bare dispersions cross. (b) Corresponding exciton ($|\chi|^2$) and photon ($|\varsigma|^2$) fractions of the lower polariton.

The first measurement of a Rabi splitting of the normal modes of a semiconductor microcavity have been done 20 years ago [5], where the two exciton/photon reflectivity dip of a five-quantum-well microcavity was shown to anticross when they came into resonance (Fig. 1.15a). Two years later the time dynamics of the same sample was studied [47]. When excited by a coherent optical pulse whose spectral bandwidth exceeds the normal-mode splitting, the initial state of the system is the linear superposition of normal modes corresponding to the photon or cavity mode, and its time-dynamics clearly showed damped Rabi oscillations (Fig. 1.15b).

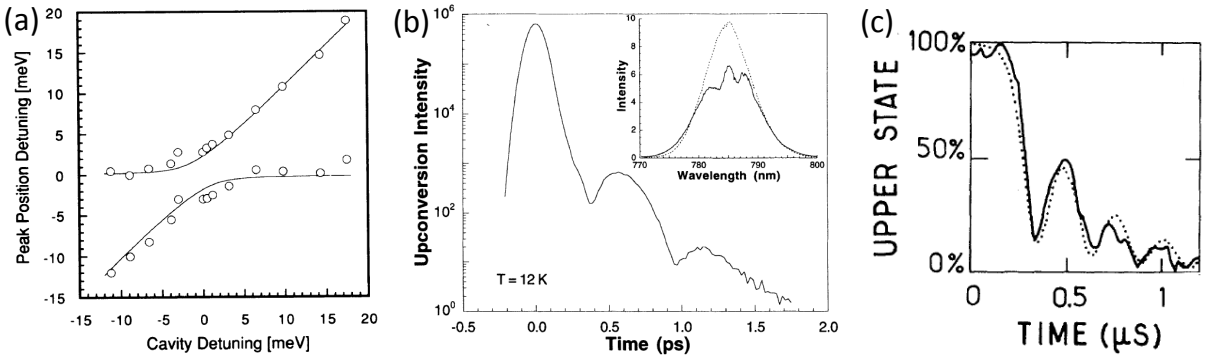

Figure 1.15: (a) Reflectivity peak positions as a function of photon-exciton detuning for a five-quantum-well microcavity sample at $T = 5\,K$ from Ref. [5]. (b) Time-resolved emission intensity from a microcavity with photonic and excitonic modes close to resonance, excited with a pulsed laser. In the inset, the dotted line shows the incident pump spectrum, and the solid line the reflected pump spectrum. The two dips in the selected pump spectrum correspond to the normal modes of the system resonance, from Ref. [47]. (c) Evolution of the normalized excited-state population of sodium Rydberg atoms inside a millimeter-wave cavity as a function of time (solid line: experiment; dotted line: theoretical calculation), from Ref. [48]

The interaction between a photon and an exciton in a semiconductor provides the solid-state analogous of photon-atom interaction in cavity QED. In fact, when an ideal two-level absorber (atom or exciton) is resonantly coupled to a single mode of the electromagnetic field, the field induces a periodic excitation and deexcitation of the atomic

excited state given by the Rabi frequency $\Omega_R = e\langle r\rangle E/\hbar$, where $\langle r\rangle$ is the transition dipole moment and E the electric field. Such Rabi dynamics has been measured 30 years ago with sodium Rydberg atoms prepared in a millimetre-wave Fabry-Perot resonator [48] — see Fig. 1.15c. This Rabi flopping is manifested in the normal-mode spectrum as a splitting (or anticrossing) of the uncoupled atom and field modes [49, 50]. Analogous phenomena have been more recently observed between a single photon and a superconducting qubit using circuit quantum electrodynamics, where a superconducting two level system, playing the role of an artificial atom, is coupled to an on-chip cavity consisting of a superconducting transmission line resonator [51].

Chapter 2

Quantum liquids

Quantum liquids are many-particle systems in which not only the effects of quantum mechanics but also those of quantum statistics — specifically, indistinguishability of elementary particles — are important.

Any elementary particle can be classified according to its intrinsic angular momentum: *bosons* have integer spin whereas *fermions* have a half-integer one. According to the *spin-statistics theorem* [52], the total wave function of any many-particle system must be even under an interchange of coordinates of any two bosons, and odd under interchange of any two fermions. This theorem implies that the distribution of particles in thermal equilibrium is given by:

$$n_i = \frac{1}{e^{\frac{\varepsilon_i - \mu_c}{k_B T}} \pm 1} \tag{2.1}$$

where μ_c is the chemical potential, T the temperature, k_B the Boltzmann constant and the $\pm$ sign now refers to fermions or bosons, respectively. The distribution given by Eq. 2.1 with the plus sign is known as the Fermi-Dirac distribution, whereas with the minus it corresponds to the Bose-Einstein distribution.

Quantum effects start to be important when the thermal energy $k_B T$ falls below a typical single-particle excitation energy. A rough estimation for this energy [53] may be obtained by imagining each particle of mass m to move in a 3D cage of side $a \sim (N/V)^{-1/3}$ (N/V = particle density) formed by its neighbours; the typical single-particle excitation energy is then of order of the first energy state of a infinite potential well $\sim \hbar^2/ma^2$, so the criterion for quantum effects to be relevant is

$$T_c \sim \frac{\hbar^2 (N/V)^{2/3}}{m k_B} \tag{2.2}$$

Thus, a quantum liquid is a many-particle system in which (i) the temperature is less than or of the order of T_c, defined by Eq. 2.2, and (ii) the particles can change places relatively easily. The most studied quantum liquids are the bosonic systems, such as liquid ^{4}He and Bose alkali gases, which undergo the phenomenon of Bose-Einstein condensation, and the fermionic systems, such as liquid ^{3}He and electrons in some metals, which display the related phenomenon of Cooper pairing. Another examples are neutrons in neutron stars and possibly more exotic forms of matter such as quark stars.

2.1 Bose-Einstein condensation

2.1.1 The ideal Bose gas

The chemical potential is the energy cost of adding a particle to a gas, and increases with the total number of particles. For a noninteracting gas of bosons described by the Bose-Einstein distribution, Eq. 2.1, the chemical potential μ_c has to be smaller then the lowest energy ε_0 in order that the occupation number n_i is always positive.

Let us write the total number of particles as

$$N = N_0 + N_T \tag{2.3}$$

where N_0 is the number of particles in the ground state and

$$N_T = \sum_{i \neq 0} n_i \tag{2.4}$$

is the number of particles out of the condensate, also called the thermal component of the gas.

When the chemical potential μ_c approaches ε_0 from below, the ground-state occupation number

$$n_0 = \frac{1}{e^{\frac{\varepsilon_0 - \mu_c}{k_B T}} - 1} \tag{2.5}$$

of the lowest energy state becomes increasingly large. This is actually the mechanism at the origin of Bose-Einstein condensation and it was used as a footprint for its first observation in 1995 [7], where a macroscopic occupation of a zero-momentum state was shown.

The value of n_i is proportional to the density of states, which for a three dimensional gas of free particles with a parabolic dispersion $\varepsilon = \varepsilon_0 + \frac{\hbar^2 k^2}{2m}$ is given by $g(\varepsilon) = \frac{m^{3/2}}{\sqrt{2}\hbar^3 \pi^2}\sqrt{\varepsilon - \varepsilon_0}$. When $\mu_c \to \varepsilon_0$, the density of particles out of the condensate is given by:

$$\frac{N_T^{\mu_c \to \varepsilon_0}}{V} = \int_{\varepsilon_0}^{\infty} \frac{m^{3/2}}{\sqrt{2}\hbar^3 \pi^2}\sqrt{\varepsilon - \varepsilon_0}\frac{1}{e^{\frac{\varepsilon - \varepsilon_0}{k_B T}} - 1} d\varepsilon = \frac{2.612}{{\lambda_T}^3} \tag{2.6}$$

where

$$\lambda_T = \sqrt{\frac{2\pi\hbar^2}{m k_B T}} \tag{2.7}$$

is the de Broglie wavelength, which reflects the average quantum size of the particles conforming the gas at temperature T, and V is the volume of the gas. For a fixed value of T, the function N_T has a smooth behaviour as a function of μ_c and reaches its maximum, critical value, $N_c = N_T^{\mu_c \to \varepsilon_0}$ at $\mu_c = \varepsilon_0$ (see Fig. 2.1). The behaviour of N_o is very different: it diverges when μ_c is close to ε_0. If the total number of particles exceeds N_c then the additional particles, $N - N_c$, will populate the ground state. In other words, above N_c if we add a new particle in such a way that this particle does not change the temperature of the system, this particle will occupy the ground state. In this way, the ground state can achieve macroscopic occupations (in free space, this is the zero-momentum state), and Bose-Einstein condensation takes place [54].

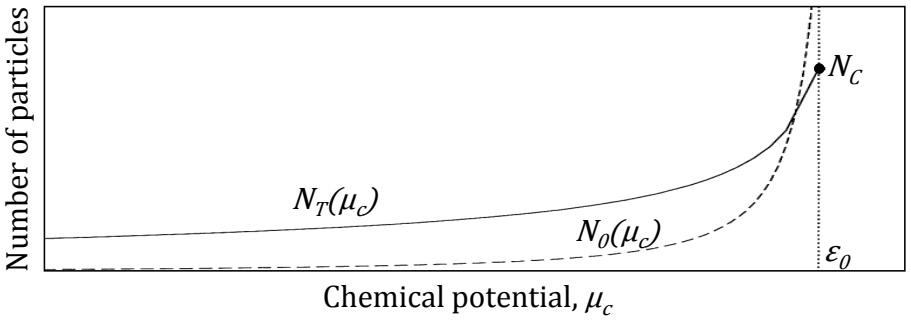

Figure 2.1: Ideal gas model. Number of particles out of the condensate (N_T, solid line) and in the condensate (N_0, dashed line) as a function of the chemical potential, for a fixed value of T. The system ground state energy is given by ε_0 and the maximum non-condensed number of particles is represented by N_c when $\mu = \varepsilon_0$. Adapted from [55].

Equivalently, at a finite T, when the number of particles increases and the chemical potential μ_c approaches the ground state ε_0 from lower values, the number of particles in all the excited states saturates asymptotically and the ground state occupation diverges (Fig. 2.2). In this way, the ground state can achieve macroscopic occupations, and Bose-Einstein condensation takes place.

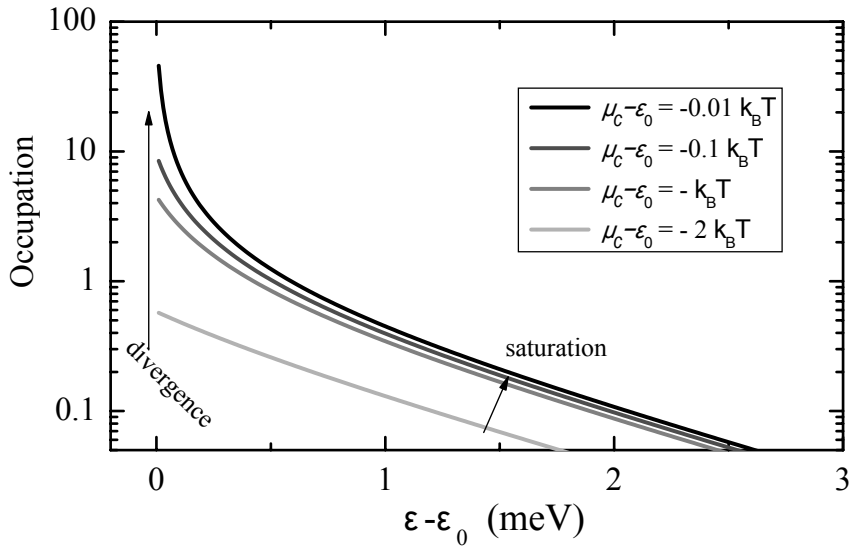

Figure 2.2: Bose-Einstein occupation distribution (Eq. 2.1) for increasing values of chemical potential (which is equivalent to higher particle densities).

Equation 2.6 means that in order for a Bose gas to condensate in a BEC, the average distance between particles must be on the order of their quantum size (note that Eq. 2.6 defines a critical temperature T_c of the same order as the one defined by Eq. 2.2). Due to the heavy mass of the atomic bosons employed in BEC studies, Eq. 2.6 implies working at sub-μK temperatures. On the other hand, polaritons have a very small effective mass, due to its photonic component, of the order of 10^9 times smaller than that of atoms, and so the transition to a BEC phase can take place at much higher temperatures - see Table 2.1.

	atomic gases	excitons	polaritons
mass m^*/m_e	10^4	10^{-1}	10^{-5}
Bohr radius	$10^{-1}\mathring{A}$	$10^2\mathring{A}$	$10^2\mathring{A}$
λ_T at T_c	$10^3\mathring{A}$	$1\,\mu m$	$1\,\mu m$
T_c	$< 1\,\mu K$	$0.1\,K$	$10 - 300\,K$

Table 2.1: Comparison between different parameters in bosonic species. m_e indicates the free electron mass.

The most common example of a noninteracting boson is the photon, however blackbody radiation (radiation in thermal equilibrium with the cavity walls) does not show a BEC phase transition, since at low temperatures photons disappear in the cavity walls instead of occupying the cavity ground state. Very recently, number-conserving thermalization was experimentally observed [56] for a two-dimensional photon gas in a dye-filled optical microcavity, which acts as a white-wall box. In this system, photons can Bose-Einstein condense [57].[1]

2.1.2 Weakly-interacting Bose gas and the Bogoliubov approximation

The ideal Bose gas considered in the previous chapter does not take into account interactions between particles, which do affect the properties of the gas and are expected to play a role even for dilute species. Interactions are particularly important in this thesis since polaritons strongly scatter via the dipole moment of its excitonic part.

Let us deal with a weakly interacting 3D Bose gas, where the scattering length a is much smaller then the average distance between particles $a \ll (N/V)^{-1/3}$. This allows one to consider only configurations involving pairs of interacting particles, while configurations with three or more particles interacting simultaneously can be safely neglected. A similar phenomenon to Bose-Einstein condensation occurs, in thermal equilibrium, in a system of interacting bosons, provided that the interaction is overall positive (repulsive). We shall always consider gases at temperatures smaller than the critical temperature for Bose-Einstein condensation (Eq. 2.2). This implies that the relevant values of momenta always satisfy the inequality $pa \ll \hbar$.

Under such conditions, the Hamiltonian of a weakly-interactiog Bose gas can be written in the second quantization picture as [55]:

$$\mathcal{H} = \sum_{\mathbf{p}} \frac{p^2}{2m} \hat{a}^\dagger_{\mathbf{p}} \hat{a}_{\mathbf{p}} + \frac{V_0}{2V} \sum_{\mathbf{p_1},\mathbf{p_2},\mathbf{q}} \hat{a}^\dagger_{\mathbf{p_1}+\mathbf{q}} \hat{a}^\dagger_{\mathbf{p_2}-\mathbf{q}} \hat{a}_{\mathbf{p_1}} \hat{a}_{\mathbf{p_2}}, \tag{2.8}$$

where $\hat{a}_{\mathbf{p}}$ ($\hat{a}^\dagger_{\mathbf{p}}$) is the operator annihilating (creating) a particle in the single-particle state with momentum $\mathbf{p}$ and V_0 is an macroscopic approximation to the microscopic two body potential.

In the so called Bogoliubov approximation [59], the single particle annihilation operator is replaced by a number, $a \equiv \sqrt{N_0}$, which is valid for the effective smooth interparticle

[1] To circumvent criticisms about the similarities with a dye-laser, a new method to generate photon BECs has been proposed recently [58].

potential V_0 [55]. For a Bose gas at $T = 0$, the occupation of states with $\mathbf{p} \neq 0$ is small, $N \sim N_0$, and V_0 depends only on the scattering length a in the Born approximation

$$V_0 = 4\pi\hbar^2 a/m = g, \tag{2.9}$$

where g is called the interaction coupling constant. The ground state energy, Eq. 2.8, takes the form

$$E_0 = \frac{N^2 g}{2V} \tag{2.10}$$

Contrary to the ideal case, the pressure of a weakly-interacting Bose gas does not vanish at zero temperature:

$$P = -\frac{\partial E_0}{\partial V} = \frac{g(N/V)^2}{2}, \tag{2.11}$$

Accordingly, the compressibility is also finite:

$$\frac{\partial(N/V)}{\partial P} = \frac{V}{gN} \tag{2.12}$$

and tends to infinity when $g \to 0$. Using the hydrodynamic relation $\frac{1}{mc^2} = \frac{\partial(N/V)}{\partial P}$ for the compressibility one obtains the sound speed:

$$c_s = \sqrt{\frac{gN}{mV}} \tag{2.13}$$

The condition of thermodynamic stability implies that the quantity compressibility must be positive, *i.e.* $a > 0$ from Eqs. 2.9–2.12. Then a dilute uniform Bose-Einstein condensed gas can exist only if the scattering length is positive.

The chemical potential is given by

$$\mu_c = \frac{\partial E_0}{\partial N} = \frac{gN}{V} = m{c_s}^2 \tag{2.14}$$

The momentum dependence (dispersion) of the weakly-interacting Bose gas can be calculated by considering the $\mathbf{p} \neq 0$ terms in the Hamiltonian 2.8. However now the lowest-order Born approximation for the two-body potential V_0 no longer holds. Using higher-order perturbation theory one finds the result [60]

$$V_0 = g\left(1 + \frac{g}{V}\sum_{\mathbf{p}\neq 0}\frac{m}{p^2}\right) \tag{2.15}$$

where g is related to the scattering length by Eq. 2.9. Equation 2.15 renormalizes the relationship between the effective potential and the physical coupling constant g. The Hamiltonian 2.8 becomes quadratic in the operators $\hat{a}_{\mathbf{p}}$ and $\hat{a}^\dagger_{\mathbf{p}}$ and can be diagonalized to [55]

$$\mathcal{H} = E_0 + \sum_{\mathbf{p}} \epsilon(p)\hat{b}^\dagger_{\mathbf{p}}\hat{b}_{\mathbf{p}}, \tag{2.16}$$

where

$$E_0 = g\frac{N^2}{2V}\left[1 + \frac{128}{15\sqrt{\pi}}\sqrt{\frac{Na^3}{V}}\right] \tag{2.17}$$

is the ground state energy calculated to the higher-order of approximation [61, 62],

$$\epsilon(p) = \sqrt{\frac{gN}{mV}p^2 + \left(\frac{p^2}{2m}\right)^2} \tag{2.18}$$

is the so called Bogoliubov dispersion law for the elementary excitations of the system, and the new quasiparticle operators $\hat{b}_{\mathbf{p}}$ and $\hat{b}^\dagger_{\mathbf{p}}$ are related to the to the single particle operator through the Bogoliubov transformation

$$\hat{a}_{\mathbf{p}} = u_{\mathbf{p}}\hat{b}_{\mathbf{p}} + v^*_{-\mathbf{p}}\hat{b}^\dagger_{-\mathbf{p}}, \tag{2.19a}$$

$$\hat{a}^\dagger_{\mathbf{p}} = u^*_{\mathbf{p}}\hat{b}^\dagger_{\mathbf{p}} + v_{-\mathbf{p}}\hat{b}_{-\mathbf{p}}, \tag{2.19b}$$

where the coefficients $u_{\mathbf{p}}$ and $v_{-\mathbf{p}}$ are given by:

$$u_{\mathbf{p}}, v_{-\mathbf{p}} = \pm\sqrt{\frac{p^2/2m + gN/V}{2\epsilon(p)} \pm \frac{1}{2}} \tag{2.20}$$

Equations 2.16 and 2.18 mean that the original system of interacting particles can be described in terms of a Hamiltonian of non-interacting quasi-particles having energy $\epsilon(p)$ and whose annihilation and creation operators are given, respectively, by $\hat{b}_{\mathbf{p}}$ and $\hat{b}^\dagger_{\mathbf{p}}$. The ground state of the interacting system then corresponds to the vacuum of quasi-particles.

For small momenta $p \ll mc_s$ the dispersion law of quasi-particles takes the phonon-like form, $\epsilon(p) \approx c_s p$, where c_s is the sound velocity defined in Eq. 2.13 — see Fig. 2.3. The Bogoliubov theory then predicts that the long wavelength excitations of an interacting Bose gas are sound waves. These excitations can also be regarded as the Goldstone modes associated with breaking of a gauge symmetry caused by Bose-Einstein condensation. In the opposite limit $p \gg mc_s$ the dispersion law approaches the free particle law, $\epsilon(p) \approx \frac{p^2}{2m} + \frac{gN}{V}$ (see Fig. 2.3).

The transition between the phonon and particle regimes takes place when $p^2/2m \sim gN/V$, *i.e.* for $p \sim \sqrt{2}mc_s$. This allows to define the characteristic interaction length (also called the healing length) by making $p = \hbar/\xi$ (see Fig. 2.3):

$$\xi = \sqrt{\frac{\hbar^2 V}{2mgN}} = \frac{1}{\sqrt{2}}\frac{\hbar}{mc_s} \tag{2.21}$$

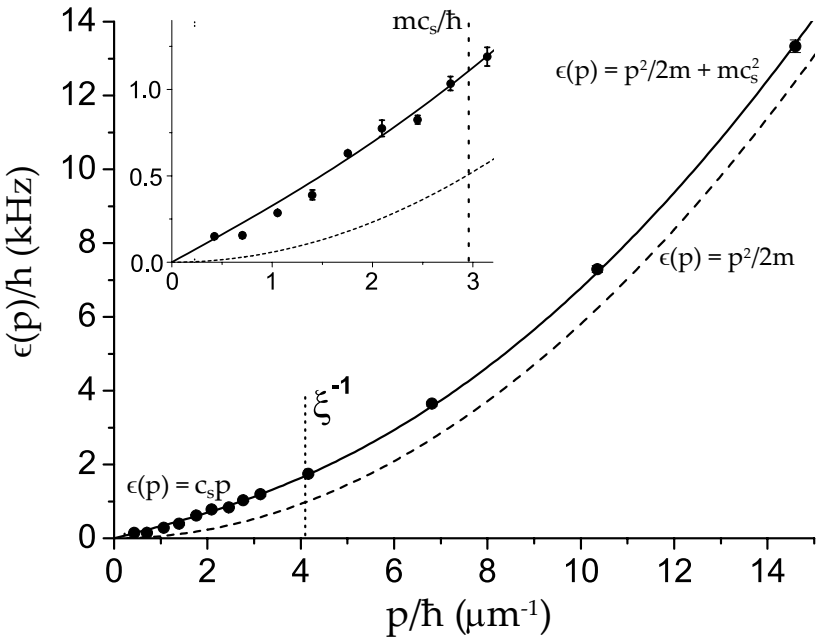

Figure 2.3: Excitation spectrum $\epsilon(p)$ of a ^{87}Rb trapped Bose-Einstein condensate measured with Bragg scattering (black circles). The solid line is the Bogoliubov spectrum, Eq. 2.18, and the dashed line is the parabolic free-particle spectrum. The inset shows the linear phonon regime. The transition between the phonon ($c_s p$) and the free particle ($p^2/2m$) regimes takes place at $p \sim \hbar/\xi$. Adapted from [63].

2.2 Superfluidity

The first observation of superfluidity was made simultaneously by Pyotr Kapitsa in Moscow [64] and John F. Allen in Cambridge [65] in 1938, using liquid ^{4}He. They measured the resistance to the flow of liquid helium clamped in narrow channels and subjected to a pressure drop. It was found that while the so-called He-I phase, *i.e.*, helium above $2.17\,K$, the lambda temperature, showed a behaviour that could be described in terms of conventional viscosity, whereas below the lambda point (in the so-called He-II phase) the liquid flowed so easily that if the concept of viscosity was applicable at all, it would have to be at least a factor of 1500 smaller than in the He-I phase.

The phenomenon of superfluidity is responsible of a number of fascinating effects that happen in liquid helium inside chambers. Figure 2.4a shows liquid ^{4}He in a dewar (thermal-insulating) bottle under atmospheric pressure. Normal evaporation (seen as many tiny bubbles) keeps the liquid at its boiling temperature $4.2\,K$. By connecting the container to a vacuum pump its pressure is decreased, as well as the liquid temperature through evaporation. As the temperature approaches the lambda temperature $2.17\,K$, boiling is increased becoming much more visible (Fig. 2.4b). In the superfluid state, below $2.17\,K$, the thermal conductivity is extremely large. This causes heat in the body of the liquid to be transferred to the surface so quickly, that vaporisation/boiling takes place only at the free surface of the liquid, hence no gas bubbles in the body of the liquid are formed (Fig. 2.4c).

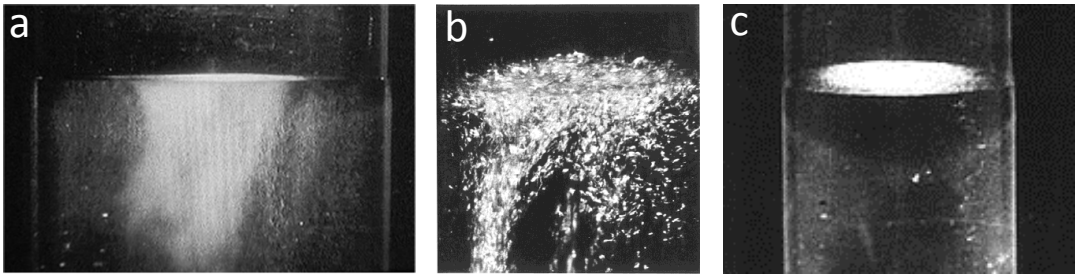

Figure 2.4: Transition to superfluidity seen through evaporation. (a), Liquid helium in a dewar bottle at $4.2\,K$ and $1\,atm$, boiling slowly. (b), Lambda point transition: as the liquid is cooled down to $2.17\,K$, the boiling suddenly becomes violent. In the superfluid state (c), below $2.17\,K$, the thermal conductivity is extremely large what makes boiling to stop completely in the body of the liquid. From [66]

Many ordinary liquids creep up solid walls, driven by their surface tension. Liquid helium also has this property, but, in the case of He-II, the flow of the liquid in the layer is not restricted by its viscosity but by a critical velocity which is about $20\,cm/s$. This is a fairly high velocity so superfluid helium can flow relatively easy up the wall of containers as a thin film, over the top, and down on the outside to form visible droplets as seen in Fig. 2.5a.

Superfluids can flow through narrow capillaries or slits without dissipating energy, their shear viscosity being equal to zero. Figure 2.5b shows a curious demonstration of what is called *the fountain effect*, photographed by Allen in the 1970's. A vessel with a capillary on the top is placed half-inside superfluid helium. The vessel's bottom is open to the liquid through a very fine powder which blocks the flow of the fluid normal component but allows flowing of the superfluid component in such a way that the vessel gets filled with superfluid helium up to the height of the surrounding liquid. By heating up the liquid inside the vessel, the flow through the power gets unidirectional towards the vessel from outside and so its volume increases eventually squirting out like a fountain.

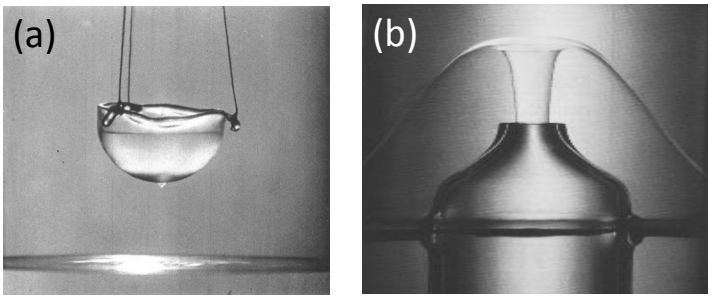

Figure 2.5: (a), Superfluid liquid helium inside a suspended vessel creeping up the its walls and coming down on the outside, forming a drop which will fall into the liquid below. From [66] (b), Demonstration of the fountain effect. A capillary tube is "closed" at the bottom end by a superleak and is placed into a bath of superfluid helium and then heated. The helium flows up through the tube and squirts like a fountain. From [67]

The fact that superfluidity appear below a critical temperature and that the ^{4}He atom is composed of an even number of elementary particles (2 protons, 2 neutrons, and 2 electrons), and so the system should obey Bose statistics, have motivated the quest for

an explanation to superfluidity phenomena based on Bose-Einstein condensation. Next section develops these ideas in a quantitative way.

2.2.1 Landau's criterion of superfluidity

To understand under which conditions a moving fluid can give rise to dissipation, let us follow the ideas of Landau [68, 69]. A moving fluid produces dissipation of energy, with consequent heating and decrease of the kinetic energy, through the creation of elementary excitations. If the excitation spectrum of given fluid is known on its reference frame, the same will be known under movement after Galilean transformations. Let us first consider a uniform fluid at zero temperature flowing along a capillary at constant velocity $\mathbf{v}$. In the fluid reference system, if a single excitation with momentum $\mathbf{p}$ appears then the total energy is $E_0 + \epsilon(\mathbf{p})$, where E_0 and $\epsilon(\mathbf{p})$ are, respectively, the energy of the ground state and of the excitation. In the reference system where the capillary is at rest (this reference moves with velocity $-\mathbf{v}$ relative to the fluid) the energy E' and momentum $\mathbf{P}'$ are given, using Galilean transformations, by:

$$E' = E_0 + \epsilon(\mathbf{p}) + \mathbf{p}\cdot\mathbf{v} + \frac{1}{2}Mv^2 \tag{2.22a}$$

$$\mathbf{P}' = \mathbf{p} + M\mathbf{v} \tag{2.22b}$$

where M is the mass of the fluid.

Equations 2.22 show that the quantities $\epsilon(\mathbf{p})+\mathbf{p}\cdot\mathbf{v}$ and $\mathbf{p}$ are, respectively, the change in energy and in momentum in the frame where the capillary due to the appearance of the excitation. The process of spontaneous creation of excitations can take place only if the excitation energy is negative:

$$\epsilon(\mathbf{p}) + \mathbf{p}\cdot\mathbf{v} < 0 \Rightarrow v > \epsilon(\mathbf{p})/p \tag{2.23}$$

In this case the flow of the fluid is unstable and its kinetic energy will be transformed into heat. If instead

$$v < v_c = \min_{\mathbf{p}} \epsilon(\mathbf{p})/p, \tag{2.24}$$

then the condition 2.23 is never satisfied and no excitation will spontaneously grow in the fluid. Condition 2.24 is the so called Landau's criterion for superfluidity. It ensures that if the relative velocity between the fluid and the capillary is smaller than the critical value v_c then there will be a persistent flow without friction.

By looking at the Bogoliubov excitation spectrum (Eq. 2.18 and Fig. 2.3), one easily concludes that the weakly-interacting Bose gas fulfils the Landau criterion for superfluidity and that the critical velocity is given by the velocity of sound c_s (Eq. 2.13). Superfluidity is then strongly related to the phenomenon of Bose-Einstein condensation. However according to the Landau criterion the ideal Bose gas is instead not superfluid since the value of v_c is equal to zero.

2.2.2 Bogoliubov-Čerenkov radiation

The meaning of superfluidity in a BEC can be better understood by considering the density perturbation induced in the condensed gas flowing against a localized obstacle at rest.

Figure 2.6 (left column) show the Bogoliubov dispersion spectra of a moving fluid, Eq. 2.22, for increasing flow speeds (marked as red crosses). The main effect of the flow consists of the additional term $\mathbf{p} \cdot \mathbf{v}$, which tilts the dispersion and adds $\mathbf{v}$ to the propagation group velocity of all the Bogoliubov excitations.

Considering that the fluid is scattered elastically by the time-independent defect potential, the excited modes are the Bogoliubov ones whose energy is $\epsilon(\mathbf{p}) = 0$, shown in the centre column of Fig. 2.6. Modulo a Galilean transformation, this condition corresponds to the usual Čerenkov resonance condition [70]. Depending on whether the flow speed is slower or faster than the speed of sound in the BEC, two regimes can be identified. In the subsonic regime $v < c_s$, no solution $\epsilon(\mathbf{p}) = 0$ exists for $\mathbf{p} \neq \mathbf{v}/m$ (Figs. 2.6a,b), which physically means that no Bogoliubov mode can be resonantly excited by the defect (Fig. 2.6c). The BEC is superfluid and can flow around the defect without suffering any dissipation, in agreement with the Landau criterion of superfluidity.

On the other hand, in the supersonic regime, $v > c_s$ (Figs. 2.6d,g,j), the set of $\mathbf{p}$ vectors satisfying $\epsilon(\mathbf{p}) = 0$ is not empty, but rather corresponds to the closed curves shown in Figs. 2.6e,h,k. Some of the kinetic energy associated to the flow is therefore dissipated as radiation of Bogoliubov modes. In real space (Figs. 2.6f,i,l), the perturbation radially propagates from the defect with a velocity given by the group velocity of the mode $\mathbf{v}_g = \nabla\epsilon(\mathbf{p})$. For each mode $\mathbf{p}$, the direction of $\mathbf{v}_g$ corresponds to the outward normal to the curve $\epsilon(\mathbf{p}) = 0$. Close to the singular point at $\mathbf{p} = \mathbf{v}/m$, the curve given by $\epsilon(\mathbf{p}) = 0$ consists of two straight lines separated by an angle 2ϕ, defined by the usual Čerenkov condition $cos\phi = c_s/v$ (Figs. 2.6e,h,k) .

The plots in the right column of Fig. 2.6 show the BEC spatial profiles around the defect at $\mathbf{r} = 0$. The strongest density perturbation lies on the Mach cone of aperture θ such that $sin\theta = c_s/v$, and directed in the downstream direction, corresponding to a Čerenkov emission of phonons by the defect; since the flow velocity is larger than the sound velocity, the density perturbation is dragged away from the defect. At the rightmost points of the curves given by $\epsilon(\mathbf{p}) = 0$, the perturbation propagates in the upstream direction with respect to the BEC flow and gives an oscillating density modulation (see Figs. 2.6f,i,l), which is a direct consequence of matter-wave interference between the incident BEC and the scattered particle–like Bogoliubov excitation–wave off the obstacle.

These findings are in agreement with experiments performed in JILA [72] by letting a BEC expand at supersonic speed, $v > c_s$ against a localized optical Gaussian potential of a far-blue-detuned laser beam. The observed density profile, Fig. 2.7, of the BEC flowing from the right to the left, is strongly reduced in a conical shadow region, separated from the unperturbed condensate region by a conical wave front starting at the defect and followed by a fan-shaped series of precursors which extends far in the upstream direction.

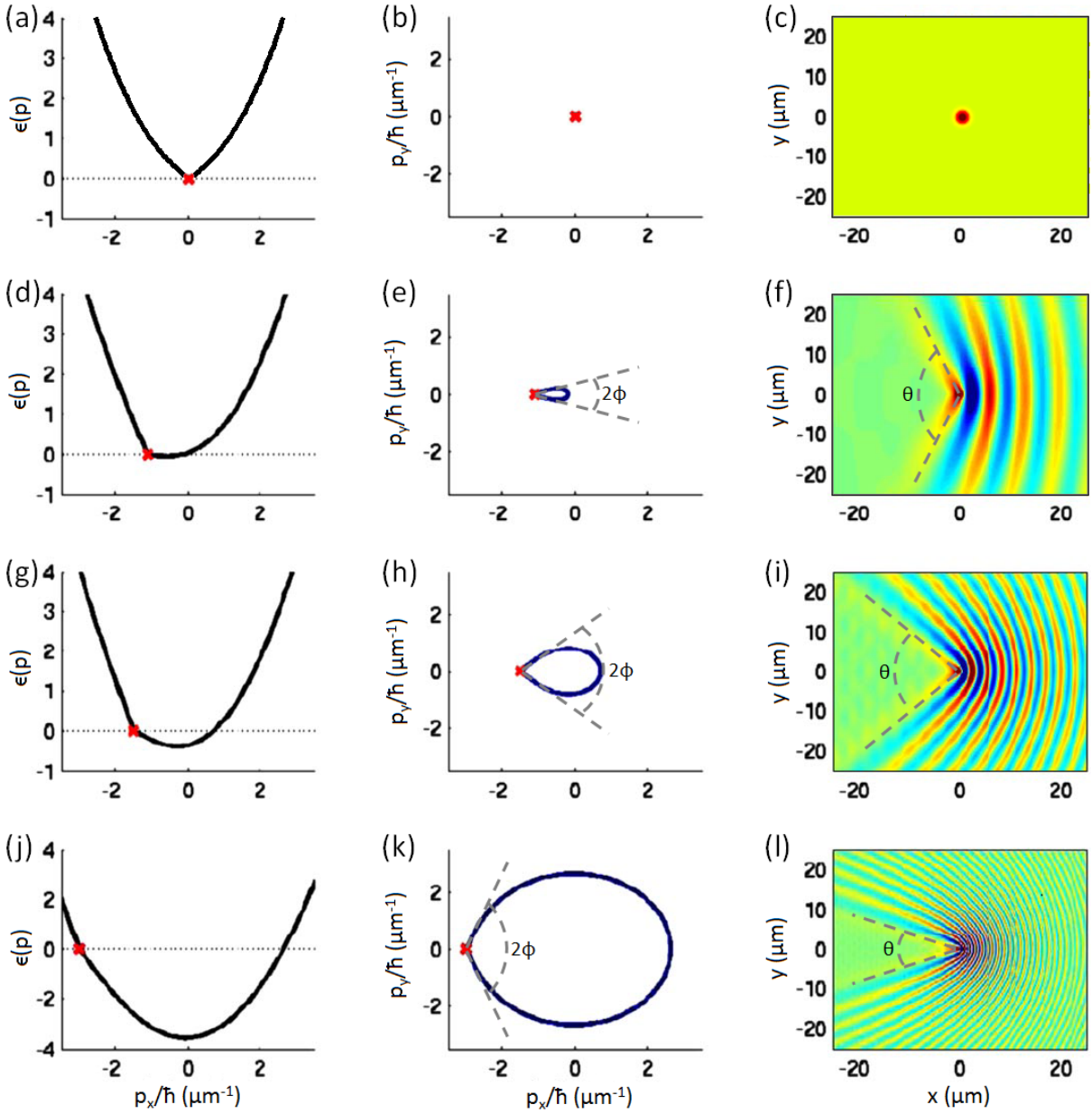

Figure 2.6: (left column) Dispersion of Bogoliubov modes. (center column) Momentum of resonantly excited ($\epsilon(\mathbf{p}) = 0$) Bogoliubov modes. Red crosses mark the BEC flow momentum, $\mathbf{v}/m$. (right column) Spatial density profiles. The flow velocities are $v/c_s = 0$, 1.1, 1.5 and 3 in each row, respectively. Adapted from [71]

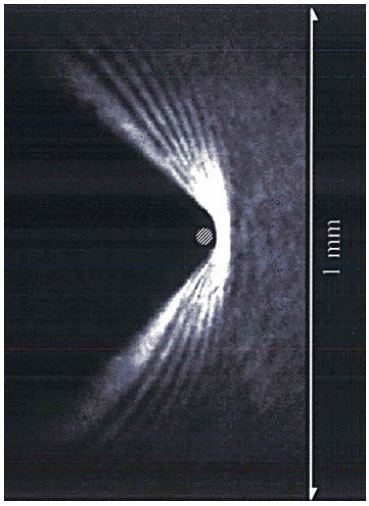

Figure 2.7: Experimental density profile of a ^{87}Rb BEC hitting an obstacle at supersonic velocity $v/c_s = 13$. The angle of the conical wave front is $sin(\theta) = 0.73$. The condensate flow is from the right to the left. From Ref. [72]

2.3 Long-range order

Given a field $\psi(\mathbf{r}, t)$, the density matrix (also called correlation function), $\rho = |\psi\rangle\langle\psi|$, in space-time representation is given by:

$$\rho(\mathbf{r}, \mathbf{r}', t, t') = \langle \mathbf{r}, t|\rho|\mathbf{r}', t'\rangle = \langle \mathbf{r}, t|\psi\rangle\langle\psi|\mathbf{r}', t'\rangle = \langle \psi(\mathbf{r}, t)\psi^*(\mathbf{r}', t')\rangle, \tag{2.25}$$

where the last $\langle\rangle$ denotes statistical average — see Section 4.3. It is clear that $\rho(\mathbf{r}, \mathbf{r}, t, t) = n(\mathbf{r}, t)$ is a real number (since ρ is an Hermitean operator, $\rho^\dagger = \rho$) that represents the number of particles in position $\mathbf{r}$ at a time t.

The field can also be represented in energy-momentum space after Fourier transform, $\widetilde{\psi}(\mathbf{k}, \omega) = \int d\mathbf{r}dt\psi(\mathbf{r}, t)e^{i(\mathbf{kr}-\omega t)}$. The Wiener-Khinchin identity [73–75] states that the energy and momentum distribution $|\widetilde{\psi}(\mathbf{k}, \omega)|^2$ of such a field can be calculated from its density matrix through a simple Fourier transform:

$$|\widetilde{\psi}(\mathbf{k}, \omega)|^2 = \int d\mathbf{r}d\mathbf{r}'dtdt'\rho(\mathbf{r}, \mathbf{r}', t, t')e^{i[\mathbf{k}(\mathbf{r}-\mathbf{r}')-\omega(t-t')]}, \tag{2.26}$$

As discussed in Section 2.1, Bose-Einstein condensation appears when the main population occupies a single energy-momentum state. Using Fourier transform properties and the Wiener-Khinchin identity 2.26, a narrow momentum distribution $|\widetilde{\psi}(\mathbf{k}, \omega)|^2$ implies a broad correlation $\rho(\mathbf{r} - \mathbf{r}')$ and so the off-diagonal terms of the density matrix $\rho(\mathbf{r}, \mathbf{r}')$ are different from zero. More specifically, if the $|\widetilde{\psi}(\mathbf{k}, \omega)|^2$ distribution is concentrated on the $k = 0$ value, $\rho(\mathbf{r} - \mathbf{r}')$ tends to a plateau value different from zero as $|\mathbf{r} - \mathbf{r}'| \to \infty$. This corresponds to the existence of off-diagonal long-range order (ODLRO) and was proposed by Penrose and Onsager in 1956 [6] as a general definition of a BEC. This is equivalent to say that N_0, the largest eigenvalue of ρ, is of the order of the total number of particles in the quantum fluid.

The density matrix of a macroscopic quantum system can be then decomposed into its ground state part and the excited states part,

$$\rho(\mathbf{r},\mathbf{r}') = \langle\psi_0(\mathbf{r})\psi_0^*(\mathbf{r}')\rangle + \langle\psi_{exc}(\mathbf{r})\psi_{exc}^*(\mathbf{r}')\rangle \tag{2.27}$$

The second term in the right hand side of Eq. 2.27 goes to zero when $|\mathbf{r}-\mathbf{r}'|$ goes to ∞, while the first term has a finite and constant value due to the well defined phase of the macroscopically occupied ground state [76].

Figure 2.8 shows the measured spatial dependence of the normalized correlation function $\rho(\Delta r)/\rho(r)$ for ^{87}Rb atoms trapped and cooled by a magneto-optical trap, from Ref. [77]. The correlation values are extracted from the visibility of interferences between distant points of the gas. The thermal non-condensed fraction of the gas is responsible for a Gaussian decay of the correlation, with a a spatial scale given by the de Broglie wavelength, Eq. 2.7. Above the critical temperature for condensation, such a decay goes down to zero for large distances, differently for the non-zero plateau observed for temperatures bellow condensation threshold — see Fig. 2.8. Such a plateau has the value of the fraction of atoms occupying the zero-momentum state, N_0/N also called condensed fraction [55].

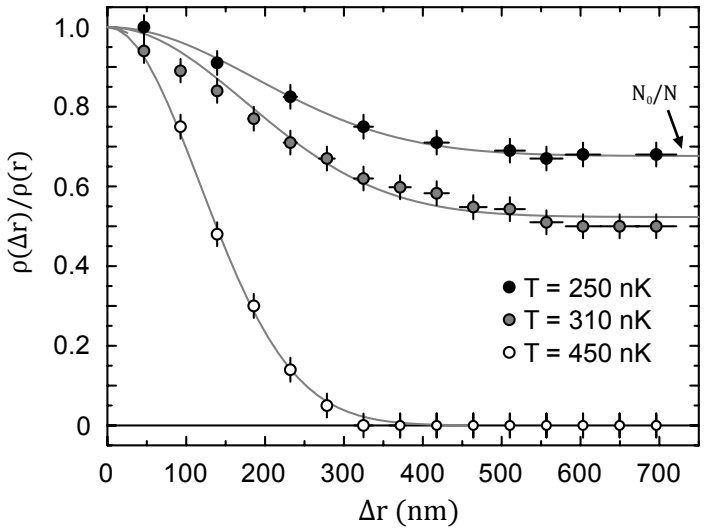

Figure 2.8: Normalized spatial correlation function $\rho(\Delta r)/\rho(r)$ of a ^{87}Rb trapped Bose gas, for temperatures above and below the critical temperature $T_c = 430\,nK$. The white circles show the measurements for thermal gases at $450\,nK$. The grey data points ($310\,nK$) and the black data points ($250\,nK$) are the results obtained for temperatures below T_c, where the visibility decays to a nonzero value due to the long–range phase coherence of the condensate fraction. The data sets are plotted with a gaussian function and an offset. Adapted from [77].

2.3.1 Condensation in low dimensions

Conventional long-range order, as in a ferromagnet or a crystal, is common in three-dimensional systems at low temperature. However, in two-dimensional systems with a continuous symmetry, true long-range order is destroyed by thermal fluctuations at any finite temperature [78]. Consequently, for the case of identical bosons, a uniform two-dimensional fluid cannot undergo Bose-Einstein condensation, in contrast to the three-dimensional case.

In fact, if one tries to calculate the critical density for condensation to take place, by performing an integral similar to Eq. 2.6 but using instead a 2D density of states, the result diverges at non-zero temperature. Thus, the non-interacting Bose gas cannot condense in an infinite 2D system. The same statement turns out to be also true when interactions are taken into account. A rigorous proof of the absence of BEC in two dimensions has been given by Hohenberg and co-workers [79]

However, the two-dimensional system can form a quasi-condensate and become superfluid below a finite critical temperature. The Berezinskii-Kosterlitz-Thouless (BKT) theory [80, 81] associates this phase transition with the emergence of a topological order, resulting from the pairing of vortices with opposite circulation. At the transition temperature $T = T_{BKT}$, the spatial correlation function decays according to a power-law with a value of the decay exponent equal to 1/4 [55,82]. Above the critical temperature, proliferation of unbound vortices is expected and the quasi-long-range order is lost.

2.4 Rotation of quantum fluids

To construct a quantitative theory of the flow properties of He-II, Landau postulated that it consisted of two components: the *superfluid* component, which he identified, in an intuitive way, with the part of the liquid that remained in its ground state, and a *normal* component, which corresponded to the thermal cloud. The superfluid component was conceived as carrying zero entropy and flowing irrotationally; by contrast, the normal component behaved like any other viscous liquid.

The presence of a large number of atoms in the ground state (Bose-Einstein condensate) allows the introduction of a classical function $\psi_0(\mathbf{r}, t)$ to describe the order parameter. In the mean field approximation, assuming that ψ_0 varies slowly on distances of the order of the range of the interatomic forces, one can introduce interactions to the Schrödinger Hamiltonian by means of the density-dependent chemical potential defined in Eq. 2.14:

$$i\hbar\partial_t\psi_0(\mathbf{r}, t) = \left(-\frac{\hbar^2\nabla^2}{2m} + V_{ext} + g|\psi_0(\mathbf{r}, t)|^2\right)\psi_0(\mathbf{r}, t) \tag{2.28}$$

where g is the interaction coupling constant defined by Eq. 2.9.

Equation 2.28 was derived independently by Gross and Pitaevskii in 1961 [83,84] and is the main theoretical tool for investigating non–uniform dilute Bose gases at low temperatures. An important peculiarity is the nonlinearity arising from the interaction among particles, which introduces an important analogy between Bose-Einstein condensation and nonlinear optics.

Equation 2.28 implies the continuity equation,

$$\partial_t|\psi_0|^2 + \nabla\cdot\mathbf{j} = 0, \tag{2.29}$$

where the current density $\mathbf{j}$ is given by

$$\mathbf{j}(\mathbf{r}, t) = -i\frac{\hbar}{2m}(\psi_0^*\nabla\psi_0 - \psi_0\nabla\psi_0^*) = \frac{\hbar}{m}\nabla|\psi_0|^2\phi \tag{2.30}$$

Here ϕ is the phase of the order parameter, $\psi_0(\mathbf{r},t) = |\psi_0|e^{i\phi(\mathbf{r},t)}$. Equation 2.30 shows that the vector

$$\mathbf{v}_s(\mathbf{r},t) = \frac{\hbar}{m}\nabla\phi(\mathbf{r},t) \tag{2.31}$$

is the velocity of the condensate flow, which turns out to be irrotational ($\nabla \times \mathbf{v}_s = 0$), a typical characteristic of superfluids. For a simply connected region of space in which $|\psi_0(\mathbf{r},t)|$ is everywhere nonzero, the application of Stokes theorem to the curl of Eq. 2.31 leads to the conclusion that the integral of $\mathbf{v}_s$ around any closed curve is zero.

2.4.1 Quantized vortices

The Gross-Pitaeviskii equation 2.28 also admits non-trivial solutions with a core region where the density goes to zero. Such a solution is no longer imposed by the Stokes' theorem to have a vanishing integral of the velocity around a circuit that encloses the core. The fact that the phase $\phi(\mathbf{r})$ must be single-valued, modulo 2π, leads to the Onsager-Feynman quantization condition

$$\oint \mathbf{v}_s d\mathbf{l} = Mh/m \tag{2.32}$$

The parameter M is an integer in order to ensure that the wave function is single valued.

Such vortex solutions are written in cylindrical coordinates as

$$\psi_0(\mathbf{r}) = e^{iM\varphi}|\psi_0(r)|, \tag{2.33}$$

with φ the azimuthal angle and r the radius. The size of the zero-density core in $|\psi_0(r)|$ is of the order of the healing length, Eq. 2.21 [55]. Equation 2.33 is an eigenstate of the third component of the angular momentum[2] with $l_z = M\hbar$, so that the vortex carries a total angular momentum equal to $L_z = N_0 M\hbar$. This wave function represents a gas rotating around the z-axis with tangential velocity $v_s = \frac{\hbar M}{mr}$, completely different from the rigid rotational field, which is also tangential, but whose modulus increases with r.

Result 2.32 is independent of the radius of the contour. This is a consequence of the fact that the *vorticity* ϖ of the velocity field is concentrated on the z-axis according to the law

$$\varpi = \nabla \times \mathbf{v}_s = \frac{Mh}{m}\delta^{(2)}(\mathbf{r})\hat{\mathbf{z}} \tag{2.34}$$

where $\delta^{(2)}(\mathbf{r})$ is the 2D Dirac delta function and $\mathbf{r}$ is the radial position vector perpendicular to $\hat{\mathbf{z}}$. Results 2.33 and 2.34 show that the irrotationality criterion, associated with the occurrence of Bose-Einstein condensation, is satisfied everywhere except on the line of the vortex. This equations establishes the irrotationality of the superfluid motion, the phase of the order parameter playing the role of a velocity potential.

[2]For the sake of simplicity, and making an abuse of language, we shall call in the rest of the manuscript angular momentum to its third component.

The existence of vortices was first predicted in superfluids [85,86], and later in coherent waves [87]. Nowadays, quantum vortices have been the subject of extensive research across several areas of physics and have been observed in type-II superconductors, ^{4}He, ultracold atomic gases and nonlinear optics media (for a review see, *e.g.*, [88, 89]).

The most interesting application of Eq. 2.32 related to the definition of superfluidity occurs when considering a liquid helium inside a rotating cilindrical container [90]. Above the lambda temperature T_λ, helium behaves like any other 'normal' liquid and the fluid angular velocity will be the same as the container after thermal equilibrium is established. The system is then cooled down below T_λ, and by measuring the changes in the angular velocity of the vessel one can extract the corresponding changes in the angular momentum of the liquid. Below T_λ, the superfluid fraction $N_0(T)/N$ is finite and moves with velocity v_s. However, the angular momentum is constrained by the quantization condition $L_z = N_0 M\hbar$. In fact, a simple statistical-mechanical argument shows that the lowest free energy is obtained when M takes the value closest to $L/(\hbar N_0)$, L being the fluid total angular momentum before cooling; for $L << N\hbar$ this is obviously zero. Consequently, the superfluid component no longer contributes to the circulating current and the total angular momentum is reduced by a factor $N_0(T)/N$. In particular, for $T \to 0$ the fluid angular momentum tends to zero even though the vessel is still rotating. At larger angular momentum values $N\hbar/2 < L < N\hbar$ a vortex line is created and the superfluid contributes to the angular momentum with an amount $N_0\hbar$, thus the apparent velocity of the liquid may exceed that of the container. This remarkable effect, which turns out to be close analog of the Meissner effect in superconductors, was originally predicted by F. London and eventually observed by Hess and Fairbank in 1967 [90]; it is a manifestation of the equilibrium behavior of the system.

The direct visualization of vortices was achieved in the experiments by Packard and Sanders [91]. In this experiment one injects a beam of electrons inside a rotating cylinder of liquid ^{4}He. Vortex lines trap the electrons, which are then accelerated along the vortical line by an electric field and are eventually detected after escaping from the liquid. Figure 2.9(upper graph) show the electrometer voltage output as a function of the rotating cylinder angular velocity. Clearly a rotation threshold is needed for the superfluid to start rotating and the electron signal to be detected. As the rotation is further increased, the detected signal increases by quantized jumps, which are related to the creation of extra vortices.

A similar apparatus with spatial resolution have been used to image arrays of quantized vortex lines distributed in a regular geometry, through electrons that create spots on a fluorescent screen [92] — Fig. 2.9 (lower panels).

Quantized vortices in trapped Bose gases have become experimentally available by making use of a suitable rotating modulation of the trap to stir the condensate [93], in close resemblance with the rotating bucket experiment of superfluid helium. However in situ measurements cannot provide any evidence of the vortex core, whose size (typically less than one micron) is too small, which introduces the need to expand the condensate cloud in order to enlarge the vortex to become visible. Above a critical angular velocity one observes the formation of the vortex. A typical picture is shown in Fig. 2.10, where one can see that, at sufficiently high angular velocities, arrays with more vortices are also formed. It is possible to create arrays containing a very large number of vortical lines — see Ref. [94] and last panels of Fig. 2.10. These arrays form a typical triangular lattice, which is similar to what happens in superconductors [95].

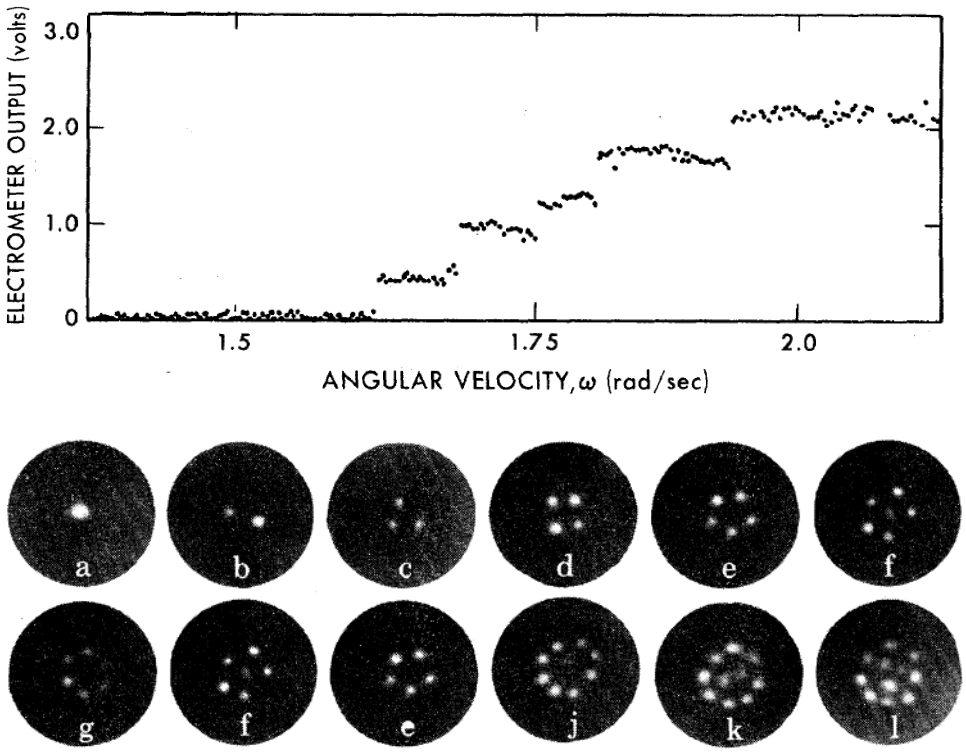

Figure 2.9: Quantized rotation of superfluid helium. (upper graph) Measured voltage of an electrometer that detects electrons transmitted by rotating superfluid helium through its vortex lines, as a function of the container angular velocity. The signal is proportional to the number of vortices in the system. (lower panels) Photographs of stable vortex arrays in superfluid helium for different angular velocities. Upper graph from Ref. [91]. Lower panels from Ref. [92].

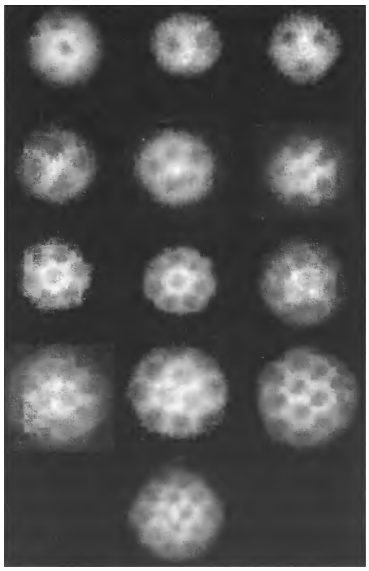

Figure 2.10: Absorption images of a Bose-Einstein condensate for increasing trap angular velocity, containing up to thirteen vortices. Experiments done at the Ecole Normale Superieure in Paris. From [96]

2.4.2 Persistent currents

A different phenomenon, which at first sight is closely related to the ones in the previous section but is conceptually quite different, is obtained for a rotating superfluid when the container is brought to still-stand and by decreasing the temperature. The experiment starts with angular momentum of the liquid $L > N\hbar/2$, above T_λ. Next it is cooled, still rotating, through T_λ, with the superfluid component taking the closest available quantized value of circulation. Finally, still keeping the temperature below T_λ, the rotation of the container is stopped. The contribution of the normal component rapidly relaxes to zero, but the superfluid contribution persists for a very long time. In other words, the system preserves the value of the superfluid circulation, Eq. 2.32, that it originally had, even though it is clearly not the equilibrium one. This is the phenomenon of metastable superflow, also known as persistency of currents.

A similar experiment has been performed in Bose-condensed sodium atoms in a toroidal trap by Ryu *et.al.* in 2007 [97]. Fig. 2.11a shows the trap shape, consisting of a magnetic trap and a plug laser bem at the centre, and Fig. 2.11b the continuous toroidal-shaped BEC imaged in the trap. Figure 2.11c shows the time-of-flight (TOF) expansion image of the nonrotating BEC taken $18\,ms$ after instantaneously extinguishing the toroidal trap. The initial hole in the BEC is filled in during expansion. Quantized rotation was initiated by transferring one unit $\hbar$ of orbital angular momentum from Laguerre-Gaussian photons to each atom. In Fig. 2.11d, the corresponding TOF image of a circulating BEC after transfer of $\hbar$ of OAM is shown, again taken $18\,ms$ after instantaneously extinguishing the toroidal trap. The hole is clearly visible, providing a simple way to detect circulation.

In Fig. 2.11e the probability of observing the circulating state is plotted (squares) as a function of time held in the trap. The circulation in the toroidal trap (*i.e.*, with the plug beam) persists without decay for up to $10\,s$. In contrast, the circulation in only the magnetic trap (without the plug beam) decays in about $0.5\,s$. In conclusion, stable flow was only possible when the trap was multiply connected.

One of the interesting aspects of persistent flow is its stability at finite temperatures. Figure 2.11f shows the measured survival probability of the circulation after $2\,s$ of trapping time for various BEC fractions, obtained by varying the gas temperature when performing evaporative cooling. Stable flow was observed with a Bose-Einstein condensate fraction as small as 20%.

Under the same experimental conditions, Ryu *et.al.* [97] also studied the stability of higher circulation in the toroidal trap by transferring higher angular momentum to the atoms. The flow was initially stabilized in the toroidal trap for $0.5\,s$, and then the plug beam power is ramped down in $30\,ms$. Figure 2.12 shows images, after $20\,ms$ TOF, of the circulating cloud with two units of angular momentum for different hold times in just the magnetic trap. Initially there is a single larger hole in the centre due to the higher angular momentum. After evolving in the magnetic–trap only for longer times, the doubly charged vortex show splits into two singly charged vortices.

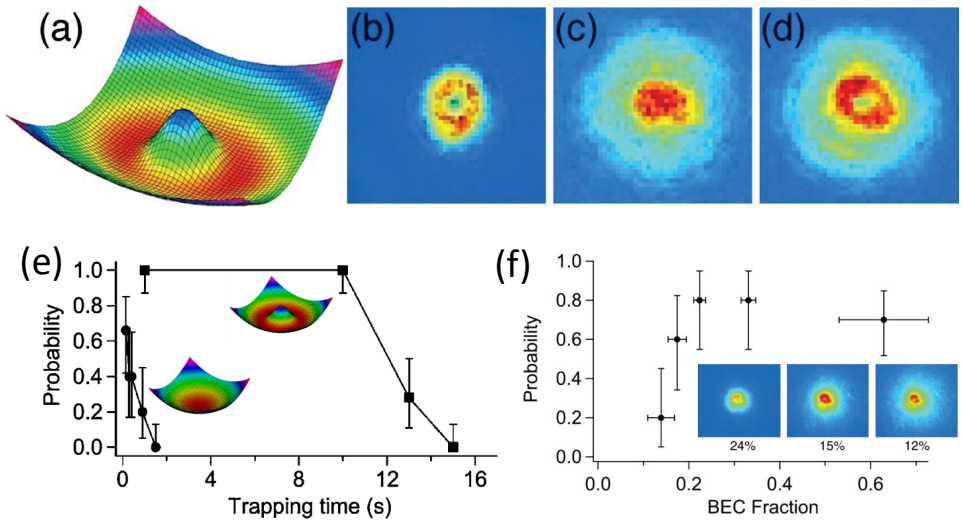

Figure 2.11: Persisten currents of sodium atoms. (a) Toroidal trap from the combined potentials of a magnetic trap and a laser beam. (b) In situ image of the BEC in the toroidal trap. (c) Time-of-flight (TOF) image of a noncirculating BEC released from the toroidal trap. (d) TOF image of a circulating BEC, released after transfer of $\hbar$ of orbital angular momentum. (e) Survival probability of circulation as a function of trapping time in the magnetic trap without the plug beam (circles) and with the plug beam (squares). (f) Survival probability of a circulating BEC for a 2 s trapping time, as a function of the BEC fraction. Inset: three TOF images of a circulating BEC for BEC fractions of 24%, 15%, and 12%. Adapted from [97]

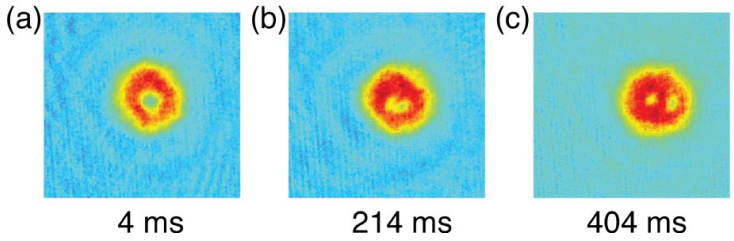

Figure 2.12: TOF pictures of doubly charged flow, initially stabilized for 0.5 s in the toroidal trap, for different holding times (4, 214, and 404 ms) in just the magnetic trap. From [97]

2.5 Exciton-polariton quantum fluids

The phenomenon of condensation has not only resided in the atomic or superfluid helium community but it has rather stimulated the semiconductor community from the early years. As early as 1962, excitons were proposed by Blatt and Moskalenko as promising candidates for the realization of Bose-Einstein condensation [98]. The bosonic nature of these quasiparticles and their light mass, were the main reasons for the long efforts to demonstrate condensation, with good progresses made in bilayer systems [99]. More recently such systems have been shown to display spontaneous spatial coherence at cryogenic temperatures [100].

The observation of strong coupling in semiconductor microcavities [5] showed that polaritons — composite bosons with a half exciton- half photon–nature — could be a

new system to study condensation in semiconductor materials. The polariton dispersion can act as a trap in momentum space and the mass of polaritons is four orders of magnitude lighter than that of excitons, theoretically allowing condensation even at room temperatures, according to Eq. 2.2.

The first theoretical discussion on the strong potential of exciton-polaritons for the realization of unusual quantum degenerate Bose gases was done by A. Imamoglu and co-workers in 1996 [101]. It was suggested that, provided that the thermal de Broglie wavelength λ_T exceeds the exciton Bohr radius a_B, an exciton laser would operate without electronic population inversion — the light emitted by a polariton condensate after decay is coherent, hence the analogy with a laser.

The properties of a polariton condensate differ from those of other known condensates, such as ultracold atomic BECs and superfluid ^{4}He. In particular, polaritons have a short lifetime of the order of picoseconds (which allows the to study of their phase and coherence in a direct way through the photons leaking out of the caivity, a feature not accessible to other bosonic quasiparticles), therefore needing continuous pumping to balance decay and reach a steady-state regime. Rather than a drawback, the intrinsic non-equilibrium nature enriches the features of polariton condensation, at the same time posing fundamental questions about the robustness of the coherence phenomena to dissipation and non-equilibrium.

Condensation-related phenomena has been experimentally observed in polaritons in different samples, excitation setups and temperatures [14–20,31,32,35–37,102–122]. However, there are still many open questions about the best way to qualify a polaritonic macroscopically occupied quantum state [123,124]. Polaritons are two-dimensional quasiparticles which cannot exhibit a strict BEC phase transition, but possibly a local condensation or a BKT phase transition (section 2.3.1). However such a description is also inaccurate since, being an out-of-thermodynamical equilibrium system, neither a temperature nor even a phase transition can be defined in planar semiconductor microcavities.

2.5.1 Excitation schemes

Polaritons can exist in semiconductor microcavities with long photon lifetimes (high-Q optical cavities) and large light-matter Rabi coupling exceeding thermal energies ($\hbar\Omega > k_BT$). The physical processes underlying the creation of a polariton condensate are strongly dependent on the way the driving field is injected into the cavity. We classify the many available excitation geometries into three different groups in the following sections, starting with the one most related with cold atom BECs.

2.5.1.1 Non-resonant pumping

In the non-resonant scheme, no coherence is introduced in the system via the excitation laser. It allows for thermodynamics to play an important role in the mechanism of polariton condensation. The laser beam excites free hot electron-hole pairs, whose main excess energy is relaxed by several very fast emissions of LO-phonons in the lattice — see Fig. 2.13. A hot exciton gas is thus formed [125]. For this population to relax into the polariton states of lowest energy, a few tens of meV below, acoustic phonon emission is the main possible channel. As the energy dispersion of polaritons is very steep as compared to acoustic phonons, this relaxation mechanism happens through very small momentum-energy exchanges, so it is very inefficient. This problem, known as

the *relaxation bottleneck* was well identified both experimentally [126, 127] and theoretically [128], using a Boltzmann description of the dynamics in the latter case. At high excitation intensity, *i.e.* at high exciton density, the relaxation bottleneck can be overcame by polariton-polariton inelastic scattering in such a way that the polariton ground state occupancy can be high enough to trigger bosonic stimulation of the relaxation [129]. However, there is a limit in the polariton density above which the photo-induced electronhole plasma bleaches the electron-hole coupling and so the exciton oscillator strength decreases.

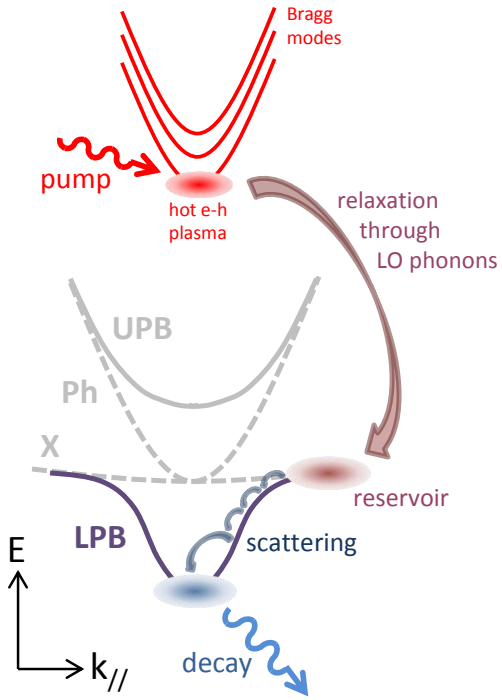

Figure 2.13: Non-resonant excitation scheme. A pump laser enter the cavity through the reflectivity minima of the Bragg modes, creating a hot electron-hole plasma that loses energy after many collisions with lattice LO-phonons. Electron-hole pairs then bind together to create an exciton reservoir at high-k values, that continue losing energy after polariton-polariton parametric scattering processes, favoured by high-density concentrations. A macroscopically occupied state is formed at the bottom of the LPB, eventually emitting a photon. This photon carries full information about the condensed polaritons.

There are three main solutions to achieve high enough polariton populations, without breaking the strong coupling, as to surpass the relaxation bottleneck: the first is to use microcavities with higher number of quantum wells inside, reducing then the carrier density per QW while the overall polariton density is unaffected; the second is to use DBRs mirrors with high reflectivity as to increase the polariton lifetime allowing enough time for the slow bottleneck relaxation towards low energies to take place; the third is to use materials where the exciton oscillator strength is high enough.

The choice of the material is also important when evaluating the critical temperature for condensation T_c. Equation 2.2 says that in principle such a temperature can be made arbitrary low by increasing the boson density n. However, in excitonic systems, if the thermal energy k_BT is higher than the biding energy the exciton dissociates and the fermionic nature of its constituents is recovered. The critical temperature for exciton

unbinding in $GaAs$ compounds is $\sim 70\,K$ [130], reaching $\sim 120\,K$ in $CdTe$ materials where the exciton binding energy is higher - see table 1.1.

In fact, a first clear observation of bosonic stimulation within a polariton gas was obtained by L.S. Dang and co-workers in 1998, in a $CdTe$-based microcavity with 16 embedded QWs, in which a non-linear increase of polariton photoluminescence has been observed when increasing the pump power, followed by VCSEL lasing from an electron-hole plasma at much higher powers [102]. Some years later the pioneering work of Richard *et.al.* [105] showed that such a non-linear increase of the polariton emission originates from a spectrally narrow ring in k-space, exhibiting enhanced spatial and angular coherence. Soon after, by increasing the excitation spot size, emission from a single quantum state lying at the bottom of the LPB was reported [131], giving a direct evidence for spontaneous formation of a nonequilibrium Bose condensate. Although this ground state emission had an spatial origin in many small islands where polaritons where trapped by sample disorder, such a state has been show to have macroscopic long-range order in the work of J. Kasprzak *et.al.* [15], where the condensate has been shown to spontaneous develop out of a thermalized Boltzmann-like incoherent reservoir. The reason for such a spatially extended coherence lies in phase-locking mechanisms between many condensates localized by the sample disorder potential [132]. Note that the final energy-momentum state chosen by the condensate is strongly dependent on the excitation spot size: whereas big pumps create a ground state stopped ($k = 0$) condensate [15], tighter pump spots favours the appearance of a expanding condensate at a finite k-ring [37, 105, 110] — the mechanism behind that will be explained in Chapter 8. The continuously adjustable proportion of exciton to photon in a polariton allows exploring a wide range of non-equilibrium situations. At higher excitonic fractions of the LPB (positive photon-exciton detuning), higher collision rates and therefore faster thermalization allows for condensation at quasi-equilibrium with a defined temperature, whereas higher photonic fractions (negative detunings) yield out of equilibrium condensation without thermalization [106].

Although many achievements has been done in $CdTe$-based samples, their strong disorder and consequently short lifetimes limit polariton free propagation. Because $GaAs$ and $AlAs$ are practically lattice-matched, the microcavity-layers have very little induced strain, which allows many DBR layers (yielding long photon lifetimes) to be grown and with very weak disorder.

The first AlGaAs-based microcavity, with 12 QW, showing evidences for condensation [14] were excited in a pumping scheme closely related but, strictly speaking, different from the one previously described: instead of creating a hot excitonic reservoir after relaxation from the electron-hole plasma, the reservoir was resonantly excited by a pump laser at very high angles, where the LPB is purely excitonic. Under fully non-resonant excitation, Bose-Einstein condensation has been observe in $GaAs$ microcavities under stress [16]. Better quality samples with low disorder and long lifetimes showed recently spontaneous condensation of polaritons in both the LPB groung state [109] or in a k-space ring, with a large spatial extension in the latter case [110].

Condensation of polaritons under non-resonant excitation has been demonstrated through the observation of a macroscopic occupation of a narrow ground energy-momentum state, which corresponds, according to the Wiener-Khinchin identity 2.26, to extended spatial- [15] and long time- [16] correlations. The spatial correlation function of a polariton condensate has a power-law decay [117] as expected in a 2D condensate (see Section 2.3.1), a signature of a BKT transition which is related to spontaneous creation of V-AV pairs [116]. However this decay is much shaper, with a decay exponent around four times

bigger than the one in an equilibrium BKT transition. Reduced energy linewidths provide high correlation times, which have been studied as a footprint of polariton condensation. However the correlation time-decay is influenced by a number of factors related to the non-equilibrium nature, including pump noise [16], interactions and reservoir fluctuations [108].

In large bandgap materials the critical temperature for exciton unbinding is as high as $400\,K$ (GaN), where the first room-temperature polariton laser has been demonstrated [17,107], and $560\,K$ (ZnO), where many recent works report on high temperature polariton non-linearities and condensation [133–138]

2.5.1.2 Coherent drive in the pump-only configuration

Thanks to their photonic component, polaritons can be coherently excited by an incident laser field resonant with the LPB at a small k vector, creating a moving polariton fluid with the same energy and momentum as the pumping laser. Its coherence clearly do not appear spontaneously due to bosonic condensation, but is inherited from the pumping field. Under CW-excitation, the phase is imprinted by the laser beam, however it can evolve freely out from the excitation spot if the polariton lifetime is long enough [121,122]. An extra pulsed beam resonant with the CW one can also be used to trigger a moving extra population [29]. Under pulsed-only excitation, the fluid phase, initially imprinted by the pulsed laser, freely evolves according to the quantum hydrodynamics of the system [118,119].

The advantage of using the pump-only excitation scheme is that an accurate control of the polariton dynamics can be achieved by properly tuning the external laser. However care should be taken when detecting the polariton emission pumped resonantly by a CW-laser. Since both laser and polariton fields have the same energy and momentum, the latter cannot be detected in the direction of the reflected laser beam, because the laser bleaches the much less intense polariton luminescence. In this case, the detection has to be made in transmission geometry [19], all the light that passes through the cavity acquires a polaritonic character before being transmitted, and so fully carries information about the polaritonic field inside. When propagating out from the excitation area [121,122], the polariton photoluminescence is not superimposed with the excitation field and therefore it can be detected in both the transmitted or reflected directions. Under pulsed excitation [29,118,119], separation between polariton and laser fields are done in time since the pulse beam lasts much less than the polariton population lifetime.

2.5.1.3 Excitation in the optical-parametric-oscillator (OPO) regime

Thanks to their excitonic component, polaritons have strong non-linear behaviour inherited from the exciton-exciton interactions. In the parametric scattering process, two polaritons from a pump mode, with wavevector and frequency $[\mathbf{k}_p, \omega_p]$, scatter into a lower energy signal mode $[\mathbf{k}_s, \omega_s]$ and a higher energy idler mode $[\mathbf{k}_i, \omega_i]$. This scattering process has to conserve energy and momentum, therefore requiring the phase matching conditions:

$$2\mathbf{k}_p = \mathbf{k}_s + \mathbf{k}_i \tag{2.35a}$$

$$2\omega_p = \omega_s + \omega_i \tag{2.35b}$$

This condition cannot be satisfied by any particle dispersion. For example, parametric scattering is forbidden for particles with a quadratic dispersion. On the other hand, the "S" shape of the LPB makes it a good candidate to have the conditions 2.35 satisfied, since the LPB is approximately symmetric in energy and momentum around its inflection point — see Fig. 2.14. In fact, if $\mathbf{k}_s = 0$ then the momenta of pump and idler are uniquely selected, for a given the value of the pumping angle — also referred to as the "magic angle" — located close to the inflection point of the LPB.

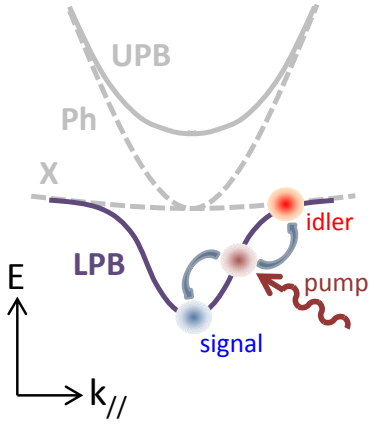

Figure 2.14: Illustration of parametric scattering excitation scheme, where polaritons injected by a laser beam resonant with the inflection point of the LPB scatter from the pump state $[\mathbf{k}_p, \omega_p]$ towards the signal $[\mathbf{k}_s, \omega_s]$ (here at zero momentum) and the idler state $[\mathbf{k}_i = 2\mathbf{k}_p - \mathbf{k}_s, \omega_i = 2\omega_p - \omega_s]$ (at higher momentum), conserving momentum and energy.

The simplest way of reach experimentally parametric scattering in a microcavity is to pump it resonantly close to the inflection point of the LPB. Parametric instabilities populate signal and idler modes which, at a certain threshold, have a state occupancy of order one, and so bosonic final-state stimulation causes polariton pairs to coherently scatter from the pump state to the signal and idler states [103], in the so-called OPO excitation regime of a polariton condensate [104].

A second laser beam can be used to trigger parametric processes if there are more available states (called conjugate states) in the LPB in such a way that the phase matching conditions 2.35 are satisfied by probe, pump and conjugate states (whose may be in principle different from the signal and idler states). This holds even if the pump beam is below OPO threshold (but close to it), in which case the probe state will still be amplified. This optical parametric amplification (OPA) regime — also called triggered optical parametric oscillator (TOPO) regime [18] — was first observed in an InAlGaAs microcavity [139]. Ultrafast parametric amplification of polaritons with extraordinary gains up to 1500 and temperatures up to $220\,K$ has been reached, in this regime, in CdTe-based microcavities [21].

On the other hand, when a CW pump laser drives the system above OPO threshold, the probe and conjugate states are extra population states, on top of the steady state OPO signal and idler states. When triggered by a pulsed laser, both probe and conjugate states are travelling decaying states that can evolve freely from the laser probe constraints once the pulse switches off. If the pulse lies at a region of the LPB with a large exciton content, the small-k conjugate extra population lasts for up to the nanosecond timescale [140], and its energy and momentum can be tuned by the pulsed probe as long as phase-matching

conditions are satisfied [18]. When the trigger is resonant with the OPO signal, the extra-population lifetime is shorter, but still bigger than the polariton lifetime [20, 35].

The OPO state, characterized by the macroscopic occupation of three polariton states only, looks at first sight very different from an equilibrium weakly interacting BEC, where the macroscopic occupation of the ground state occurs from a thermal distribution of bosons. The OPO state does, however, share with a BEC the fundamental property of spontaneous symmetry breaking of the phase symmetry [141]. In fact, the external laser fixes the phase of the pump state ϕ_p and parametric scattering processes constrain the sum of the signal and the idler phase only, $2\phi_p = \phi_s + \phi_i$ [142], but leaves the system to arbitrarily choose the phase difference $\phi_s - \phi_i$. In fact, above OPO threshold, the signal and idler spontaneously select their phase, though not independently. This spontaneous symmetry breaking when choosing a phase above OPO threshold implies that the long-wavelength excitations (Bogoliubov) of the OPO signal state have similarities to the ones of an equilibrium BEC — see section 2.5.2.3 for details.

The excitation spectrum of the OPO signal state is expected to have a vanishing energy linewidth [141], which would give extremely long correlation times, another footprint of condensation, according to the Wiener-Khinchin identity 2.26. In fact, using an extremely low noise pump laser, correlation times in the nanosecond time scale has been reported [112] one order of magnitude longer if compared to non-resonant excitation geometries [108], where the reservoir noise play an important role.

In addition, the appearance of spontaneous spatial coherence in the OPO signal has been shown via quantum Monte Carlo simulations [143], and recently confirmed by experiments [112, 113] through the divergence of the coherence length when the pump energy approaches that of the LPB from below.

2.5.2 Polariton quantum hydrodynamics

Unlike BECs of weakly interacting Bose gases for which the Gross-Pitaevskii (GP) equation has been shown to accurately represent the states of the condensates, the polariton condensates are nonequilibrium systems, which are best understood as a steady-state balance between pumping and decay, rather than true thermal equilibrium.

Using a mean-field description of the condensate [144, 145] one can recover a complex Gross-Pitaevskii equation (cGPE), including terms representing gain, loss and an external trapping potential, describing the dynamics of the lower polariton wavefunction, ψ,

$$i\hbar\partial_t\psi = \left[-\frac{\hbar^2\nabla^2}{2m^*} + g|\psi|^2 + V_{ext}\right]\psi + \frac{i\hbar}{2}\left[P - \Gamma\right]\psi \tag{2.36}$$

where Γ is the polariton decay rate, P the pumping rate, g the polariton repulsive interaction coupling constant, V_{ext} the external potential, and the polariton dispersion has been approximated by a parabola with m^* being the effective mass.

This modification of the GP equation to account for such nonequilibrium properties of the condensates is a complex Ginzburg-Landau equation (cGLE), a universal equation of mathematical physics describing the behaviour of systems in the vicinity of an instability and symmetry breaking [146], *e.g.* nonlinear waves, superconductivity, superfluidity, liquid crystals and strings in field theory, and capable of spontaneous pattern formation. Formally, it is a nonlinear Schrödinger equation with complex coefficients.

The superfluid properties of nonequilibrium condensates in a dissipative environment

still need to be completely understood [147]. For polariton fluids, one has to singularly assess the system properties in the three different pumping schemes available.

2.5.2.1 Pump-only configuration

Let us consider the propagation of a resonantly created polariton fluid in the presence of a static small defect $V_{ext}(\mathbf{r})$. The driving field is assumed to be a coherent and monochromatic laser field of frequency ω_p, $P(\mathbf{r},t) = e^{i(\mathbf{k}_p\cdot\mathbf{r}-\omega_p t)}$, which generates a polariton fluid with a nonzero flow velocity and a spatial plane-wave profile of wave vector $\mathbf{k}_p$ along the cavity plane.

Under resonant excitation, the polariton field oscillation frequency is not fixed by an equation of state relating the chemical potential to the particle density, but it can be tuned by the frequency of the exciting laser. This opens the possibility of having a collective excitation spectrum which has no analog in usual systems close to thermal equilibrium.

The response of the system to a weak perturbation is obtained using a linearized theory analogous to the well-known Bogoliubov theory of the weakly interacting Bose gas. Close to the bottom of the lower polariton branch, $\omega_{LPB}(\mathbf{k}=0)$, the spectrum of the Bogoliubov excitations can be approximated by the simple expression [144]

$$\omega^{\pm}_{Bog} \simeq \omega_p + (\mathbf{k}-\mathbf{k}_p)\cdot\mathbf{v}_p - i\Gamma \pm \sqrt{[2g|\psi|^2 + (\mathbf{k}-\mathbf{k}_p)^2/2m^* - \Delta_p][(\mathbf{k}-\mathbf{k}_p)^2/2m^* - \Delta_p]}, \tag{2.37}$$

where $\mathbf{v}_p = \hbar\mathbf{k}_p/m^*$ is the flow velocity and $\Delta_p = \omega_p - \omega_{LPB}(\mathbf{k}_p) - g|\psi|^2$ the effective pump detuning. The $\pm$ branches correspond to, respectively, the particle– and the hole–like branches of the Bogoliubov dispersion, and are images of each other under the transformation $k \to 2k_p - k$, $\omega \to -\omega$.

The solutions of Eq. 2.37 for different pump conditions are plotted on the left column of Fig. 2.15. The effect of the finite flow velocity $\mathbf{v}_p$ is to tilt the standard Bogoliubov dispersion via the term $(\mathbf{k}-\mathbf{k}_p)\cdot\mathbf{v}_p$. When colliding against the static defect, polaritons can scatter elastically, exciting modes given by the intersections of the Bogoliubov dispersion with the horizontal dotted lines. The spectrum of the Bogoliubov-like excitations reflects onto the shape and intensity of the resonant Rayleigh scattering (RRS) emission pattern in both momentum and real space. The central and right panels of Fig. 2.15 show the polariton intensity in the momentum and the real space for the different regimes on the left column, respectively.

In the resonant case ($\Delta_p = 0$), the $\pm$ branches (full/dashed lines, respectively) touch at $\mathbf{k} = \mathbf{k}_p$ (Figs 2.15a,d,g). In the noninteracting case (Fig. 2.15a) the dispersion remains parabolic, with the $\mathbf{k}$-space emission pattern (Fig. 2.15b) containing a peak at the incident wave vector $\mathbf{k}_p$, plus the RRS ring. In the real space pattern (Fig. 2.15c), as the polariton fluid is moving to the right, the defect at $(0,0)\mu m$ induces a propagating perturbation with parabolic wave fronts oriented in the left direction.

In the presence of interactions (Fig. 2.15d,g) the dispersion slope has a discontinuity at $\mathbf{k} = \mathbf{k}_p$: on each side of the corner, the + branch starts linearly with group velocities, respectively, given by $v_g = c_s \pm v_p$, c_s being the usual sound velocity of the interacting Bose gas $c_s = \sqrt{\hbar g|\psi|^2/m^*}$. In this resonant case, when $g|\psi|^2$ is large enough for the sound velocity c_s in the polaritonic fluid to be larger than the flow velocity v_p, there is no intersection of the Bogoliubov branches (Fig. 2.15d) with the horizontal dotted line

any longer. In this regime, RRS is no longer possible (Fig. 2.15e), and the polaritonic fluid behaves as a superfluid in the sense of Landau criterion. As no propagating mode is resonantly excited, the perturbation in real space remains localized around the defect, as shown in Fig. 2.15f.

Still in the resonant case, but now with $v_p > c$, the stronger Bogoliubov tilt of the dispersion is responsible for an intersection with the horizontal dotted line (Fig. 2.15g) that forms a RRS curve in a ∞-like shape, with the low-k lobe more intense than the high-k one (Fig. 2.15h), a sign of the disappearance of superfluidity. The aperture angle 2ϕ of the singularity at $\mathbf{k}_p$ satisfies the simple condition $\cos\phi = c_s/v_p$. In this Čherenkov regime where the polariton fluid is moving at a supersonic speed, the defect produces a peculiar real-space pattern (Fig. 2.15i) showing linear Čherenkov-like wavefronts. The aperture 2θ of the Čherenkov angle has the usual value $\sin\theta = c_s/v_p$.

Coming back to excitation below the sound velocity, $v_p < c_s$, but now decreasing the mean-field shift $g|\psi|^2$ in such a way that the effective pump detuning Δ_p is positive, the argument of the square root in Eq. 2.37 is negative for the wave vectors $\mathbf{k}$ such that $\Delta_p > (\mathbf{k}-\mathbf{k}_p)^2/2m^* > \Delta_p - 2g|\psi|^2$. In this region, the $\pm$ branches stick together and have an exactly linear dispersion of slope $\mathbf{v}_p$ (Fig. 2.15j). The resonant Rayleigh scattering intensity in this non-superfluid regime is a deformed RRS ring strongly amplified on a segment parallel to y including the point $\mathbf{k}_p$ because of the reduced linewidth of the Bogoliubov modes in the regions where the $\pm$ branches stick together (Fig. 2.15k). The main consequence of this in the real-space pattern of Fig. 2.15l is an overall amplification of the density modulation induced by the defect, in stark contrast with the superfluid regime. In particular, the derivative of the dispersion at the rightest point of the ring gives a group velocity point towards the right, which is responsible for the long "shadow" in the downstream direction with respect to the central defect, which extends to relatively far distances thanks to the linewidth narrowing effect

By increasing the pumping strength $|P|$, the mean-field shift $g|\psi|^2$ increases and the effective pump detuning Δ_p becomes negative. In this case, as it is shown in Fig. 2.15m, the branches no longer touch each other at $\mathbf{k} = \mathbf{k}_p$. The two lobes in the RRS circle are separated by a gap (Fig. 2.15n). The real-space wavefronts shown in Fig. 2.15o are still Čherenkov-like, if the separation between the two branches is relatively small. A full gap between them opens up for sufficiently negative values of Δ_p or for smaller $\mathbf{k}_p$ values (not shown). In this case, there are no available states for scattering and the system becomes superfluid in the sense of Landau.

In conclusion, superfluidity of resonantly-excited polaritons depends on the pump-polariton mode detuning Δ_p. Three qualitatively different types of spectra appear for the interacting case: linear for $\Delta_p = 0$, diffusive-like for $\Delta_p > 0$ and gapped for $\Delta_p < 0$. A moving polariton fluid is superfluid if its velocity is smaller than a critical value and $\Delta_p = 0$ or $\Delta_p < 0$. In this case, analogously to liquid Helium and atomic condensates, the resonantly-driven polariton fluid has a superfluid behavior in the sense of Landau criterion with respect to both elastic and inelastic processes.

The $\Delta_p = 0$ detuning is the only one that can be achieved experimentally, since if the laser is not resonant with the (blueshifted) polariton mode no field enters the cavity and so no polaritons are excited. Indeed, recent experiments agree with the theoretical predictions [19]: below the sound velocity, a quenching of the RRS intensity due to polariton-polariton interactions can be observed in both momentum and real space; above the sound velocity, linear Čherenkov waves were also observed.

Under a monochromatic and spatially homogenous plane–wave pump, neither vortices

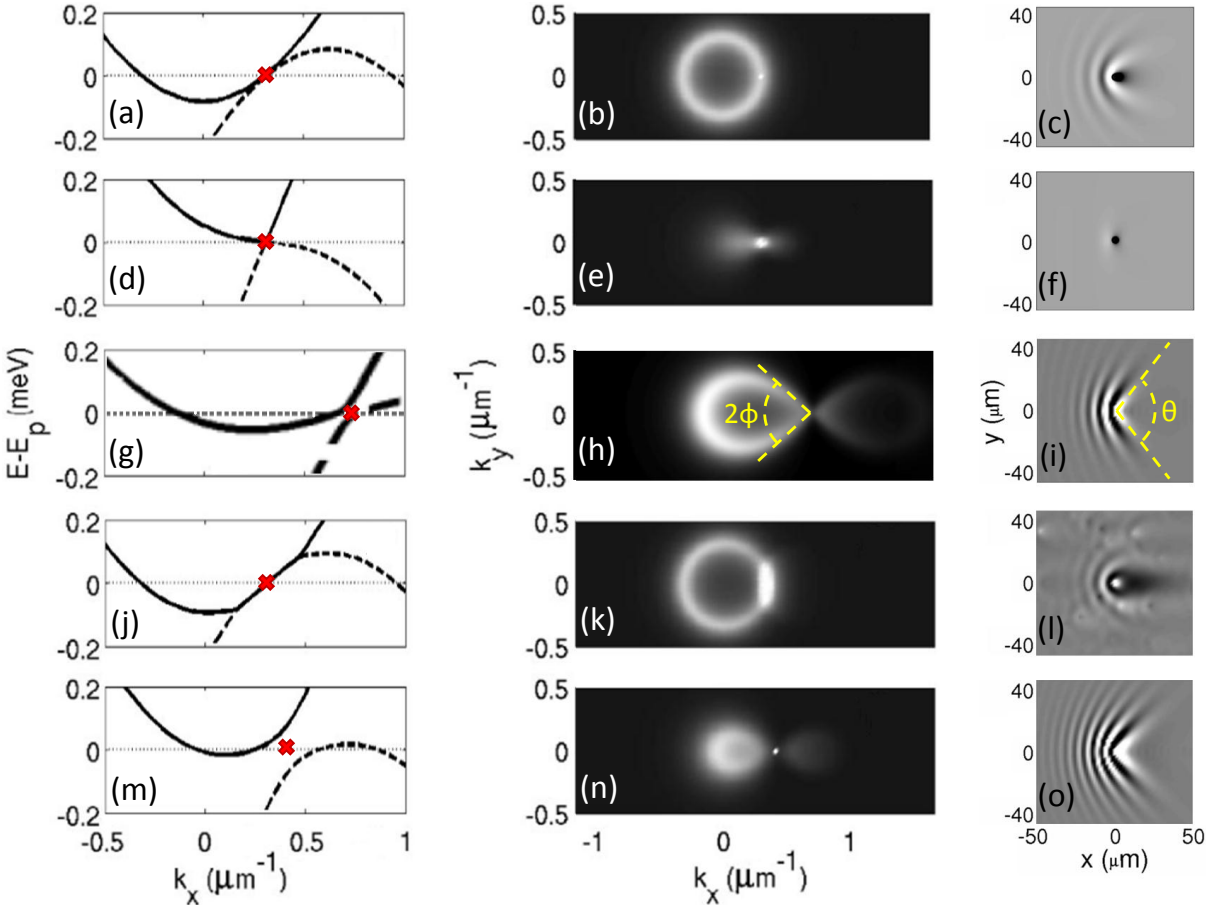

Figure 2.15: (left column) Bogoliubov dispersions $\hbar(\omega^{\pm}_{Bog} - \omega_p)$ (full/dashed lines, respectively) of the elementary excitations in microcavity polaritons under resonant excitation, calculated from Eq. 2.37, and their effect on the intensity and shape of the resonant Rayleigh scattering by defects in (central column) momentum space and (right column) real space. Red crosses represent the resonant pump energy and momentum for each row. The dispersion in (a) is parabolic ($g|\psi|^2 = 0$, $\Delta_p = 0$). For $g|\psi|^2 > 0$, close to k_p the dispersions are (d,g) linear ($\Delta_p = 0$), (j) diffusive ($\Delta_p > 0$) and (m) gapped ($\Delta_p < 0$). Adapted from Refs. [144, 148]

can be observed in the polariton fluid, nor solitons. The local phase of the polariton field is in fact fixed by the pump phase, which inhibits the appearance of topological defects. By using a properly spatially-shaped pump profile, polaritons can be resonantly created immediately before a defect and made to freely propagate past it with no phase imposed by the pumping field [149]. If the defect size is big enough, rich phenomena appear: for low enough fluid speeds and high densities, the flow is superfluid and no excitation appear; as the density is decreased, turbulence occurs in the form of vortex pairs ejection [118, 119, 121], vortex streets [120] and dark solitons [121].

The superfluid behaviour of a system can also be characterized as a function of the drag force exerted by the defect on the flowing fluid [150–153]:

$$\mathbf{F}_d = \int d\mathbf{r} |\psi(\mathbf{r}, t)|^2 \nabla V_{ext}(\mathbf{r}) \tag{2.38}$$

For a flowing polariton condensate satisfying the Landau criterium, like in Fig. 2.15d, the broadening of the polariton modes due to its finite lifetime allow for a weak amount

of scattering, which is asymmetric in the propagation direction (Fig. 2.15e). This yields an also asymmetric small density perturbation close to the defect (Fig. 2.15f), and so the fluid always experiences a residual drag force, Eq. 2.38. When flowing through defects, non-equilibrium superfluids do not have zero viscosity even in the superfluid regime.

However, the drag force and the onset of fringes in the density profile have a sharp threshold as a function of the velocity [152, 153] and so a generalized Landau criterion, with a critical velocity v_c, can still be defined. This is true for all the cases in Fig. 2.15 (linear, d, diffusive, g, and gapped, m), the critical velocity for pronounced drag being the same as the sound velocity in the linear and diffusive cases (Figs. 2.15d,g) but higher in the gapped case (Figs. 2.15m). The crossover becomes sharper for increasing polariton lifetimes [152,153]: in the supercritical regime, $v_p > v_c$, the lifetime tends to suppress the propagation of the Čherenkov waves away from the defect and therefore to suppress the drag, whereas in the subcritical regime, $v_p < v_c$, the residual drag increases linearly from zero when the polariton lifetime decreases.

2.5.2.2 Nonresonant pumping

When creating a polariton condensate by means of non-resonant excitation (Section 2.5.1.1), the macroscopically coherent field ψ in Eq. 2.36 is fed by an incoherent reservoir $N(\mathbf{r}, t)$ instead of directly by the laser beam [154]:

$$P(\mathbf{r}, t) = R_R N(\mathbf{r}, t) \tag{2.39}$$

where R_R is the rate at which polaritons scatter from the reservoir. Eq. 2.39 means that the amplification rate of the condensate due to stimulated scattering of polaritons from the reservoir increases linearly with N.

The full system is described by two populations: polaritons around the lower energy minimum of the dispersion, $\psi(\mathbf{r}, t)$, and polaritons with larger momenta at the reservoir, $N(\mathbf{r}, t)$. These two populations are weakly coupled, which allows us to define a quasi-thermal equilibrium for each one. The state of the reservoir is fully determined by its local density N [31, 154]:

$$\partial_t N(\mathbf{r}, t) = -\left[\Gamma_R + \beta R_R |\psi|^2\right] N(\mathbf{r}, t) + P_{NR}(\mathbf{r}) + D\nabla^2 N \tag{2.40}$$

Polaritons are pumped into the reservoir by the laser beam at a rate $P_{NR}(\mathbf{r})$ and relax at a rate Γ_R. D is the reservoir spatial diffusion coefficient and β is a phenomenological coefficient whose value is chosen to describe particular experimental situations [31].

It is very important to account for energy shifts originated from Coulomb repulsion between condensed and reservoir polaritons. The strength of interactions is assumed to be similar to the rate of transition of the reservoir particles into the condensate [31]:

$$V_{ext}(\mathbf{r}, t) = \hbar R_R N(\mathbf{r}, t) \tag{2.41}$$

The net polariton potential $V(\mathbf{r}) = g|\psi|^2 + \hbar R_R N(\mathbf{r}, t)$ is produced by the repulsive interactions between polaritons themselves as well as with the reservoir excitons (N) close to the pump spots.

The Bogoliubov spectrum of a non-equilibrium condensate described by Eqs. 2.36, 2.39, 2.40 and 2.41 has a diffusive Goldstone mode around $k = 0$ [154], and so a naïve

application of the Landau criterion predicts a vanishing critical velocity, $v_c = 0$. Even though strictly speaking there cannot be superfluid behavior, there are regimes close to equilibrium, where the drag force exerted on a small moving defect shows a sharp threshold at velocities close to the speed of sound [151]. For velocities below the sound velocity, the drag force increases as the decay, Γ, increases [151].

There has been experimental indications of a diffusive Bogoliubov mode in non-resonantly excited polariton condensates [111], where the diffusive region of the spectra could be tuned with power from zero diffusion at threshold up to a $\Delta k \sim 0.8\,\mu m^{-1}$ diffusive region at high powers an negative photon-exciton detunings. However the condensate excitation spectrum and the lower polariton luminescence are superimposed and so it is not immediately clear whether the equilibrium Bogoliubov dispersion or the diffusive Goldstone mode dispersion corresponds better to the experimental results. The existence of an equilibrium Bogoliubov mode has been reported in a previous work [155].

As a result of the non-equilibrium nature of the polariton condensate in an inhomogeneous system, there are spontaneous supercurrents that may carry polaritons from gain- to loss-dominated regions. This give rise to spontaneous formation of vortices pinned by sample defects [114, 115] in analogy to classical water sinks, which do not necessarily imply superfluidity [145, 147].

Using a stochastic classical field model, Wouters *et.al.* studied the metastability of an quantized vortex injected (probe) into a non-resonantly excited polariton condensate. In this scenario, fluctuations play an important role, determining the presence or absence of spatial long-range order and inducing a random motion of the vortex core. Their main results are plotted in Fig. 2.16. The condensate is created by a ring-shape pump and has zero angular momentum. The effect of the probe is to introduce an extra short-lived condensed population ($\sim 10\,ps$) and angular momentum L (Figs. 2.16d-f). For low condensate densities, no long-range order is present (Fig. 2.16a) and the injected angular momentum decays as soon as the extra population is gone (Fig. 2.16d). On the other hand, as the condensate density is increased, the long-range order also increases (Figs. 2.16b,c) and the angular momentum persist for much longer times (Figs. 2.16e,f). Here the specific probe power does not play an important role as long as a certain threshold is reached. The presence of a vortex represents another metastable solution other than the zero angular-momentum condensate.

In conclusion, apart from having a diffusive excitation spectra, the superfluid behavior of a non-equilibrium polariton condensate can also be characterized by a dramatic increase in the lifetime of a quantized vortex, analogously to BECs that persist rotating after stirring [97], showing one more connection between the two intriguing phenomena of superfluidity and long-range spatial coherence. This is the main idea underlying the experiments performed in Chapter 5, done however in the OPO excitation regime, whose superfluid properties are discussed in the following section.

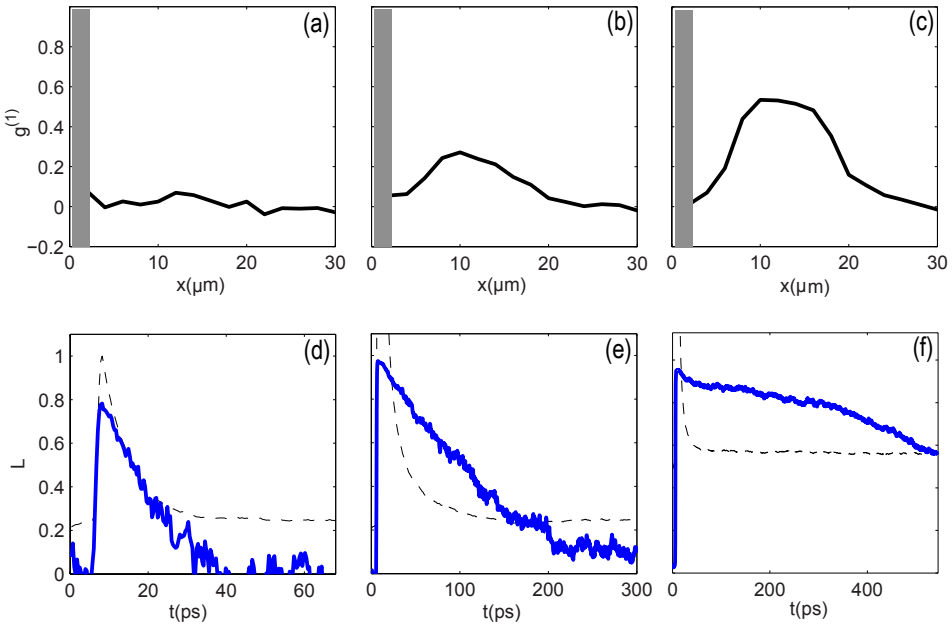

Figure 2.16: Top panels show the first-order spatial correlation between inversion symmetric points of a polariton condensate created with a ring–shaped excitation laser (inner radius $7\,\mu m$ and outer radius $20\,\mu m$) for increasing values of the density, (a) 1.3, (b) 5.7, and (c) $32\,\mu m^{-2}$, before the arrival of the vortex pulse. Bottom panels show the temporal evolution of the total polariton density (gray dashed line) and angular momentum (blue full line) after a $1ps$-long vortex probe pulse with a waist of $20\,\mu m$ has perturbed the polariton condensates. The additional density introduced by the resonant probe pulse is (d) four, (e) forty, and (f) twenty times the condensate density. Adapted from Ref. [156]

2.5.2.3 OPO regime

When excited under the OPO geometry (section 2.5.1.3), the full LPB dispersion, calculated in section 1.4.2, has to be taken into account. The quantum fluid dynamics of a non-equilibrium polariton condensate excited under the OPO geometry can be then simulated by adding excitonic interactions, pump and decay to the Hamiltonian defined by Eq. 1.44

$$i\partial_t \begin{pmatrix} \psi_X \\ \psi_C \end{pmatrix} = \left[\mathcal{H}_{e-ph} + \begin{pmatrix} g_X|\psi_X|^2 & 0 \\ 0 & V_C(\mathbf{r}) \end{pmatrix} \right] \begin{pmatrix} \psi_X \\ \psi_C \end{pmatrix} + \begin{pmatrix} 0 \\ P \end{pmatrix} \tag{2.42}$$

Here the polariton field is described by a spinor containing its excitonic, ψ_X, and photonic, ψ_C, parts. g_X is the excitonic repulsive interaction coupling constant, $V_C(\mathbf{r})$ is the potential seen by photons due to changes in the cavity width and P is the pumping field acting on the cavity mode. The non-interacting Hamiltonian $\mathcal{H}_{e-ph}$ accounts for the polariton modes dispersion including decay broadening:

$$\mathcal{H}_{e-ph} = \begin{pmatrix} \omega_X - i\kappa_X & \Omega_R/2 \\ \Omega_R/2 & \omega_C - \nabla^2/(2m_c) - i\kappa_C \end{pmatrix} \tag{2.43}$$

Here the excitonic dispersion is assumed to be flat, $\omega_X(\mathbf{k}) = \omega_X$, due to its heavy mass, whereas the photonic dispersion is parabolic, $\omega_C(\mathbf{k}) = \omega_C + \mathbf{k}^2/(2m_c)$. κ_X and κ_C are the excitonic and photonic decay rate, respectively and Ω_R the exciton-photon Rabi splitting.

Above a pump strength threshold $P = P_{th}$, the system is driven into the OPO regime where the solutions to Eq. 2.42 are three-mode (pump, signal and idler) states [141, 157]. Such solutions are in principle invariant under a simultaneous phase rotation of both signal and idler states, however the signal and idler spontaneously select their phase in the OPO regime, spontaneously breaking the phase rotation symmetry. The Goldstone theorem [158] states that this symmetry breaking implies that the excitation spectrum goes to zero (both in the real and imaginary parts) in the long wavelength limit $\mathbf{k} \to 0$. This can be better understood as follows: as any global phase rotation maps into the same eigenvector of the Bogoliubov Hamiltonian, no restoring force opposes a global rotation of the signal-idler phases.

The dispersion for the Goldstone mode in the OPO regime has been derived in Ref. [141] by analytically solving Eq. 2.42 in momentum representation, with the calculated gap-less excitation spectrum being diffusive ($\partial_k E = constant$) at $k = 0$, in analogy with positively-detuned-resonant and non-resonant excitation schemes — see Sections 2.5.2.1 and 2.5.2.2, and Fig. 2.15j. This implies that a polariton condensate created under the OPO excitation regime is not a superfluid when the Landau criterion is applied.

Moreover recent calculations [159] show that coupling between two coherently-injected, at different momenta and energies, polariton condensates requires that either both components flow without friction or both scatter against the defect. This suggests that when investigation superfluidity of a multimode OPO state, all of its modes have to be taken into account.

However, when triggered by a short-duration pulse, the travelling parametrically-scattered polariton wave-packet has been shown to display superfluid-like behaviour in the form of frictionless flow and suppression of Rayleigh scattering [18]. Moreover, in experiments done during this thesis, we have shown that the signal state can sustain persistent flow after the resonant injection of a vortex [20, 35], as will be described in Chapter 5. In fact, numerical solutions of the two-component Gross-Pitaevskii equation 2.42, using a CW pump close to the inflection point of the LPB summed up with a $2ps$-pulsed probe resonant to the signal state, show that the OPO state have metastable vortex solutions that can betriggered externally [160], in full analogy with superfluidity, and that even spontaneous stable vortex formation can be found.

Part II

Experimental techniques

Introduction

Since polaritons have both electronic and photonic character, their creation, manipulation and detection could in principle be achieved by both electrical and optical means. Although some progress has been made towards electrical injection [161–163] and manipulation [22, 164] of polaritons, the injection of free carries to the system screens the Coulomb interaction in such a way that excitons dissociate at densities below the condensation threshold. In fact, the creation and manipulation of polariton condensates was restricted, up to now, to optical excitation. Moreover, being neutral particles, polaritons are also only detected by optical means, through the photons emitted after decay processes. This provides direct a direct measurement of the condensate properties - contrary to superconductors, superfluids and atomic BECs.

In this Part we describe the ways of creating, manipulating and detecting polariton condensates that were used to acquire the data presented in Parts III and IV. Two samples are described, as well as the data analysis methods used to recover the time dynamics, condensate density, phase and coherence.

False-color schemes for scales

In all results presented on this thesis, unless otherwise stated, the figures containing real– and/or momentum–space images, as well as phasemaps, are false-colored using the colorcodes described in Fig. 2.17. Note that intensity values are only relative, with arbitrary units.

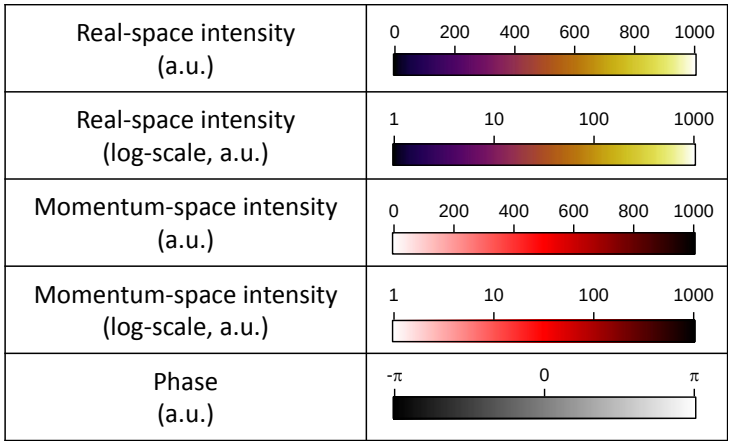

Figure 2.17: False colorscales used in real– and/or momentum–space images, as well as in phasemaps, all over this thesis.

Chapter 3

Samples

The physical structures used in this thesis to create cold polariton two-dimensional fluids are planar DBR-microcavities with embedded quantum wells, already described in Chapter 1. These are basically constituted of tens of parallel layers, with widths in the nanoscale, of $Al_xGa_{1-x}As$ alloys, where the ratio between Aluminium and Gallium concentration determines the layer refractive index and electronic band structure. They are grown by a molecular beam epitaxy (MBE) process [165], where Aluminium and/or Gallium solid sources are heated releasing a high-velocity beam travelling in a ultra-high-vacuum chamber, directed towards a $GaAs$ substrate where the layers grow epitaxially. Usually, the substrate wafer, typically circular of $\sim 10\,\mu m$-diameter, is mounted on a rotating platter to provide equal grow rates all over the substrate. By controlling the flow of each component over the wafer, different concentrations of Al and Ga are achieved for each layer. The surface geometry, morphology and constitution can be further controlled by electron diffraction techniques, allowing precise control of the thickness of each layer down to a single layer of atoms.

When growing cavity layers, the wafer rotation is stopped and a growth rate gradient appears, yielding a cavity whose thickness varies along the radial direction of the sample. This *wedge* allows for the cavity mode energy to be chosen by moving the excitation spot around the sample, selecting the cavity-exciton detuning. However, the wedge is small enough so that it can be neglected within the extension of the excitation spot.

Under OPO excitation geometry, in which only three states (pump, signal and idler) are present — see section 2.5.1.3, the carrier density is much smaller than those involved in a non-resonant pumping scheme, in which a dense reservoir population is present together with the condensed fraction (2.5.1.1). In fact, in all the results described in Part III, where the experiments were carried on under OPO excitation geometry, condensation is achieved in a single QW microcavity, whereas under non-resontant excitation (Part IV), the excitonic density is divided between 12 QWs.

3.1 Single-QW sample

The sample used in the experiments described in Part III has been grown under the supervision of Dr. Aristide Lemaître in the group of Prof. Jacqueline Bloch at the Laboratoire de Photonique et de Nanostructures (CNRS, Marcoussis, France). It consists of a $\lambda/2$ $AlAs$ microcavity (nominal width of $\sim 120\,nm$) with a $20nm$ $GaAs$ quantum well placed at the antinode of the cavity electromagnetic field. The cavity is surrounded by two Bragg mirrors made of alternating $\lambda/4$ layers of $Al_{0.15}Ga_{0.85}As$ ($57.2\,nm$ thick)

and $AlAs$ (67.5 nm thick), with 24 pairs of layers at the bottom and 15.5 on the top of the structure.

One additional narrow $GaAs$ QW (2.6 nm thick) is present at each side of the wide QW, separated by an $AlAs$ layer of 10 nm. The exciton resonances of these QWs are much higher in energy than any of the polariton resonances of interest here (in fact these QW's can be excited by a HeNe laser to study polariton relaxation dynamics in the presence of an electron gas [166–168]), and do not affect the polariton physics investigated in Part III.

Figure 3.1 shows the sample luminescence at 10 K when excited with a low power CW laser tuned to the first Bragg mode of the cavity ($\sim$ 1.65 eV), for three different positions of the excitation spot on the sample corresponding to decreasing photon-exciton detuning. The emission comes mainly from three branches that we fit to three polariton modes whose energies are given by the eigeinvalues of the coupling frequency matrix — analogously to Eq. 1.44 but with three modes:

$$\begin{pmatrix} \omega_c(k_{//}) & \frac{\Omega_{hh}}{2} & \frac{\Omega_{lh}}{2} \\ \frac{\Omega_{hh}}{2} & \omega_{hh} & 0 \\ \frac{\Omega_{lh}}{2} & 0 & \omega_{lh} \end{pmatrix}, \tag{3.1}$$

where $\omega_{c,hh,lh}$ are the photon, heavy- and light-hole excitons frequencies, $k_{//}$ the in-plane wavevector and $\Omega_{hh,lh}$ are the photon-heavy-hole and photon-light-hole Rabi splittings. The three fits are done using the same photon mass and Rabi splittings $\hbar\Omega_{lh} = 3.0\,meV$ and $\hbar\Omega_{hh} = 4.4\,meV$

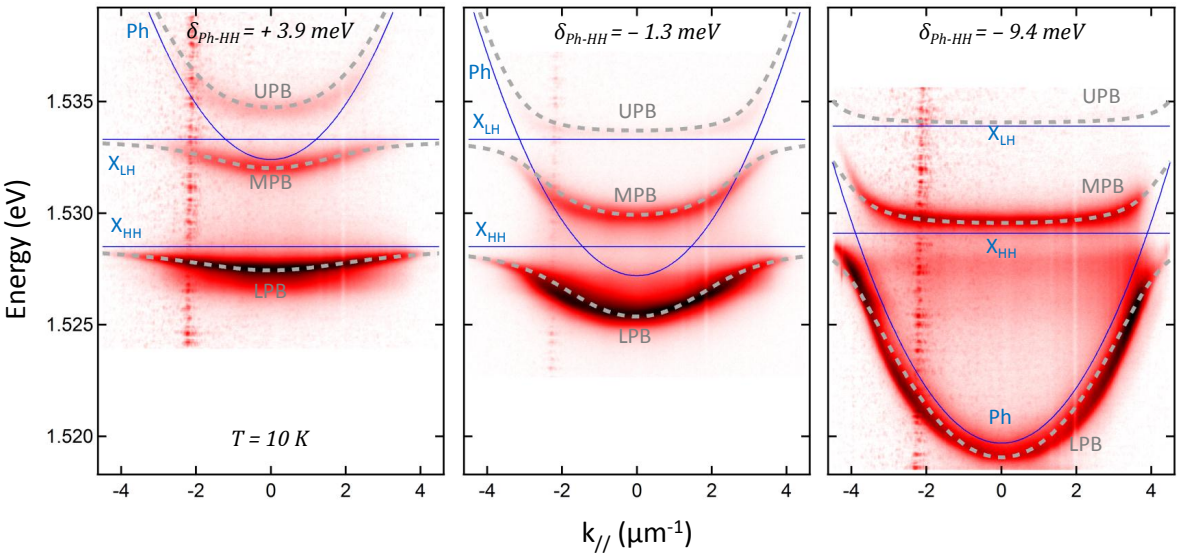

Figure 3.1: Single-QW microcavity photoluminescence dispersion images for different photon-heavy-hole-exciton detunings δ_{Ph-HH} (indicated), taken at 10 K, showing fitted (blue line) bare light- and heavy-hole excitons (X_{LH} and X_{HH}) and cavity mode (Ph) and (gray dashed line) lower, middle and upper polariton branches (LPB, MPB and UPB). The photon-light hole splitting is $\Omega_{lh} = 3.0\,meV$ and the photon-heavy hole splitting is $\Omega_{hh} = 4.4\,meV$. Color in log scale.

The use of a single QW results in very narrow exciton linewidths, as the effect of interface fluctuations and width distributions are greatly suppressed. In this case the

heavy-hole QW exciton presents a low-temperature linewidth of about $0.3\,meV$, while the cavity-mode lifetime is sf the order of $4\,ps$, which yields a Q-factor of ~ 9000.

3.2 Multiple-QW sample

The sample used in the experiments described in Part IV has been grown under the supervision of Prof. Zacharias Hatzopoulos in the group of Prof. Pavlos Savvidis at the Institute of Electronic Structure and Laser (FORTH, Heraklion, Greece). It consists of a $5\lambda/2$ $Al_{0.3}Ga_{0.7}As$ cavity (nominal width of $583.1\,nm$) containing four sets of three $10nm$-thick $GaAs$ quantum wells placed at the antinodes of the cavity electric field — see Fig. 3.2a. The cavity is surrounded by two Bragg mirrors made of alternating $\lambda/4$ layers of $Al_{0.15}Ga_{0.85}As$ ($57.2\,nm$ thick) and $AlAs$ ($65.4\,nm$ thick), with 35 pairs of layers at the bottom and 32 on the top of the structure, respectively. Fig. 3.2b shows a Scanning Electron Microscopy image of the cavity, where it is possible to appreciate the microcavity between the two Bragg mirrors, the substrate at the bottom and vacuum on the top.

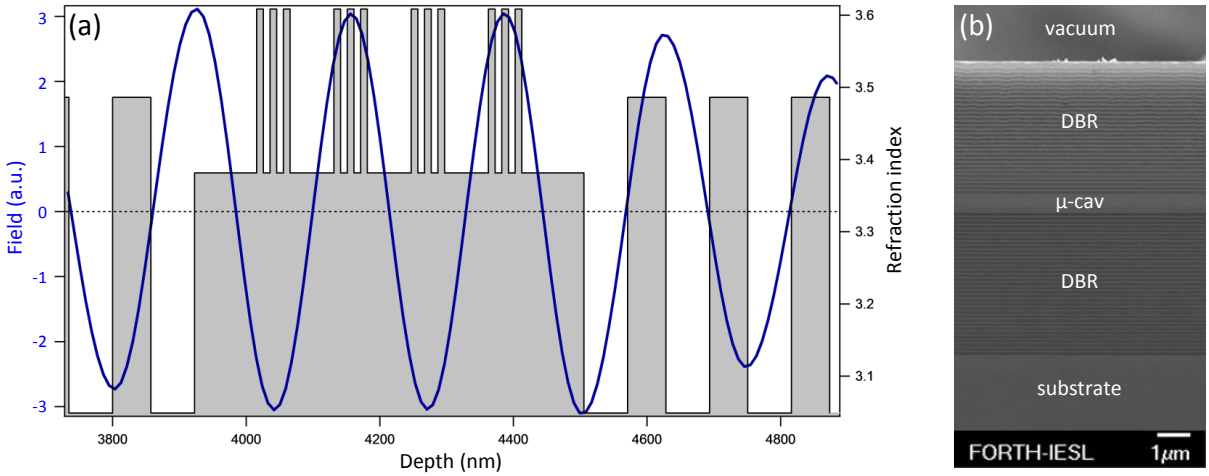

Figure 3.2: (a) Refractive index profile of the cavity with 12 QWs and first Bragg layers surrounding it, together with the electric field profile simulated with a transfer matrix code. (b) Scanning Electron Microscopy image of the full microcavity structure showing the cavity (μ-cav) and DBR layers on the top of the $GaAs$ substrate. Courtesy from P.G.Savvidis group, FORTH-IESL, Crete

Figure 3.3 shows the sample luminescence at $50\,K$ when excited with a low power CW laser tuned to the first Bragg mode of the cavity. We fit the emission to the three polariton modes whose energies are given by the eigeinvalues of the coupling frequency matrix, Eq. 3.1. The fit yield Rabi splittings $\hbar\Omega_{lh} = 6.0\,meV$ and $\hbar\Omega_{hh} = 11.2\,meV$

The linewidth of the lower polariton branch (LPB) at very negative detuning ($\delta = -9.7meV$) is measured to be $90\mu eV$, corresponding to an experimental Q-factor of at least 16000 (cavity photon lifetime $\tau_c = 9ps$) [169] in close agreement with the theoretical value of 20000.

The sample is capable of polariton lasing in the strong coupling regime for temperatures of up to $\sim 50K$ [169], in accordance to theory [130].

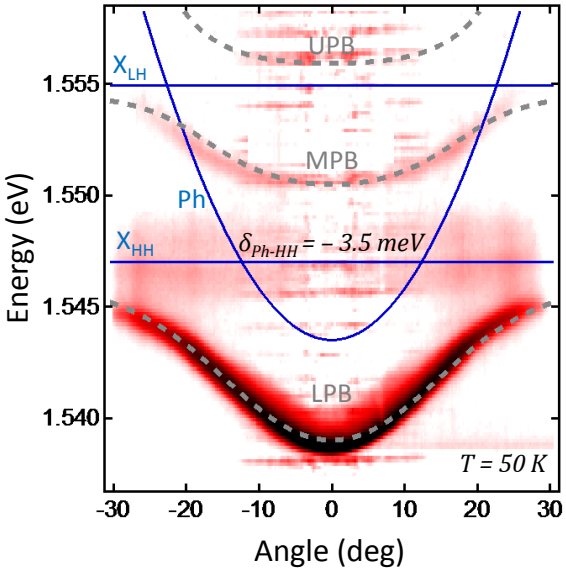

Figure 3.3: Multiple-QW microcavity photolomunescence dispersion image taken at 50 K, showing fitted (blue lines) bare light- and heavy-hole excitons (X_{LH} and X_{HH}) and cavity mode (Ph), and (gray dashed lines) lower, middle and upper polariton branches (LPB, MPB and UPB). The detuning is found to be $\delta = -3.5meV$, the photon-light hole splitting is $\Omega_{lh} = 6.0\,meV$ and the photon-heavy hole splitting is $\Omega_{hh} = 11.2\,meV$. Color in log scale. Experimental data is a courtesy from P.G.Savvidis group, FORTH-IESL, Crete.

Chapter 4

Experimental setups

The samples are kept in cold finger-cryostats, which are connected to high-vacuum pumps yielding pressures on the order of $10^{-7}\,mbar$ inside. The cryostat is also connected to a liquid helium dewar and to another weaker pump. This pump is responsible for a flow of helium gas through the cryostat, making possible to decrease the sample temperature down to $\sim 3.5\,K$. A temperature sensor is placed very close to the sample holder, where the sample is attached with silver paint to ensure a good thermal contact. All the data presented in this thesis were taken with the samples at $10\,K$

Excitation lasers are focused onto the sample by an *objective lens* — see Fig. 4.1 — which is chosen accordingly to better suit the specific experiment to be performed — see section 4.1. The same objective lens is used to collect the polariton photoluminescence, in the retro-reflection direction. The sample emission comes from a region on the micrometre-scale, which can be considered as a point-like source since the objective diameters are in the centimetre scale. It follows that the beam of the condensate light emission acquires a plane wavefront after the objective, and propagates parallel to the objective optical axis over a long distance, so-called far field, before being focused, by an *imaging lens*, into the detection apparatus, where images are taken — see section 4.2.

In the far-field, different combinations of optical elements are used depending on what is to be measured. If only mirrors are used, the image created by the two lenses is simply a magnified image of the sample emission, and in this case the setup is equivalent to an optical emission microscope. If one is interested in resolving the angular emission of the sample, which is equivalent to image the momentum space, a third lens is placed on the far-field in such a way that its focus coincides with the objective Fourier plane[1], and in this case the image formed by the imaging lens is the Fourier (momentum) space of the sample emission. The specific position and focal distance of the third lens determines the momentum space magnification. Note that switching from the real to the momentum space configuration, and vice–versa, is straightforward taking just a few seconds, and the excitation conditions are not altered.

When taking position-space images, a pinhole can be placed at the emission far-field to select a specific momentum distribution and take the spatial profile of such a momentum distribution. This is done *e.g.* in Part III where only the spatial profile of the signal state is measured by filtering-out in far-field the pump and idler states. When taking

[1]The objective Fourier plane is defined as the plane perpendicular to the optical axis and located at the objective focus opposed to the focus where the sample is located. All rays coming out from the sample at a given angle (which correspond to a well defined in-plane momentum) form a point in the Fourier plane, which is therefore a map of the angular emission from the sample. In other words, the third lens is a Fourier transform performer

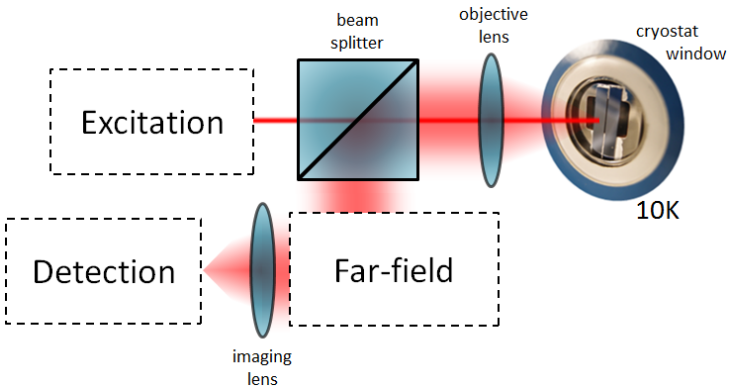

Figure 4.1: Excitation and detection setup scheme. The "Excitation" labelled rectangle represents CW and pulsed lasers used to pump polariton condensates. They propagate through a beam splitter and are focused by a objective lens onto the sample, held at $10\,K$ inside a cold finger cryostat, whose window is shown in the figure. The objective lens also collects the emitted photoluminescence, which is reflected by the beam-splitter and enters the "Far-field" region. Such a region can contain either a mirror, if position-space intensity images are recorded, a lens, if momentum-space intensity images are recorded, or interferometers if interferences images are taken. The field is finally focused by another lens into the "Detection" apparatus, which contains a spectrometer coupled to a CCD and/or to a streak-camera.

momentum-space images, the extra lens forms a position-space image at its focus on the opposite side of the Fourier plane. A pinhole can be put in this position-space region to select a specific spatial region from which the momentum dependence can be measured. This is done *e.g.* in Chapter PartIV, 8 and Section 11.3.

When performing non-resonant excitation and imaging the full, not resolved in energy, emission of the sample, a Bragg mirror is place at the far-field to filter out the laser reflection without blocking the polariton emission which is at a different wavelength.

Finally, combinations of beam-splitters and mirrors can be used to build interferometers in the far-field. These provide information about the field coherence and phase as will be described in section 4.3.

4.1 Excitation

In Part III the sample is resonantly excited with CW and pulsed beams. The CW laser, from Spectra Physics, is based on a Ti:Al_2O_3 crystal pumped by a CW Ar^+ laser. The wavelength can be continuously tuned between $720\,nm$ and $860\,nm$. The pulsed laser is a Tsunami, from Spectra Physics, and in this case the Ti:Al_2O_3 crystal is pumped by a CW laser (Spetra Physics Millennia Pro, which contains a Nd:YVO_4 laser crystal and a LBO frequency-doubling crystal), which is pumped by a diode laser. It has a tunability between $680\,nm$ and $950\,nm$. The laser is mode-locked with the help of an acousto-optical modulator, and was operated in the picosecond configuration, yielding pulses with a width of $\sim 2\,ps$ and a repetition rate of $82\,MHz$.

Under TOPO excitation configuration, a good angular resolution is needed. We use an achromatic lens with $\sim 6.4\,cm$ of diameter and $4\,cm$ of focal length, yielding a numerical aperture $NA = 0.6$. Each excitation beam is directed towards the sample by an independent mirror. By positioning them at different distances from the optical axis

(Δx) of the objective lens, the angle of incidence θ_{inc} of each beam can be selected ($\theta_{inc} = \arctan\left(\frac{\Delta x}{f}\right)$, where f is the focal distance of the objective lens).

In Part IV, excitation is provided by a single-mode narrow-linewidth Ti:Al_2O_3 CW laser (Coherent MBR, passive etalon model, pumped by a 5W Coherent Verdi V5) focused to a $1\mu m$-diameter spot through a $NA = 0.7$ lens[2] (Mitutoyo M plan apo NIR $\times 100$ 0.7NA), and tuned to $750\,nm$, the first spectral dip at energies above the high-reflectivity microcavity stopband. To prevent unwanted sample heating the pump laser is chopped at 100 Hz with an on:off ratio of 1:30.

4.2 Detection

The simplest way of detecting the polariton photoluminescense is to place a CCD camera at the focus of the imaging lens. In this case, the emission intensity is time-averaged (acquisition time-scales are usually on the millisecond or second range) and all the wavelengths are superimposed. In Part III a *Hitachi KP-M2RN* CCD was used whereas in Part IV an *Lumenera Infinity 3* camera was chosen.

Alternatively, the emission intensity can be resolved into its energy components by using a spectrometer, whose working principle goes as follows: a one dimensional slice of the image on the focus of the imaging lens passes through the spectrometer entrance slit and reaches a diffraction grating. Here each energy component is reflected at a different angle in the direction perpendicular to the entrance slit. After propagating over tens of centimetres, the field is collected by a CCD, recording an image that contains the energy-dependent field intensity for each image point the passes through the slit.

In Part III we use a $0.50\,m$ imaging triple–grating spectrometer (*Acton SpectraPro 2500i* with a 1200 lines/mm diffraction grating) with a high resolution CCD (*Acton Pixis 1024* with 1024×1024 pixels). In Part IV, a $0.55\,m$ spectrometer (*Horiba Triax 550* with a 1200 lines/mm diffraction grating) with a liquid-nitrogen-cooled CCD (*Jobin Yvon CCD3000* with 1024×256 pixels) was used.

More complete information about the sample emission and its energy dependence is provided by tomographically reconstructing its two-dimensional image onto the spectrometer slit. This is done by sequentially translating the imaging lens perpendicularly to the optical axis, which moves the image across the entrance slit of the spectrometer, thus recording spectra for each line scan of the image. By acquiring a number of these one-dimensional spatial slices vs energy, the energy dependence of each point of the 2D image is composed.

The step-motors, as well as the image acquisition sequence, are controlled by a home-made software programmed with LabView and Igor Pro.

[2]The same lens collects light emitted by the sample, with a spatial resolution $R = \lambda/(2NA) \approx 0.5\mu m$.

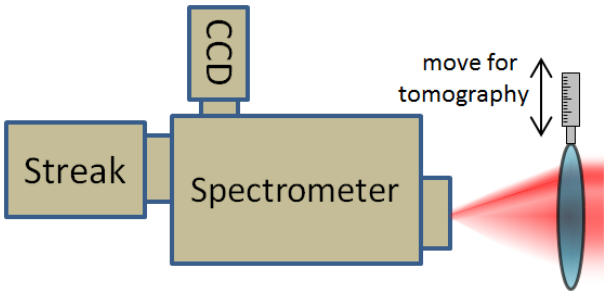

Figure 4.2: Apparatus used to detect the sample luminescence. A moveable imaging lens focus the emission onto the entrance slit of th spectrometer. The light is dispersed inside and its energy dependence recorded by a CCD camera or its time-dynamics by a streak-camera.

4.2.1 Streak-camera

In order to measure the time dynamics presented in Part III, a streak-camera is coupled to one of the exits window of the spectrometer — see Fig. 4.2, with the camera entrance slit oriented in the same direction as the spectrometer one, in such a way that the time evolution of the image cross-section that enters the spectrometer is measured. Although this can be done for a specific energy, by properly rotation the monochormator's diffraction grating we take the 0^{th} diffraction order to achieve better time-resolution since no energy is selected.

The streak camera is a device used to measure ultra-fast time-dynamics of the light emitted by the samples. We use a Hamamatsu C5680 streak camera with a M5675 synchroscan sweep unit and a C5680 blanking unit, coupled to a Hamamatsu C4742-95 digital camera. The principles of operation are depicted in Fig. 4.3. The field whose dynamics is to be measured passes through a slit and is focused by a lens into a photocathode of the streak tube, where photons are converted into electrons. The latter are accelerated by an accelerating mesh passing then between a pair of sweep electrodes, where a high-speed sweeping voltage is applied, making electrons swept in the direction from top to bottom). The electrons are deflected at different times, and at slightly different angles in the perpendicular direction, and are then conducted to a micro-channel plate (MCP). As the electrons pass the MCP, they are multiplied several thousands of times, after which they impact against a phosphor screen, where they are converted back into photons. On the phosphor screen, the earliest electron to arrive is placed in the uppermost position, with the other electrons being arranged in sequential order from top to bottom. In other words, the vertical direction on the phosphor screen serves as the time axis. Also, the brightness of the various phosphor images is proportional to the intensity of the respective incident light. The position in the horizontal direction of the phosphor image corresponds to the horizontal location of the incident light. Finally, the light emitted by the phosphor screen is recorded by a CCD (not shown). In the CCD the vertical direction means time while the horizontal direction has the same meaning as the horizontal dimension of the light arriving at the photocathode, which can be wavelength or spatial dimension (real space or momentum space).

The emission intensity of a polariton condensate is very weak to be time-resolved with picosecond resolution in a single-shot measurement, even a high excitation powers. This yields a very low signal/noise ratio, which can be overcome by making multiple-shot measurements. In this case, each laser pulse excites the polariton condensate under the

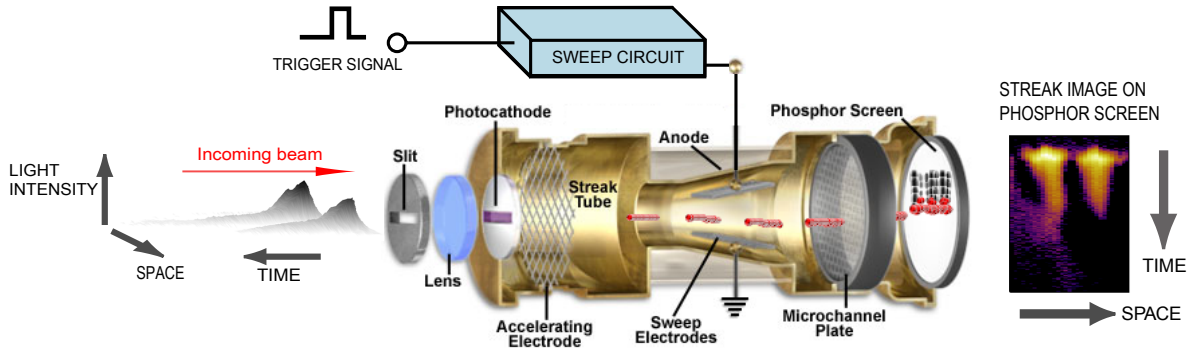

Figure 4.3: Schematic representation of the working principle of a synchroscan streak camera. See text for details. Adapted from Ref. [170]

.

same conditions, with the follow-up dynamics being recorded multiples times, one per pulse, by the streak camera, and averaged of the many realisations. To perform such a measurement, the sweeping voltage that deviates the photoelectrons is synchronized with the repetition rate of the excitation laser via a fast photodiode. The acquisitions times employed in this thesis are on the order of 1 second, meaning that a single image is a average over 82 million experiments ($82\,MHz$ being the laser repetition rate). The sweeping voltage has a sinusoidal shape, but only the linear part of the sinusoidal is employed. The largest time window of the streak camera has a size of $2100\,ps$ with a resolution of about $30\,ps$. However the resolution can be improved below $10\,ps$ by operating the camera in regimes with smaller time windows.

A streak-camera image contains the time-dynamics of a one-dimensional slice of the image created at the focus of the imaging lens. The dynamics of the full image can be measured using a tomographic procedure similar to the one described to measure the energy dependence of the full condensate: by progressively moving the imaging lens, the time-dynamics is measured for each 1D slice of the 2D image. To perform such a measurement, we take the time dynamics sequence of about 100 slices of the condensate, each image being integrated for about a second. The full measurement lasts some minutes, during which care should be taken that the lasers and the sample are extremely stable in such a way that all the steps correspond to the same excitation conditions. The full experiment is stored in a 3D matrix whose time-slices correspond to the condensate image at a specific time.

4.3 Interferometry

The interference between two fields, $\psi_1(\mathbf{r}) = A_1(\mathbf{r})e^{i\varphi_1(\mathbf{r})}$ and $\psi_2(\mathbf{r}) = A_2(\mathbf{r})e^{i\varphi_2(\mathbf{r})}$, is given by:

$$I_{12} = \langle|\psi_1 + \psi_2|^2\rangle = \langle|\psi_1|^2 + |\psi_2|^2 + \psi_1^* \cdot \psi_2 + \psi_2^* \cdot \psi_1\rangle \tag{4.1}$$

$$I_{12}(\mathbf{r}) = \langle A_1(\mathbf{r})^2\rangle + \langle A_2(\mathbf{r})^2\rangle + (g^{(1)} + g^{(1)^*}) \cdot \sqrt{\langle A_1(\mathbf{r})^2\rangle + \langle A_2(\mathbf{r})^2\rangle} \tag{4.2}$$

Where $\langle\rangle$ denotes statistical average. For non-stationary states, such as a decaying polariton condensate created by a pulsed laser, the ensemble is made up by many pulses. When one deals with stationary states, where the statistical properties do not change

with time, such as those created in continuous-wave experiments, one can replace the ensemble average with a time average.

$g^{(1)}$ is the complex degree of coherence between ψ_1 and ψ_2, given by [171]:

$$g^{(1)}(\psi_1,\psi_2)=\frac{\langle\psi_1^*\cdot\psi_2\rangle}{\sqrt{\langle|\psi_1|^2\rangle+\langle|\psi_2|^2\rangle}} \tag{4.3}$$

$$g^{(1)}(\psi_1,\psi_2)(\mathbf{r})=\frac{\langle A_1(\mathbf{r})\cdot A_2(\mathbf{r})\cdot e^{i(\varphi_2(\mathbf{r})-\varphi_1(\mathbf{r}))}\rangle}{\sqrt{\langle A_1(\mathbf{r})^2\rangle+\langle A_2(\mathbf{r})^2\rangle}} \tag{4.4}$$

The argument of $g^{(1)}$ gives the averaged phase difference between the two fields and its modulus the predictability of such a phase difference, known as coherence.

$g^{(1)}$ is a complex number in general satisfying the following properties:

$g^{(1)}(\psi_1,\psi_1)=1$ (autocorrelation)

$g^{(1)}(\psi_1,\psi_2)^*=g^{(1)}(\psi_2,\psi_1)$

The first order correlation function is very important when fully describing a quantum state as it is related to the density matrix, $\rho=|\psi\rangle\langle\psi|$, since:

$$\rho(\mathbf{r},\mathbf{r}')=\langle\mathbf{r}|\rho|\mathbf{r}'\rangle=\langle\mathbf{r}|\psi\rangle\langle\psi|\mathbf{r}'\rangle=\psi(\mathbf{r})\psi^*(\mathbf{r}')=g^{(1)}(\mathbf{r},\mathbf{r}')|\psi(\mathbf{r})||\psi(\mathbf{r}')| \tag{4.5}$$

4.3.1 Interferometers

Let $\psi_1=A_1e^{i\varphi_1}$ be the wavefunction of a polariton condensate. Its intensity, $|A_1|^2$, is directly recorded by a CCD camera. Its phase, φ_1, and coherence properties are recorded by placing an interferometer on the emission **far-field** (Fig. 4.1) and recording interference maps. The way interferences are obtained, given by the interferometer geometry, depends on the physical entities to be determined.

When measuring spatial coherence it is convenient to use a Michelson interferometer in the so called retroreflected configuration, in which one of the interferometer arms contains a normal mirror whereas the other arm contains a retroreflector (Fig. 4.4a). In this way, at the image plane on the entrance slit of the spectrometer, each point of the condensate is interfered with another one at the opposite side with respect to the condensate centre. The visibility of the interference fringes is related to $g^{(1)}\left(\psi_1(\mathbf{r}),{\psi_1}^*(-\mathbf{r})\right)$ [15]. Such a measurement also provides a phasemap [114], given by the difference between two phases in opposite sides of the condensate, so it clearly does not represent the wave-function phase. This interferometer geometry is used in Section 8.1 to measure the long-range coherence of a non-resonantly excited polariton condensate.

When measuring time coherence, the most appropriate configuration is a Michelson interferometer with one retroreflector in each arm, with one of them mounted on a delay stage (Fig. 4.4b). Under this geometry, each condensate point is interfered with itself at a time delay that can be controlled by the path difference between both arms. Again, the fringe visibility is related to the coherence $g^{(1)}(\mathbf{r},\mathbf{r},\Delta t)$, which can be extracted after performing Fourier transform analysis - see section 4.3.2.

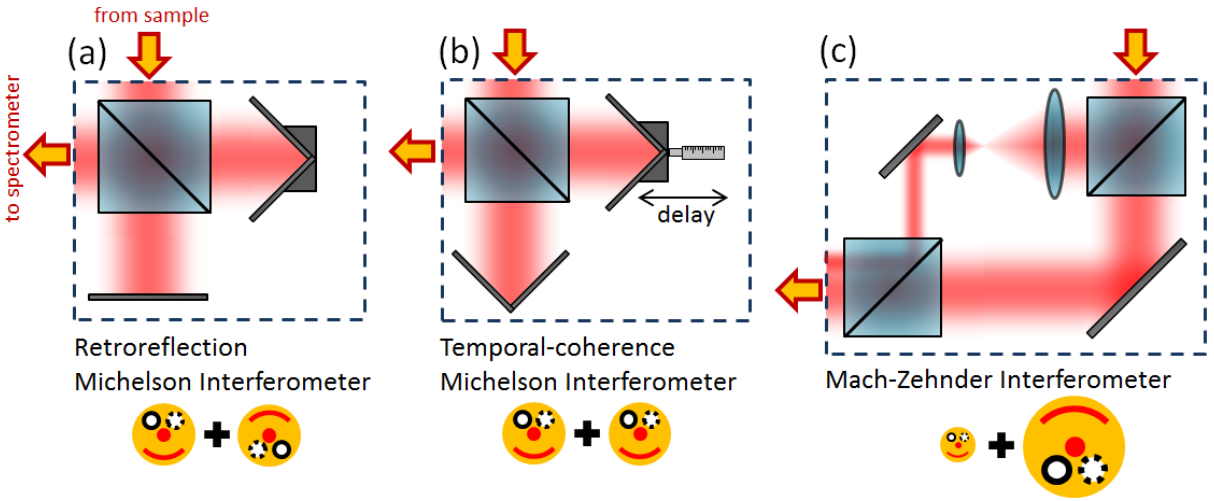

Figure 4.4: Interferometer geometries used to split the sample photoluminescence into two separate beams that are made to interfere again on the spectrometer slit entrance, providing fringes for interferometry. The bottom face-like images schematically represent, in each panel, the two images originating from each interferometer arm that are made to interfere. In (a) each spatial point is interfered with another one on the opposite side of the condensate, whereas in (b) each spatial point is interfered with itself at a different time delay. In the Mach-Zehnder interferometer (b), one of the arms contains two lenses that decreases the far-field propagation diameter and so magnifies the emission image, making the condensate emission to be interfered with an small expanded part of itself.

In order to correctly extract the condensate phase, $\varphi_1(\mathbf{r})$, a constant-phase field $\psi_2(\mathbf{r}) = A_2(\mathbf{r})e^{i\varphi_2}$ is needed as a reference. When the condensate is created resonantly by a pump laser, the laser itself can be used as a reference [118–121] — note that the polariton emission and the reference wave should have the same energy in order to see interferences in a time-averaged measurement. An alternative is to use an expanded small part of the condensate which can be considered as a constant phase reference. In this technique, introduced in Refs. [20, 36], the condensate emission is split into two arms of a Mach-Zehnder interferometer, one of them containing two lenses that magnify the emission (Fig. 4.4c). A small portion of the expanded image, considered as a constant phase reference, is interfered with the sample emission. After Fourier transform analysis (section 4.3.2), a phase map is extracted which contains the relative phase between both interfering field. Since the expanded image is assumed to have a constant phase, the extracted phasemap actually contains the condensate phase spatial profile.

4.3.2 Analysis of the interferograms

In this section we describe how the recorded interference fringes between two fields, $\psi_1(\mathbf{r}) = A_1(\mathbf{r})e^{i\varphi_1(\mathbf{r})}$ and $\psi_2(\mathbf{r}) = A_2(\mathbf{r})e^{i\varphi_2(\mathbf{r})}$, can be analysed in order to calculate the complex degree of coherence, defined by Eqs. 4.3 and 4.4.

As a practical example, let us consider the field profile of a vortex, whose intensity ${A_1}^2$ is shown in Fig. 4.5a, being interfered with an expanded part of itself, ${A_2}^2$ (Fig. 4.5b), by using a Mach-Zehnder interferometer similar to the one shown in Fig. 4.4c. By properly tilting the mirrors of each interferometer's arm, the arrival angles, at the spectrometer entrance, of the light from both interferometer arms are set to be slightly different, in such a way that the interference image, I_{12}, Fig. 4.5c, contains approximately straight fringes

(note the fork-like dislocation present at the small doughnut core, related to the 2π phase winding characteristic of a vortex). This makes possible to extract each component of Eq. 4.2 using Fourier transform analysis, as explained below.

The Fourier transform (FFT) of the interference image has three main terms, O_{-1}, O_0 and O_1 (Fig.4.5d), whose inverse Fourier transforms (iFFT) can be associated, according to Eq. 4.2, to:

$$iFFT(O_0) = \langle A_1(\mathbf{r})^2 \rangle + \langle A_2(\mathbf{r})^2 \rangle \tag{4.6a}$$

$$iFFT(O_1) = g^{(1)} \cdot \sqrt{\langle A_1(\mathbf{r})^2 \rangle \cdot \langle A_2(\mathbf{r})^2 \rangle} \tag{4.6b}$$

$$iFFT(O_{-1}) = g^{(1)^*} \cdot \sqrt{\langle A_1(\mathbf{r})^2 \rangle \cdot \langle A_2(\mathbf{r})^2 \rangle} \tag{4.6c}$$

The modulus of the inverse Fourier transform of O_1, $|iFFT(O_1)|$, is shown in Fig. 4.5e. It is straightforward to extract $g^{(1)}$ from Eq. 4.6b:

$$g^{(1)} = \frac{iFFT(O_1)}{\sqrt{A_1^2 \cdot A_2^2}}, \tag{4.7}$$

where A_1^2, A_2^2 and $|iFFT(O_1)|$ are shown in Figs. 4.5a,b,e, respectively.

The modulus of $g^{(1)}$, Fig.4.5f, corresponds to the coherence between the fields whose intensities are represented by Figs. 4.5a and 4.5b. The phase of $g^{(1)}$, Fig.4.5g, is the averaged phase difference between the two fields. Since Fig.4.5g is the iFFT of a distribution in k-space, O_1, centred at a finite $\mathbf{k} \sim (1.3, 0.3)\mu m^{-1}$, the extracted phase of $g^{(1)}$ has a global phase-gradient pointing in that direction. Since the phase is plotted modulo 2π, this is reflected in the many $\pi \rightarrow -\pi$ jumps in the same direction. Such a phase gradient is due to the relative difference in the incidence angle of the light from each interferometer's arm, and it can be removed by translating the O_1 term to the origin $\mathbf{k} \sim (0, 0)\mu m^{-1}$ before performing the iFFT. The resultant phasemap (Fig.4.5h) is smoother, and a characteristic 2π-phase winding appear close to the vortex core (Fig.4.5h). A second vortex, corresponding to the enlarged one, is also seen on the right-side of the image; in the experiments presented in the following sections, the expanded image is enlarged by a bigger factor in order to avoid that vortices corresponding to the expanded arm appear on the recorded phase-dynamics.

The phasemap extracted from interference measurements can be used to calculate physical quantities that depend on the condensate phase. Its gradient yields the *local fluid velocity*,

$$\mathbf{v}_s = \frac{\hbar}{m} \nabla \varphi, \tag{4.8}$$

whose rotational gives the *local vorticity* (Fig.4.5i),

$$\varpi = \nabla \times \mathbf{v}_s \tag{4.9}$$

Since the condensate phase is single-valued and continuous, the vorticity is zero everywhere except at the vortex core, and so vorticity maps are very useful to detect the vortex precise position and charge.

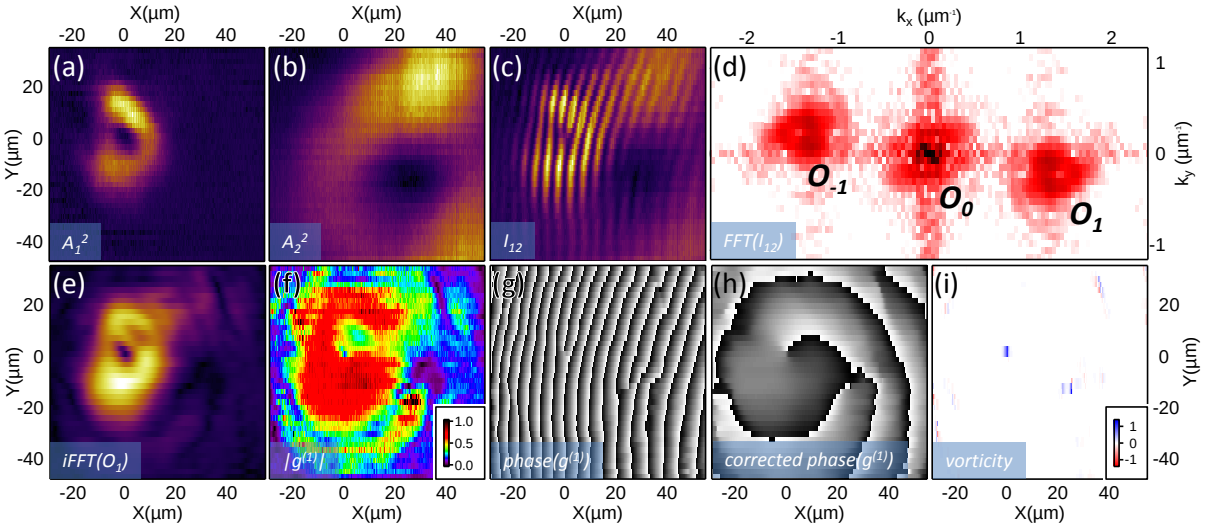

Figure 4.5: Calculation of $g^{(1)}$ (coherence and phase) from Fourier analysis. Intesity profiles of a vortex from a Mach-Zehnder interferometer's (a) normal arm and (b) expanded arm. In (b), the image of the vortex is expanded 3 times by the interferometer. (c) Interference between (a) and (b) with a finite in-plane momentum. (d) Fourier transform of (c) with three main terms classified as O_{-1}, O_0 and O_1. (e) Inverse Fourier transform of the term O_1 in (d). Extracted $g^{(1)}$ (f) modulus and (g) phase, using Eq. 4.7. (h) Corrected $g^{(1)}$ phase, found when removing the global phase gradient from (g). (i) Vorticity map calculated by applying Eqs. 4.8 and 4.9 to the phasemap (h).

4.3.3 Phase time-dynamics

The interference image formed when using a Mach-Zehnder interferometer can be focused onto the entrance slit of a spectrometer in order to energy- or time-resolve a 1D slice of the image. If moreover the imaging lens is sequentially displaced while images are being acquired, tomographic reconstruction is performed, with each energy- or time-slice containing an interference image from which coherence- and phase-properties can be extracted. In this way, the condensate wavefunction (density, phase and coherence) is fully characterized in position-time space, $\psi(\mathbf{r}, t)$, if the images are acquired by an streak-camera, or in position-energy space, $\psi(\mathbf{r}, E)$, if images are energy-resolved by a spectrometer-CCD combination. In the latter case, a simple Fourier transform allows the condensate phase and density to be tracked in time: $\psi(\mathbf{r}, t) = \sum_E \psi(\mathbf{r}, E) e^{iEt/\hbar}$.

In Part III the time-dynamics of the condensate phase is measured by acquiring interference images in an streak-camera, whereas in Part IV, Chapter 9, a Fourier transform of the condensate phase energy-dependence yields its time-dynamics.

Part III

Superfluidity and vortex dynamics in the OPO regime

Introduction

After the discovery of zero viscosity in liquid helium, other fundamental properties of the superfluidity phenomenon have been revealed. One of them, irrotational flow, gives rise to quantized vortices and persistent currents. In a superconductor, persistent flow means electric current without resistance: if electrons are made to move in a loop of superconducting wire that is immediately isolated from the environment afterwards, the current will flow essentially forever. In a superfluid, such as liquid helium below the lambda point, the frictionless flow allows persistent circulation in a hollow toroid. A Bose-Einstein condensate of an atomic gas also exhibits superfluidity. Experiments have confirmed the superfluid behavior by demonstrating a critical velocity below which a blue-detuned laser beam could be moved through the gas without causing excitations [172], and irrotational flow through the creation of vortices [93] and vortex lattices [94] in both rotating and nonrotating traps. Persistent flow can be observed when a BEC is confined into a toroidal trap and the quantised rotation is initiated by a pulsed Laguerre-Gauss beam [97, 173, 174] – see Section 2.4.2. The toroidal trap is essential to allow the vortex stability because of the energy cost of the vortex core to move through the high density region from the centre of the torus where the density is zero.

Polariton condensates share with weakly interacting BECs phenomena such as the spontaneous breaking of the phase symmetry and the appearance of a Goldstone mode (see Section 2.5). However, being intrinsically non-equilibrium, all polaritonic systems need continuous pumping to balance fast decay and maintain a steady state regime. In strong contrast with equilibrium superfluids, whose ground state is flow-less, pump and decay lead to currents that carry polaritons from gain- to loss-dominated regions. Moreover the photonic disorder present in samples breaks the spatial symmetry of the condensate, allowing the spontaneous formation of vortices as stable solutions to the system dynamics [114], without invoking any superfluid properties [145, 157].

The fundamental relationship between superfluidity and condensation in two-dimensional polariton systems has to be carefully addressed for each pumping scheme. Pump-only polaritons at high enough densities have a linear Bogoliubov sprectrum similar to equilibrium BEC, being superfluids when flowing below its sound velocity [19, 144]. Non-resonantly pumped polariton condensates does not present off-diagonal long-range order [117] and have a diffusive Goldstone mode [111, 151], therefore are not superfluids in the sense of Landau. However, vorticity can be fully sustained by a spontaneous polariton condensate and its lifetime is expected to be much longer than the perturbation in the density induced by the probe [156]. Finally, although under OPO excitation a polariton condensate also have a diffusive Goldstone mode [141], such a system has been recently shown to present off-diagonal long-range order [112, 113] and suppression of Rayleigh scattering when triggered by a pulsed probe [18].

The very same idea of questioning the persistency of flow in a BEC via a pulsed Laguerre-Gauss beam as a diagnostic for superfluidity, can be applied to polaritons: as recently proposed for non-resonantly pumped polariton condensates [156], this definition of superfluidity as metastable flow is equally meaningful in non-equilibrium systems as in equilibrium ones. This part of the thesis includes the first observation of persistent currents in a polariton condensate [20, 35] by means of a long-lived injected vortex. The same technique allowed us to study the formation of vortex-antivortex pairs [36] and the stability of doubly-quantized circulation [20], finding effects unique to polariton fluids.

All the results are collaborative achievements by the *SEMICUAM* group, leaded by

Prof. Luis Viña. The experiments have been performed by the author of this thesis in the *Laboratorio de Espectroscopia Ultrarrápida* at the *Universidad Autónoma de Madrid*, under the supervision of Prof. Luis Viña, with help and advise from Dr. Daniele Sanvitto, and in collaboration with Carlos Antón and Matthias Baudisch. The simulations have been carried out by the theoretical members of the group, leaded by Prof. Carlos Tejedor, in special by Dr. Francesca M. Marchetti and Dr. Marzena H. Szymańska (from the University of Warwick), with help from Andrei Berceanu.

The sample used is a single-QW microcavity, described in Section 3.1. For all the data presented, the cavity photon energy is slightly negatively detuned (between -3 and $-0.7\,meV$) from the exciton energy.

Chapter 5

Persistent currents

In order to investigate persistence of currents we apply a technique already used in nonlinear and quantum optics, cold atoms and biophysics [175]: excitation by a light field carrying orbital angular momentum. Transfer of light orbital angular momentum has been demonstrated in parametric processes in nonlinear materials [176,177] and has been used to generate atomic vortex states in BECs [97,173][1]. However, although even a classical fluid acquires angular momentum in the presence of an external rotating drive, only a superfluid can exhibit infinitely-lived circulating flow in a dissipative environment once the external drive is turned off.

5.1 Experimental setup

A CW laser is focused onto a Gaussian big spot, with $100\,\mu m$ FWHM, on the single-QW sample. When exciting with low powers, far below condensation threshold, and energies around $1.65\,eV$, far above the polariton modes energy, linear luminescence from the polariton branches are recorded (Fig. 5.1a), obtaining for the chosen position in the sample a photon-heavy-hole-exciton detuning $\delta_{Ph-HH} \sim -1.3\,meV$. In order to create a polariton condensate under OPO excitation, the laser energy is brought into resonance with the lower polariton branch (Fig. 5.1b-d), injecting polaritons close to the inflection point, $E_p = 1.5268\,eV$ and $k_p = 1.35\,\mu m^{-1}$ ($\theta_p = 10°$). At $50\,mW$ excitation power (Fig. 5.1b), the LPB is slightly blueshifted due to the high concentration of polaritons and the population distribution starts getting concentrated around the zero momentum ($k_s = 0$) state. As the pump power is further increased, the blueshift is enhanced and the OPO signal state gets macroscopically occupied (Fig. 5.1c,d). The signal generated close to zero momentum ($k_s = 0$) has a flat dispersion that implies zero group velocity, $v_g = \partial_k E = 0$. This, however, does not mean that there is no flow of polaritons, which is described by the phase velocity or current, given by the phase gradient (Eq. 2.30). In fact, the broad momentum distribution of the steady state signal indicates a pronounced out-of-equilibrium dynamics, where local currents carry polaritons from gain- to loss-dominated regions.

The bottom panels of Fig. 5.1 show the spatial profile of the emission from the signal state for increasing excitation powers above OPO threshold, which have been acquired by

[1]Note, however, that even if in the atomic and polaritonic cases the same Laguerre-Gauss laser field is used, the mechanism of spinning the BEC atoms is different from the one which rotates polaritons: whereas the transfer of orbital angular momentum to atoms is accomplished by a resonant two-photon stimulated Raman process, the photonic component of polaritons is directly created in a vortex state.

filtering out all the momentum states $|k_{//}| > 1.15\,\mu m^{-1}$ in the emission far field. Since the pump spot has a Gaussian spatial shape, the threshold for condensation is first surpassed close to its centre. As the pump power is increased, a bigger spatial region overcomes threshold for condensation and the signal becomes bigger. Moreover, as the power is increased, the density landscape becomes more inhomogeneous, which is possibly related to an increase of the out-of equilibrium flow of polaritons from gain- to loss- dominated regions, increasing the polariton density at specific spatial points. This is confirmed by noting that the signal momentum distribution is broader for high pump powers (compare Figs. 5.1b,d).

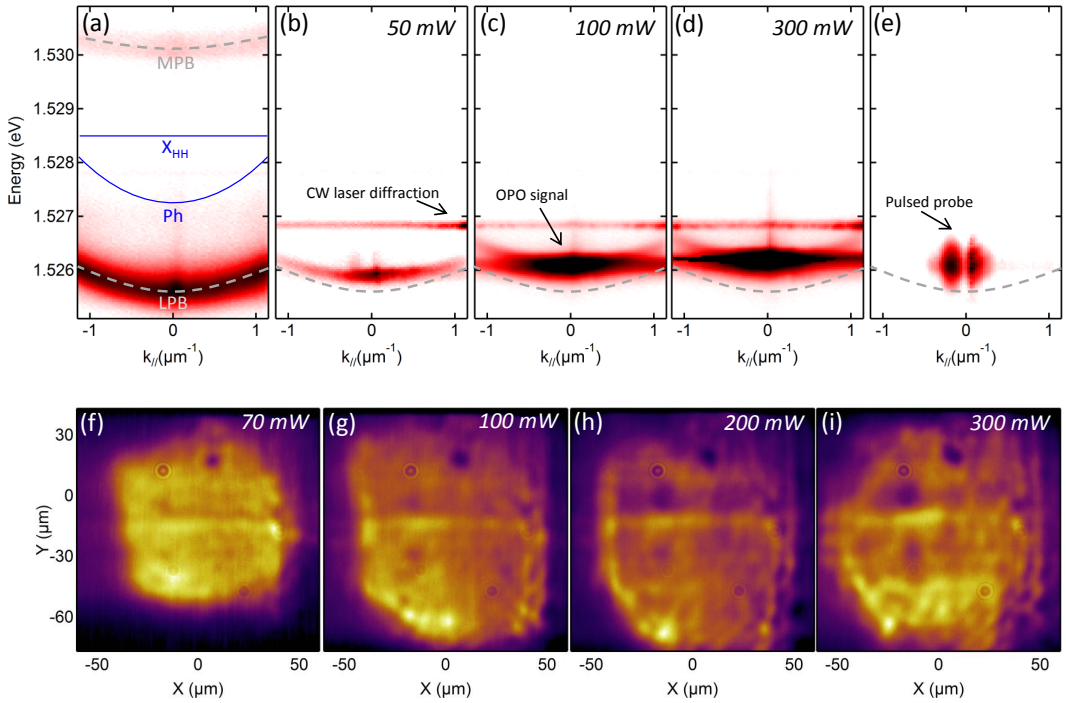

Figure 5.1: (a) Polariton luminescence dispersion under a weak CW non-resonant pump, showing fitted lower and middle polariton branches (LPB and MPB) together with bare photon (Ph) and heavy-hole (X_{HH}) modes. Polariton luminescence under resonant excitation close to the LPB inflection point, as a function of excitation power, in momentum (b-d) and real (f-i) spaces. The CW laser energy can be see in (b-d) by its broad-momentum diffraction line. (e) Dispersion of the pulsed vortex probe. In (b-e), the fitted LPB under weak excitation power is plotted for comparison.

To demonstrate persistent currents, we note that the lifetime of an injected vortex is expected to be higher for higher condensate densities [156]. While driving an OPO signal steady state with the CW pump laser at $300\,mW$ (Figs. 5.1d,i), we trigger a new scattering process on top of the OPO signal by shining a $6.65\,\mu W$ $2\,ps$-long pulsed probe, focused onto a $\sim 25\,\mu m$-diameter region, with the same energy and momentum as the OPO signal steady state (Fig. 5.1e). The experiment setup to create such a configuration is shown in Fig. 5.2a. The CW laser arrives perpendicularly to the objective lens but displaced from its centre in such a way that it is focused onto the sample with a angle of incidence of 10°. The pulsed laser passes through a diffraction hologram with a fork-like dislocation at its centre. The 1^{st} order diffracted beam carries a Laguerre-Gauss $M = 1$ vortex, whose phase and intensity profiles are schematically shown at the

bottom of Fig. 5.2b, and is focused onto the sample at perpendicular incidence. The schematic representation of the excitation in momentum space is shown in Fig. 5.2b. Figure 5.2c shows a composition, in real space, of the signal condensate 100 μm-wide emission (recorded by a CCD) together with the probe reflection at its time of arrival (recorded by the streak–camera), marked by the dashed rectangle. The vortex core arrives at the $(0, 0)$ μm position and its size is smaller than that of the condensate (by a factor ≈ 4, being ~ 25 μm wide) to allow free motion of the vortex within the condensate, thus avoiding a spurious confinement. After a short time, $\sim 2ps$, the probe vanishes, leaving the polariton coherent state free to rotate, without the driving field.

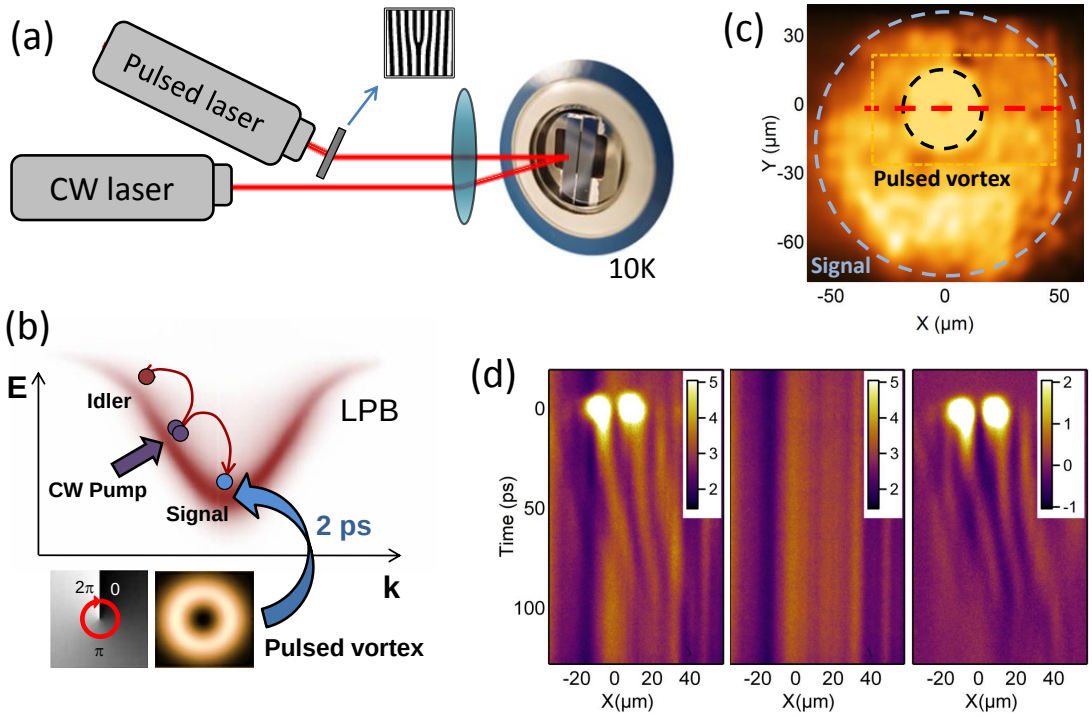

Figure 5.2: Setup used in the Triggered Optical Parametric Oscillator (TOPO) experiment. (a) A CW-laser pumps the sample with an angle of 10°. A $\sim 2ps$-pulsed laser beam acquires a $M = 1$ vortex profile after diffracting through a fork-like hologram and arrives on the sample perpendicularly. (b) TOPO excitation scheme in momentum space and vortex probe phase and intensity spatial profiles. A CW-laser pumps the lower polariton branch (LPB) close to its inflection point, initiating an OPO process that creates two equally energy- and momentum-separated coherent populations - idler and signal. The signal is triggered by an $M = 1$ vortex pulsed beam. (c) Position-space composed image corresponding to the probe arrival time, showing a $\sim 100 \mu m$ condensate and a smaller doughnut-shape probe (see text). The time-dynamics of the 1D slice marked by the red dashed line in shown in (d) where the left panel corresponds to the TOPO dynamics, the middle panel the CW-only steady state dynamics and the right panel is obtained by subtracting the middle panel from the left one. A strongly negative density depletion is observed where the vortex core is injected and can be followed up to the last detectable signal. The dashed rectangle in (c) marks the region whose time-dynamics is measured.

Using a streak camera we follow the time evolution of the condensate after the arrival of the pulsed probe. The left panel of Fig. 5.2d shows the time dependence of the 1D spatial slice defined by the dashed red line in Fig. 5.2c that crosses the vortex core.

The vortex arrives at $t = 0\,ps$ and its cross-section is seen as the two bright lobes. In order to isolate the changes in density produced by the probe, we record the CW-only signal background state time-evolution (middle panel) and subtract it from the left panel, yielding the dynamics seen in the right panel. The main effect of the probe on the triggered signal (t-signal) is to create a negative density region of the background subtracted image (black traces in the right panel) that can be seen up to the bottom of the image ($> 120\,ps$). Such negative values mean that the density of the t-signal is lower in this region as compared to the signal steady state, which is the first proof that the vortex core is actually imprinted into the condensate.

5.2 Superfluid rotation

To further study the created vortex, we next use tomography to reconstruct the condensate full spatial time-dynamics — see Section 4.2.1. Fig. 5.3a shows the CW-only steady state, before the arrival of the probe, inside a $68 \times 53\,\mu m^2$ region that contains the point where the vortex arrives. The next three panels (b-d) show the time evolution of the triggered condensate, with the steady state background subtracted. The probe arrives at $t = 0\,ps$ generating a negative density core (inside the dashed circle) that moves towards the right and can be seen even after a hundred picoseconds. This dip, with a diameter of $\sim 10\mu m$, is around $\sim 20\%$ of the signal intensity.

In order to confirm that the deep core is due to rotation persistence of the injected $M = 1$ vortex, we make the condensate interfere with an expanded region of itself far from the vortex core (where the phase is approximately constant) in a Mach-Zehnder interferometer (see Section 4.3.2). The resultant interference image for the steady state condensate is shown in Fig. 5.3e. At $t = 0\,ps$ the fringe visibility is greatly enhanced in the doughnut region of the probe and a characteristic fork-like dislocation can be seen at its core (Fig. 5.3f). The fork can be resolved up to $\sim 100\,ps$ and its position always coincides with the deep density core seen in the upper panels.

A more quantitative understanding of the interference patterns is achieved when performing Fourier transform analysis (see Section 4.3.2) in order to extract the degree of coherence, $g^{(1)}$, from panels (a-d) and (e-h). The resultant phase is shown in panels (i-l) and the absolute value of $g^{(1)}$ in panels (m-p). The initial condensate phase is smooth, with no topological defect, before the arrival of the probe (Fig. 5.3i) — we actually experimentally choose such a configuration in order to be sure that the persistence of a vortex is purely related to superfluidity and not due to pinning of vortices by defects where the polaritons flow to. The phase of the probe, Fig. 5.3j, clearly winds clockwise from $-\pi$ to π around its core; a similar behaviour is seen for the phase of the triggered condensate around the deep negative densities. The main effect of the probe on $|g^{(1)}|$ (Fig. 5.3m-n) is to create a persistent doughnut-shaped region of high coherence around the vortex core that persists up to later times, with a dip of low coherence at the vortex core position.[2]

[2]The low values of coherence — below 5% — of the condensate steady state (Fig. 5.3m) is in apparent discrepancy with higher values — around 50% — recently observed in polariton condensates created under OPO configuration [112, 113]. We attribute such a discrepancy to the fact that the pumping laser used here is much more noisier than the actively stabilized monomode laser used in [112, 113], which introduces more decoherence to our system, and that our interference geometry yields lower values of coherence if compared to retroreflected geometries.

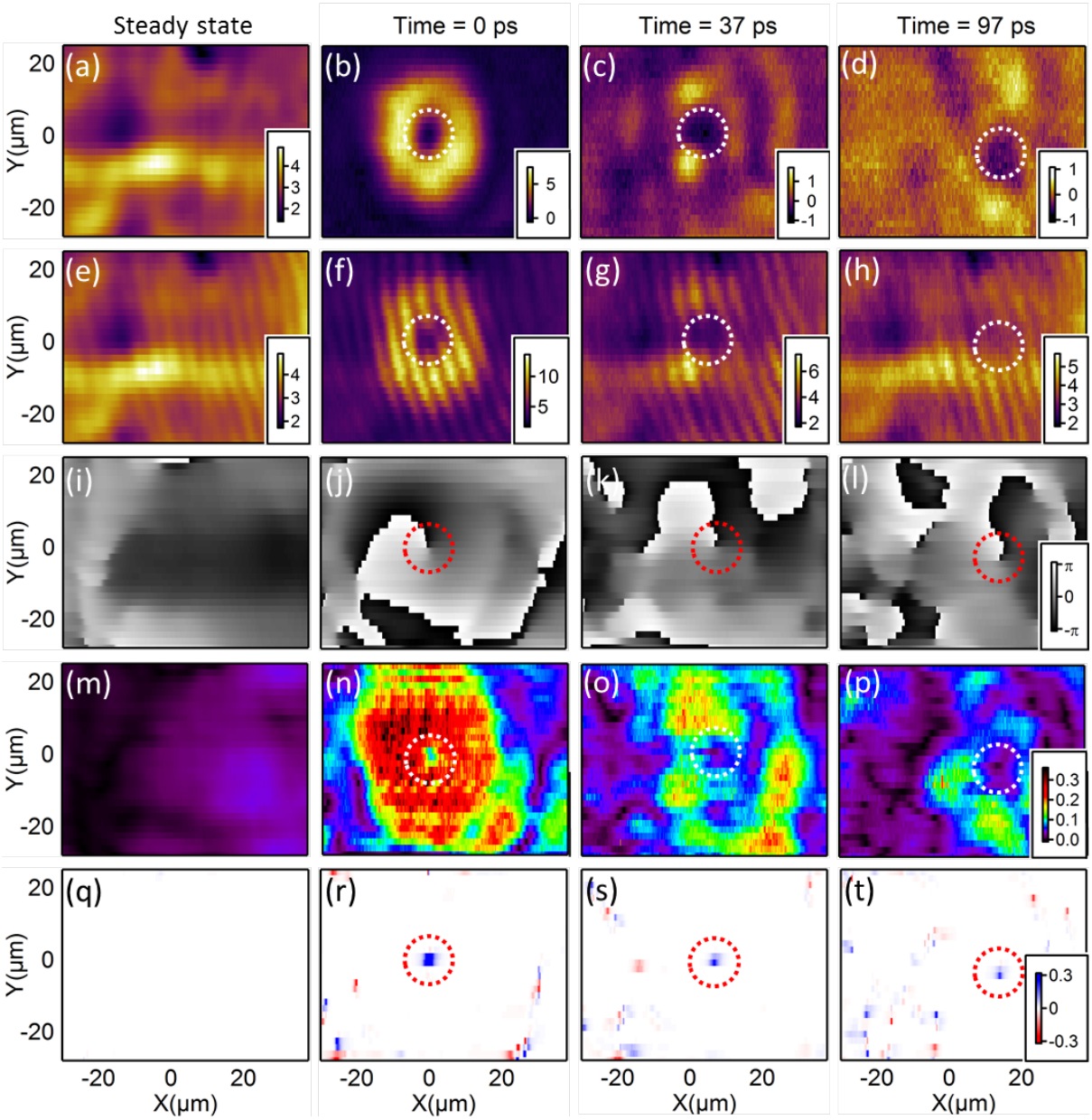

Figure 5.3: Time evolution of the polariton condensate (a-d) density and (e-h) interference with an expanded region of itself. The complex degree of coherence $g^{(1)}$ is extracted from (a-d) and (e-h): its phase, which is an approximation to the condensate phase, is plotted in (i-l) and its absolute value in panels (m-p). The correlation-weighted vorticity (see text for definition) is shown in panels (q-t). The images corresponding to the condensate steady state are shown in the left panels (a,e,i,m,q) and the time-evolution, after the arrival of the probe at $t = 0$, on the rest of the panels. In the density time-dynamics (b-d) the steady state background density (a) is removed to highlight the changes induced by the probe. The position of the imprinted vortex is marked in all panels by a dashed circle. It can be tracked for up to $100\,ps$ by a dip in density and coherence, a fork-dislocation in interferences, a branch-cut in phase, and a peak in vorticity. The data correspond to excitation powers of $300\,mW$ (CW-laser) and $6.65\,\mu W$ (pulsed laser). When colorbars are not shown in a panel, the color code is the same as the right-most panel in the same line. The correlation-weighted vorticity (q-t) is normalized to its highest value, at the probe arrival time.

Before discussing the lower panels of Fig 5.3, let us consider the effects of changing the CW- and pulsed-lasers power on the persistence of an injected vortex.

When tracking the density dip at the imprinted vortex core, we note that small effects are observed when changing the probe power by two orders of magnitude once a minimum threshold is crossed (Fig 5.4a). In fact, a minimum probe power is required for the vortex to be imprinted to the OPO, but once the vortex is imprinted, the probe power does not change significantly the depth of the vortex in the condensate, in agreement with predictions for non-resonantly pumped polariton condensates [156]. On the other hand, the behavior of the injected vortex depends strongly on the excitation power of the CW driving field. The strength of the negative dip produced by the probe strongly decreases for low CW powers (Fig 5.4b), and its is actually hard to track the vortex position in the interference images. This is an indication that the lifetime of a vortex is strongly dependent on the density — and hence coherence — of the condensate where it is injected, in agreement with theoretical predictions [156]. Moreover, at $200\,mW$, four times above the OPO threshold, we observe a saturation in the depth of the core.

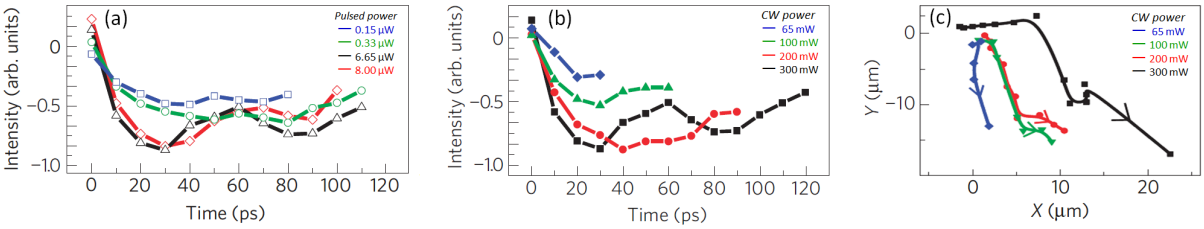

Figure 5.4: (a), Effect of probe power — $0.15\,\mu W$, blue squares; $0.33\,\mu W$, green circles; $6.65\,\mu W$, black triangles; $8.00\,\mu W$, red diamonds — on the duration and depth of the core of the vortex, with the pump power kept at $300\,mW$. (b) Depth and (c) position of the imprinted vortex core as a function of time for four different pump powers ($65\,mW$, blue diamonds; $100\,mW$, green triangles; $200\,mW$, red circles; $300\,mW$, black squares) — all above the OPO threshold (50 mW), with the probe power kept at $6.65\,\mu W$. In (c) each point correspond to a time interval of $\sim 10\,ps$.

Since the probe excitation conditions are left intact when changing the CW-pump power, it could be argued that the reduction of the density dip of the imprinted core with decreasing CW-pump power could due to the probe getting out of resonance with the OPO signal that gets less blueshifted for lower densities. However, by carefully inspecting the dispersion images, Figs. 5.1b-e, we see that the main effect of the small changes in the blueshift of the $k = 0$ signal is that the resonance conditions between the signal (Figs. 5.1b-d) and the broad probe (Figs. 5.1e) change slightly. It follows that the amount of the probe that actually enters the cavity slightly changes for different CW-powers. Since we do not expect any change on the vortex injection dynamics once a minimum probe power threshold is reached, and we performed the CW power dependence measurements for high enough probe powers ($6.65\,\mu W$), we can be confident that the only reason for the vortex core dip to be dependent on the CW power is that the condensate properties change.

Coming back to Fig. 5.4b, note the variation of the vortex core depth in time for the two higher pump powers. This is related to different pathways followed by the vortex when changing pump intensity (Fig. 5.4c), which depends on the kind of inhomogeneities met by the vortex along its trajectory (see Fig. 5.1f-i). This is an indication of the

great importance of non-equilibrium currents, originating from pump and decay, of the steady-state condensate on determining the trajectory followed by the imprinted vortex.

In the superfluid state, fluctuations would induce a random motion of the vortex core. It would be desirable to avoid this effect, but it is at present technologically impossible to perform single shot measurements to visualize directly a moving vortex in the density or phase profile of the condensate. However, since our experiments are averaged over a hundred million repetitions, the good vortex visualization at later times indicates a deterministic trajectory. Despite this deterministic behaviour, it is certainly possible that some percentage of the experiments follow a random walk, leading to a reduction of the visibility of the imprinted vortex. In fact, using Monte-Carlo simulations, the angular momentum of condensate made to rotate after the injection of a quantized vortex has been shown to continuously decay in time due to random motion of the vortex in a multiple-shot experiment [156].

If one calculates the angular momentum by applying the definition $L_z = \oint \mathbf{r} \times \mathbf{p} = \oint m\mathbf{v}_s d\mathbf{l}$ to the clockwise path defined by the dashed circles in Figs. 5.3, the same result $L_z = \hbar$ will be always found (see Eq. 2.32). In this way the angular momentum of a region of the condensate where a vortex has been injected is always $\hbar$ or 0 if the branch-cut can or cannot be seen, respectively. Moreover, this definition implies that many vortices appear in regions of low coherence where many branch-cuts are seen in the phase maps — see *e.g.* the bottom-left side of Figs. 5.3h,l,p –, which is clearly misleading. This is due to the fact that when extracting the phase using Fourier transform techniques, we are only looking at the 1^{st} order term, which is the one related to the fringe visibility. All the polariton flow that is not coherent with the reference beam is then ignored when extracting a phase map. This yields to the intuitive conclusion that, when calculating the angular momentum from a phase map, the modulus of the correlation function should be taken into account. In fact, the decrease in the visibility of a fork-like dislocation can be associated with two phenomena: a) a random motion of coherent vortices that gives fork-dislocations at different position for each single realization of the experiment, yielding a multiple-shot averaged interference map with poor visibility; b) a decrease in the polariton population occupying the vortex mode due to decoherence mechanisms. Both phenomena lower the averaged angular momentum in a continuous way, as expected from calculations [156].

Finally, let us remember that any physical quantity described by an operator O and associated with a quantum state can be calculated from the state's density matrix ρ using the relation [178]:

$$\langle O \rangle = tr(\rho O) = \int \langle \mathbf{r}|\rho|\mathbf{r}'\rangle\langle \mathbf{r}'|O|\mathbf{r}\rangle d\mathbf{r}d\mathbf{r}' \tag{5.1}$$

Where the density matrix in position space, $\langle \mathbf{r}|\rho|\mathbf{r}'\rangle$, can be written as, using Eq. 4.5,

$$\langle \mathbf{r}|\rho|\mathbf{r}'\rangle = g^{(1)}(\mathbf{r},\mathbf{r}')|\psi(\mathbf{r})||\psi(\mathbf{r}')| \tag{5.2}$$

Although very recently the density matrix of a 1D condensate has been obtained [75], measuring $g^{(1)}(\mathbf{r},\mathbf{r}')$ of a 2D condensate is a extremely difficult task, as it is a 4-dimension tensor and so the time to acquire such a data is extremely long. This renders impossible a direct application of Eq. 5.1 to determine the average angular momentum of a polariton condensate after the injection of a quantized vortex.

However, let us remind that the angular momentum can be calculated simply by integrating the vorticity in space,

$$L_z = \oint m\mathbf{v}_s d\mathbf{l} = m\int_S (\nabla \times \mathbf{v}) d\mathbf{S}, \tag{5.3}$$

where we have used the Stokes' theorem. If the first integral is calculated in the clockwise path defined by the dashed circles in Figs. 5.3, S is the area inside the circle. We already argued that the coherence has to be taken into account when performing the calculation 5.3: Equation 5.1 suggests that the appropriate way of doing that is by weighting the vorticity by the coherence, $|g^{(1)}|$, and the condensate density $|\psi(\mathbf{r})|^2$ (the reference field density, $|\psi(\mathbf{r}')|^2$, is ignored since it is assumed to be constant). We thus intuitively define a *correlation-weighted vorticity*,

$$\Omega(\mathbf{r}, t) = (\nabla \times \nabla\varphi(\mathbf{r}, \mathbf{t})) \cdot |g^{(1)}(\mathbf{r}, t)| \cdot |\psi(\mathbf{r}, t)|^2, \tag{5.4}$$

calculated by multiplying the vorticity, obtained by taking the rotational of the phase (Figs. 5.3i-l), by the absolute value of the coherence (Figs. 5.3m-p) and by the density (Figs. 5.3a-d, but without background subtraction). The result is shown in Figs. 5.3q-t. Before the arrival of the probe, the condensate is vortex-free and Ω is negligible everywhere. At $t = 0$ a positive peak is associated with the vorticity carried by the probe. The positive peak moves around, its position always coinciding with the vortex positions shown in the upper panels, and can be seen up to $\sim 100\,ps$, where its intensity is weaker then at $t = 0$, an indication that the circulation is actually decaying.

Ω is expected to be directly related to the condensate angular momentum. To measure the persistence of circulatory flow stirred by the probe, we define the *coherent rotation*, CR, as being the integral of Ω inside a $\sim 10\,\mu m$-big region around its peak, delimited by the dashed circles in Figs. 5.3r-t,

$$CR(t) = \int_S \Omega(\mathbf{r}, t) d\mathbf{r} \tag{5.5}$$

The result, normalized to its value at $t = 0$, is plotted versus time in Fig.5.5a, for four different CW-pump excitation powers. The behaviour of $CR(t)$ is well described by an exponential decay, with decay time τ_{decay} towards a constant finite value (imprinted rotation); these fitting parameters are plotted in Fig. 5.5b as a function of power. Close to OPO threshold, the coherent rotation decays to zero within $\sim 6\,ps$. The situation is quite different for higher condensate densities. For $300\,mW$, the CR decay time is doubled, a fact that we attribute to an increase in the lifetime of the triggered OPO population, which also carries a vortex. What is most impressive is that CR reaches an approximately constant value as high as 20% of the one carried by the probe. This means that the rotation is actually imprinted into the condensate, and most notably that the vortex follow in most cases the same trajectory in the hundred million experiment realizations, in such a way that the visibility of the fork-dislocation of the interference images do not decay in time. The amount of rotation that is transferred into the condensate, 20 %, is in agreement with the vortex density dip being also $\sim$ 20 % of the condensate density. Accordingly, the imprinted rotation saturates at 4 times the OPO threshold in the same way as the imprinted vortex density dip.

At equilibrium, the presence of long-range spatial coherence is a necessary condition for the appearance of superfluidity [179]. Highly coherent states can be achieved in Bose systems when increasing their density (see Section 2.1), which is done in a polariton condensate by increasing the pump power. For the data presented here, when the pump power is increased, apart from the already mentioned increasing of imprinted vorticity, the steady state background coherence, defined as the spatially integrated value of $|g^{(1)}|$ is also enhanced (Fig.5.5b - inset). This provides one more similarity between non-equilibrium and equilibrium quantum fluids: in both, the superfluid character is stronger when the fluid has higher long-range spatial coherence.

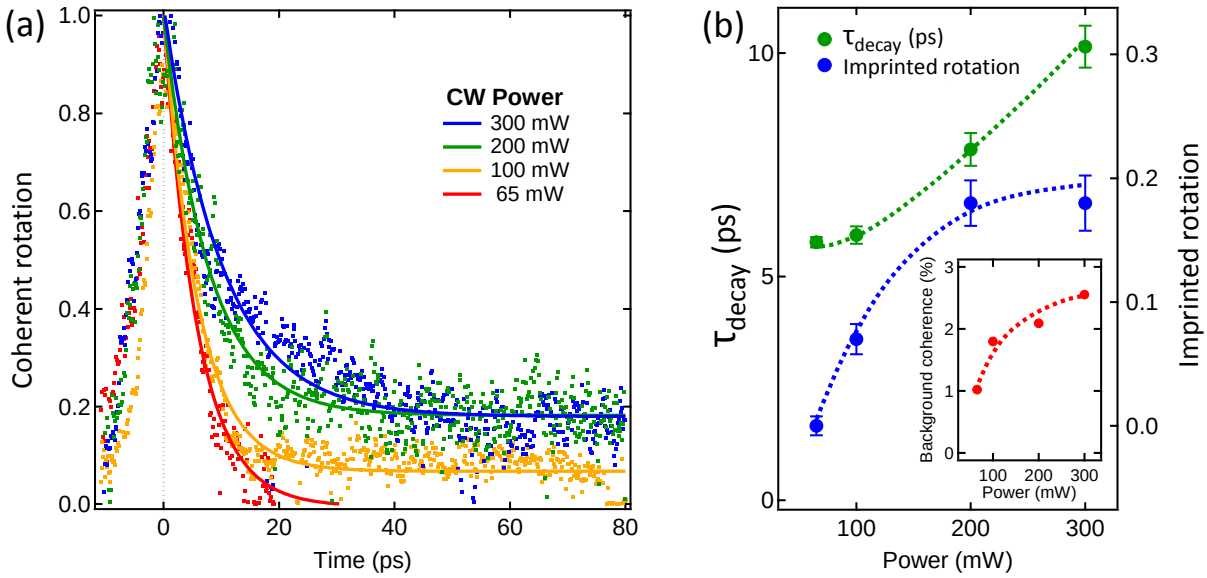

Figure 5.5: (a) Coherent rotation (CR) decay as a function of power. Each curve is normalized to its value at $t = 0$. The data are fitted by exponential decays towards a constant value that we call *imprinted rotation* The fitted decay times, τ_{decay}, and imprinted rotation, for each pump power, are plotted in (b). The inset shows the integrated signal background coherence for each power (see text). Dashed green, blue, and red lines are guides to the eye.

However we note that the amount of rotation transferred into a polariton condensate is strongly dependent of specific positions of the sample: the potential landscape caused by defects, dislocations and cavity mirror fluctuations yield current patterns which favour certain regions rather than others. It is even possible to find conditions in which the probe triggers extra population containing a vortex that lasts for tens of picoseconds, however no rotation is imprinted into the condensate steady state [35]. Such a regime will be discussed in more details in Chapter 7.

Another way of measuring angular momentum is probing the difference in momentum at two opposite sides of the vortex core, as proposed in Ref. [156] and depicted in Fig. 5.6a. If the polariton fluid is circulating, the momentum of the two sides marked in the figure must have opposite directions, what results in a finite difference in their momenta (Δk). In Fig. 5.6b the momentum distribution corresponding to the regions marked with $\uparrow$ ($\downarrow$) are depicted by a red (black) line, respectively, at a time $t = 35\,ps$ after the arrival of the probe. A clear splitting between the two peaks is observed, amounting to $\Delta k = 0.18\,\mu m^{-1}$. The finite difference in the momentum distribution between the left and right parts of the far field spectra of the signal polaritons soon decays to a constant

value that persist for times much longer than the extra population lifetime (Fig. 5.6c). This again demonstrates that the signal steady state holds a permanent rotation long after the amplified gain population is gone. After 40 *ps* the difference falls to zero due to the movement of the vortex core outside the observation region.

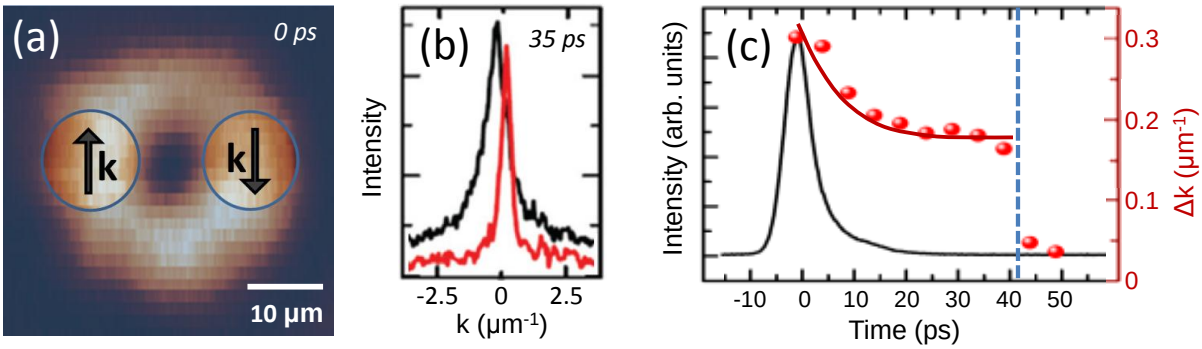

Figure 5.6: An alternative way of measuring the vortex rotation. (a) The momenta at opposite sides of the vortex core point toward contrary directions due to circulation. (b) Wavenumber distributions — black and red lines — corresponding to the two regions marked on (a) — right and left, respectively –, showing small and opposite finite values, which characterize the circulation. (c) Time evolution of the difference between the peak wavenumbers (Δk) (red dots) and of the extra population introduced by the probe (black line). Note that the circulation persists longer than the extra population, until 40 *ps*, marked by the dashed blue line, when the vortex leaves out the region of measurement. The red line in (c) is a guide to the eye.

5.3 Numerical simulations

In order to better understand the experimental results, simulations have been performed using the two-component Gross-Pitaevskii equation defined by Eqs. 2.42 and 2.43 with external pumping given by $P = F_p + F_{pb}$, where F_p represents the CW laser,

$$F_p(\mathbf{r}, t) = f_p(|\mathbf{r} - \mathbf{r}_p|)e^{i(\mathbf{k}_p \cdot \mathbf{r} - \omega_p t)}, \tag{5.6}$$

with frequency ω_p and incidence parallel momentum $\mathbf{k}_p$, and with the strength f_p having a top-hat profile with FWHM σ_p, centred at $\mathbf{r}_p$; and F_{pb} represents the Laguerre-Gaussian (LG) pulsed probe,

$$F_{pb}(\mathbf{r}, t) \simeq f_{pb}|\mathbf{r} - \mathbf{r}_{pb}|^M e^{-\frac{|\mathbf{r}-\mathbf{r}_{pb}|^2}{2\sigma_{pb}^2}} e^{iM\varphi(\mathbf{r})} e^{-\frac{(t-t_{pb})^2}{2\sigma_t^2}} e^{i(\mathbf{k}_{pb} \cdot \mathbf{r} - \omega_{pb} t)}, \tag{5.7}$$

centred at $\mathbf{r}_{pb}$ with a density increasing linearly at its centre and decaying Gaussianly with width σ_{pb}. The probe, with frequency ω_{pb} and in-plane momentum $\mathbf{k}_{pb}$ (resonant with the OPO signal frequency and momentum), lasts σ_t and contains a vortex with charge $M = 1$.

Considering a vanishing static photonic disorder potential, $V(\mathbf{r}) = 0$ (the presence of the photonic disorder does not change qualitatively the results), the Equations 2.42 and 2.43, describing the dynamics of amplitudes and phases of the coupled cavity and exciton

fields $\psi_{C,X}(\mathbf{r},t)$, read ($\hbar = 1$):

$$i\partial_t \begin{pmatrix} \psi_X \\ \psi_C \end{pmatrix} = \begin{pmatrix} \omega_X - i\kappa_X + g_X|\psi_X|^2 & \Omega_R/2 \\ \Omega_R/2 & \omega_C - \nabla^2/(2m_c) - i\kappa_C \end{pmatrix} \begin{pmatrix} \psi_X \\ \psi_C \end{pmatrix} + \begin{pmatrix} 0 \\ F_p + F_{pb} \end{pmatrix} \tag{5.8}$$

where ω_X and $\omega_C - \nabla^2/(2m_c)$ are the exciton and photon dispersions, respectively. We use $m_C = 2.3 \times 10^{-5} m_e$, m_e being the free electron mass, and a Rabi splitting $\Omega_R = 4.4\, meV$, both determined experimentally, and a photon-exciton detuning $\delta = 0$. The cavity and exciton fields decay with rate $\kappa_C = \kappa_X = 0.26\, meV$). Other parameters are $\sigma_p = 70\, \mu m$, $\mathbf{r}_{pb} = (-6, -5)\mu m$ and $\sigma_{pb} = 4.5 \mu m$, noting that all the parameters are chosen to be close to the experimental ones.

Equation 5.8 is numerically solved on a $140 \times 140\, \mu m$ grid, with $0.47\, \mu m$ spatial resolution, by using a 5^{th}-order adaptive-step Runge-Kutta algorithm. By setting the pump at $k_p = 1.66\, \mu m^{-1}$ in the x-direction and at $\omega_p - \omega_X = -0.44\, meV$, *i.e.* roughly $0.5\, meV$ above the bare LP dispersion, the pump strength is gradually increased until the system is driven into the OPO regime where signal and idler states, blueshifted with respect to the bare LP dispersion because of interations, get exponentially populated — see the OPO dispersion in Fig. 5.7a, obtained by taking the Fourier transform in both space and time of $\psi_{C,X}(\mathbf{r},t)$.

In the OPO steady state regime, the pump, signal, and idler satisfy the phase-matching conditions and have a typical flat dispersion. This means that the group velocity of the signal, defined as the derivative of the energy dispersion at $\mathbf{k}_s$, is therefore zero. This, however, does not mean that there is no flow of polaritons. In fact, the broad momentum distribution, due to the finite size pump, implies that the signal state is characterised by non-trivial configurations of the phase velocity or currents, given by the phase gradient (Eq. 2.30). The associated flow of polaritons is a superposition of a dominant uniform flow $\mathbf{k}_s$ and more complex currents (caused by the system being finite size), which move particles from gain to loss dominated regions.

Figure 5.7b shows the spatial profile of the photon component (which is what is measured experimentally) of the OPO signal steady state. Similarly to what is done in experiments, the signal emission is isolated by filtering the full emission in momentum space in a cone around the momenta $\mathbf{k}_s$. The streamlines represent the phase gradient to which the dominant uniform flow, proportional to $\mathbf{k}_s$, has been subtracted. Note that the fact that the pump is shone on the microcavity with a finite angle with respect to the normal incidence implies that, for rotationally symmetric pump profiles, the symmetry inversion $\mathbf{r} \to -\mathbf{r}$ is broken in the direction of the pump wavevector $\mathbf{k}_p = (k_p, 0)$, leaving the y-axis symmetry intact.

The probe carrying an $M = 1$ vortex, resonant with the signal for only $2\, ps$ arrives at $t = 0$ (Fig. 5.7c). It triggers a gain that lasts for around $10\, ps$, which is followed by a transient time ($\sim 30\, ps$) during which the imprinted vortex drifts around inside the signal. After the transient time, the vortex settles into a metastable solution lasting around $400\, ps$ (Fig. 5.7d).

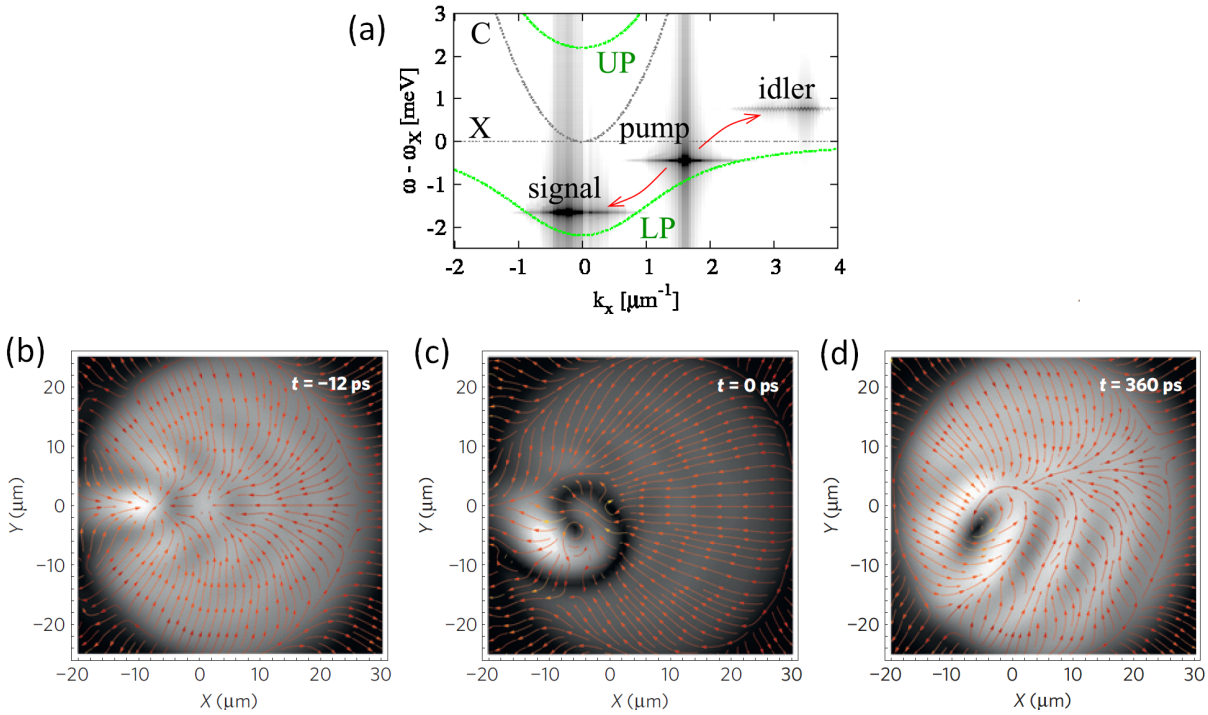

Figure 5.7: (a) Simulated OPO pump, signal and idler states spectrum, before the arrival of the probe, for a pump intensity $f_p = 1.24 f_p^{th}$, where f_p^{th} is the threshold strength for OPO. Lower polariton (LP) and upper polariton (UP) dispersions are marked by green dotted lines, whereas cavity photon (C) and exciton (X) dispersions are plotted as gray dotted lines. Polaritons injected resonantly at the pump state and undergo coherent stimulated scattering into the signal and idler states, which are blueshifted with respect to the bare LP dispersion because of interactions. The spatial profile of the signal state is shown in (b), obtained by momentum filtering in a cone of around $\pm 7°$. At $t = 0$ (c), the pulsed probe carrying an $M = 1$ vortex, resonant with the signal momentum and energy, generates a gain that fades out after about $10\,ps$ leaving an $M = 1$ vortex imprinted into the signal. After a transient time of $\sim 30\,ps$, the vortex settles into a metastable solution (d). The supercurrents are plotted in the frame of the signal. Panel (a) from Ref. [160].

The final state of the metastable vortex strongly depends on the pumping conditions: in some cases, during the transient period, the excited vortex either spirals out of the signal or recombines with an antivortex forming at the edge of the signal. There are also cases where, instead, the imprinted vortex settles into a metastable state, which can last several hundred picoseconds as shown in Fig. 5.7d, and then starts drifting again. If $f_{pb} \geq 0.45 f_p$, it is also possible that the vortex settles down into a position where the OPO signal has the currents pointing inwards, remaining stopped for as long as the simulation is performed ($1.8\,ns$), in this case defining a metastable solution of Eq. 5.8 [160]. Further simulations of the dependence of the vortex solutions on the probe intensity have shown the existence of a threshold in the probe power below which the vortex does not get imprinted into the signal anymore. Thus, the results of the theoretical simulations are in excellent qualitative agreement with the experimental observations.

5.4 Conclusions

In conclusion, we have observed the persistent rotation of polaritons, in a condensate created under OPO excitation geometry, after the injection of a single-quantized vortex, demonstrating the superfluid behaviour in the non-equilibrium polariton systems. The vorticity has been shown to persist not only in absence of the rotating drive, but also longer than the gain induced by the probe, and therefore to be transferred to the OPO signal. Flow persistency is possible even in a simply connected geometry, *i.e.*, without the need of a toroidal trap which pins the vortex, as in the case of atomic condensates.

Different regimes have been investigated. In particular, it has been possible to establish that only under high pump powers and at specific points in the sample the vorticity was transferred from the TOPO to the OPO signal, generating a persistent vortex solution. After the vortex is imprinted into the OPO signal, it has been possible to observe the vortex core slowly drifting, changing in shape and moving with different velocities.

Chapter 6

Onset and dynamics of vortex-antivortex pairs

In the previous Chapter we have shown that the vortex state of an $M = 1$ Laguerre-Gaussian (LG) probe beam can be transferred into a polariton condensate created under OPO excitation. In that case, the extension of the probe is smaller than the size of the vortex-free OPO signal, an hence the single-valued condensate phase has to be continuously linked between the doughnut-shaped region where the vortex is imprinted and the vortex-free condensate region. Imposing a topological defect requires the branch-cut ($-\pi \rightarrow \pi$ phase jump), present in the new vortical state, to terminate where the phase is not imposed by the probe, *i.e.*, at the border between the probe and the OPO signal state. This is only possible if a vortex, with a charge opposite to the injected one, is created at the probe edge. In fact, if we look carefully at Figs. 5.3j,k,r,s, we note that an $M = -1$ vortex actually appears at the left corner of the images. In this section we investigate in detail the mechanisms underlying the appearance of such antivortex and its following up dynamics.

6.1 Numerical simulations

We start with numerical solutions to the two-component Gross-Pitaevskii equation defined by Eqs. 2.42 and 2.43, obtained for similar parameters as those used in the previous Chapter, but considering instead that a static photonic disorder potential $V(\mathbf{r})$ that varies spatially in a $\sim 20\mu m$ scale with $0.1meV$ standard deviation[1].

Figure 6.1a shows the density profile of the steady state signal after the arrival of the probe, together with the currents streamlines, obtained by taking the spatial gradient of the signal phase. The photonic disorder is represented by the contour-level lines in Figs. 6.1c,e. In order to identify vortices by fork-like dislocations in interference images, analogously to what is done in experiments, we plot the intensity of the signal state interfered with the pump state — which has a flat phase imposed by the pumping field — in the right panels of Fig. 6.1. The OPO conditions are chosen to give a vortex-free signal (see Figs. 6.1a,b). The signal currents have a dominant component pointing leftwards and an equilibrium position where all currents point inwards at around $(-8, -14)\,\mu m$.

[1]Note that the presence of the photonic disorder does not change qualitatively our results. Its role is to break the $y \rightarrow -y$ symmetry left by the pump with $\mathbf{k}_p = (k_p, 0)$ and to change the supercurrents accordingly.

In order to reproduce properly multiple-shot experiments, simulations of the time-dynamics are averaged over a thousand times with random relative phase between pump and probe, what is done by considering the external pumping term as

$$P = F_p + F_{pb} e^{i\Phi_{rdm}}, \tag{6.1}$$

where F_p and F_{pb} are defined by Eqs. 5.6 and 5.7, respectively, and Φ_{rdm} is the random relative phase.

In single shot simulations (one realisation of the random phase Φ_{rdm}), we find that if the probe is positioned well inside the OPO signal, then the imprinting of an $M = +1$ vortex (V) at $t = 0$ imposes the system to spontaneously generate, at the same time, an $M = -1$ antivortex (AV) at the edge of the probe (Fig. 6.1d). Equivalently an injected $M = -1$ antivortex (AV) forces the appearance of an $M = +1$ vortex (V) — see Fig. 6.1f. This is a consequence of the continuity of the photonic and exciton wave functions already discussed. However this argument only does not predict the specific position around the probe where the antivortex appear.

When simulating the dynamics following the arrival of a vortex probe for 1000 different random realizations of the relative phase Φ_{rdm}, uniformly distributed between 0 and 2π, we find that the antivortex appear in different locations around the vortex probe. The pink circles in Fig. 6.1c mark the positions where the antivortex appear, with its size being proportional to the number of random phase realizations in which it appears at that specific position. We found out that the antivortices are more likely to appear on positions where the current of the steady state OPO signal before the probe arrival and the probe current are opposite. For example, for a vortex probe $M = +1$ (Fig. 6.1c), the current constantly winds anti-clockwise, therefore, comparing with the OPO signal steady currents (Fig. 6.1a), ones realizes that both currents are mostly anti-parallel in the bottom right region on the probe edge, where is found that very likely an antivortex is formed. Similarly, both currents are parallel in the top left region on the probe edge, where is very unlikely that an antivortex is formed.

In the same way, if the probe carries an antivortex $M = -1$, we expect that the spontaneous vortex is more likely to appear in the top left border of the probe, *i.e.* in a location given by changing (x, y) to $(-x, -y)$ with respect to the previous case. The blue stars in Fig. 6.1e mark the positions where the vortex appear, with its size being proportional to the number of random phase realizations in which it appears at that specific position. The upper left border of the probe containing the highest concentration of big stars confirms ours expectations. Finally, let us note that phase continuity arguments allows the formation of additional V-AV pairs on the probe edge, which are in fact observed in simulations, but are however rare events.

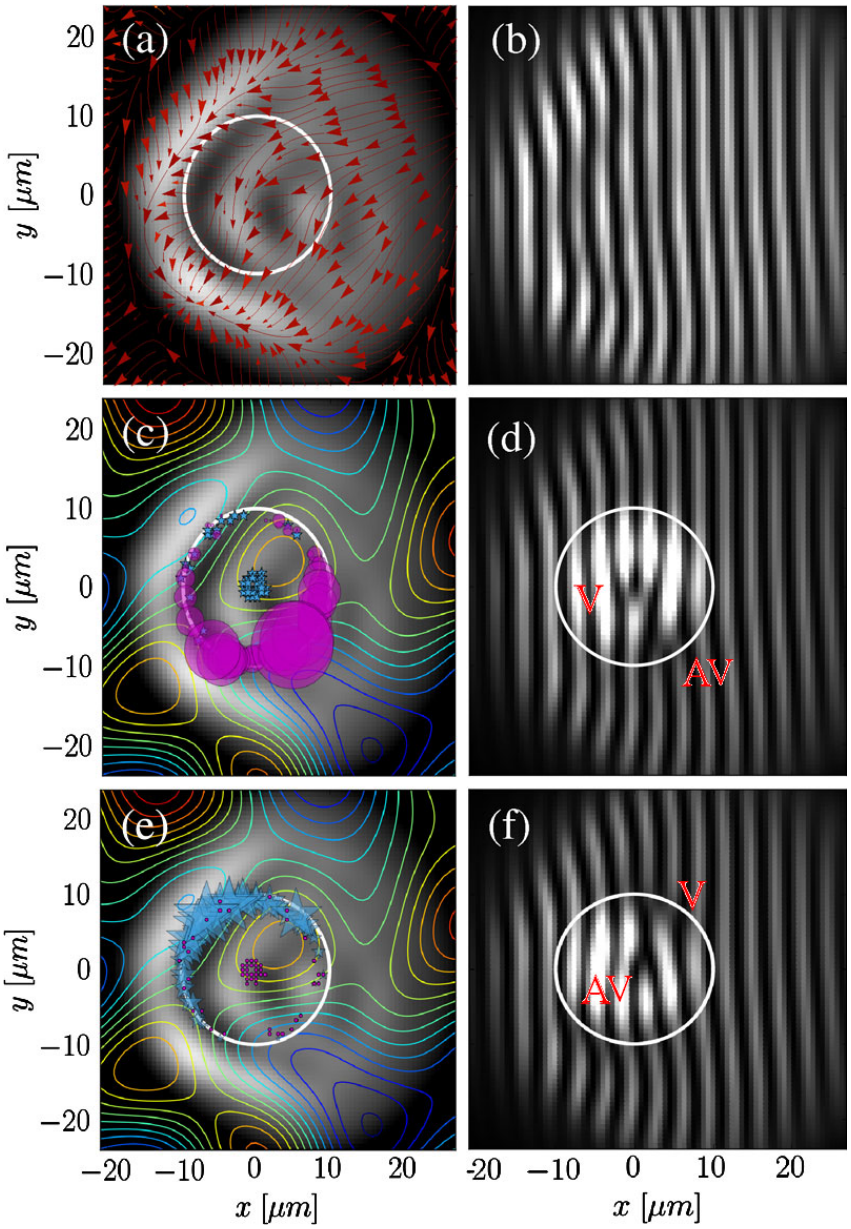

Figure 6.1: Simulated profile and supercurrents of the steady state OPO signal before the arrival of the probe (a) and associated interference fringes (b). Location of (c) antivortices (dots) and (e) vortices (stars) at the arrival ($t = 0$) of (c) a vortex (stars) or (e) an antivortex (dots) probe, for 1000 realizations of the random relative phase between pump and probe. The size of the dots in (c) [stars in (e)] is proportional to the number of times the antivortices [vortices] appear in that location. Panel (d) [(f)] shows single shot interference fringes when the probe carries a vortex [antivortex]. Contour-level lines in (c) and (e) represent the photonic disorder $V(\mathbf{r})$. The white circle represents the edge of the probe.

If we now take the signal wave function, triggered by a vortex probe, averaged over the 1000 realizations, $\langle|\psi^s_C(\mathbf{r},t)|e^{i\phi^s_C(\mathbf{r},t)}\rangle_{\Phi_{rdm}}$, similarly to what is done in multiple-shot experiments, neither the imprinted vortex nor the antivortex can be seen at the probe arrival time $t = 0\,ps$ (see the first column of Fig. 6.2), because on average the differently positioned branch-cuts wash away both phase singularities. However, remarkably, the steady state condensate currents push the V and AV, initially positioned in different

locations, towards the same equilibrium position where all currents point inwards. As a consequence, as shown in the other panels on Fig. 6.2, while at $t = 0\,ps$, on average, we do not see the V-AV pair, after $\sim 10\,ps$ both V and AV appear and last $\sim 75\,ps$, till they eventually annihilate.

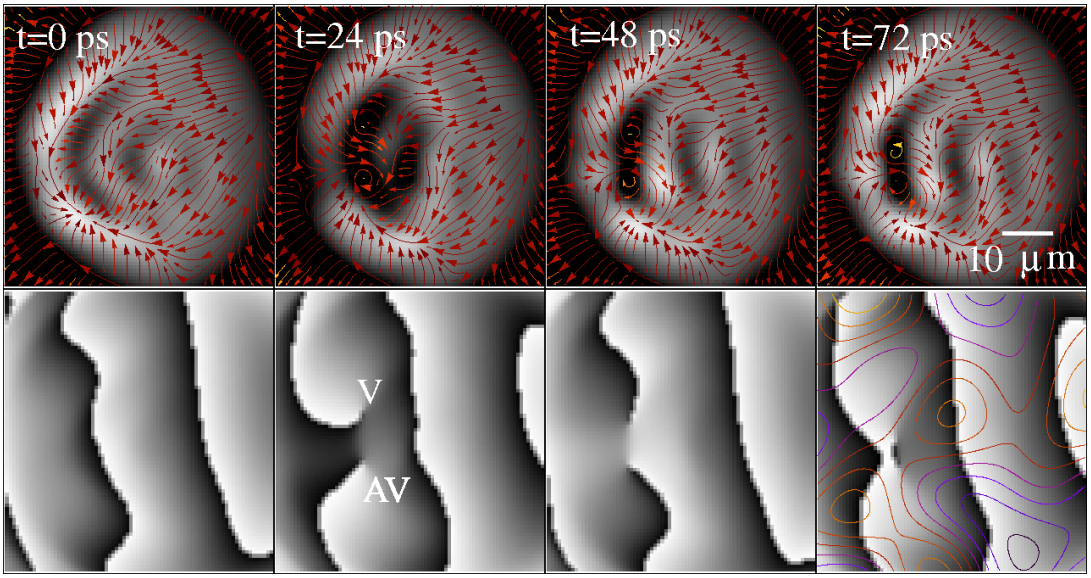

Figure 6.2: Simulated time evolution of signal after the arrival of the vortex probe, averaged over 1000 realisations of the random phase Φ_{rdm}, $\langle \psi_C^s(\mathbf{r}, t)\rangle_{\Phi_{rdm}}$. Spatial profiles of density and currents (top) and phase (bottom). Contour-level lines in the last panel represent the photonic disorder.

6.2 Experimental results

In order to check if the theoretical predictions indeed describe properly the onset and dynamics of V-AV pairs, we perform experiments where the single-QW sample is resonantly pumped, in a region where the photon-exciton detuning is $\delta = -0.7\,meV$, by a CW-laser at $1.528\,eV$ and $k_p = 1.4\,\mu m^{-1}$. Since we are interested in the regime where the vortex is transferred into the OPO signal, which is preferably achieved when the polariton condensate is highly dense, the CW-pump power is set to $450\,mW$. The OPO signal is created at $1.5268\,eV$, $\sim 1\,meV$ blueshifted from the LP bare dispersion.

In order to confirm the role played by the relative currents of probe and OPO signal on the appearance of the unintended antivortex, we inject the vortex probe with a power of $3\,\mu W$, far above threshold for the vortex to be transferred into the condensate, and with finite in-plane momentum with respect to that of the signal. In Fig. 6.3a we plot the momentum distribution of the probe as a function of $\mathbf{k} - \mathbf{k}_{pb}$, indicating with a straight arrow the value of $\mathbf{k}_s - \mathbf{k}_{pb}$. Figure 6.3b shows the real space profile of the probe carrying an $M = 1$ vortex. The relative in-plane momentum between signal and probe means that, sitting in the reference frame of the probe, the OPO signal has a definite homogeneous current (straight arrow in Fig. 6.3b), while the vortex probe has anti-clockwise winding currents.

According to the previous theoretical analysis (see Fig.6.1), we can therefore predict the location of the unintended antivortex, namely where the signal and probe currents are anti-parallel, which is in the upper-right corner of Fig. 6.3b.

In order to measure the time-dynamics of the condensate phase after the arrival of the probe, therefore being available to track the appearance and dynamics of vortices and antivortices, we interfere the region where the vortex is injected with an expanded, flat-phase, part of the condensate by using a Mach-Zhender interferometer. The interferograms are later analysed using Fourier transform techniques in order the extract the condensate phase.

Figs. 6.3c-e show the time-evolution of the condensate phase (now in its own reference frame), after the vortex have been imprinted into it. In accordance to our predictions, the unintended antivortex in Fig. 6.3c appears on the upper-right side of the injected vortex. Despite the many-shot average, the dynamics of the V-AV pair can be experimentally followed after its onset for tens of picoseconds (Figs. 6.3c-e), thereafter the pair eventually annihilates.

If we now invert the topological charge of the probe LG beam (which is done by taking the opposite diffraction order of the pulsed laser beam after the hologram) and inject an $M = -1$ antivortex at the same position and with the same in-plane momentum as in the just described $M = 1$ case, the unintended vortex should now appear at the inverse side of the probe, namely the lower-left corner of Fig. 6.3f, which is where the clockwise currents of the probe are antiparallel to the strait current of the OPO signal. In fact, this is observed in the phase spatial dynamics shown Fig. 6.3g-i, where here the V-AV pair also annihilates at long times.

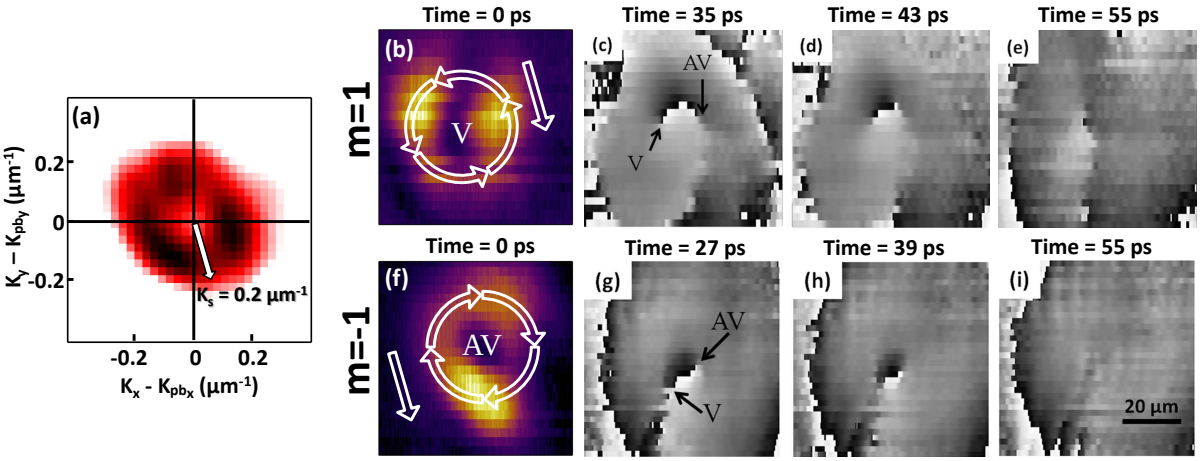

Figure 6.3: Measured momentum distribution of the vortex probe vs $\mathbf{k} - \mathbf{k}_{pb}$ (a). The arrow indicates the signal momentum $\mathbf{k}_s - \mathbf{k}_{pb}$. Panel (b) [(f)] shows the real space intensity profile of the $M = 1$ ($M = -1$) LG probe. The straight arrow in (b),(f) represents the signal current direction in the probe reference frame, while the probe current winds anticlockwise for $M = 1$ (clockwise for $M = -1$). Panels (c)(e) [panels (g)(i)] compile, through phase images, the time evolution of an imprinted $M = 1$ vortex ($M = -1$ antivortex) and its associated $M = -1$ antivortex ($M = 1$ vortex). The unintended antivortex (vortex) appears in (c) [(g)] at the edge of the probe where the signal and probe currents are antiparallel. V-AV pair dynamics can be followed in both cases for about 30 ps, after which they annihilate. The spatial scale of panels (b-i) is indicated in panel (i).

6.2.1 Gaussian probe

We have already shown that vortices are likely to appear where the currents of an injected probe and the ones of the OPO signal counterpropagate. To check that this idea is valid in the more general case where the probe carries no angular momentum, we shine a flat-phase Gaussian probe, with a tunable in-plane momentum, onto a vortex-free condensate, pumped under similar conditions to the ones described at the beginning of this section.

Figure 6.4a shows the spatial profile of a Gaussian pulsed beam shone at rest with respect to the OPO signal, $\mathbf{k}_{pb} \simeq \mathbf{k}_s$. Since in this case no appreciable counterpropagating currents are generated in the condensate, we do not expect any topological defect to be created. Indeed, by inspecting the condensate phase $20\,ps$ after the probe injection, no branch-cut is observed (Fig 6.4c).

Figure 6.4b shows the spatial profile of a Gaussian probe beam injected with a finite momentum with respect to the OPO signal one, $\mathbf{k}_{pb} = 0.5\,\mu m^{-1} \neq \mathbf{k}_s = 0$. Note that tilting the beam implies that its shape is elongated in the direction of incidence (horizontal in the figure). We have chosen the momentum of the probe to be $\mathbf{k}_{pb} - \mathbf{k}_s = 0.5\,\mu m^{-1}$ based on the experimental findings, shown in Fig. 6.3, that conterpropagating currents with a magnitude of $|\mathbf{k}_{pb} - \mathbf{k}_s| \simeq 0.4\,\mu m^{-1}$ were enough to create a topological defect. Since there is a difference in the signal and probe currents in the upper and lower edges of the probe, according to the experiments and simulations described above we expect that vortices appear at such places. More precisely, an anti-clockwise $M = 1$ vortex should appear at the upper border whereas a clockwise $M = -1$ antivortex should appear at the lower border. The dynamics of the condensate indeed agree with the predictions, with its phase, $20\,ps$ after the probe injection, showing a vortex in the upper part and an antivortex in the lower part (Fig 6.4d).

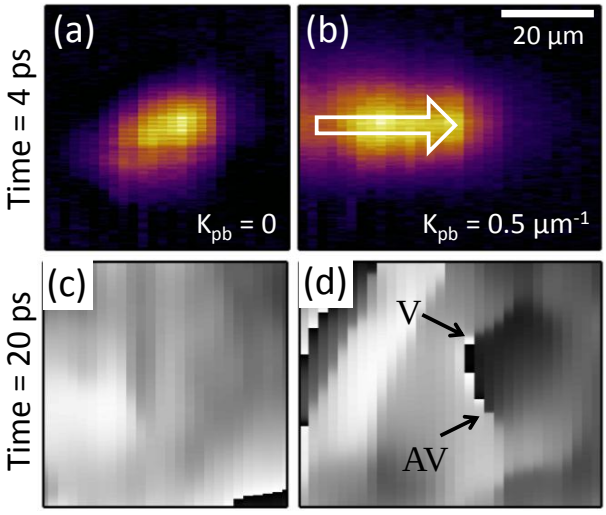

Figure 6.4: Spatial profile of the Gaussian probe at rest $\mathbf{k}_{pb} = 0$ (a) and moving $\mathbf{k}_{pb} \neq 0$ (b) shone on the vortex-free OPO signal. The condensate phase, measured $20\,ps$ after the probe arrival, shows that no V-AV pair is created if the probe is at rest (c), while a V-AV pair appears for a moving probe (d).

6.3 Conclusions

We have demonstrated that unintended antivortices appear in the signal at the edge of an imprinting vortex probe and explained, both theoretically and experimentally, the origin of the deterministic behavior of the antivortex onset and dynamics. In particular, we showed where antivortices are more likely to appear in terms of the supercurrents of the imprinting probe and the currents of the underlying OPO. The theoretical predictions are borne out by the experimental observations. In addition, our study reveals that the onset of vortices in polariton superfluids does not require a LG imprinting beam, but instead vortex-antivortex (V-AV) pairs can also be generated when counterpropagating currents are imposed, similarly to what happens in normal (classical) fluids.

Crucially, via numerical simulations, we elucidate the reason why an experimental average over many shots allows detecting a vortex by direct visualizing the density and phase profiles. Recently, it has been suggested by stochastic simulations [156] that vortices in nonresonantly pumped polariton condensates undergo a random motion which will hinder their direct detection, unless they are close to being pinned by the stationary disorder potential and thus follow a deterministic trajectory [180]. In the case considered here of a superfluid generated by the OPO, we can instead explain a deterministic dynamics of the V-AV pair in terms of the OPO steady state supercurrents, which determine a unique trajectory for the pair, allowing their observation in multishot measurements.

To conclude, the mechanism for V-AV pair formation reported here differs from the V-AV binding-unbinding associated to the Berezinskii-Kosterlitz-Thouless phase transition — see Section 2.3.1 —, recently adopted to interpret the V-AV observation in nonresonantly pumped polaritons [116]. In our case, the pair onset can be explained in terms of the OPO and probe relative currents, a simple mechanism which does not require resorting to phase fluctuations induced by the pump.

Chapter 7

Stability of doubly-quantized vortices

Ignoring interactions, a doubly charged vortex has higher energy than two single vortices [55]. However, including interactions between vortices, the energy of an $M = 2$ vortex turns to be the same as the energy of two $M = 1$ interacting vortices close together [157]. Instability of doubly quantized vortices in a BEC has been observed in several systems (see, *e.g.*, Ref. [181]), but there are only a few examples of their stability, such as in superconductors in the presence of pinning forces [182] or in a multicomponent order–parameter superfluid such as ^{3}He-A [183]. In ultracold atomic gases, stable free $M = 2$ vortices have been theoretically predicted for some range of densities and interaction strengths [184, 185]. Furthermore, they have been observed only in a toroidal pinning potential with an external optical plug [97], which mechanically prevents the persistent flow to undergo any movement, stabilising the $M = 2$ against splitting. However, the doubly-quantised vortex has been demonstrated to split soon after the plug has been removed — see Section 2.4.2.

In this chapter we study, both from experimental and theoretical points of view, the stability of $M = 2$ vortices in out-of-equilibrium polariton condensates. We do not make use of a plug beam, letting the vortices freely move within the pumping spot.

7.1 Experimental results

In order to study the stability properties of an $M = 2$ vortex imprinted into a coherent polariton condensate, we keep the pumping conditions similar to the ones described in Chapter 5, where, at high CW-pump and pulsed-probe powers, a single vortex has been shown to get imprinted into an OPO-created condensate. Fig. 7.1a shows the spatial profile of the OPO-signal state, pumped under similar power, resonance and detuning conditions as the ones used to obtain the condensate depicted in Fig. 5.1i ($\delta_{Ph-HH} \sim -1.3\,meV$, $E_p = 1.5268\,eV$, $k_p = 1.35\,\mu m^{-1}$ and pump power $300\,mW$), interfered with an expanded, vortex-free, region of itself. Note the high-visibility of interference fringes, a necessary condition for a vortex to get imprinted into the condensate, as discussed in Section 5.2. We next shine a $2\,ps$-long pulsed probe containing an $M = 2$ vortex, in resonance with the OPO-signal state ($k_{pb} = 0$). The interference profile at its time of arrival is shown in Fig. 7.1b. Note the double-fork, highlighted by the green dashed lines, present at the centre of the doughnut-shaped probe. In this case, after the vortex gets imprinted into the condensate, it soon splits into two $M = 1$ vortices, seen as two single

forks marked by the green dashed lines in Fig. 7.1c. To confirm that the two vortices are in fact imprinted into the condensate, we show their density profiles at a later time, with the steady-state-background subtracted, in the inset of Fig. 7.1c. The two negative-valued vortex cores are clearly seen, confirming that the CW-pumped condensate contains two spatially-separated vortex units. Interference fringes show forks at the vortices positions (not shown).

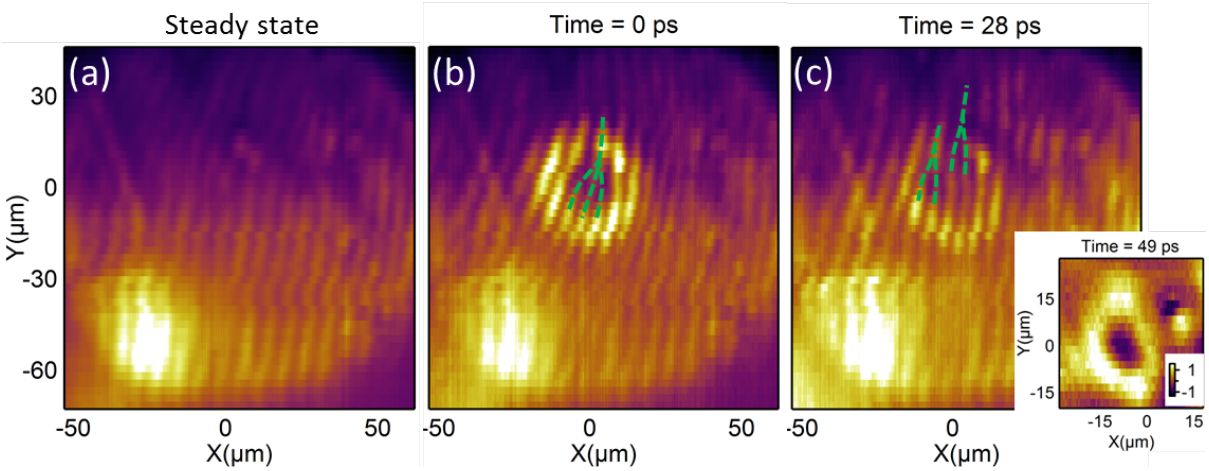

Figure 7.1: Imprinted $M = 2$ vortex time-dynamics (see experimental conditions in the text). (a) Spatial profile of the steady state OPO-signal, interfered with an expanded, flat-phase, region of itself. (b) Interference pattern at the probe arrival time, with its double-fork marked by the green dashed lines. (c) Interference pattern 28 ps after the probe arrival, showing two single forks marked by green dashed lines. The density profile of the condensate 49 ps after the arrival of the probe (with the steady state density subtracted), is shown in the inset of panel (c), for a small region around the vortex arrival point.

The mechanisms underlying the splitting of an imprinted $M = 2$ vortex will be discussed in detail in Section 7.3, but let us already remind that the OPO-signal has a complex structure given by the currents carrying polaritons from loss- to gain-dominated regions. Indeed, these inhomogeneous currents are partially responsible for the fact that the fringes in Fig. 7.1a are not perfectly straight. Therefore, when the $M = 2$ gets imprinted into the condensate, even though it arrives at $k_{pb} = 0$, it feels a net current that destabilizes its structure and splits it up into two $M = 1$ vortices.

It is therefore desirable that the stability of an $M = 2$ vortex can be studied without the presence of a condensate that contains a complex flow structure that always destabilizes the vortex. This can be obtained, as already discussed in Section 5.2, if a vortex is injected into a weakly-coherent polariton population created close to OPO threshold. In this case, the circulation lasts only until the extra population created by the probe is gone, and thus the does not get imprinted into the CW-fed condensate. Moreover, it is possible to find excitation conditions in which the probe triggers a parametric scattering process that lasts for times much longer than the polariton lifetime [18, 140]. Such a regime would be the ideal one to study the dynamical stability of doubly-quantized vortices.

Therefore, we change the excitation conditions in search for a long-lived vortex state not-imprinted into a CW-fed polariton condensate. The microcavity is excited with a

CW-laser [with energy $E_p = 1.5262\,meV$, in-plane momentum $k_p = 1.54\,\mu m^{-1}$ ($\theta_p = 11.5°$) and power $P_p = 65\,mW$], in a region where the photon-exciton detuning is $\delta \simeq -3\,meV$. A pulsed–probe carrying an $M = 2$ vortex (with energy $E_p = 1.525\,meV$, momentum $k_{pb} = 0$ and power $P_{pb} = 3\,\mu W$) triggers an extra population whose density time-evolution is shown in Fig. 7.2a. Note that the extra population lasts for tens of picoseconds while the two density peaks — cross-section of the vortex doughnut shape — remain in the same position. Although the contribution of the steady-state polariton population has been removed, no negative values are observed in between the density lobes, confirming that the vortex is not imprinted into the steady state. Moreover, since the properties of the extra population are inherited from the triggering probe, it is also possible to inject vortices with a finite in-plane momentum. We change the probe momentum to $k_{pb} \simeq 0.5\mu m^{-1}$ ($\theta_{pb} = 3.5°$) and measure the time-evolution of the extra population, shown in Fig. 7.2b. Here, the long-lived polariton state moves towards the right with an approximately constant speed, demonstrating the ability of tuning the flow velocity of polaritonic wavepackets by tuning the probe excitation angle, similarly to what has been done in Ref. [18] but here triggering the parametric scattering at angles and energies smaller than the CW-pump ones.

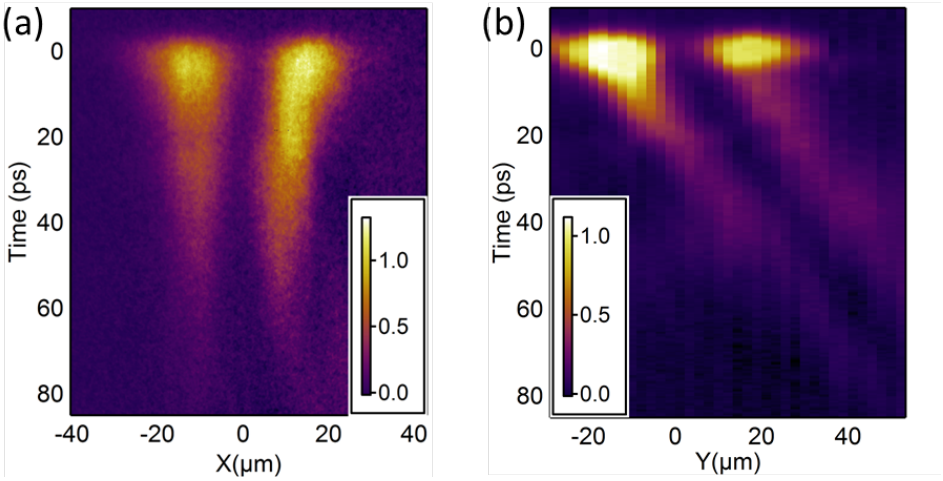

Figure 7.2: Time-evolution of the polariton density triggered by an $M = 2$ vortex probe with in-plane momentum (a) $k_{pb} = 0$ and (b) $k_{pb} \simeq 0.5\mu m^{-1}$, for a cross section through the probe core. The steady state polariton density has been subtracted in both images.

Figure 7.3 shows the time-resolved emission of the full pumping spot region, interfered with an expanded part of itself, for the stopped (first row) and moving (second row) cases, corresponding to Figs. 7.2a,b, respectively. The background steady polariton density has not been removed in any of the images. We first see that, in both cases, practically no fringes are seen in the CW-only steady state (Figs. 7.3a,d), specially in the region around $(0, 0)\,\mu m$ where the vortex is injected. This is required for the vortex to evolve freely without being affected by the complex flow pattern of a macroscopic condensate. We observe that when the vortex is excited at $k_{pb} = 0$, it does not split within its lifetime (Fig. 7.3a-c). However, exciting the signal with a finite momentum, $k_{pb} \simeq 0.5\mu m^{-1}$, thus making it move inside the pump spot, we observe the doubly quantized vortex splitting into two singly quantized vortices, as shown in Fig. 7.3d-f.

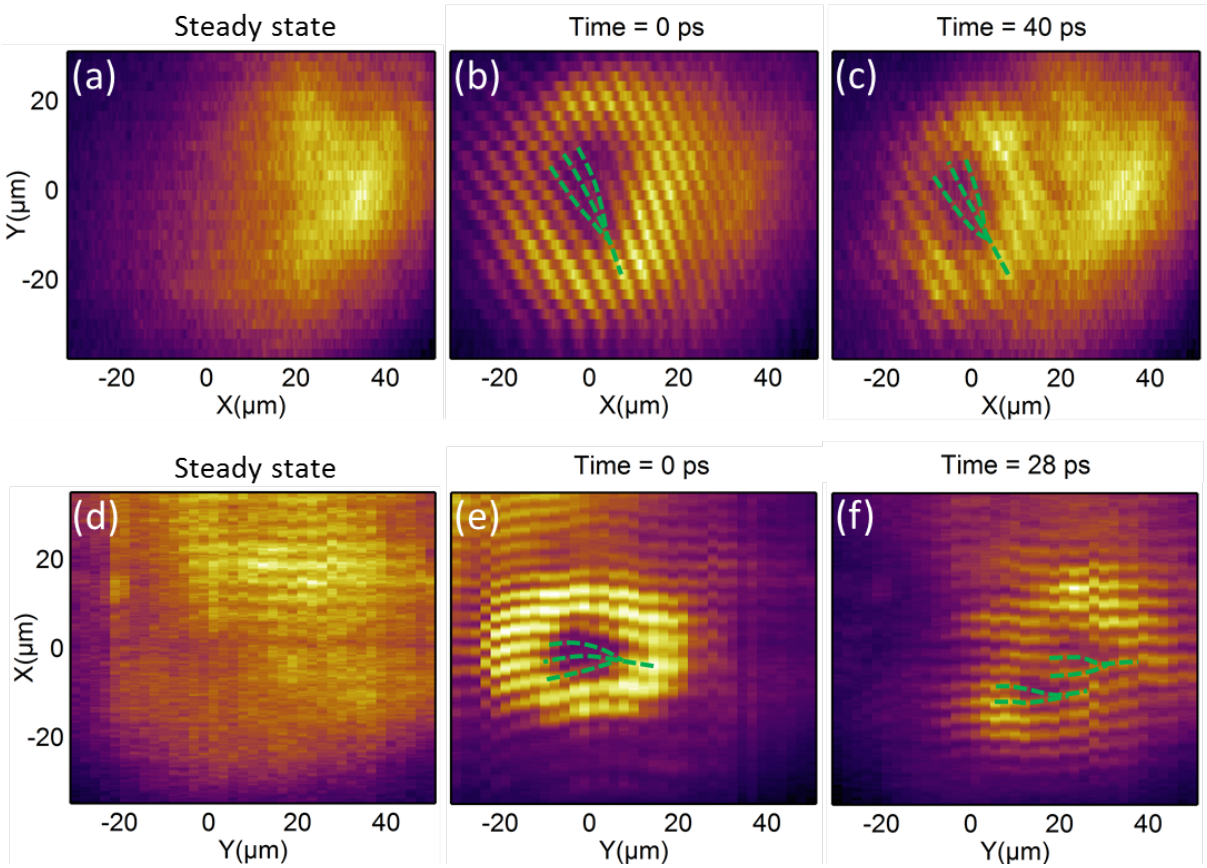

Figure 7.3: Time-dynamics of injected $M = 2$ vortices under excitation conditions in which they are not imprinted into a macroscopic coherent condensate. All the images are obtained by interfering the polariton emission inside the pumping spot with an expanded part of such a region. Panels (a-c)[(d-f)] correspond to excitation by a probe with in-plane momentum $k_{pb} = 0$ [$k_{pb} \simeq 0.5\mu m^{-1}$]. Panels (a,d) show the emission from the CW-only steady state, (b,e) at the probe arrival time, (c) 40 ps and (f) 28 ps after the probe arrival time. Dashed green lines mark (b,c,e) doubly- and (f) singly-quantized vortices. The background steady state density has *not* been removed in any image.

The physical mechanisms underlying the transition between these two stability regimes and their dependence on the injection probe momentum will be discussed in Section 7.3. Before let us compare the experimental results described here with the ones found by numerical simulations.

7.2 Numerical simulations

In order to simulate the time-dynamics of an $M = 2$ vortex imprinted into the OPO-signal, Eq. 5.8 is again numerically solved by using similar parameters as the ones used to obtain the solutions plotted in Fig. 5.7, but now using an $M = 2$ Laguerre-Gaussian probe in Eq. 5.7, instead of an $M = 1$.

Figure 7.4 shows the simulated dynamics of the condensate spatial profile with the $M = 2$ vortex probe arriving at $t = 0$. The $M = 2$ vortex splits into two singly quantised vortices almost immediately when the probe arrives, already during the imprinting process — confirmed by the two $\sim 5\,\mu m$-separated density dips around $(-10, -5)\,\mu m$ in Fig. 7.4b,

where however the currents streamlines plot does not have enough resolution as to resolve each vortex. The two vortices coexist for a short time, after which one is expelled from the condensate, usually annihilating with an anti-vortex present at the signal boundary. The other $M = 1$ vortex stabilises into the signal (Fig. 7.4c), constituting a new metastable solution similar to the one shown in Fig. 5.7d.

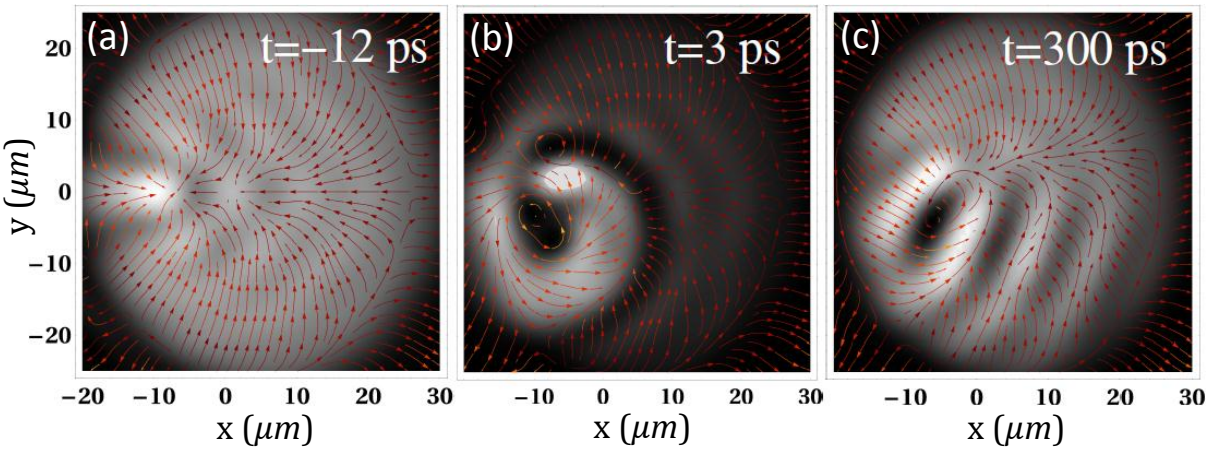

Figure 7.4: Simulated $M = 2$ imprinted regime. Calculated time evolution of the OPO signal emission for an $M = 2$ triggering probe before (a) the arrival of the probe at $t = 0$ and after (b,c), showing the splitting of the imprinted doubly quantised vortex (b) and the stabilisation of an $M = 1$ vortex into the signal. The supercurrents are plotted in the frame of the signal.

In order to numerically simulate the evolution of an $M = 2$ vortex not imprinted into the OPO-signal, the pumping strength f_p is set to be below the OPO threshold and the pulsed probe is shone resonantly with the linear LPB dispersion — more details of parameters are given in Refs. [157, 186].

Figure 7.5 shows the time evolution of the TOPO $M = 2$ vortex when injected by a probe at $k_{pb} = 0.1\,\mu m^{-1}$ (first row) and at $k_{pb} = 0.7\,\mu m^{-1}$ (second row). The simulated dynamics shows that the $M = 2$ vortex is stable in the first case — note that the currents wind around the same single core in Fig. 7.5b —, whereas it splits in the second case — the currents wind around two different points, separated by $\sim 10\,\mu m$, in Fig. 7.5d. Moreover, simulations performed using different probe momenta show that a doubly-quantized TOPO vortex is stable if injected with in-plane momentum below a critical value, k_{pb}^{cr}, above which the moving vortex always splits.

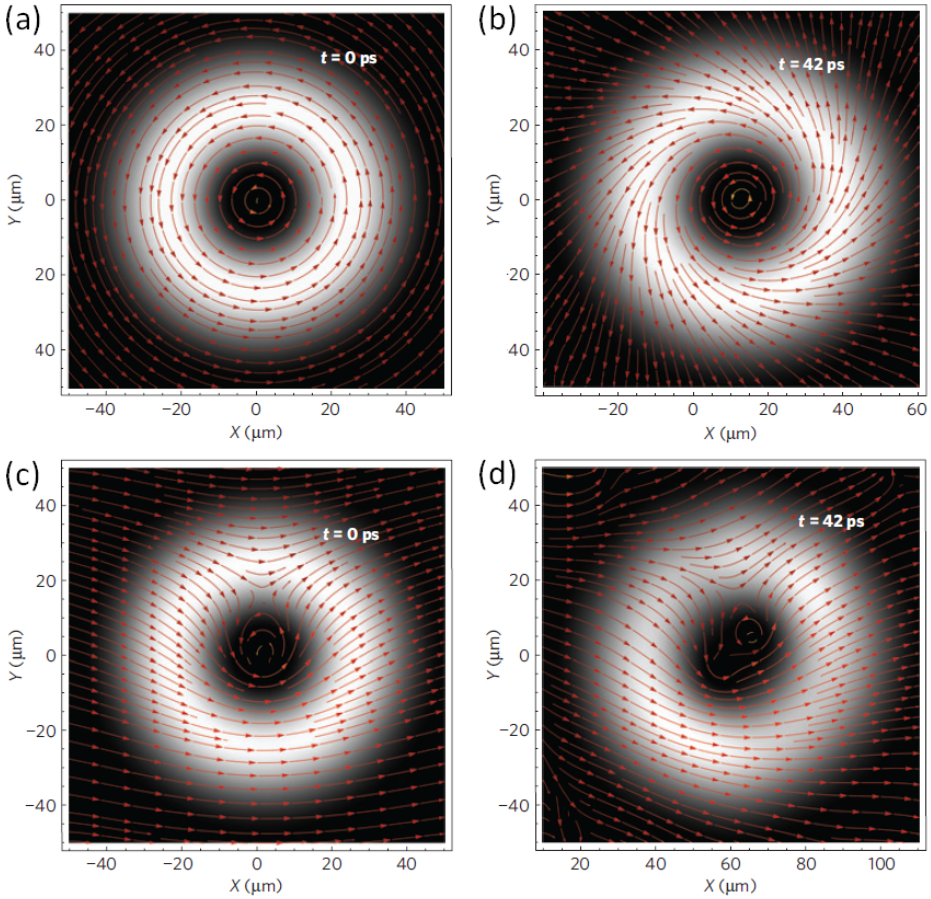

Figure 7.5: $M = 2$ simulated not-imprinted regime. Calculated TOPO signal emission for an $M = 2$ triggering probe at $k_{pb} = 0.1\,\mu m^{-1} < k_{pb}^{cr}$ (a,b) and at $k_{pb} = 0.7\,\mu m^{-1} > k_{pb}^{cr}$ (c,d) at the arrival time of the probe, $t = 0$ (a,c) and $42\,ps$ later (b,d). The currents are plotted in the frame of the moving vortex.

7.3 Splitting mechanisms

We discuss here the physical mechanisms involved on the splitting of an injected $M = 2$ vortex in OPO polariton condensates.

The OPO is a steady-state regime, where the pump, signal and idler states are time-independent. This is also recognizable in the typical flat dispersion of signal, idler, and pump PL spectra (see Figs. 5.1c,d and 5.7a). The OPO-signal (and -idler, -pump) group velocity, defined by the derivative of the dispersion $\mathbf{v}_g = \partial_{\mathbf{k}} E/\hbar$ at $\mathbf{k}_{pb}$, is therefore zero.

On the other hand, the spectrum of the TOPO regime is linear, with a finite and equal slope for the probe and conjugate states [18, 186], which can be explained by the fact that, to have efficient parametric scattering, a large spatial overlap between both states is required and so their group velocities lock to the same value. By analysing the time–evolution of the spatial profile of the TOPO signal, it is found that its group velocity $\mathbf{v}_g$, given by the velocity of its density maxima, is simply given by the derivative of the LPB dispersion in the linear regime, evaluated at $\mathbf{k}_{pb}$ [186]. This is shown in Fig. 7.6a, in which the red line show the group velocity of a TOPO-wavepacket calculated by taking derivatives of the simulated LPB dispersion, perfectly matches the black points which correspond to the the wavepacket group velocity.

Moreover, because of the dynamical nature of the TOPO state and the loss of polariton population, the system evolves between different regimes. In particular, only in the strong amplification regime, at early times, is the spectrum linear, while it evolves back to the LPB at longer times [186].

Let us start discussing the case of imprinted vortices. When an $M = 2$ vortex is injected into a macroscopically occupied condensate created above OPO threshold, the OPO signal dispersion goes from flat to linear, becoming flat again once the vortex gets imprinted. This complicated evolution of the dispersion causes structural instability and splitting of the vortex during the transient time [186]. Another reason for the structural instability is the aforementioned non-uniformity of signal currents — caused by the interplay between spatial inhomogeneity, pump and decay –, which the OPO vortex experiences in its reference frame.

In contrast, for the case of non-imprinted vortices — when the $M = 2$ vortex is injected in the TOPO regime —, numerical analysis shows that the crossover from non–splitting to splitting happens for a critical probe momentum k_{pb}^{cr}, where the LPB dispersion deviates from quadratic [186], which corresponds in Fig. 7.6a to values of k_{pb} for which the red line deviates from the dashed green line, which represents the derivative of a parabolic fit to the LPB. This can be understood as follows: just after the arrival of the probe, the TOPO linear dispersion yields a soliton–like behavior, with the signal and conjugate propagating and not changing shape or intensity. When parametric amplification vanishes, the wavepacket dispersion comes back to the LPB one. For quadratic dispersion, propagation is analogous to the ballistic time-of-flight expansion of ultracold atomic gases, i.e., the wavepacket size grows in time, but its shape is preserved. A uniform expansion of the wavepacket leads to an increase of the vortex core but does not cause the vortex to split. In contrast, if the LPB dispersion deviates from quadratic, propagation becomes complex and the wave packet gets distorted. This distortion during the propagation, very pronounced at later times of the evolution, leads to the mechanical splitting of the $M = 2$ vortex, analogous to the structural instability discussed in Ref. [187].

We briefly discuss now the experimental results related to the splitting of an $M = 2$ vortex. The red line in Fig. 7.6b shows the derivative of the experimental LPB dispersion for the conditions in which the data showed in Fig. 7.3 have been taken. The two black dots are the velocities of the vortex cores in Figs. 7.2a,b, which perfectly matches the red line. Note that the right-most black dot correspond to a regime where the LPB dispersion starts deviating from parabolic (the red curve starts deviating from the green dashed line), which is the reason we attribute to the splitting of the $M = 2$ vortex seen in Figs. 7.3.

We also investigate a second mechanism that could be the reason for the existence of a critical velocity for the vortex splitting in the TOPO regime. When inspecting the currents distribution in Fig. 7.4, plotted in the moving packet reference frame, we note that, whereas in the top panels the currents are radially symmetric, in the lower panels they have a main component pointing to the right direction. In the latter case, the propagating vortex feels a rather strong net current in its own frame, which may provide an additional explanation for splitting.

Reminding that the polariton effective mass is given by $\mathbf{m}^* = \hbar^2 \left(\nabla_{\mathbf{k}}^2 E\right)^{-1}$ and noting that $\nabla\phi = \mathbf{k}$, Eq. 2.31 can be written as

$$v_s = \hbar^{-1} \nabla_{\mathbf{k}}^2 E \cdot \mathbf{k} \tag{7.1}$$

We have calculated, using the experimental fit to the LPB dispersion, the dependence

of the flow velocity, v_s, on the probe momentum. The result is plotted as a blue line in Fig. 7.6b. We note that the critical momentum for which the flow velocity deviates from the group velocity approximately coincides with the LPB losing the parabolic character- Therefore, when created above k_{pb}^{cr}, a moving $M = 2$ TOPO vortex feels a net current that causes it to split.

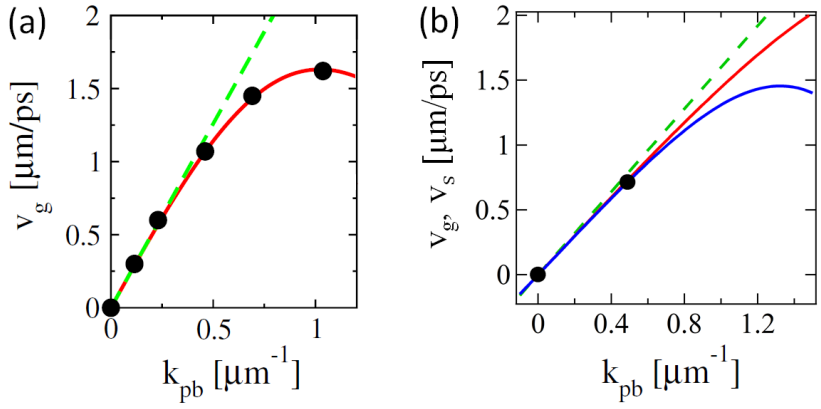

Figure 7.6: Dependence of the group velocity of a TOPO wavepacket, v_g and as function of the probe momentum k_{pb}. Red line is the derivative of the (a) simulated and (b) experimental LPB dispersion, evaluated at k_{pb}. Green dashed line is the derivative of a parabolic fit to the LPB. Black dots are the group velocity v_g of the propagating signal wave packet, (a) determined from simulations and (b) experimentally measured, versus the probe momentum k_{pb}. Blue line in (b) shows the flow velocity, v_s, evaluated using Eq. 7.1 with the effective mass extracted from the experimentally fitted LPB. Panel (a) adapted from Ref. [186]

7.4 Conclusions

In this chapter we have investigated the dynamical stability of $M = 2$ vortices created in polariton OPO condensates. Three different behaviours have been found depending on the excitation conditions. In cases for which the vortex is imprinted into the signal steady state, it always splits into two $M = 1$ vortices. On the other hand, when the vortex is not imprinted in the steady state but lasts only as long as the amplification induced by the probe, an $M = 2$ vortex is stable when excited below a critical k_{pb}^{cr} value, or splits into two $M = 1$ vortices when the vortex is injected with a probe at higher momentum.

Part IV

Non-resonantly excited polariton condensates made to interact

Introduction

The first indications of spontaneous macroscopic coherence in microcavity polaritons out of a thermal distribution of particles appeared when pumping high-quality samples with tiny pump spots, in which case a non-linear increase of the polariton luminescence [102] was observed in a finite k-ring in momentum space exhibiting spontaneous coherence [105]. The quest for ground-state thermalised condensation has motivated the use of bigger pump spots [15, 106, 131], which became the predominant ones in the subsequent investigations of polariton quantum fluidics [18–20, 114–116, 188]. The successful fabrication of high-quality *AlGaAs*-based microcavity samples motivated the resurgence of pumping geometries using tightly focused beams, which have been shown to produced extended outflowing polariton condensates [109, 110] that can be easily manipulated optically within semiconductor chips.

In this part of the thesis we report on the fully-optical control of outflowing condensates in two-dimensional high-quality microcavities [37] — see Chapter 8. Going a step further, we put two or more of such non-resonantly created condensates to interact, giving rise to many different pattern formation structures, including ladders of energy states, in a realization of the quantum harmonic oscillator [31] — Chapter 10 —, and stable interference patterns containing lattices of vortices [32] — Chapter 9. We demonstrate that quantum fluidic circuits can be thus created on the fly using suitable pump configurations.

The interaction between spatially-separated polariton condensates has received special attention in the last years, with many different phenomena reported such as mode-locking between trapped condensates [132], coherent linear [189] and non-linear [190] Josephson oscillations, self-trapping [190] and condensation in photonic molecules [191]. In our results, however, the interactions between condensates happen in a different scenario. Instead of being trapped and interact via tunnelling phenomena, the condensates spatially overlap and mode-lock to create a single condensate, pumped at different positions but described by a single macroscopic wavefunction.

We also present different results where it is important the concept of a *dark-soliton*, which are zero-density solutions of the complex Ginzburg-Landau equation, with a π-phase jump at the density minima. Here they appear either spontaneously as an oscillating wavepacket confined between two harmonic blueshift–"hills" — see Chapter 10 —, or are imposed by the interference of counterpropagating polariton flows — see Chapter 9. In both cases we discuss the stability of such dark-solitons and its relation with non-linear optics [192, 193] and in BECs with repulsive interactions [194, 195].

All the results have been achieved in PhD stay, sponsored by the Spanish Ministry of Science and Innovation, at the *Nanophotonics* group, leaded by Prof. Jeremy J. Baumberg, in the University of Cambridge. The experiments have been performed by the author of this thesis with the invaluable help of Dr. Gabriel Christmann. The simulations have been carried out by Prof. Natalia G. Berloff from the Department of Applied Mathematics and Theoretical Physics, also in the University of Cambridge. All the results have a strong input from the ideas of Prof. Jeremy Baumberg. The author also thanks discussions on the data analysis with Carlos Antón and Prof. Luis Viña.

The sample used is a high quality factor ($Q > 16000$) *AlGaAs*-based microcavity containing 12 *GaAs* quantum wells, and exhibiting a $11.2\,meV$ photon-heavy-hole Rabi splitting — see Section 3.2. A wedge in the sample thickness allows the detuning between the cavity mode and the heavy hole exciton to be varied. All data presented use a negative

cavity detuning ranging from -6 to $-3\,meV$.

Chapter 8

Outflowing condensates

Controlling the propagation of coherent matter-waves has been sought for many years in cold atom systems, where the condensate is released from its trapping potential and expands [7–9] and/or fall subject to gravity [196].

Moreover, the successful implementation of fully quantum mechanical rules in order to build the so-called quantum computers will be based on propagating information without loosing its coherence, which is s necessary ingredient to scaling up multiple-qubit[1] logical operations [197].

Here it is shown that in semiconductor-based polariton condensates, this coherent manipulation is made in-situ by the pumping laser beam. A spatial tiny pumping field is found to create an outflowing condensate coherent over tens of microns on a chip. It is shown how the condensate chemical potential and flow can be tunned by the driving field power.

8.1 Spontaneous long-range order

We first excite the multiple-QW sample, described in Section 3.2, with a CW-laser focused into a $1\mu m^2$ spot. To prevent any coherence from the laser beam to be transferred into the polariton condensate, the pumping energy is tuned to the first Bragg mode above the cavity energy, creating a hot electron-hole plasma that cools down to polariton reservoir modes after loosing energy through multiple scattering with lattice phonons – see section 2.5.1.1. Under low pump powers, the pumping region emits a weak broad-band phololuminescence (Fig. 8.1). As the excitation power approaches $\sim 10\,mW$ an abrupt increase of the polariton emmission is observed together with a sudden collapse of the energy distribution to a single energy mode with decreased linewidth. Moreover, as seen in the two real-space images at the top of Fig. 8.1, below $\sim 10\,mW$ the PL comes mainly from a small spatial region that corresponds to the pumping spot, whereas above such threshold the emission from the bosonic-stimulated single mode comes from a spatial region covering tens of microns, much bigger than the pumping spot size.

[1] A quantum bit (qubit) is a two-state quantum mechanical system that serves as the a unit of quantum information – the quantum analogue of the classical bit.

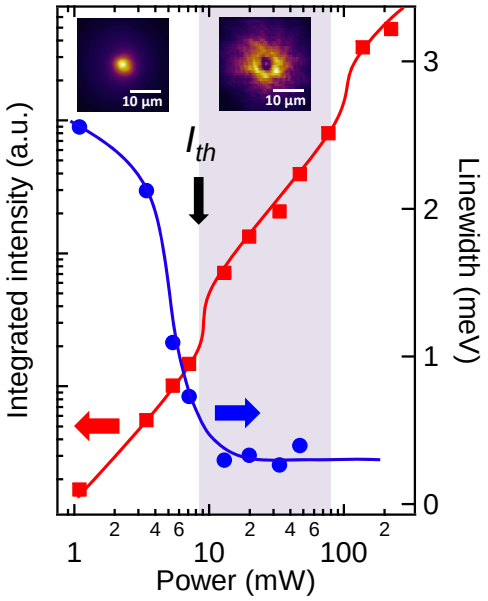

Figure 8.1: Integrated polariton emission intensity (red squares, left axis) and linewidth (blue circles, right axis) *vs* pump power; insets are real space emission images below (left) and above (right) condensation threshold ($9\,mW$). Blue and red lines are guides to the eye. Light-shadowed region corresponds to a single-mode, narrow-linewidth, polariton condensate.

An important feature of a macroscopic coherent state is the appearance of long range order, meaning that two distant points will be mutually coherent and so have a fixed phase relation. This characteristic is directly related to the first order correlation function between two equidistant points of a condensate with respect to its centre, $g^1(\mathbf{r}, -\mathbf{r})$, which has been used as a landmark of spontaneous coherence [15, 117].

In order to confirm that the transition to a macroscopically occupied single energy mode is accompanied by a build up of long range order, we pump the sample at $20\,mW$ and interfere the sample emission with an inverted image of itself by using a Michelson interferometer in the retroreflected configuration – see Section 4.3.1 for details on the setup. The resulting interferogram is shown in Fig. 8.2a, where the condensate has been retroreflected with respect to the pumping spot at $(0, 0)\,\mu m$. Figure 8.2b shows the coherence function, $|g^1(\mathbf{r}, -\mathbf{r})|$, extracted after applying Fourier transform analysis – see Section 4.3.2 – to the interferogram. The image clearly shows the condensate is coherent over tens of microns[2]. The observed cross-like symmetry is probably due to an asymmetry in the condensate polarization which depends on the propagation direction[3]. In the rest of the data presented in Part IV, in order to avoid polarization-related phenomena, we made sure that such an asymmetry is not present by using different locations on the sample.

[2]The low coherence in the centre is due to a broadband emission at the pump spot position

[3]It has been recently shown that the circular polarization of an ouflowing polariton condensate has a four-fold circular symmetry due to the optical spin hall effect [198]. Since this symmetry is inverted in a retroreflected image, the four diagonal low coherence regions in Fig. 8.2b represent interferences between orthogonal circular polarization, yielding no fringe visibility.

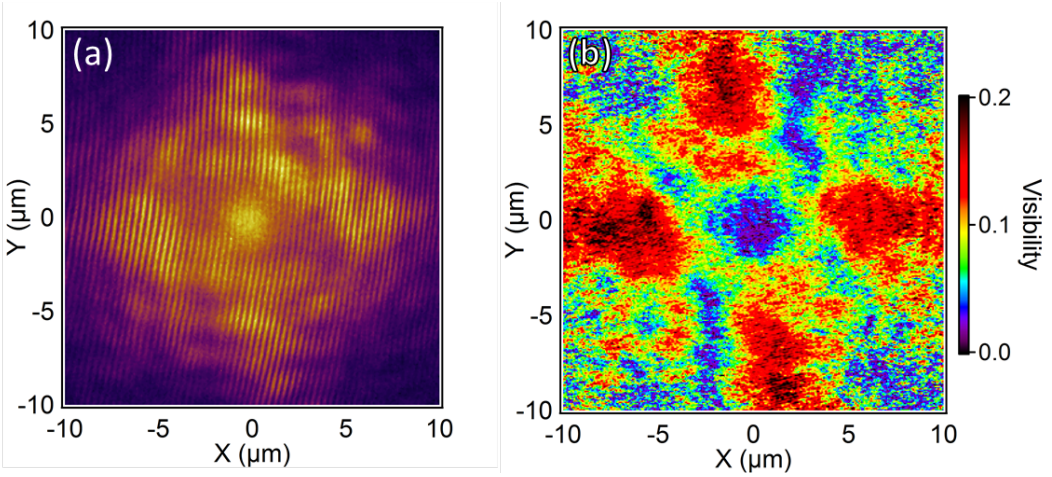

Figure 8.2: (a) Interference fringes between a polariton condensate, non-resonantly pumped by a $\sim 1\,\mu m$ spot at $(0,0)\,\mu m$, and a retroreflected, with respect to the pump spot, image of itself. (b) Extracted $|g^1(\mathbf{r},-\mathbf{r})|$

The fact that an spatially-extended polariton condensate can appear out of a tiny pumping spatial region is quite astonishing and was only observed a couple of years ago, after the appearance of new-generation samples with extremely weak disorder [110]. In the following section we discuss the physical mechanisms underlying the creating of such macroscopic quantum fluids.

8.2 Shaping polariton potential and flow

Polaritons are highly nonlinear quasiparticles: they experience strong mutual repulsion resulting in energy shifts to higher energies (blueshifts) wherever the density is high [15, 31]. We investigate the energy dependence of the condensate photolominescence for different polariton densities, N (Fig. 8.3). Since excitons have a small diffusion coefficient, the polariton reservoir is mainly concentrated is the small pumping spot region. Such a radially-decaying polariton density creates a radially-dependent energy shift $\Delta(r)$, which defines an optically-controlled potential landscape. This effect can be clearly seen at high pumping powers (Fig. 8.3c): near the pump spots, the emission is suppressed for energies below that of the condensate, Δ_0, which depends on the polariton density.

The polariton condensate is created at the top of the curve depicting the blueshift (thick dashed-dotted in Fig. 8.3c), $\Delta(0)=\Delta_0$, with energy $E_c = E_{LP}+\Delta_0$, where E_{LP} is the polariton energy for vanishing densities, and suffers an outwards force given by $F = -\partial_r[\Delta(r)] = \hbar\partial_t k$. As polaritons outflow from the pumping spot, their potential energy $\Delta(r)$ is converted into kinetic energy making polaritons to be ejected radially [110]. The condensate, being described by a single wave function, cannot decelerate simultaneously all around the ring through single local scattering events, thus the macroscopic states maintains is energy constant while outflowing.

Such an outflowing condensate can only be created in new-generation $AlGaAs$-based microcavity samples, where the reduced strain between layers allow for growing DBR-mirrors with very weak photonic disorder and high reflectivity. Coherent polaritons are then capable of propagating over distances of many microns with high speed before decaying into photons. In $CdTe$-based samples, polariton condensation at finite-momentum states has been reported [105], and its existence has been theoretically explained as a

consequence of the small pumping profiles used in the experiments [199]; however, in this case, the strong sample disorder prevented the observation of an spatially-extended condensate.

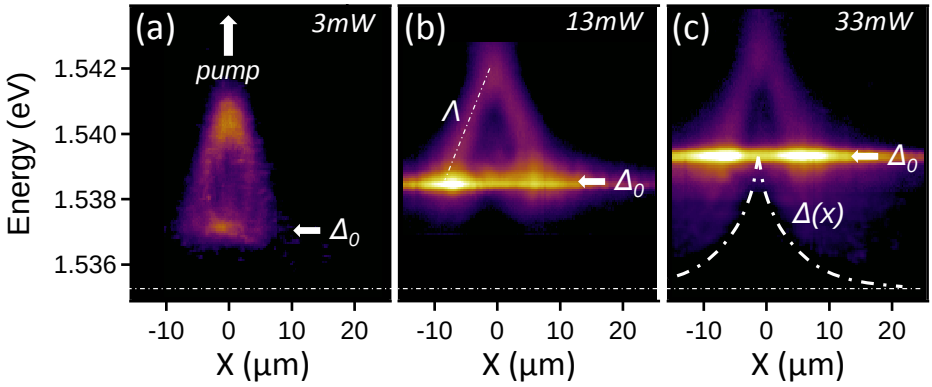

Figure 8.3: Spectra emitted at different distances from the pump spot, for three different excitation powers (colours in log scale). Horizontal dashed line is the nonblueshifted energy (E_{LP}), $\Delta(x)$ is a schematic representation of the blueshift at each spatial point, Δ_0 being the blueshift at the pump spot. The Λline is a guide to the eye for the spatially dependent reservoir intensity maxima – see Section 11.1

The polariton acceleration mechanism can be better understood using the momentum space picture. By placing two lenses with same focal length at the emission far field and an iris between the two lenses, at the common focal plane, it is possible to take the dispersion of a small spatially selected region – see Section 4. Doing so for a $10\mu m$-diameter circle centred at the pumping spot, the condensed emission is observed at in-plane $k = 0$ at the bottom of a blueshifted lower polariton branch (LPB) (Fig. 8.4a). As the small spatial filter is gradually moved away from the pump spot, the dispersion emission peak keeps its energy but gains a finite momentum as the LPB red-shifts (Fig. 8.4b), eventually reaching its maximum value at a distance $\sim 10 - 15\mu m$ (Fig. 8.4c,d), where the reservoir density becomes small and the LPB dispersion goes to it unshifted value. Therefore, the farther the filter is placed from the pump spot, the higher is the condensate momentum and the lower the dispersion bottom, in a clear indication of the blueshift-induced acceleration mechanism. These observations form the 2D counterpart to that observed in 1D polariton wires [110], leading to the formation of condensates with circular symmetry extended over $> 100\mu m^2$.

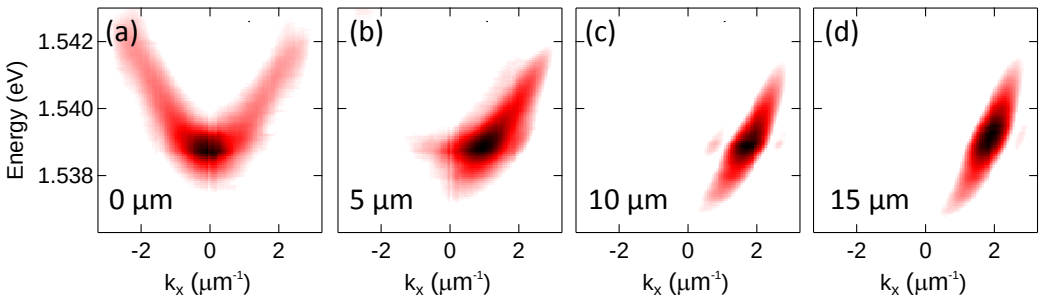

Figure 8.4: Measured dispersion emission, when pumping with $\sim 15\,mW$, filtered in near-field through a $10\mu m$-diameter pinhole whose distance from the pumping spot is indicated at each panel. Colours are in log scale.

It follows that the condensate wavefunction cannot be described by a single momentum state, as accelerating polaritons in each radial direction have varying momenta $k_c(r)$ set by the position dependent blueshifts:

$$k_c(r) = K[E_{LP} + \Delta_0 - \Delta(r)], \tag{8.1}$$

where $K[E]$ is the inverse dispersion relation, $K(E) \approx \sqrt{2m(E - E_{LP})}/\hbar$ for small k. Instead the condensate wave function is a superposition of different k_c states at different radial positions,

$$\psi(r,t) = e^{ik_c(r)r - i(E_{LP}+\Delta_0)t} e^{-\tau/\tau_c(r)} g(r) \tag{8.2}$$

where τ_c is the polariton decay time, and τ is defined below. The amplitude $g(r)$ takes into account the pronounced radial dependence of the emission intensity from the ring around the pump spot (right inset on Fig. 8.1), which is related to an outflowing high-k incoherent reservoir that is converted by stimulated scattering into the coherent expanding condensate of Eq. 8.2 at the ring radius – see Section 11.1. As the condensate expands, its velocity changes so that the distance r is reached after a time τ,

$$\tau(r) = \int_0^r \left. \frac{dK(r')}{dE} \right|_{E_c} dr' \tag{8.3}$$

This unusual condensate thus has a wave vector that varies with radial position. The dispersion of the full condensate is then a single energy state occupying a wide momentum distribution ranging from $-K[E_{LP}+\Delta_0]$ to $K[E_{LP}+\Delta_0]$ (Fig. 8.5a for a power of $13\,mW$), which corresponds to the sum of panels as those shown in Fig. 8.4. It has two intense peaks at $-K[E_{LP}+\Delta_0]$ and $K[E_{LP}+\Delta_0]$ since the main condensate emission comes from polaritons propagating at maximum speed (the accelerating region is small compared to the condensate size).

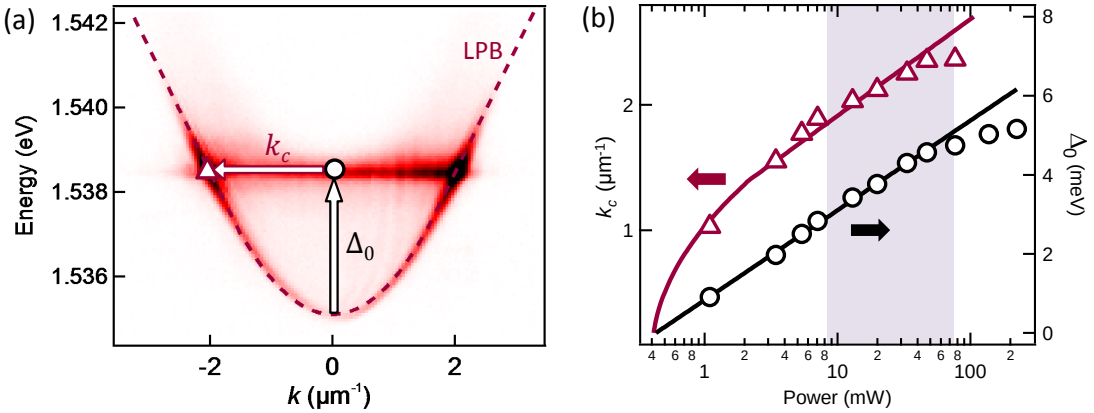

Figure 8.5: (a) Dispersion image of the full sample photoluminescence, pumping with $13mW$, just above condensation threshold. Purple dashed line is a fit to the lower polariton branch, Δ_0 the blueshift at the pump spot and k_c the maximum momentum achieved by the outflowing condensate which is the main peak in the dispersion. (b) Blueshift at pumping spot (Δ_0 – black cirles) and condensate maximum momentum (k_c – purple triangles) dependence with power. Black line is a logarithmic fit to Δ_0 up to single-mode condensation break-up ($80\,mW$) and purple line is found when taking the wave vector k_c corresponding to each energy Δ_0 given by the black line, by using the inverse dispersion relation from (a), $K[\Delta_0]$

By increasing the excitation power the reservoir population is increased, which also increases the interaction-dependent blueshit. We observe a remarkable logarithmic increase of the blueshift at the pumping spot for up to $\sim 80\,mW$ excitation power (black circles in Fig. 8.5b), with no abrupt increase of the blueshift at the condensation threshold, as opposed to previous results [200]. This is probably due to the fact that, once created, the condensate is fast ejected from the pump spot, so its density at the pumping spot is negligible as compared to the reservoir one, which is thus mainly responsible for the observed blueshift.

At $\sim 80\,mW$, the blueshift start increasing sub-logarithmically. This fact, together with the second non-linear increase of the polariton PL, at the same power, observed in Fig. 8.1, is related to the appearance of a second macroscopic outflowing mode as it will be discussed in Appendix 11.4.

We can therefore tune on the fly the repulsive potential seen by polaritons in a simple way, just by changing the excitation power, paving the way towards the confinement of macroscopic wavefunctions, as will be discussed in Chapter 10.

The maximum outflowing speed achieved by the condensate, $k_c = K[E_{LP} + \Delta_0]$, set by the LPB dispersion inverse value at the blueshited energy, is also tuned by the excitation power (see purple triangles in Fig. 8.5b), since it depends on the blueshift at the pump spot. In this way a wide range of flow speeds can be chosen in the polariton fluid. Although such a control can also be achieved under resonant-excitation geometries [18,19], here the phase of the fluid is not imposed by the pumping field, but rather chosen spontaneously by the condensation mechanism itself.

8.3 Conclusions

We have reported on a nonlinear polariton emission increase under increasing pump power while staying in the strong coupling regime. Spatially-resolved spectroscopy showed a local blueshift of the $k = 0$ condensate emission at the pump spot position, while the energy of the condensate remains the same all over its extension. The condensate has $k = 0$ at the pump spot and gains momentum as it flows away from it, revealing polariton propagation.

In the following chapter we make use of the all-optical control of polariton flow in 2D chips discussed here to create different coherent flow patterns that contain standing waves and vortex lattices. Chapter 10 uses the ability to manipulate the confining potential in order to generate confined polariton quantum oscillators.

Chapter 9

Geometric phase-locking and Vortex lattices

Polaritons provide a semiconductor bosonic plattaform with extremelly light mass and huge non-linearities. Up to this point of the thesis, different ways of condensing polaritons injected by a single pump spot have been presented. The following step is to check how two or more independently created condensates interact.

9.1 Mode-locking and stable in-situ interferences

Mode-locking of different polariton condensates has been studied when pumping non-resonantly with a big single pump spot [132]. In this case, different polariton condensates, created by the same large-area laser beam and trapped inside defects originating from disorder, were shown to phase lock to produce a single condensate with extended spatial coherence. The locking is due to Josephson tunnelling between the trapped condensates [201].

In the experiments carried on during this thesis, the sample has very low disorder and the condensates can propagate freely. Instead of being trapped, they are formed on the top of blueshift-induced potentials, so no Josephson physics between condensates separated by tunnelling barriers appear here. We rather study how two or more condensates placed spatially close to each other interact.

First, we incoherently and continuously pump the microcavity sample with two $1\mu m$-diameter lasers $40\mu m$ apart [placed at $(-20, 0)\,\mu m$ and $(20, 0)\,\mu m$ in Figs. 9.1a,c,e]. The two laser beams come from the same laser by splitting it into two in a beam-splitter placed before the focusing objective lens. We start equally increasing the excitation power at each pump spot. Just below condensation threshold ($\sim 15\,mW$), the emission region extends away from both spots(Fig. 9.1a) and the spectrum from a $20\,\mu m$-diameter circular region centred between the two spots is clearly concentrated in two finite and opposite momentum states (Fig. 9.1b), corresponding to the outflow from each spot (see Chapter 8). Above condensation threshold, a non-linear increase of the emission intensity is observed together with a remarkable interference pattern in the region where the two outflowing condensates overlap (Fig. 9.1c). The dispersion spectra between the spots, Fig. 9.1d, reveal that the fringes are formed by interferences between two counterpropagating fluids, each of them having a single and equal energy mode. The fringe-pattern is stable for many minutes, meaning that the outflow from each spot is mode-locked with the other one at the same energy – note that such a mutual coherence

has no relation with the two spots being pumped by the same laser, since all the laser coherence is lost in the relaxation processes before creation of the two condensates. In this case, each of the pumped spots is affected by the outflow from the neighbouring condensate, i. e., each condensate resonantly fills the other. Condensation is therefore more likely to occur at the same energy and thus mode-locking occurs.

In Bose-Einstein condensation, single particle waves synchronize to create a coherent state (condensate) because of the nonlinear interactions. Here, the interactions within the outflow from different pumped spots lead to a synchronization of phases, in a full analogy with condensation itself. What is new here is that such a high coherence is present even when using multiple spots (see rest of Chapter), meaning that the outflow from each spot spontaneously mode-locks with the neighbouring ones.

Two condensates do not manage to phase lock when the discrepancy between pumping strengths is too large, in which case the outflow from each spot happens at different energies and no fringes are seen in our time-integrated measurements (see Figs. 9.1e,f). Because of the nonlinear potential landscape caused by the feedback between polariton density and local blueshifts, the mode-locking conditions subtly vary with excitation details.

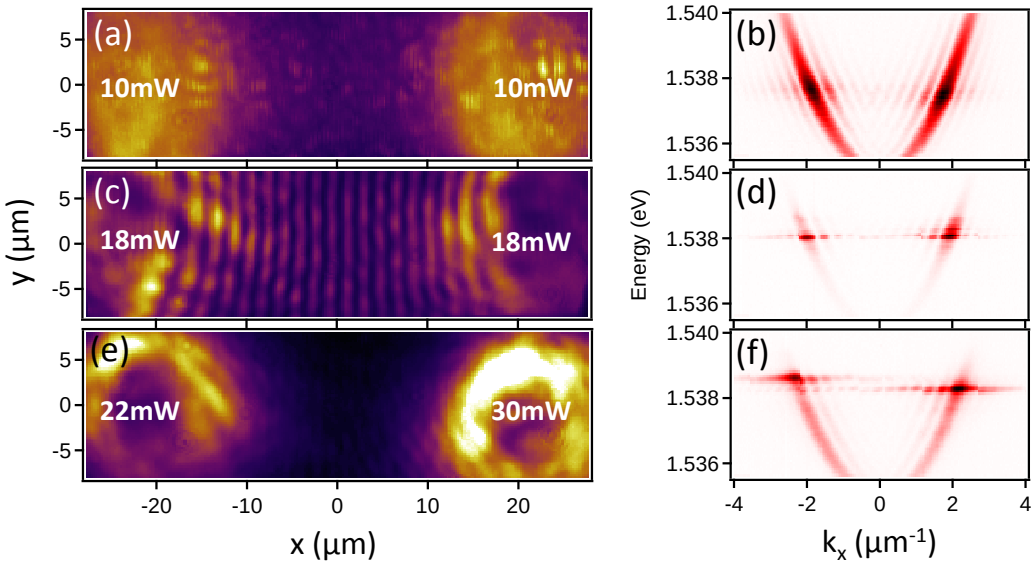

Figure 9.1: Conditions for phase locking and appearance of standing waves. (a,c,e) Polariton emission images in real-space for two pump spots placed at $(-20, 0)\,\mu m$ and $(20, 0)\,\mu m$. (b,d,f) Dispersion spectra corresponding to a spatially-apertured $20\mu m$-diameter circle centred between the two spots in (a,c,e), respectively.

The experimental setup can be easily changed to include 3 or more pump spots, in which case interferences are expected to generate vortex lattices [202, 203]. In the following sections we discuss how the non-linearities of polaritons change the nature of such topological textures.

9.2 Honeycomb vortex-antivortex lattices

Vortex lattices were first predicted [95] and later observed [204] in type-II superconductors, in response to an externally applied magnetic field. In neutral quantum fluids,

external rotation was used to generate vortex lattices in superfluids of helium [92] and later in atomic Bose-Einstein condensates [205]. Recent proposals include the generation of honeycomb vortex-antivortex lattices through linear interference of three expanding BECs [202, 206]. Such lattices have never been observed experimentally, although related techniques have been used to nucleate vortices in BECs [207] or vortex solitons in non-linear media that have been used as waveguides [208] and photonic crystals [209]. Being neutral systems, polariton condensates cannot produce vortex lattices in response to a magnetic field, but theoretical proposals suggest generating such lattices using harmonic traps [145], resonant laser injection [210, 211] and interference between outflowing condensates [203]. The latter scheme is used in this Section to generate honeycomb vortex-antivortex lattices.

We start by placing three $1\mu m$-diameter laser beams — again produced by splitting the CW–laser into three by using beam-splitters before the focusing objective lens — equidistant from each other. Interference patterns appear in the region where the condensates overlap between the three pump spots (see Fig. 9.2a, where the three pump spots are marked by black circles), with a characteristic honeycomb structure. Such a structure is predicted to support a stable vortex lattice [203], and to confirm this we record interference images (Fig. 9.2c) generated in a Mach-Zehnder interferometer and extract from those the coherence (Fig. 9.2d) and phase (Fig. 9.2e) by using Fourier transform analysis (see Section 4.3.2). Here we have used, as a reference wave for interferometry, an expanded small region outside the lattice, $30\,\mu m$ outwards one of the pump spots — see Appendix 11.5. The precise vortex positions are evidenced when calculating the *vorticity*, $\varpi = \nabla \times \mathbf{v}$ (Fig. 9.2f). Each vortex is surrounded by three vortices of opposite winding number, and so the hexagonal lattice can be seen as two Abrikosov-like triangular lattices [95] of opposite sign. The lattice is highly coherent over tens of microns, Fig. 9.2d (one must keep in mind that the fringes are obtained by interfering the region between spots with a $\sim 40\,\mu m$-apart expanded region, see Appendix 11.5), with interference visibilities over 50%, while the non-emissive vortex cores are seen as points of zero coherence with undefined phase. The full phase image (Fig. 9.2b) shows up to 50 vortices and antivortices located at the vertices of the honeycomb structure.

The lattice wavefunction is an intricate superposition of outflowing polaritons from each pump spot: Polaritons are created with $k = 0$ at each pump spot and accelerate outwards through decreasing blueshifts $\Delta(\mathbf{r})$ at larger distances, with $\Delta(r > 10\mu m) = 0$ — see an schematic representation of the three–hill blueshift surface $\Delta(\mathbf{r})$ in Fig. 9.3a. In the centre between the three pumped spots the wavefunction is thus the superposition of three k_c vectors at 120° to each other, directed out from each pump spot (Fig. 9.3c), whose linear combination generates the honeycomb lattice [206]. The separation between adjacent vortices, A in Fig. 9.2f, is given by the simple relation $A = 4\pi/(3k_c\sqrt{3})$.

The magnitude of each wavevector k_c at each spatial point is given by the condensate energy and the local blueshift, $\Delta(r)$ through the LPB inverse dispersion relation, Eq. 8.1 — see Fig. 9.3. The higher the blueshift at the pumping spots, the higher the wavevectors magnitude between spots. We again observe a logarithmic dependence of the blueshift Δ_0 with excitation power — see black circles in Fig. 9.3d. This allows us to predict the wavevector magnitude between spots, k_c, using Eq. 8.1 — see purple line in Fig. 9.3d, in excellent agreement with the measured values (purple triangles) — and therefore the separation between adjacent vortices — see orange line in Fig. 9.3d, again in good agreement with measurements (orange dots). The non-linear condensate properties can thus be used to stretch the vortex lattice spacing, here by over 50% from 1.2 – 1.8 μm.

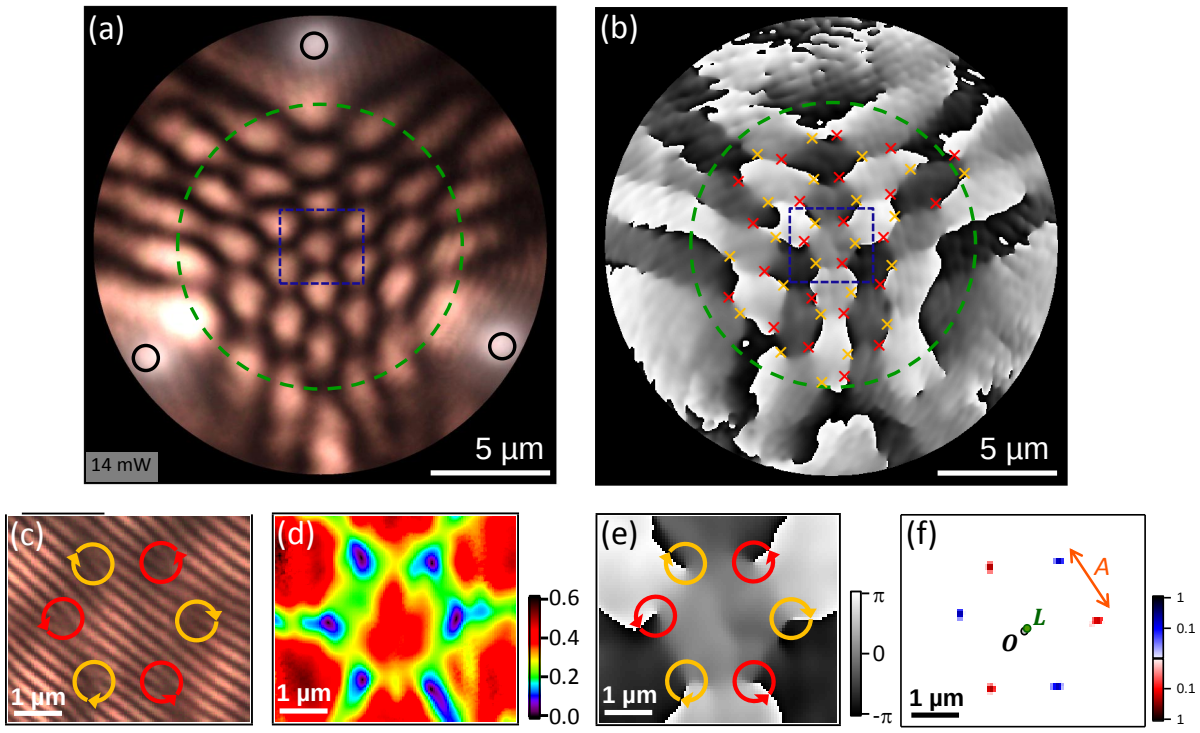

Figure 9.2: Experimental demonstration of honeycomb vortex-antivortex lattice. (a) Intensity and (b) phase image of the polariton emission, showing the honeycomb density pattern between the three excitation spots (black circles) with vortices (red crosses) and antivortices (orange crosses) marked. (c) Interference image of the region inside the dashed blue rectangle in (a), showing vortices (red anticlockwise circles) and antivortices (orange clockwise circles) at the vertices of the triangular sub-lattices. (d) First order coherence function, $|g^{(1)}|$, extracted from (c). (e) Expanded phase map of the dashed blue rectangle in (b), again showing vortices and antivortices. (f) Normalised vorticity calculated from (e), showing the separation (A) between adjacent vortices, with lattice centroid (L) and spots centroid (O). Each spot is pumped with $14\,mW$ for all the images.

Each pump spot contributes to the global wave-function with different k-states at different radial positions (see Eq. 8.2). The global wavefunction is a superposition of the three outflows from each spot:

$$\psi(\mathbf{r}) \approx \sum_{n=1}^{N_{spots}} e^{i(K_c(r)|\mathbf{r}-\mathbf{r}_n|+\varphi_n)} e^{-\tau(|\mathbf{r}-\mathbf{r}_n|)/\tau_c} g(\mathbf{r}) \tag{9.1}$$

The individual condensate phases φ_n are extremely important to determine the specific vortices positions, since varying one of the phases φ_n displaces the whole lattice pattern in the direction of the spot n. Therefore, by measuring the position of the vortices with respect to the pumping spots positions we can get information about the relative phases between spots. Let us call O the spots centroid and L the central vortex-hexagon centroid — see Fig. 9.2f. If the relative phases between spots vanishes, O and L spatially overlap. For the lattice shown in Fig. 9.2, both points almost perfectly spatially overlap, and this is also the case for many other measurements not shown here. In the following section we discuss the reason for such a perfect match.

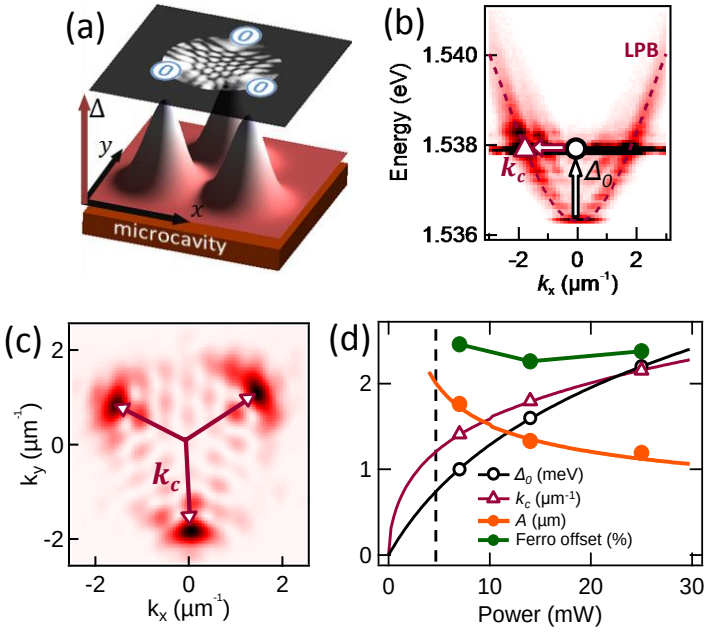

Figure 9.3: Lattice control. (a) Schematic landscape of the blueshift-induced potential $\Delta(r)$ underlying the geometrically-phase-locked vortex lattice. (b) Dispersion of the region inside the dashed green circle in Fig. 9.2(a), showing the fitted lower polariton branch (LPB, purple line). Blue shift of the condensate energy (Δ_0, black circle) is set by the blueshift at the excitation spots, with condensate momentum (k_c, purple triangles) at the spots centroid. (c) Measured wavevector distribution corresponding to region inside the dashed green circle in Fig. 9.2(a). Purple triangles show lattice momentum at the spots centroid, k_c. (d) Power dependence of the lattice energy (Δ_0, black circles) with logarithmic fit (black line), measured lattice maximum momentum (k_o, purple triangles) with prediction based on the dispersion (purple line), measured lattice separation (A, orange dots) with prediction (orange line) from $A = 4\pi/(3k_c\sqrt{3})$, and ferro offset ($F = |\vec{L} - \vec{O}|/(2\pi/k_0)$, green dots, see text). The dashed line depicts the power for condensation threshold- Ordinate units are indicated in the legends.

9.2.1 Numerical simulations and ferromagnetic coupling

In order to fully describe the lattice wave-function, simulations are performed using a simple form of the mean field model of polariton condensates [145, 151, 154] through the complex Ginzburg-Landau (cGL) equation 2.36, which includes both dissipation and pumping,

$$i\hbar\partial_t\psi = \left[-\frac{\hbar^2\nabla^2}{2m^*} + g|\psi|^2 + V_{ext}\right]\psi + \frac{i\hbar}{2}\left[P - \Gamma\right]\psi \tag{9.2}$$

where g is the strength of polariton interactions and the polariton decay rate is $\Gamma = 0.1\,meV$. The details of pumping are included in:

$$P(\mathbf{r}, \psi) = \gamma - i\eta\partial_t - \kappa|\psi|^2, \tag{9.3}$$

where γ is the pumping rate and κ the rate of nonlinear dissipation leading to gain saturation [145]. The dimensionless parameter η, introduced in Ref. [212] to describe experiments showing multimode condensation in confined geometries [110], describes the energy relaxation due to interactions between polaritons. We use $\eta = 0.1$ and $\kappa/g = 0.3$.

Three $1\mu m$–wide pumping spots have been considered at 3 times threshold ($\gamma = 3\Gamma$). The disorder potential V_{ext} simulates the sample random imperfections and is related to Rayleigh scattering — see Appendix 11.3, but for all the physics discussed in this Chapter it is irrelevant and so it is taken to be $V_{ext} = 0$.

The numerical solution of Eqs. 9.2 and 9.3 for three equally spaced pump spots (Figs. 9.4a,b) reproduces the vortex lattice found in experiments (Fig. 9.4c). It gives a wavefunction with the same phase at each pump spot position (Fig. 9.4b), independent of the initial state, and hence the central bright lobe appears at the spots centroid (placed at the intersection between the three green lines in Fig. 9.4a). This is the only solution that is invariant under an interchange of the spot positions, and so is geometrically imposed by the pumping configuration. However it is spontaneously chosen by the condensate system because the phase carried by the pumping laser is completely lost during the relaxation processes. If we make an analogy with ferromagnetic systems, by considering each pump spot as a psedo-spin, our triangular configuration avoids pseudo-spin frustration by insisting on ferromagnetic nearest neighbour interactions, then the pumped spots acquire the same spontaneous phase (or equivalently, pseudo-spin). Thus the vortex lattice is controlled by the pseudo-spin symmetry of the optically-induced condensates, analogous to ferromagnetism in 2D spin systems.

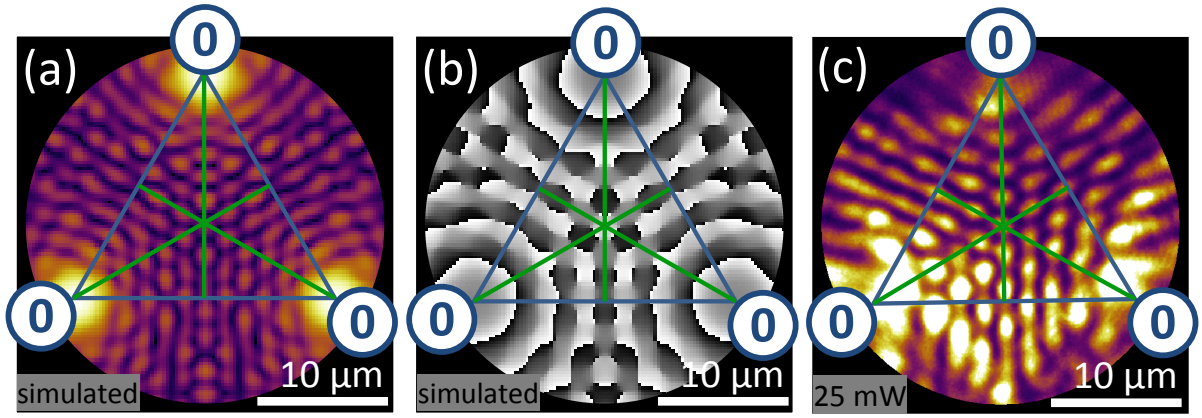

Figure 9.4: Numerical simulations and geometric locking. Simulated wavefunction (a) density and (b) phase, showing vortices and the equal phases at each pump spot position (represented by blue 0's inside circles). (c) Measured polariton photoluminescence for $25\,mW$ excitation power per spot. Green lines cross at the spots centroid.

The separation (as a fraction of the periodicity $2\pi/k_c$) between the centroids of this vortex lattice (L) and the pumped spots (O) quantifies the deviation from perfect ferromagnetic coupling (ie. the state where the phase at each pump spot is identical). For three different powers, this 'F–offset' is found to be always below 3% (Fig. 9.3d), showing that ferromagnetic coupling is always dominant in the triangular geometry. The stability of the lattice persists then due to the non-linear geometric phase locking of the free condensate phase of each pumped spot. This implies that rich spin phenomena such as ladder magnets [213] may be directly investigated in the polariton system.

9.3 Square bistable lattices

Lattices with different geometry can be simply engineered by changing the number and position of pump spots. Square lattices are created when pumping the sample with four spots placed at the vertices of a square. Fig. 9.5a-d show the numerical solutions to Eqs. 9.2 and 9.3 when using four equally-spaced pumping spots. Unlike the three-spot geometry in which the condensates lock with the same phase, here two different relative phases between nearest neighbour condensates are possible depending on initial conditions: either 0 (Fig. 9.5a,b) or π (Fig. 9.5c,d) relative phases. These are analogous to ferromagnetism (F) and anti-ferromagnetism (AF), respectively, in 2D spin systems (Fig.9.5h), and can again be distinguished in experiments by looking at the polariton density at the centroid between the spots: F-coupled condensates have an antinode at the centre (Fig.9.5e) whereas AF-coupled have a node (Fig. 9.5g). Again, these are the only solutions that preserve the rotation symmetry of the pumping spots configuration.

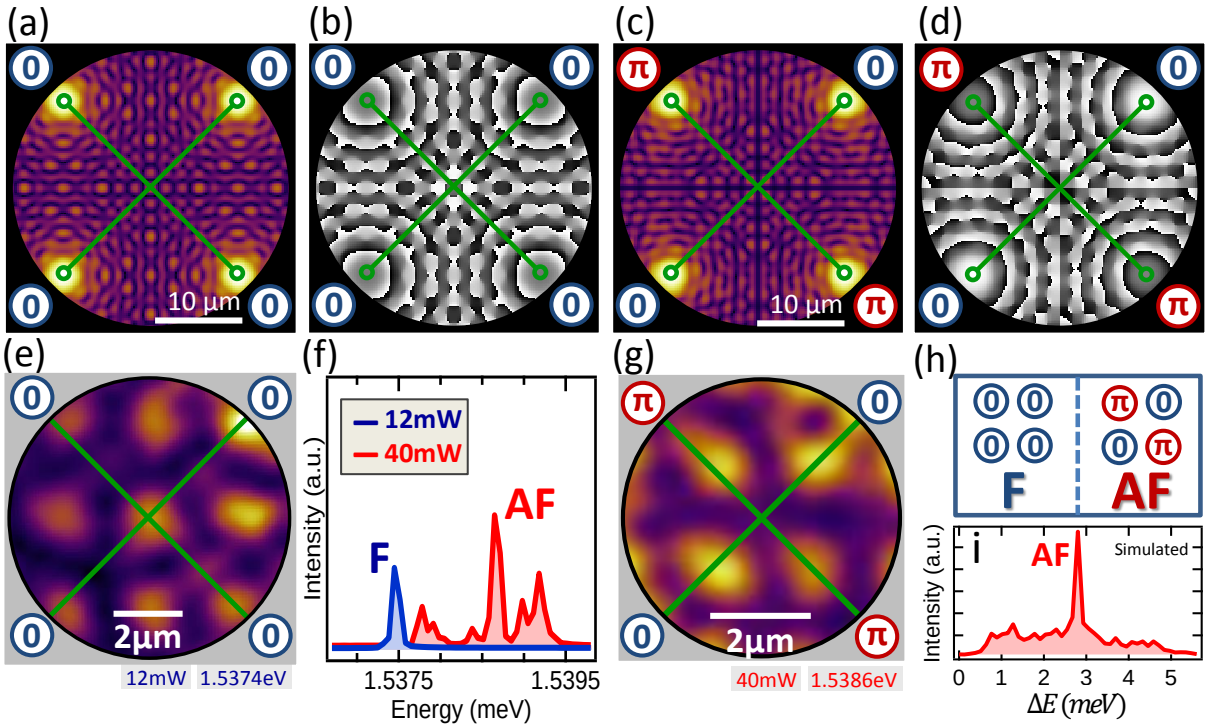

Figure 9.5: Square lattice and pseudo-spin symmetry. (a-d) Numerical solutions of Eqs. 9.2 and 9.3 using four equally-spaced pump spots, under different initial noise, giving (a,b) F or (c,d) AF lattices. (e,g) Observed polariton density at main energy peak, for 12 mW and 40 mW excitation power per spot, respectively, with the intersection between the two green lines marking the spots centroid. (f) Lattice spectra for the two different powers corresponding to (e,g), with main peaks classified according to the polariton density at the spots centroid. (h) Schematic ferromagnetic (F) and antiferromagnetic (AF) stable pseudo-spin configurations. Numbers inside circles represent the condensate phase at each pump spot. (i) Spectra of simulated square lattice using higher polariton densities, as compared to (a-d), and thus non-linear dynamics.

The F-coupled lattice has been found in experiments under a pumping power equal to 12 mW, just above condensation threshold. Its spectra contains a single energy mode (Fig.9.5f), and thus we expect that the lattice density is static in time. However the AF-

coupled lattice has been observed under high pumping powers, hence non-linear effects are expected to play a role since the polariton densities are high. In fact, the lattice spectra for $40\,mW$ pumping power per spot (Fig. 9.5f) show a main energy peak, whose density profile follows the one expected for an AF-coupled lattice (Fig. 9.5g), accompanied with weaker energy sidebands that indicate non-linear temporal dynamics.

Moreover, although the simulated lattices shown in Figs. 9.5a-d are steady state solutions whose spatial densities are constant in time, we obtain a lattice spectra whose main peak also contain sidebands (Fig. 9.5i), in agreement with experiments; to obtain this agreement it has been necessary to increase the polariton densities on the inter-spot region, which has been achieved by making the parameter κ vanish outside from the pumping spots. We discuss in the following Section the time-dynamics of such nonlinear lattices.

9.4 Nonlinear square lattice dynamics

Let us first consider an approximation to the wavefunction of the AF-coupled lattice, close to the spots centroid, as being a linear superposition of four perpendicular waves with π-phase shifts between each wave, as schematically represented in Fig. 9.6a. The density and phase of such an interference is shown in Figs. 9.6b,c, respectively. Instead of vortices, we note high-density square lobes with a flat phase separated by zero-density lines whose phase on each side differs by π. Such dark-lines with abrupt π-phase jumps are known in non-linear optics as dark-soliton stripes [192, 193]. These structures are unstable when considering propagation through a saturable self-defocusing nonlinear medium, breaking up into optical vortex solitons [192]. Similar phenomena also appear in BECs: simulations show that, if two nonrotating BEC pieces with a repulsive nonlinearity are made to interfere, in a scheme analogous to the Young's two-pinhole interferometer, the interference fringes — also known as dark-soliton stripes — decay via a 'snake instability' into a string of vortices [194, 195]. This vortex formation mechanism relies on the nonlinearity of the BEC self-interaction and has never been observed experimentally.

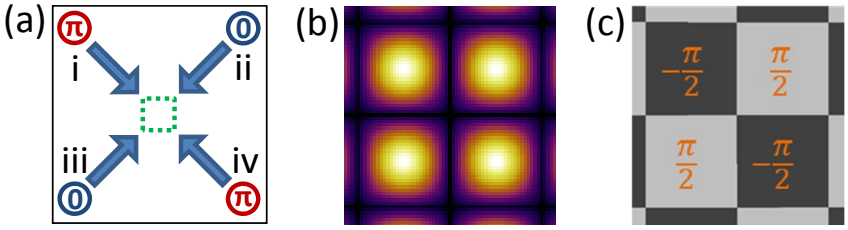

Figure 9.6: Square dark-soliton stripes produced by linear interferences. (a) Schematic representation of four-perpendicular beams created at the spots positions *i, ii, iii* and *iv*, with π-phase difference between them. The propagation direction of each beam is represented by the blue arrows and their relative phases by 0's and π's inside circles. (b) Intensity and (c) phase images of simulated interference between the beams inside the region marked by a dotted green square in (a).

In order to investigate the stability of dark-soliton stripes in polariton condensates, we track the time-evolution of the AF-coupled lattice wavefunction in simulations and experiments. In the latter case, we energy-resolve and tomographycaly-reconstruct the lattice emission in a spectrometer, recording real-space and interference images that yield the

lattice density and phase, $\psi(\mathbf{r}, E)$ – see Section 4.3.3. A simple Fourier transform allows the condensate phase and density to be tracked in time:[1] $\psi(\mathbf{r}, t) = \sum_E \psi(\mathbf{r}, E) e^{iEt/\hbar}$.

We first plot the time-averaged polariton density, which is equivalent to the energy-averaged density, $|\psi(\mathbf{r})|^2 = \int |\psi(\mathbf{r}, t)|^2 dt = \int |\psi(\mathbf{r}, E)|^2 dE$, for the simulated and measured data, in Figs. 9.7a,b, respectively. In both figures the spots centroid is at $(0, 0)\,\mu m$. Although small distortions are present, the main characteristic of both density profiles is to have the four lobes separated by a low density region at the spots centroid, characteristic of the AF-coupled lattice. This is due to the fact that the main mode peak in Figs. 9.5f,i contains an AF-like density pattern — see Fig. 9.5g.

It is also possible to track, in simulations, the time-dynamics of the lattice phase at each pump spot position[2] (Fig. 9.7c). Here the AF-coupling, with π-phase jumps between neighbouring spots, is preserved in time, therefore non-linearities are not capable of breaking the rotational symmetry between spots. The relative phases between the four central lobes in Figs. 9.7a,b, which are also expected to maintain a π-phase relation in the linear case, fluctuate with a $\sim \pi/5$ amplitude in a picosecond time-scale (Figs. 9.7d,e), indicating non-linear dynamics, although on average the π-phase relation is preserved.

Dark-solitons are predicted to break up in the region between each of the four lobes, and therefore non-linear dynamics are expected to be clearly manifested at these places. Lets us therefore analyse the time dynamics of the regions delimited by the dashed white rectangles in Figs. 9.7a,b. For a fixed time, the density profile of both simulated and measured data contain a dark line aligned approximately in the horizontal direction — see upper panels of Figs. 9.8a,b, respectively. The corresponding phase profiles — middle panels — show vortices placed where the density, in the upper panels, reach the lowest values. These vortices are linked by lines where the phase jumps by a π factor, corresponding to the low-density lines in the upper panels. The dark line in the upper panels contain therefore vortices linked by dark-solitons. The precise positions of the dark-solitons appear when plotting the phase derivative in the y direction (*black* $\rightarrow$ *green* colorscale in lower panels), the same for the vortices when plotting the vorticity in the same compatible image (*red* $\rightarrow$ *blue* colorscale in lower panels). Note that a dark-soliton separate two vortices of opposite winding number, and similarly a vortex separate two dark-solitons of opposite phase derivatives.

We next present the time-dynamics of the simulated and measured vorticity and phase y-derivative in Figs. 9.8c,d, respectively. We evidence the dynamics only in the x-direction by integrating the region inside the dashed rectangle in Figs. 9.7a,b along the y-direction between the two lobes. Both images show the movement of vortices and antivortices in the x-direction, separated most of the time by dark-solitons. It is also remarkable the spontaneous appearance of V-AV pairs out of a dark-soliton break-up (see, *e.g.*, the point $x \simeq -0.3\,\mu m$, $t \simeq 5\,ps$ in Fig. 9.8d), in accordance with our previous

[1] Being more precise, the relative phase between each energy mode cannot be determined experimentally, since a global increase of the phase $\varphi(E)$ of each energy mode does not change the recorded interference pattern. Thus an unknown phase per mode should be added to the Fourier transform calculation, $\psi(\mathbf{r}, t) = \sum_E \psi(\mathbf{r}, E) e^{iEt/\hbar + \varphi(E)}$. However as time passes the relative phases between energy modes change since the modes are time-evolving with different frequencies, thus an infinite number of combinations of relative phases $\varphi(E)$ can be mapped into a single combination by changing the origin of time. We have checked that, giving random values, between $-\pi$ and π, to $\varphi(E)$, the reconstruction of the dynamics is not substantially changed. We set therefore $\varphi(E) = 0$ for all the data presented here.

[2] In experiments, although the condensate phase can be extracted, the limited precision in the method used for this — in particular the unknown global phase-gradient introduced by the interferometer geometry — does not allow to make a good enough comparison between the phase at each pump spot.

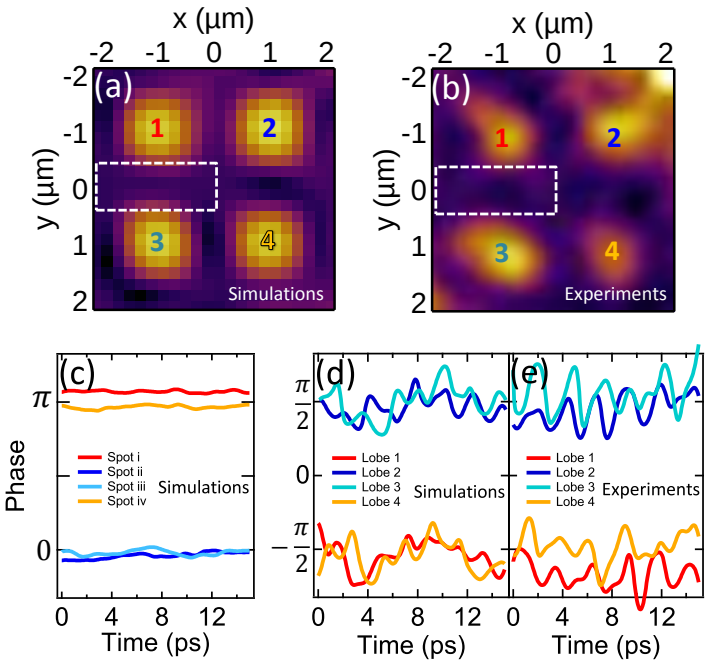

Figure 9.7: (a) Simulated and (b) measured time-averaged polariton emission of an AF-coupled lattice corresponding to Fig. 9.5i and Fig. 9.5f,g, respectively. The spots centroid is at $(0, 0)\,\mu m$. Dashed white rectangles marks region where the time-dynamics is plotted in Fig. 9.8. (c) Time evolution of the simulated wavefunction phase at each pump spot position (as sketched in Fig. 9.6a). (d) Simulated and (e) measured time evolution of the condensate phase at each lobe centre indicated in (a,b).

discussions. Finally, note that the opposite phenomena, namely the annihilation of V-AV pairs, also happens (see, *e.g.*, the point $x \simeq -1.1\,\mu m$, $t \simeq 8.3\,ps$ in Fig. 9.8d).

Even though the AF-coupled lattice is stable (Fig. 9.7), the regions between the bright spots, which are expected to contain dark-soliton stripes, are destabilised by the strong nonlinear interactions. This leads to modulational instabilities that nucleate vortex pairs, resembling effects in non-linear optical media [192, 193] and BEC's [194, 195]. We have shown in this thesis the first observation of this vortex formation mechanism in a non-equilibrium condensate.

In order to determine the regions where vortices are created and/or move to, we plot the probability of finding a vortex at a specific spatial point by taking the normalised time-averaged vorticity, $\langle \varpi(r) \rangle = \left[\int_0^{\Delta t} |\varpi(r,t)| dt \right] / \Delta t$, mapped in Fig. 9.9a,b for the simulated and measured data, respectively. Despite their non-linear time-dynamics, the topological defects remain constrained in the gaps between the density lobes (compare with Figs. 9.7a,b), which form analogues of waveguides for the vortices and dark-solitons movement.

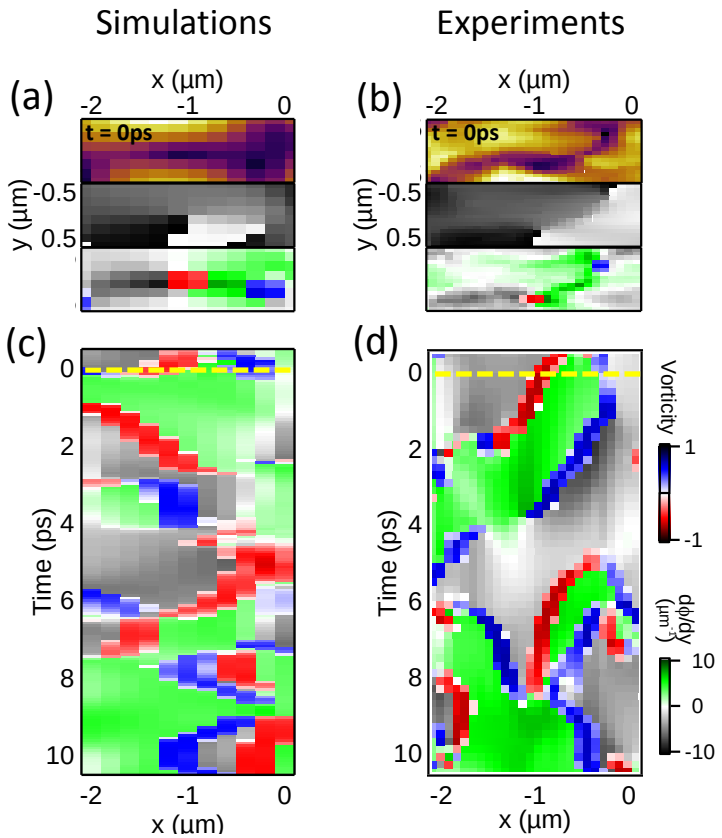

Figure 9.8: Vortex and dark-soliton nonlinear dynamics. (a) Simulated and (b) measured emission intensity (upper panels), phase-map (middle panels) and vorticity and phase-derivative (lower panels), correponding to the region inside the dashed red box in Fig. 9.7a,b at $t = 0$. The ordinates are the same for all the six panels, ranging from $-0.5\,\mu m$ to $0.5\,\mu m$. (c) Simulated and (d) measured time evolution of the vorticity and phase-gradient of the same rectangular region, integrated along the y-axis. The colorscales of lower panels in (a,b) and panels (c,d) are all the same, depicted in panel (d).

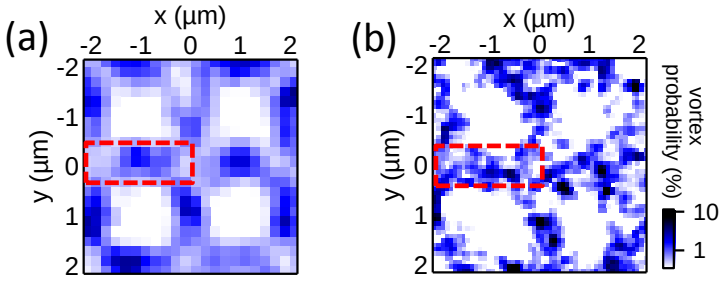

Figure 9.9: (a) Simulated and (b) measured time-averaged normalised vorticity, $\langle \varpi(r) \rangle$, for the same conditions as the ones used to record Figs. 9.7a,b.

It is important to note that although the calculated vorticity on Fig. 9.8c,d allows the localization of vortices with the precision of $\sim 100\,nm$ (pixel size) the spatial resolution of our setup is $\sim \lambda/2NA \simeq 500\,nm$. In fact such a resolution limit is reflected on Fig. 9.9b, where colour variations appear in a scale $\simeq 400\,nm$. Finally, it is worthwhile saying that the $2\,meV$ spectral bandwidth seen in Fig. 9.5f determines the time resolution $h/dE \simeq 2\,ps$ obtained in Fig 9.8d.

9.5 Conclusions

We have shown how two or more independent propagating condensates can be made to interact together by properly engineering the pump spots configuration. Polaritons originating from separated and independent incoherently-pumped spots were shown to phase-lock and produce up to 100 vortices and antivortices that extend over tens of microns across the sample, constituting the first observation of vortex lattices in a semiconductor microcavity. This is only possible in new high quality devices, where the reduced imperfections allow the polaritons to propagate over long distances without being disturbed.

The vortex separation within the lattice could be tuned using the non-linear properties of polaritons simply by changing the pump power. The resultant regular vortex lattices are sensitive to the optically imposed geometry: whereas three equally-space pump spots generate a honeycomb lattice in which its centroid always coincides with the pumping spots one, four spots admit two solutions that satisfy the rotation symmetry imposed. Therefore the geometry and position of the lattice created under 4-spot excitation are sensitive to the spontaneously-locked relative phase between each excited condensate. Such systems describe the optical equivalents to spin systems with (anti)-ferromagnetic interactions controlled by their symmetry, paving the way towards the simulation of microscopic quantum systems using macroscopic quantum fluids, which can be reconfigured on the fly. This bistable pseudo-spin configuration, which can then correspond to a qubit or an interferometer, can potentially be manipulated through direct laser excitation, as well as in lithographically patterned samples.

The pumping geometries presented in this Chapter provide a new way to generate periodic 2D structures in polariton condensates, with no need of a built-in periodic potential, as opposed to Ref. [214], and with the ability to store quantized values of vortex charge at specific positions. We also uncovered a nonlinear regime for topological defects at high densities, in which dark-solitons break up to generate vortex-antivortex pairs, in analogy with non-linear optical systems. In this case interacting topological defects are guided in a square matrix, paving the way towards all-optical creation and manipulation of quantum fluidic circuits.

The vortex lattices presented here are created with no need of global stirring or external rotation, and the vortex/antivortex pairs yield no global angular momentum. They are thus markedly distinct from lattices due to global phase symmetries described in Ref. [205], and present a close analogy to the formation of vortex solitons in Kerr nonlinear self-defocusing media [208]. The phase locking between separately pumped condensates is a key ingredient for the lattice generation and stability, but here the locking mechanism has no relation with previously-reported Josephson tunnelling in disorder-induced trapped condensates [132, 201]. Instead, each of the pumped spots is resonantly pumped by the outflow from the neighbouring condensates inducing mode-locking to the same energy. Because the phase of the polariton fluids has no relation to that of our pumping lasers, the lattice is a purely nonlinear polaritonic effect spontaneously emerging from the optically-induced potential.

Chapter 10

Spontaneous harmonic oscillations

In the last two chapters polariton-polariton and polariton-reservoir interactions have been shown to produce a blueshift-induced potential that accelerates polaritons as they outflow from the excitation spot. In this Chapter we optically arrange such a potential in order to confine polaritons and engineer their wavefunction accordingly.

10.1 Polariton quantum oscillator

We use all over this chapter two spatially-separated, and tightly focused, pumping spots. The decreasing reservoir density (and decreasing blue-shifts) away from the two pumped spots induces a two-peaked potential profile (Fig. 10.1a). We start with the two pump spots far apart ($\sim 40\,\mu m$) with the same power just above threshold, $17\,mW$, in conditions very similar to the ones used to obtain the standing wave profile seen in Fig. 9.1c. Figure 10.1b show the energy profile of a spatial cross-section that includes the two pump spots. Surprisingly, the colours on logscale evidence not only the strong single-mode, high-energy, standing-wave profile, but also energy relaxation towards lower modes in a trapped-like distribution. The decreasing blueshift away from the pump spots also influences the spatial distribution of polariton modes: only higher modes are populated close to the pump spots, whereas lower modes appear in the centre. Thus the luminescence gives a hint on the trapping potential that, in this case, seems to be parabolic.

At closer pump separation ($20\,\mu m$) and higher excitation powers ($42\,mW$), the polaritons experiencing the blueshift potential redistribute in energy and space to occupy the lower energy modes (Fig. 10.2a). The energy spacing between levels (Fig. 10.2b) is almost identical, like that of a simple harmonic oscillator (SHO), the quantum equivalent of a pendulum, in which the energy separation between modes is given by $E_n = \hbar\omega(n_{SHO} + 1/2)$, where $n_{SHO} = 0, 1, 2, ...$ and ω is the SHO angular frequency. Moreover, again similarly to a SHO, the number of spatial nodes of each energy mode increases with energy, $n_{nodes} = n_{SHO}$ (see Fig. 10.2a).

Following the analogy with an SHO, we extract the density profile of the $n_{SHO} = 5$ energy mode (red points in Fig. 10.2c), along the line between pump spots (red dashed line in Fig. 10.2a), and fit with the eigenfunction of the SHO, which are Hermite-Gaussian $\psi_{SHO}(x)$ states:

$$\psi_n(x) = e^{\frac{-m\omega x^2}{2\hbar}} H_n\left(x\sqrt{m\omega/\hbar}\right) \tag{10.1}$$

where $H_n(x)$ is the standard Hermite polynomial, and the polariton mass m is mea-

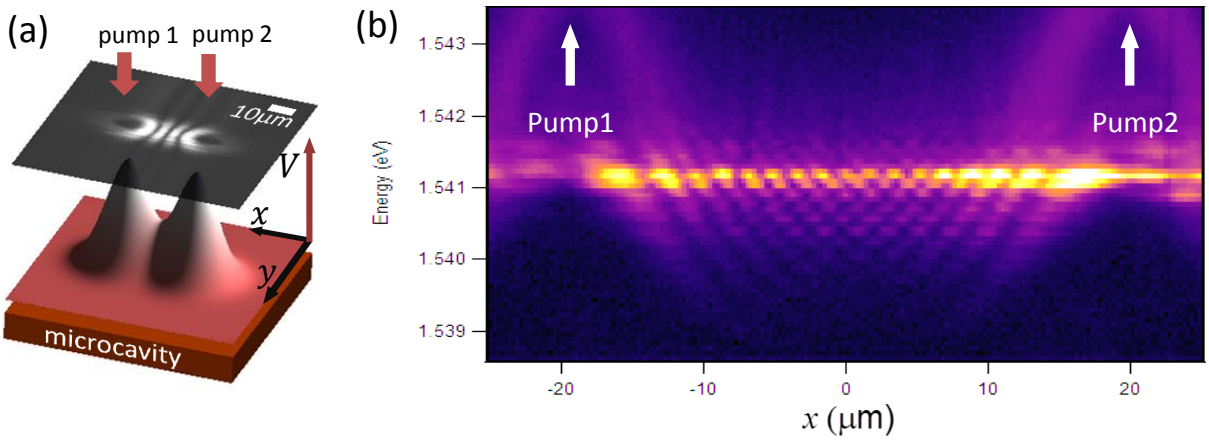

Figure 10.1: (a) Schematic representation of two separated pump spots focused on the planar microcavity, showing the effective potential V that accelerates polaritons outwards and the interference pattern that appear between the two counterpropagating outflows. (b) Experimental spectra of a spatial cross section that includes the 2 spots separated by $40\,\mu m$, each one pumped with $17\,mW$.

sured from the curvature of the LPB below condensation threshold, finding $m = 4.2 \times 10^{-5} m_e$. The fit of the experimental data with the $\psi_{n=5}$ oscillator eigeinfuntion agrees quite well (see black line in Fig. 10.2c), yielding the angular frequency $\hbar\omega = 0.34\,meV$, in very good agreement with the data shown in Figs. 10.2a,b . This allows to reconstruct the SHO potential $V = \frac{1}{2} m\omega^2 x^2$, as superimposed in a dashed white line in Fig. 10.2a. This extracted potential coincides with all the ones extracted by fitting the other energy modes (not shown) and clearly surrounds the polariton luminescence in Fig. 10.2a, confirming the appropriateness of the SHO model to describe the polariton density distribution in energy and space.

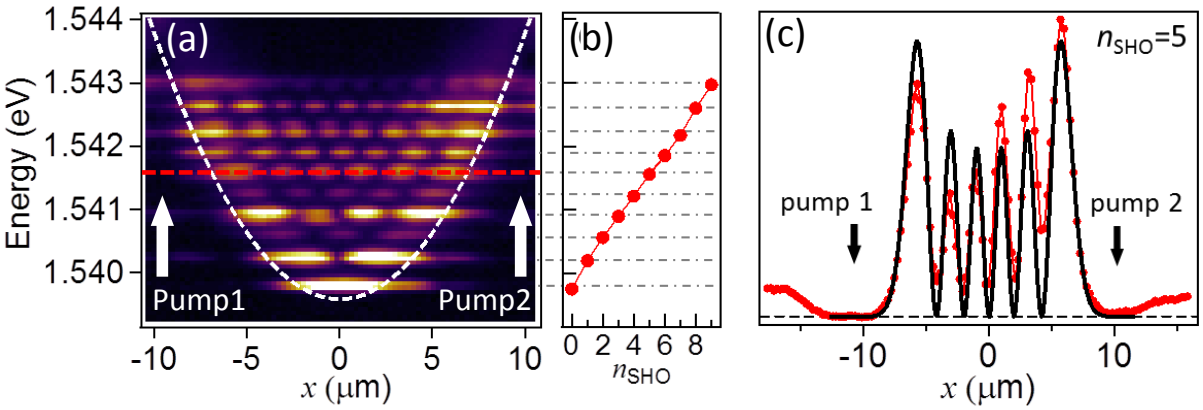

Figure 10.2: Polariton Simple Harmonic Oscillator (p-SHO). (a) Real-space spectra along a line between two $1\mu m$-diameter pump spots separated by $20\,\mu m$, each one pumped with $42\,mW$. (b) Extracted mode energies versus quantum number. (c) Hermite-Gaussian fit (black line) of $\psi_{n=5}(x)$ to the red points, which are extracted from the red-dashed line in (a).

Its is important to note that, although the polariton density distribution resembles the ones of a single particle in a parabolic trap, the data presented in Fig. 10.2 has been taken above condensation threshold, and thus polaritons macroscopically occupies coher-

ent states. The coherence of the full condensate, including the intercoherence between different energy modes, will be discussed in Section 10.3.

The full spatial profile of each energy mode of the condensate wavefunction is measured by tomography — see Section 4.2. The eight lowest energy modes are plotted in Fig. 10.3. They extend tens of micrometres across and the number of wavefunction lobes increase with energy. The cone-like shape of the blueshift induced by each pump spot is reflected on the two dark circular regions whose diameter decreases as the energy increase. Such direct image of extended coherent quantum states has no precedence in semiconductor systems.

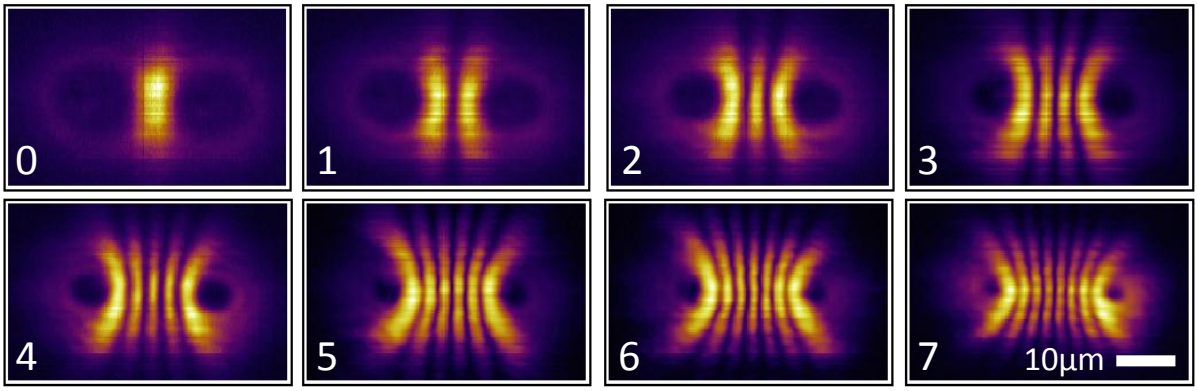

Figure 10.3: Spatially mapped polariton-condensate wavefunctions. Tomographic images of polariton emission (repulsive potential seen as dark circles around pump spots), labelled according to n_{SHO} assigned from Fig. 10.2b.

10.1.1 Tuneability

In the SHO model, the energy separation ΔE between modes depends only on the parabolic potential curvature $\frac{\partial^2 V}{\partial x^2}$ which, for the p-SHO, is obtained from the blueshift at the pump spots, $g|\psi|^2 + \hbar R_R N$ (see Eq. 2.41), and their separation, L:

$$\Delta E = \sqrt{\frac{2\hbar^2}{m}\frac{\partial^2 V}{\partial x^2}} \simeq \sqrt{\frac{2\hbar^2}{m}\frac{V_{max}}{L^2}} \simeq \frac{\hbar}{L}\sqrt{\frac{2(g|\psi|^2 + \hbar R_R N)}{m}} \tag{10.2}$$

The p-SHO states are thus only resolved owing to the strong polariton repulsion and the ultra-light polariton mass. By controlling the spacing between the pump spots the shape and orientation of this SHO potential, $V(r)$, can be directly modified in real time, thus changing the energy level spacing $\hbar\omega$. In Fig. 10.4a,b we show the spectra of a cross section along the two pump spots for two different separations, maintaining the excitation at $17\,mW$. Note that when the spots are closer together, the curvature of the potential is higher and thus the energy modes become more separated, in accordance with Eq. 10.2. Plotting the quantized energy levels for several pump separations, L, confirms their equal energy spacing (Fig. 10.4c) and the predicted inverse dependence on separation (inset).

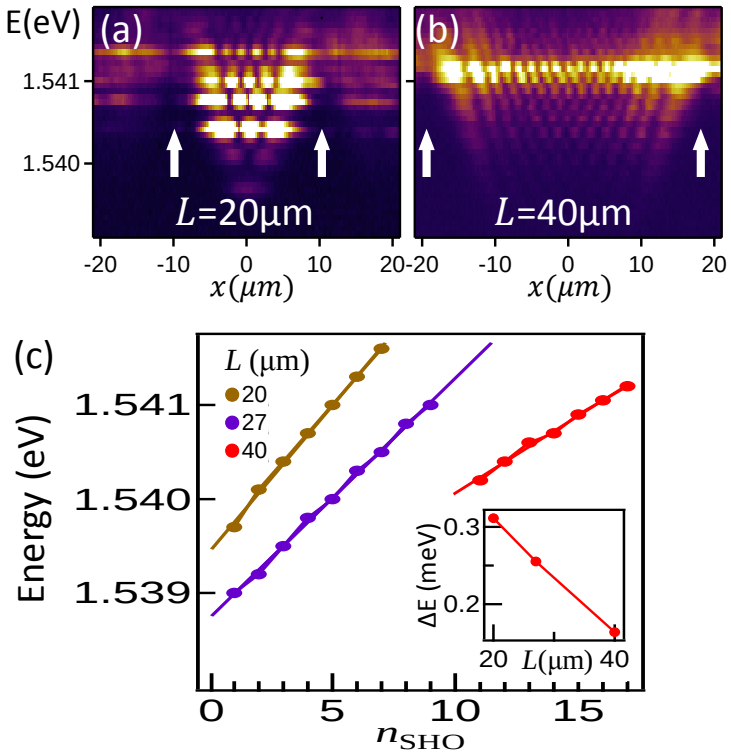

Figure 10.4: Tunning energy separation with pump separation for $17\,mW$ at each spot. (a,b) Spatially resolved polariton spectra on a line between pump spots (white arrows). The pump separation L controls the SHO energy spacing. (c) Ladder of SHO energies for three different pump separations L, with average energy spacings extracted in the inset.

In the same way, if the pump separation is kept constant while both pump powers are increased by the same amount, increasing the polariton density increases the blueshift, and hence the potential curvature, increasing the mode separation accordingly (Fig. 10.5a,b). Moreover the enhanced depth of the potential increases the number of SHO states trapped inside (N_{SHO}). In Fig. 10.5c we plot the blusehift at the pumping spots, which coincides with the energy of the highest SHO mode, as open circles. Putting these values into Eq. 10.2 we can predict the energy separation between modes since we know the spots separation and the polariton mass. The predicted values, shown in the same graph, Fig. 10.5c, as the solid red line, agree quite well with the experimentally measured energy separation, depicted as red dots.

By carefully inspecting Figs. 10.4a,b and 10.5a,b, we note that the polariton SHO states are populated differently under different conditions, with high pump powers and close pump separations favouring relaxation to the lower condensate SHO states. For two polaritons initially in SHO states (E_1, E_2) their mutual scattering to states (E_1', E_2') is only energy-phase matched if $E_1' + E_2' = E_1 + E_2$. Scattering is thus most rapid if the energy separations between states are equal. At low powers the reservoir is more localised close to the pump spots, therefore the potential deviates from parabolic, giving unequal energy spacings, and thus scattering is slower. At higher excitation powers, the potential becomes more parabolic and thus the energy separation more constant, favouring parametric scattering. Moreover the higher polariton densities increase scattering events, which select equally-separated energy modes thus leading to more parabolic potentials, speeding up scattering and feeding back positively — the scattering rate increases so that polariton relaxation populates lower energy states. The self-organized nature of the highly

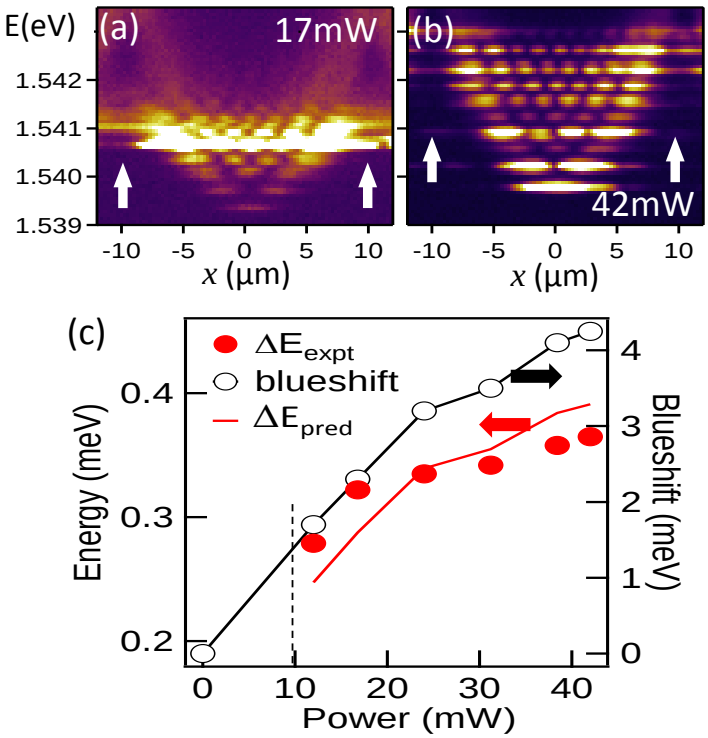

Figure 10.5: Dependence of SHO states on pump power for a pump spot separation of $L = 20\,\mu m$. (a,b) Spatially-resolved polariton spectra on a line between the two pump spots (white arrows) as the equal pump powers are increased (as labelled). (c) SHO ladder spacing (red dots) for different pump powers above threshold ($10\,mW$, vertical dashed line), together with prediction (red line), obtained from Eq. 10.2 and the experimentally determined blueshifts at each pump power (black circles).

nonlinear polaritons is to produce the most rapid non-equilibrium energy flow through the system, by forming an SHO parabolic potential with an energy ladder that maximizes polariton relaxation. This solid-state quasiparticle is so nonlinear as to modify its own potential in this way, and links to current theories of nonequilibrium systems [146].

10.2 Numerical simulations

A more detailed understanding on the p-SHO dynamics is provided by simulations using again the complex Ginzburg-Landau equation 2.36. Here however, in contrast with all the previous simulations presented on this thesis, it is very important to account for the reservoir interactions that yield high energy blueshifts capable of trapping polaritons. The theoretical explanation starts with the mean-field equation [145, 154, 212] for the lower polariton wavefunction, ψ, in the presence of a reservoir population, N, of optically injected hot excitons, that feeds, Eq. 2.39, and repel, Eq. 2.41, the condensate. All put together, Eqs. 2.36, 2.39 and 2.41 yield:

$$i\hbar\partial_t\psi = \left[-\frac{\hbar^2\nabla^2}{2m} + g|\psi|^2 + \hbar R_R N(\mathbf{r},t)\right]\psi + i\frac{\hbar}{2}\left[R_R N(\mathbf{r},t) - i\eta N\partial_t - \Gamma\right]\psi \qquad (10.3)$$

Note that we are again using the energy relaxation term dependent on the rate η, already introduced in Section 9.2.1, however now it explicitly depends on the reservoir

density N. Microscopic justification of the η term in the context of atomic condensates was provided by Refs. [215, 216] which showed that is proportional to the rate at which thermal atoms enter the condensate due to collisions. The coefficient η depends on the temperature and the density of the thermal cloud. In our system the role of the thermal cloud is played by the reservoir of excitons, so it is suitable to assume that depends on N linearly. This relaxation term is important to get the low energy modes of the p-SHO ladder populated, since polaritons are created, at the pump spots, in the highest energy mode. The reservoir exciton density N is governed by Eq. 2.40, that we repeat here for ease-reading:

$$\partial_t N(\mathbf{r},t) = -\left[\Gamma_R + \beta R_R |\psi|^2\right] N(\mathbf{r},t) + P_{NR}(\mathbf{r}) + D\nabla^2 N \tag{10.4}$$

Eqs. 10.4 and 10.3 were numerically integrated using the following parameters: $\Gamma = 1/(12\,ps)$ (inverse photon lifetime), $\Gamma_R = 0.01\,ps^{-1}$ (reservoir lifetime), two pump spots $P_{NR}(\mathbf{r})$ with FWHM diameter $1\,\mu m$, $g = 0.05\,meV\mu m^2$ (polariton repulsive interaction), $R_R = 0.3\,ps^{-1}\mu m^2$ (rate of scattering polaritons from the reservoir), $\eta = 0.07\,\mu m^2$ (parameter representing the energy relaxation rate). The value of the phenomenological coefficient β has been chosen to be 0.8 for a good agreement with experimental results. The diffusion coefficient, D, is optimised to give a good fit to the experimental reservoir shape. The net polariton potential $V(\mathbf{r}) = g|\psi|^2 + \hbar R_R N(\mathbf{r},t)$ is produced by the repulsive interactions between polaritons themselves as well as with the reservoir excitons (N) close to the pump spots.

Figure 10.6a show the simulated time-averaged condensate spatial profile (which is equivalent, in experiments, to all the energy modes plotted in Fig. 10.3 integrated), when using two tiny pump spots placed at $(-10, 0)\,\mu m$ and $(10, 0)\,\mu m$. The time dynamics of the line between pump spots (marked by a dashed white line in Fig. 10.6a) is plotted in Fig. 10.6b. It reveals a harmonically oscillating dark region between both spots, which is always accompanied by a π-phase jump (not shown). Such solitary waves with zero density are expected in cGL equations, and resemble the spatial solitons recently observed in atomic Bose-Einstein condensates [217–219]. Dark solitons are expected for a perfect 1D parabolic potential [220], however in our 2D sample such a dark-soliton-like profile extend in the y-direction eventually breaking up into vortex pairs (not shown here), similarly to the snake instability already discussed in the preceding chapter. The spectra of the same line between spots are obtained by taking the Fourier transform of the time dynamics shown in Fig. 10.6b. The result, shown in Fig. 10.6c, reproduces quite well the experiments, yielding equally-spaced energy modes with SHO-like density profiles.

The observed multiple energy modes are therefore better described by a single condensed coherent state, ψ, describing a polariton wavepacket in the quantum liquid oscillating back and forth with period t_r (Fig. 10.6b), whose representation in energy space produces the characteristic SHO sidebands observed experimentally. From the properties of the Fourier transform, the oscillating period t_r sets the separation between energy modes as $\Delta E = h/t_r$ (this simple relation is also derived in the SHO model). A single oscillatory wavefunction implies that the observed SHO states are the confined states of a condensate in the parabolic potential. We investigate the coherence between the p–SHO modes in the next Section.

Let us finally highlight that the dynamics presented in Fig. 10.6 is only one of the possible solutions to Eqs. 10.4 and 10.3. Different solutions include multiple oscillating dark-solitons and even more chaotic dynamics. Dark-solitons solitons are solutions of

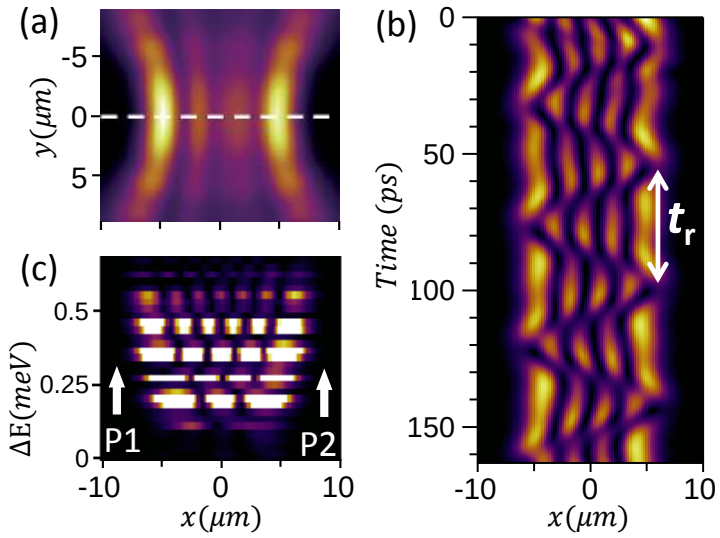

Figure 10.6: Theoretical simulation of Eqs. 10.3 and 10.4 for a $20\,\mu m$ pump separation (pump spots at $P_1 = (-10, 0)\,\mu m$ and $P_2 = (10, 0)\,\mu m$). (a) Time-averaged spatial profile. (b) Spatial cross section along the line between pump spots (dashed in (a)) vs time, showing an oscillating low-density region with period t_r. (c) Resulting time-averaged spectra along the dotted line in (a).

the cGL equation when the fluid has positive mass, which is the case of polaritons close to the bottom of the LPB. However bright-solitons can also be formed in a polariton fluid created at k-values high enough so that the polariton mass is negative [29]. In fact, the crossover between oscillating dark- and bright-solitons has been recently observed, in time-resolved measurements, as the pumping power is increased in such a way that the wave-packets are created with initial k-vectors that can be tuned from positive-mass regions to negative-mass ones [221].

10.3 Coherence revival and mode-locking

As discussed in the previous Section, the equally-spaced energy modes distributed in a harmonic oscillator configuration can be understood in time-domain as a periodically oscillation polariton wavepacket that bounces back and forth between each pump spot. This implies that a single coherent wavefunction describes all the wavepacket dynamics, which is only true if all the p-SHO modes are mutually coherent. In this Section we check this assumption by measuring the condensate coherence in the time domain.

We first split the full sample emission (not energy filtered) in the far field into two arms of a Michelson interferometer containing one retroreflector in each arm and a delay stage in one of them — see Fig. 4.4b. The light from each interferometer arm is focused into a CCD camera and the resulting interferences in real-space is recorded. By translating one of the retroreflectors laterally, the angle between both beams beam can be adjusted, and the interference fringes accordingly. Figure 10.7a show the resulting interferences, with the fringes aligned in the horizontal direction, when pumping the sample at two spots, placed at $(-11, 0)\,\mu m$ and $(11, 0)\,\mu m$, with $40\,mW$ each. In this case each interferometer arm have the same optical path length in such a way that both beams interfere with zero time-delay. The interference images, Figs. 10.7a-c represent each condensate spatial point interfered with itself at a time-delay that can be adjusted. The first order coher-

ence is then extracted using Fourier transform analysis — see Section 4.3.2 – yielding $|g^{(1)}(\mathbf{r},\mathbf{r},\Delta t)|$ (Figs. 10.7d-f) Note that, for zero time-delay, The fringes simply represent autocorrelation and their visibility, and hence $|g^{(1)}(\mathbf{r},\mathbf{r},0)|$, is maximum. As the time delay between the interfering images increases, the energy modes become out-of-phase and the fringe visibility rapidly decreases everywhere (Figs. 10.7b,e). This is a direct consequence of the condensate broad spectrum — by the Wiener-Khinchin identity 2.26, the broader the energy spectrum, the faster the coherence decay. However, remarkably, at $13\,ps$ time-delay, the coherence revives strongly (Figs. 10.7c,f). Figure 10.7g show the spatially–integrated coherence, obtained by averaging $|g^{(1)}(\mathbf{r},\mathbf{r},\Delta t)|$ over the whole area of Figs. 10.7d-f. Note that the revival peak is symmetric with respect to $t = 0$.

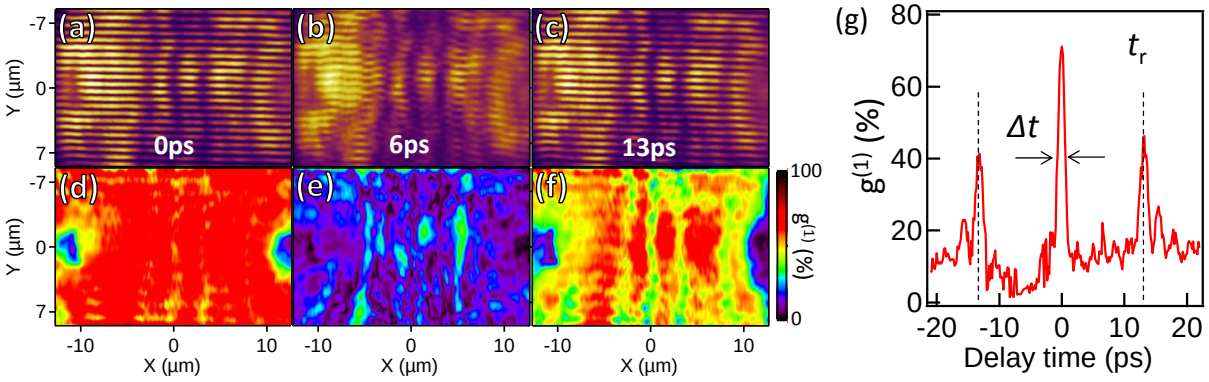

Figure 10.7: Interferometry reveal condensate coherence revival. (a-c) Real-space interference patterns for time delays shown. Pump spots placed at $(-11,0)\,\mu m$ and $(11,0)\,\mu m$, each one pumping $40\,mW$ power. (d-f) Extracted first-order coherence, $|g^{(1)}(\mathbf{r},\mathbf{r},\Delta t)|$. (g) Fringe visibility averaged over each image versus Michelson interferometer time delay.

The coherence revival can be understood in two equivalent ways: 1) Considering the wavepacket picture, at zero delay the wavepackets from both interferometer arms oscillate in-phase, yielding maximum fringe-visibility; as the delay increases, the oscillations from each arm arrive at the CCD out-of-phase, hence the polariton solitons from each arm are displaced in space at most of the time, yield weak fringe visibility. As the delay becomes equal to the oscillating period, both wavepakets oscillate in-phase again, recovering high fringe visibility. In fact, for the data shown in Fig. 10.7, we measured $\Delta E = 3\,meV$, which predicts an oscillating period $t_r = h/\Delta E = 13\,ps$ in accordance with the measured value. 2) Considering the fringes as a superposition between the interferences of each energy mode with itself, as we start delaying one of the optical paths, the fringes start moving in the vertical direction with a velocity that is different for each energy mode; therefore the superposition of many fringe patterns at different positions washes out the overall fringe visibility; However, when the delay is such that $\omega t_r = 2\pi$, all the fringes are spatially superimposed again, hence the visibility is recovered. This is only possible because at $t = 13\,ps$ all the modes come back in phase again, which implies not only that the individual SHO states are phase coherent but that they are condensates with a mutually stable phase relationship. The condition $\omega t_r = 2\pi$ is equivalent to $t_r = h/\Delta E$ hence both descriptions are compatible.

Since the energy separation between modes can be tuned with the pump spots separation and power, as described in Section 10.1.1, we measure the coherence revival time t_r for different oscillator frequencies controlled by the pumps configuration. The measured coherence revival times (red dots Fig. 10.8) scale as expected, with the energy separation,

$t_r = \hbar/\Delta E$ (red line in same figure).

In the oscillating wave-packet picture, the oscillating period can be predicted from the pump spots configuration by using Eq. 10.2:

$$t_r \simeq \sqrt{\frac{2\pi^2 m L^2}{g|\psi|^2 + \hbar R_R N}} \tag{10.5}$$

This oscillating time, dependent on blueshift and pump spot separation, is plotted as open circles on Fig. 10.8, clearly matching the coherence revival time.

The coherence revival is not perfect, meaning that at t_r time delay the coherence does not recover its maximum value presented at $t = 0$ (compare Figs. 10.7d,f). For each coherence revival under different pump configurations, we plot the ratio between the coherence peak at $t = t_r$ and its maximum value at $t = 0$ (see Fig. 10.7g) as blue triangles in Fig. 10.8. After fitting the measured values with an exponential decay, we find that the revival fringe amplitude at increasing time delays decays with a $\sim 25\,ps$ lifetime.

Many physical mechanisms are involved in such a coherence decay process, including coherent wavepacket dispersion, decay, dephasing and diffusion. Wavepacket dispersion arises from the variation in the energy level spacing, $\Delta E_{rms} \sim 50\mu eV$, contributing $h/\Delta E_{rms} = 80\,ps$ to the coherence decay. The coherent lifetime of the condensate is on the order of a few tens of picoseconds, found by converting the decay length of the ballistically expanding condensate into time.

The temporal width of the condensate wavepacket (coherence revival width), Δt (Fig. 10.7g), corresponds to the number of SHO states observed, $\Delta t \simeq t_r/N_{SHO}$, (with $N_{SHO} \sim 10$ well above threshold).

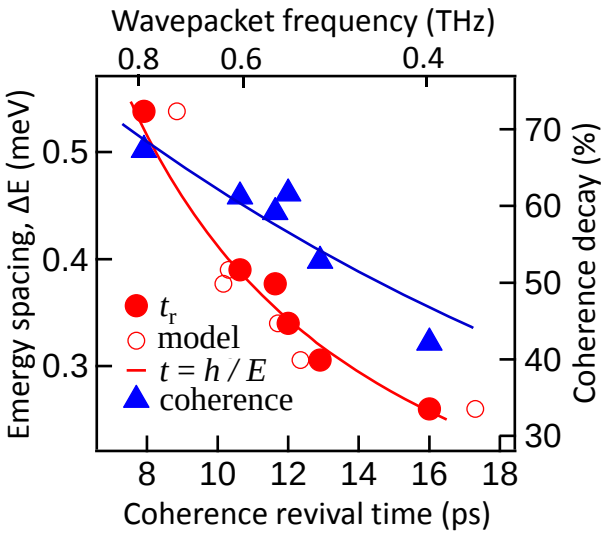

Figure 10.8: Measured time-delay of the coherence revival (bottom axis), for different pump configurations, plotted against the SHO energy separation (left axis, red dots). Predictions are from Fourier relation (red line) and measured potential (red open circles, see text). Right axis: Coherence revival amplitude ratio vs time delay (blue dots), with exponential fit (blue line). Top axis is obtained from the bottom one.

The p-SHO present many analogies with optical pulses propagating inside a nonlinear medium. In fact, the cGL equation describing polariton dynamics is a generalization of

the nonlinear Maxwell equations with susceptibility χ so that $i\partial_t E = [\chi^{(1)} + \chi^{(3)}|E|^2]E$. Whereas propagating optical pulses generate equally spaced sidebands through four-wave mixing [222], condensate polaritons analogously parametrically scatter to give new coherent polariton states. In optics, such nonlinear dispersions can produce solitons and lead to mode-locking of laser cavity modes to produce trains of coherent intense pulses [222]. Here polaritonic wavepackets appear spontaneously, bouncing back and forth between the two pump spots, corresponding exactly to the spectral and spatial organization observed. These $0.3 - 1.0$ THz SHO sidebands, generated by a propagating condensate wavepacket moving through its own nonlinear potential, correspond to the frequency micro-combs recently observed in cavity optomechanics [223].

10.4 Conclusions

We have shown that, under two separate spots excitation, the blue shift of polaritons created by the two spots self-assembles into a harmonic potential, making our system the quantum analogue of a pendulum. Instead of typical Josephson-junction coherent coupling phenomena [224], new effects arise when two neighbouring polariton condensates interact because of the quasiparticle interactions.

Imaging spectroscopy revealed the occupation of several states equally spaced in energy, which could be accurately fitted by Hermite polynomials, the solution of the quantum harmonic oscillator.

Our results resembles previous measurements reported in Ref. [110], where polaritons confined by the edge of a 1D microcavity and the pumping spot have been shown to occupy quantised energy states with a number of nodes that increase with energy. However in our case the confinement is fully provided by the pumping spots, and in this case the reservoir shape and non-linearities provide a fully harmonic trap.

Furthermore, simulations using the complex Ginzburg-Landau equation reproduced this occupation of equally spaced levels in a harmonic potential and exhibited features that resemble oscillating dark solitons.

Mode-locking of the different condensates, resembling that in mode-locked lasers based on nonlinear refraction, was demonstrated by interferometry: loss and renewal of the coherence was observed by scanning the time delay between two arms of an imaging Michelson interferometer. This demonstrated that our polariton harmonic oscillator can be properly described by spontaneously oscillating wavepackets. We achieved control of such polariton-condensate wavepackets, with changes in the pump spacing and power changing the oscillation period. This demonstrates the great potential of semiconductor MCs for integrated semiconductor-based condensate devices.

Chapter 11

Appendices

11.1 Reservoir outflow and spatial-ring condensation

In Chapter 8 it has been shown that the micron-scale polariton reservoir resulting from the tight pump spot efficiently feeds the macroscopic quantum state, which appears above the threshold pump power for condensation (Fig. 8.1). However, in complete contrast to Ref. [110], our experiments, for the first time, show a clear ring emission profile in *real space*, with minimum intensity in the centre. Here we discuss the relation of this ring-shaped condensate to the way reservoir polaritons cool down and condense.

While spatial images below threshold show incoherent emission from the central pumped spot [Figs. 8.3a and 8.1(left inset)], above threshold the coherent condensate emission develops in a ring surrounding the pump $10\mu m$ across [Figs. 8.3b and 8.1(right inset)] independent of precise position on the semiconductor wafer, which becomes more pronounced at high powers (Fig.8.3c).

The mechanism leading to this spatial ring is revealed by the weak uncondensed hot background polariton luminescence in the same spectra (Figs. 8.3) above the condensate energy. The Λ-shaped emission observed originates $5\,meV$ above the $k = 0$ polariton and drops in energy with distance from the centre (dashed) until it meets the ring condensate exactly at its intensity maximum at $r = r_c$. The Λ-shaped emission is also observed below threshold. These hot polaritons possess a large momentum and come from the high momentum polariton reservoir close to the bottleneck. Despite expanding from the pump spot, they decelerate, thus dropping down the polariton dispersion (see sequence in Fig. 11.1). While condensed polaritons cannot inelastically scatter, the incoherent polaritons decelerate in a systematic way. Eventually this incoherent reservoir meets the energy of the condensate and amplifies it strongly (see Fig. 11.1), leading to a ringshaped condensate. This ring is produced therefore by expanding incoherent bottleneck polaritons, which coherently amplify the ballistic polaritons without need to relaxes down to the bottom of the lower polariton branch.

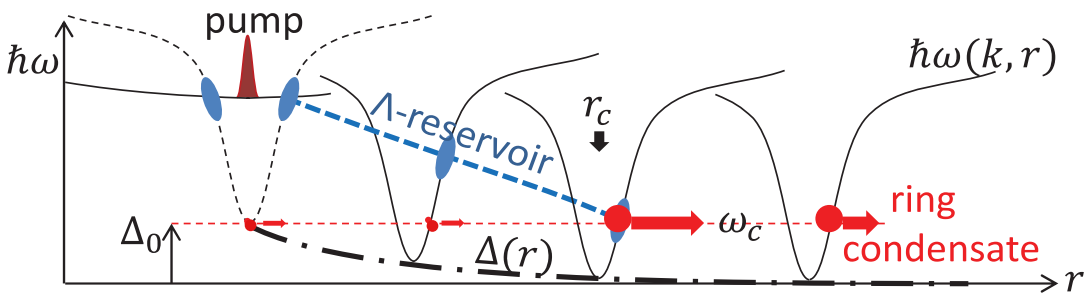

Figure 11.1: Schematic mechanism, in both real and momentum spaces, of the formation of a ring-shaped polariton condensate in real space. Dispersion relations at increasing radial positions are shown. At $r = 0$ the blueshifted dispersion contains a high-k reservoir and a $k = 0$ condensate. As the blueshift $\Delta(r)$ decreases radially from the pumping spot, the dispersion goes down in energy, the reservoir loses energy and assume a Λ-shape in real space, and the condensate maintains its energy $\hbar\omega_c$ while acquiring momentum. At a radial distance $r = r_c$, the reservoir meets the condensate whose density is greatly enhanced.

In order to clearly show that the polariton emission above the condensation threshold comes mainly from a ring in real space, we plot in Fig. 11.2a the radial dependence of the sample photoluminescence, which is integrated around a closed circle whose distance from the pump spot is plotted in the bottom axis. The different black lines are taken at different excitation powers, according to the arrow labelled as I_p, corresponding to the data shown plotted in Figs. 8.1 and 8.5b. Below threshold, incoherent polaritons building up at $k = r = 0$ are accelerated outwards with a decay length of $2.1\,\mu m$. However they experience no amplification at r_c since there is no large population in any one state (they are not Bose condensed) and stimulated scattering is thus negligible. As soon as the threshold for condensation ($10\,mW$) is surpassed, we clearly observe a bump in the emission intensity (see 5^{th} black line, from bottom to top). The ring forms at $r_c = 5.6\mu m$, and the intensity there increases by almost tenfold. As the excitation power increases the ballistic propagation of the condensate is increased due to the blueshifts which move ω_c further up the dispersion giving larger outward velocities. This makes the ring to shrink in diameter linearly with the blueshift (down to $\sim 4\mu m$ – Fig. 11.2b), and the ring intensity increases in a power law (as in Fig. 8.1).

This shrinking ring tracks the position at which the Λ reservoir intersects with the increasingly blueshifted condensate emerging from the pumped spot (see Fig. 11.1). The Λ-shaped reservoir is rigidly blueshifted with power, but less than the condensate mode itself (Fig. 11.2c), which explains why the ring radius shrinks linearly with increasing blueshift at the pumping spot.

Let us finally note that the emission peak observed at the pump spot ($r = 0$) in the graphs shown in Fig. 11.2a are due to incoherent emission and not to the condensate itself, which is confirmed by filtering the luminescence at the condensate energy — see right inset in Fig. 8.1.

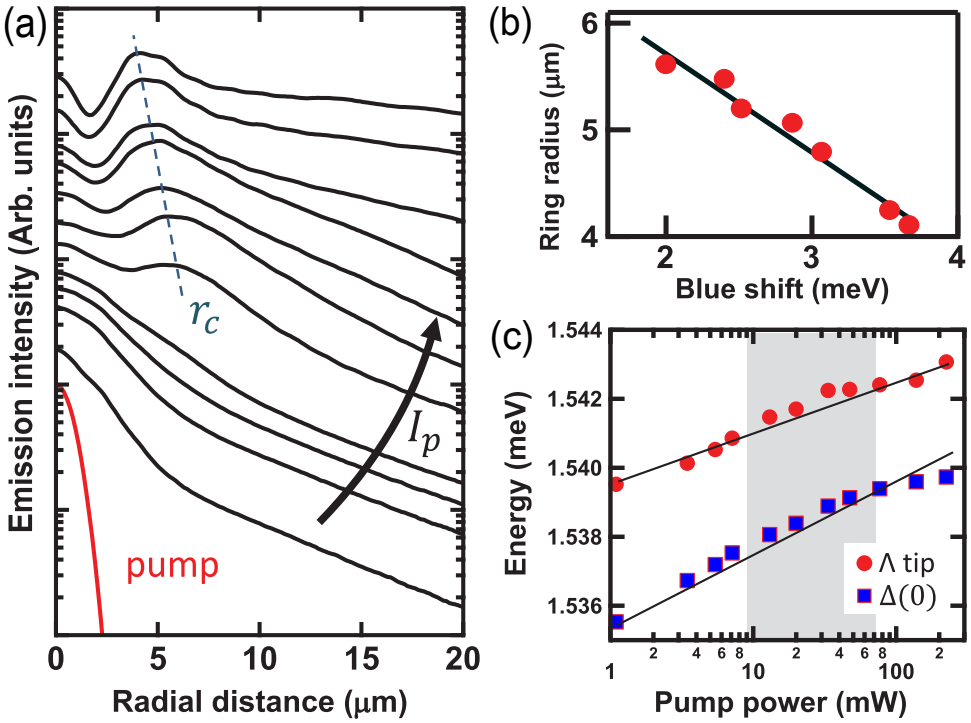

Figure 11.2: (a) Averaged radial intensity for increasing excitation powers (black lines), with excitation profile (red line). (b) Distance of the ring condensate from excitation spot vs blueshift at the excitation spots. (c) Energy of the bottom of the lower polariton branch at the excitation spot (blue squares) and energy of the Λ tip (red dots) vs excitation power. Lines are guides to the eye.

11.2 Modes shift at the pump spot

In the previous section we have seen that the reservoir injection energy is less blueshifted than the LPB itself (Fig. 11.2c), hence we conclude that the reservoir polaritons are not injected at a fixed energy above the polariton dispersion, but may experience thermally-induced energy changes at the pump spot.

Let us compare the full LPB dispersion at the excitation spot and far from it. We first fit the full condensate emission with a simple two-coupled-oscillators model (see Fig. 11.3a, in which the red arrow indicates the condensate energy). The fit yields an uncoupled photonic mode that lies below the condensate energy. This may lead to the conclusion that the cavity mode blueshifts with density, in agreement with Refs. [200,225] but in contrast with Refs. [226–228]. This however does not imply a transition to the weak-coupling regime at the pumping spot. In fact, in Fig. 8.4, from right to left (position from side to centre, or increasing densities) the dispersion becomes less steep indicating weaker photon fraction (less negative detunings).

A careful fit of the LPB, filtered in real-space to collect only the emission from the pump spot (Fig. 11.3b), indeed yield a blueshift of the cavity mode but a redshift of the excitonic mode. Possible explanations to this may include the temperature-dependence of the exciton and photon modes, which can be due to heating from laser-pumping. We investigate such a dependence under weak pumping powers in order to avoid laser-heating and dependence on free-carriers [227,228]. Figure 11.3d show fitted photon and exciton modes for different sample temperatures, tuned by electrically heating up the sample

inside the cryostat. Clearly both modes redshift when increasing the temperature, the exciton mode by higher amounts. The fit shown in Fig. 11.3c takes into account redshifts of both exciton and photon modes in accordance to Fig. 11.3d. We later rigidly blueshift the LPB in order to match the experimental data. The data is well described by a $0.8\,meV$ photon redshift, $6.0\,meV$ exciton redshift, and $3.9\,meV$ LPB rigid blueshift, all consistent with a local temperature $T \simeq 50\,K$ according to Fig. 11.3d.

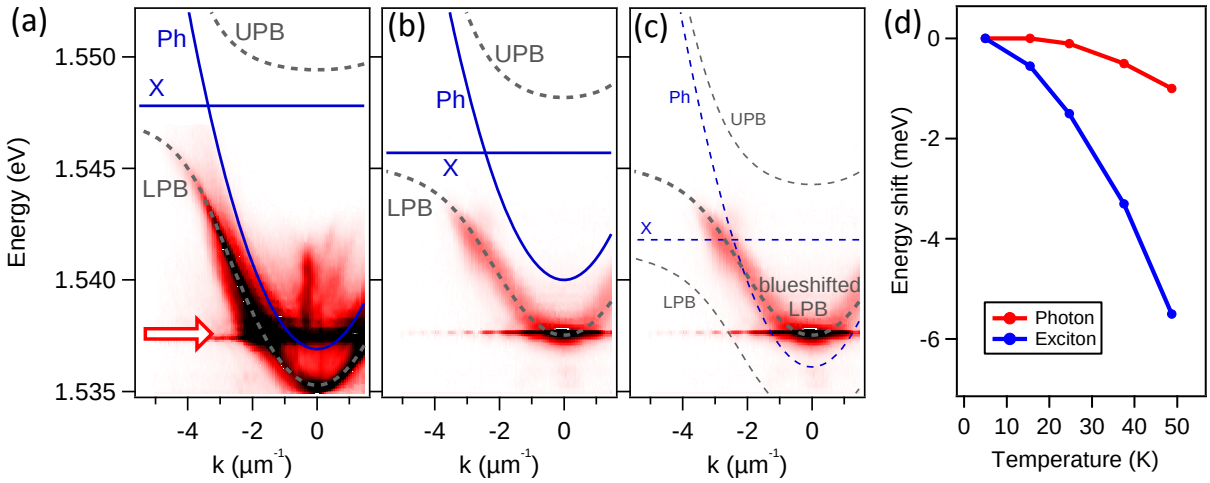

Figure 11.3: (a) Polariton outflowing condensate full dispersion, at $11\,mW$ excitation power. Fit uses a two-coupled-oscillator mode, showing bare photon (Ph) and exciton (C) modes, together with upper (UPB) and lower (LPB) polariton branches. The red arrow indicates the condensate energy. (b) Dispersion of polariton emission spatially-filtered close to the pumping spot, with fitted modes considering a $3.1\,meV$ photon blueshift and $2.1\,meV$ exciton redshift from the values used in (a). (c) Same as (b) but considering a $0.8\,meV$ photon redshift, $6.0\,meV$ exciton redshift, and $3.9\,meV$ LPB rigid blueshift. (d) Exciton and photon modes dependence on the sample temperature, under excitation powers well bellow condensation.

11.3 Sunflower ripples

In this section we discuss the influence of the sample disorder potential on the propagation of polariton condensates and its influence on the time-averaged spatial profiles experimentally recorded.

Figure 11.4a shows the real-space emission of an outflowing condensate pumped at $(0,0)\,\mu m$ above threshold ($\sim 10\,mW$). Its intensity is false-coloured in logscale in order to highlight the density profile far from the pump spot. In contrast with the smooth emission below threshold (left inset in Fig. 8), the condensate density acquires a peculiar "sunflower" spatial pattern of interference ripples, which are always observed and stable for many minutes. These self-interference ripples clearly demonstrate that a component of the quantum liquid propagates in non-radial directions. The patterns are persistent and regular, and can be decomposed by local 2D Fourier transforms within different regions of the image. Figure 11.4d show the Fourier transform intensity of the region inside the dashed-yellow circle in Fig. 11.4a. This analysis reveals that the fringe pattern results from interference of a main $\Delta k = 0$ component with many waves whose momenta lie on a circular distribution touching the origin (the symmetric circle is due to fact that

the spatial image is real-valued and so its Fourier transform is Hermitian). We also experimentally measure the momentum distribution of such a spatial region, plotted in Fig. 11.4e. Apart from the main flow peak at $k_x \simeq -2\,\mu m^{-1}$, corresponding to left-moving polaritons (represented by a red arrow in Fig. 11.4a), we observe scattered waves distributed over a circle of radius $k_c = K[\omega_c]$ (see Eq. 8.1). We therefore associate the main peak in the Fourier transform, Fig. 11.4d, with the outflowing condensate momentum, and the ring in the same figure with scattered waves whose Δk is plotted in the reference frame of the moving fluid — see Fig. 11.4e

The sunflower ripples in the condensate density is therefore an interference pattern between outwards moving polaritons and scattered waves at every point, with the summation over all Δk corresponding to the fringe periods and directions.

Confirmation of this analysis is provided firstly by simulations that interfere a circular wave (the condensate) with weaker (Rayleigh-scattered) plane waves in random directions and with random phases. The resulting image from this simple model, using 6% of the total energy in the Rayleigh components and modulating the fringe pattern by a radial profile extracted from Fig. 11.2a, reproduces impressively well the experimental observations — see Fig. 11.4b.

A more accurate theoretical description of the system is achieved when solving numerically the cubic Ginsburg-Landau (cGL) equation 9.2 using a single pump spot. To demonstrate the Rayleigh scattering we assume that the external potential V_{ext} contains disorder and is modelled by a random distribution of Fourier modes of maximum amplitude $0.1meV$ with wavelengths between $2-50\mu m$. The condensate healing length in our model is approximately $2\,\mu m$. The random potential therefore creates obstacles of size on the order of the healing length for the polariton flow. It is well-known [229] that linear sound waves are emitted as a result of supersonic flow around such small impurities. Such Čerenkov emission of sound waves is seen in Fig. 11.4c. For larger obstacles the emitted waves are not linear but are dispersive shocks consisting of oblique solitons, also seen in the same figure. Observation of these patterns implies the breakdown of superfluidity in the polariton condensate. A simple estimate shows that away from the pump spot the flow velocity, $\mathbf{v} = \hbar/m\nabla\phi$, becomes much greater than the local sound velocity, $v_c = \sqrt{g/m|\psi|^2}$, a couple of healing lengths away from the boundary of the pump spot. Therefore the flow velocity is supersonic which places the system in the Čerenkov regime where scattering is allowed.

Note that the outflow speed is much higher than the condensate speed of sound, therefore the Bogoliubov spectrum of excitations can be approximated as parabolic, which gives a circular resonant scattering ring. Studies of superfluidity in non-resonantly excited polariton condensates are still missing, and could be in principle realised in the system described here if the flow speed can be made smaller than the speed of sound. This could be achieved by appropriately shaping the pumping laser in order to spatially extend the accelerating region in such a way that the limits imposed by uncertainty relations do not blur the excitation spectrum when taking spatially-selective measurements — note that for our data the outflow is expected to be superfluid up to $2\,\mu m$ close to the pumping spot, however a spatial resolution as high as $10\,\mu m$ is enough to decrease the momentum space resolution (as seen in Fig. 8.4)

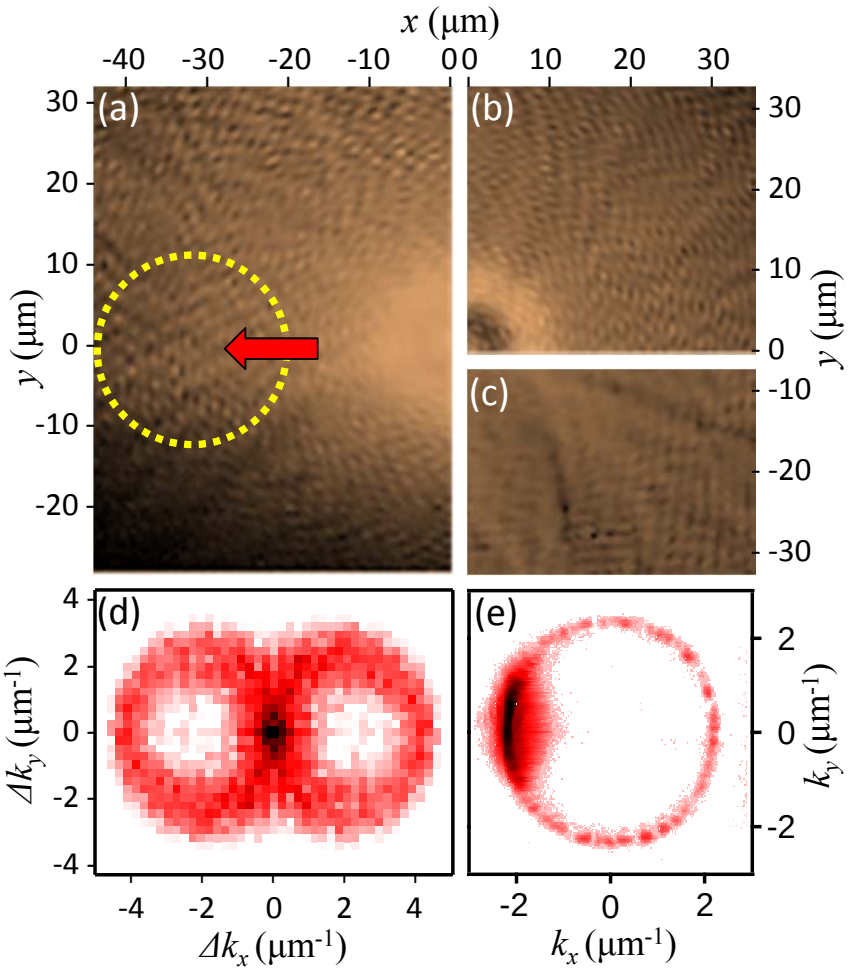

Figure 11.4: (a) Real space image of the emission (log scale), together with (d) Fourier transform and (e) k-space image spatial filtered within the circle marked. (b) Simulated interference of the condensate with Rayleigh scattered waves. (c) Simulation of the spatial polariton density using the cGL equation (see text).

11.4 Second threshold

In all studies of polariton condensation it is convenient to make a clear distinction between the strong-coupling and weak-coupling regimes. This eventually changes the interpretation of the phenomena observed, as in the case of the weak coupling regime, photon lasing is observed instead of polariton condensation: with nonlinearities requiring high excitation densities there is always a concern that the electrons are screened and that instead photon lasing is observed [226].

In this section we discuss the second intensity threshold of Fig. 8.1 and the sub-logarithmic increase of blueshift of Fig. 8.5, bot appearing at $\sim 80\,mW$.

Figures 11.5a-c show dispersion images of the full sample emission as the power is increased across the second threshold. It is clear the appearance of a second dispersion curve $\sim 2\,meV$ above the LPB. The outflowing condensate momentum, P1, is gradually transferred to the inside curve, acquiring a value C1 at the same time that a second macroscopic emission appears at lower energies. This second emission is mainly distributed over two momentum rings, one with smaller radius C2 on the inside curve, another with higher radius P2 on the LPB — see Figs. 11.5b,c. The power dependence of each of the four

momentum peaks is plotted in Fig. 11.5d.

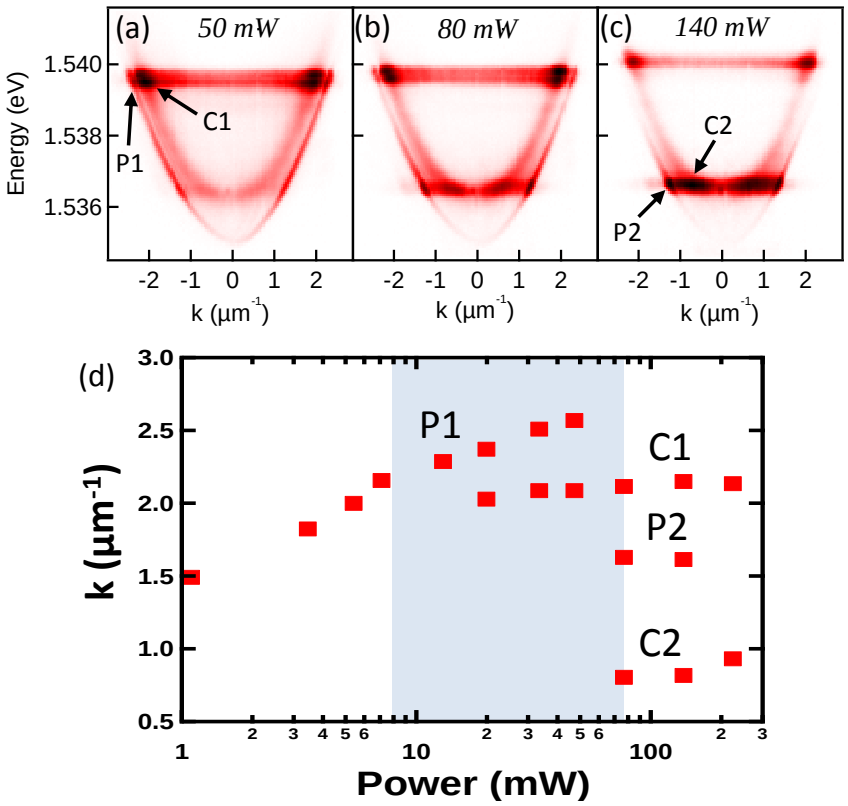

Figure 11.5: (a-c) Polariton full luminescence dispersion for increasing pump powers (indicated), with main momentum peaks marked by P1, C1, P2 and C2. Colours in log scale. (d) Power dependence of the main four momentum peaks.

The appearance of a second dispersion branch and a second energy mode, lying at $\sim 1.5365\,meV$, may have its origins in different mechanisms. A second non-linear increase of the polariton emission intensity has been identified in previous works as the break up of strong coupling and the consequent appearance of photon lasing [200,230]. The sudden appearance of a high-energy branch in Fig. 11.5 may seem to confirm such a behaviour, however the fact that the high energy macroscopic mode, at $\sim 1.54\,eV$, lies well above the bottom of the second branch and that it keeps blueshifting with power indicates that if it originates from a strong- to weak-coupling transition, the levels involved in the lasing process are shifting. This can be thought as a carrier-density-dependent blueshift of the photonic mode at the pump spot, as already discussed in Section 11.2. However this does not explain the appearance of a second, lower-energy, macroscopic mode. This mode can have its origin on parametric scattering of the upper mode into signal and idler states, an argument that is reinforced by the fact that the lower-energy mode starts building up as soon as the upper state approaches the inflection point of the LPB. However an idler state has never been observed experimentally, even when acquiring data with high-enough angular apertures and long integration times.

In Reference [110] lower energy modes have also been observed and it has been argued that they appear due to polariton relaxation that becomes more efficient at higher excitation powers. These modes presented highly extended spatial densities.

Figure 11.6a shows the spatial energy profiles corresponding to the data shown in Fig. 11.5c. The main difference with respect to lower excitation powers (Fig. 8.3) is

the appearance of a greatly-extended lower energy mode (compare its full spatial profile, Fig. 11.6c, with the higher mode one, Fig. 11.6b). Note also the dark $\sim 10\,\mu m$-wide region inside the lower energy mode, which corresponds to the blueshift-induced potential barrier.

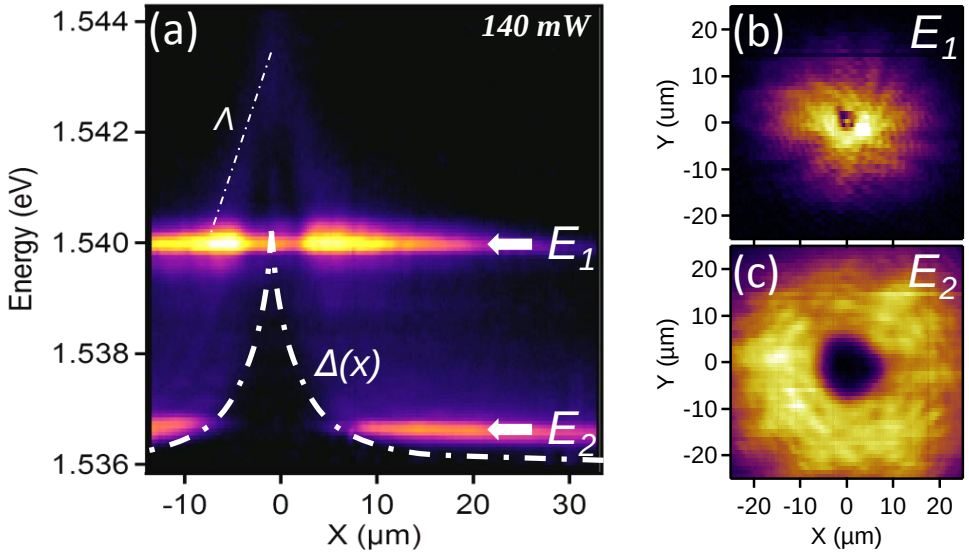

Figure 11.6: (a) $y = 0$ cross section of the spectra emitted at different distances from the pump spot, placed at $(0, 0)\,\mu m$, for $140\,mW$ excitation power (colours in log scale). $\Delta(x)$ is the schematic representation of the blueshift at each spatial point, E_1 (E_2) the energy of the first (second) macroscopic coherent mode and Λ a guide to the eye for the reservoir shape. (b,c) Tomographically reconstructed spatial profiles of first and second coherent modes, respectively.

By comparing Figs. 11.5c and 11.6a we can infer the spatially dependent dynamics of both coherent energy modes. Coherent particles are created, at the pump spot, with $k = 0$ and $E_1 \simeq 1.54\,meV$. They start moving downhill and acquire a finite momentum C1 since they keep a constant energy and the dispersion goes down. At $r \simeq 10\,\mu m$ the dispersion reaches the blueshifted branch seen in Fig. 11.5c and new coherent particles are created in the lower mode E_2 with small momentum $k_{C2} \sim 0.8\,\mu m^{-1}$. From this radius both macroscopic modes propagate outwards keeping their energy and momentum for long distances, until eventually the dispersion comes back to the LPB and both modes acquire momenta P1 and P2.

The appearance of a second macroscopic mode explains why the blueshift at the pumping spot starts saturating at the second threshold (see Fig. 8.5b, open dots): particles are swiftly ejected from the pumping spot with energy E_2, reducing the amount of carriers at the pump spot. It is also remarkable that, although possessing a smaller flow speed (small momentum), the second mode is much more extended than the first mode. This is compatible with the aforementioned parametric scattering processes between the first and second energy modes.

11.5 Reference flat-phase region for interferometry

When performing interferences in order to extract phase profiles, a reference constant-phase beam can be approximated by a vortex-free expanded region of the condensate.

In this technique, introduced in Refs. [20, 36], a small portion of this constant phase reference wave is magnified, and interfered with the sample emission in a Mach-Zehnder interferometer — see Section 4.3

For the data presented in Chapter 9 we have chosen as a flat-phase profile an expanded region behind one of the pumping spots. The schematic representation of the interferometry procedure is shown in Fig. 11.7, in which Eq. 9.1 has been used with three pumping spots to simulate the lattice wavefunction. The beam from one Mach-Zehnder arm, Fig. 11.7a, is interfered with a region outwards one of the pump spots, expanded in the other interferometer arm, marked by a circle in Fig. 11.7b. The resulting interference pattern in the region marked by a dashed-black square in Fig. 11.7c, and enlarged in Fig. 11.7d, is obtained with an angle in such a way that the phase of the condensate can be extracted after Fourier transform analysis.

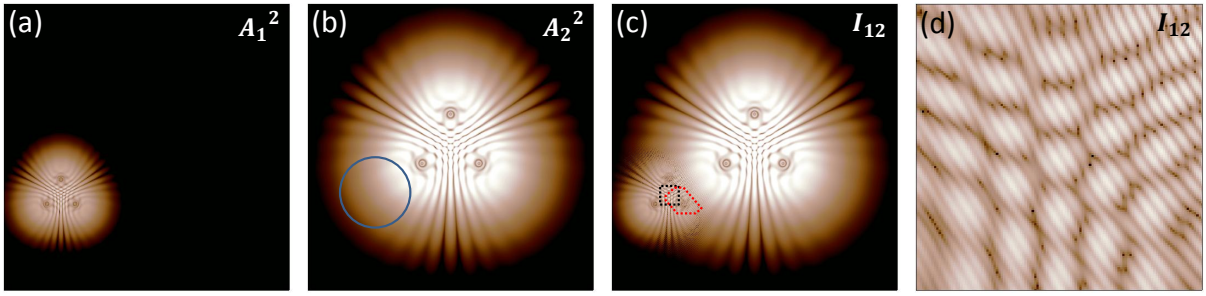

Figure 11.7: Interference geometry used in Chapter 9. All images are simulated using Eq. 9.1. Lattice emission from the Mach-Zehnder (a) normal and (b) expanded arm. (c) Interference between both arms, with (d) showing the region inside black dashed square in (c).

We have experimentally checked that our choice is a good approximation for a reference wave by looking at the fringes a region corresponding to the one marked by the polygon depicted with a red dashed line in Fig. 11.7c — see Fig. 11.8. Whereas fringe dislocations are seen in the vortex lattice region, outwards the pump spot the fringes are continuous.

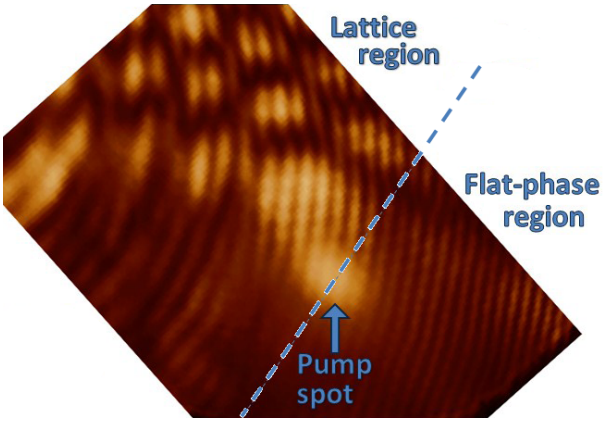

Figure 11.8: Experimental interference between the full lattice emission and an expanded region outwards one of the pump spots, as sketched in Fig. 11.7c.

General conclusions and future perspectives

The research carried on during this PhD thesis is part of the world efforts to further develop photonic technologies based of semiconductor chips, which developed as an outgrowth of the first practical semiconductor light emitters invented in the early 1960s and optical fibres developed in the 1970s. The samples investigated are conceptually similar to VCSEL structures, invented in the late 1970s and present in a great number of devices nowadays, but it was only with the development of modern epitaxial growth techniques that microcavities achieved a high enough quality as to reveal the strong–coupling regime [5]. This inaugurated a new era of cavity-quantum-electrodynamics studies in nanostructured semiconductors, which is an extremely active field nowadays and a promising candidate for the development of quantum information technologies, including cryptography, simulation and computation [197].

The state-of-the-art microcavities, working in the strong-coupling regime, allow for the carrier density to be increased up to values where the quantum nature of the bosonic particles start to be important, in which case exciton-polaritons enter a new state where a macroscopic number of particles occupy a single quantum state. In this new regime, similar to a Bose-Einstein condensate, polaritons can propagate and be manipulated along macroscopic distances without loosing their coherence. Moreover, due to their strong repulsive interactions, coherent polariton fluids have been shown to present a number of non-linear phenomena with potential applications in photonic circuits [21–34].

Apart from a new platform for technological applications, polaritons form an experimental system in which the frontiers of physics can be investigated in a relatively easy way, since their properties are inherited by the photons emitted by the cavities and therefore can be readily measured. Although presenting many analogies with Bose-Einstein condensation and with superfluidity, the out-of-equilibrium character of polariton quantum fluids poses fundamental questions about the proper way of describing their behaviour.

Our research group in Madrid has observed the suppression of Rayleigh scattering when making polariton bullets, created in the OPO regime, flow against defects [18]. A year later, at the start of this PhD thesis, our main goal was to check whether polariton quantum fluids, also created in the OPO regime, display one of the most remarkable properties of superfluids: persistent flow.

In Chapter 5, we showed that polaritons can indeed sustain the quantised circulation of an injected vortex for times much longer than the polariton and the parametrically-excitation population lifetimes. Moreover, we gave clear indications that circulation can be transferred into a polariton condensate initially at rest, and in this case the vortex state constitutes a new metastable solution to the system, with no apparent dissipation.

A careful analysis, made in Chapter 6, showed that the injection of a quantised vortex into a polariton quantum fluid is accompanied by the appearance of an unintended

antivortex. We explained the mechanisms underlying the creation of such an antivortex in terms of the fluid currents that appear due to the condensate out-of-equilibrium character. Such currents are responsible for the deterministic trajectory followed by vortices in such a way that they can be detected in multiple-shots measurements.

Following the concepts developed in atom BECs, we proceeded to study the stability of doubly-quantised vortices in Chapter 7, finding behaviours unique to polariton fluids: 1) an $M = 2$ vortex imprinted into the coherent fluid was found to split into two $M = 1$ vortices, which was explained in terms of the flow currents experienced by the vortex and the intricate OPO dispersion dynamics during the imprinting process; 2) a TOPO-only $M = 2$ vortex is stable only if injected with an in-plane momentum smaller than a critical value for which the LPB dispersion starts deviating from parabolic.

The use of last-generation samples has allowed us to non-resonantly excite polariton condensates highly extended in space and to optically-control their flow, as described in Chapter 8. We reported, in Chapters 9 and 10 on different fascinating phenomena appearing when making many of such outflowing condensates interact. The use of multiple regularly-spaced spots showed that each condensate behave analogously to spins in (anti-)ferromagnetic systems, paving the way towards quantum simulation using polariton condensates. In this case we also showed that the interference between the outflows from each pump spot generate regular vortex-antivortex lattices, constituting their first observation inside semiconductor microcavities and suggesting that new polariton-based interferometric devices can be built.

In Chapter 9 the non-linear character of polaritons has been shown to destabilize square lattices of dark-solitons, generating vortices that move inside square guides, paving the way towards to generation of quantum fluidic circuits. Polariton non-linearities also play an important role in Chapter 10, where the quantum fluid self-organizes to create an harmonic trap that contains an oscillating wavepacket, self-sustained by parametric scattering processes that preferably create equally-spaced, mutually-coherent, energy modes. These findings present many analogies with mode-locking processes found in non-linear optical systems, suggesting once more that polaritons can be a new platform for optoelectronic devices.

Our methods allow the optical generation and manipulation of 2D condensates in arbitrary locations inside semiconductor chips, but also requires further investigations to be done. We showed how to control the flow speed of non-resonantly excited polariton condensates and how Rayleigh scattering processes change the spatial pattern in a peculiar way, as discussed in Appendix 11.3. Although superfluidity has been carefully addressed under resonant pumping geometries, the excitation spectrum of non-resonantly-excited polariton fluid is expected to by remarkably different (diffusive [156]). It is therefore of great importance to carefully investigate superfluidity in these systems. Moreover, although superfluid-related phenomena has been found in polariton fluids created under OPO excitation [18, 20], the predicted diffusive Goldstone mode [141] has never been observed, which requests new experiments to be done.

Let us finally say that, at the frontier of research, microcavities bring the quantum optics and photonics laboratories into a single chip. Using modern crystal growth techniques, photonic components can be nanostructured into semiconductor chips, allowing for light propagation and manipulation in the micrometer scale. The study of light-matter interactions in semiconductor microcavities is an interdisciplinary field at the interface between optics and solid-state physics, having a fascinating cross-talk with fluid dynamics, thermodynamics, magnetism, quantum information, cavity QED, astrophysics, etc.

Bibliography

[1] Miller, D. A. B. Are optical transistors the logical next step? *Nature Photonics* **4**, 3–5 (2010).

[2] Baehr-Jones, T. *et al.* Myths and rumours of silicon photonics. *Nature Photonics* **6**, 206–208 (2012).

[3] Hall, R. N., Fenner, G. E., Kingsley, J. D., Soltys, T. J. & Carlson, R. O. Coherent light emission from GaAs junctions. *Physical Review Letters* **9**, 366–368 (1962).

[4] Soda, H., ichi Iga, K., Kitahara, C. & Suematsu, Y. GaInAsP/InP surface emitting injection lasers. *Japanese Journal of Applied Physics* **18**, 2329–2330 (1979).

[5] Weisbuch, C., Nishioka, M., Ishikawa, A. & Arakawa, Y. Observation of the coupled exciton-photon mode splitting in a semiconductor quantum microcavity. *Physical Review Letters* **69**, 3314–3317 (1992).

[6] Penrose, O. & Onsager, L. Bose-Einstein condensation and liquid helium. *Physical Review* **104**, 576–584 (1956).

[7] Anderson, M. H., Ensher, J. R., Matthews, M. R., Wieman, C. E. & Cornell, E. A. Observation of Bose-Einstein condensation in a dilute atomic vapor. *Science* **269**, 198–201 (1995).

[8] Davis, K. B. *et al.* Bose-Einstein condensation in a gas of *sodium* atoms. *Physical Review Letters* **75**, 3969–3973 (1995).

[9] Andrews, M. R. *et al.* Observation of interference between two bose condensates. *Science* **275**, 637–641 (1997).

[10] Anderson, B. P. & Kasevich, M. A. Macroscopic quantum interference from atomic tunnel arrays. *Science* **282**, 1686–1689 (1998).

[11] Cataliotti, F. S. *et al.* Josephson junction arrays with Bose-Einstein condensates. *Science* **293**, 843–846 (2001).

[12] Gupta, S., Dieckmann, K., Hadzibabic, Z. & Pritchard, D. E. Contrast interferometry using Bose-Einstein condensates to measure h/m and α. *Physical Review Letters* **89**, 140401 (2002).

[13] Wang, Y.-J. *et al.* Atom Michelson interferometer on a chip using a Bose-Einstein condensate. *Physical Review Letters* **94**, 090405 (2005).

[14] Deng, H., Weihs, G., Santori, C., Bloch, J. & Yamamoto, Y. Condensation of semiconductor microcavity exciton polaritons. *Science* **298**, 199–202 (2002).

[15] Kasprzak, J. *et al.* Bose-Einstein condensation of exciton polaritons. *Nature* **443**, 409–414 (2006).

[16] Balili, R., Hartwell, V., Snoke, D., Pfeiffer, L. & West, K. Bose-Einstein condensation of microcavity polaritons in a trap. *Science* **316**, 1007–1010 (2007).

[17] Christopoulos, S. *et al.* Room-temperature polariton lasing in semiconductor microcavities. *Physical Review Letters* **98**, 126405 (2007).

[18] Amo, A. *et al.* Collective fluid dynamics of a polariton condensate in a semiconductor microcavity. *Nature* **457**, 291–295 (2009).

[19] Amo, A. *et al.* Superfluidity of polaritons in semiconductor microcavities. *Nature Physics* **5**, 805–810 (2009).

[20] Sanvitto, D. *et al.* Persistent currents and quantized vortices in a polariton superfluid. *Nature Physics* **6**, 527–533 (2010).

[21] Saba, M. *et al.* High-temperature ultrafast polariton parametric amplification in semiconductor microcavities. *Nature* **414**, 731–735 (2001).

[22] Bajoni, D. *et al.* Optical bistability in a GaAs-based polariton diode. *Physical Review Letters* **101**, 266402 (2008).

[23] Liew, T. C. H., Kavokin, A. V. & Shelykh, I. A. Optical circuits based on polariton neurons in semiconductor microcavities. *Physical Review Letters* **101**, 016402 (2008).

[24] Shelykh, I. A., Pavlovic, G., Solnyshkov, D. D. & Malpuech, G. Proposal for a mesoscopic optical Berry-phase interferometer. *Physical Review Letters* **102**, 046407 (2009).

[25] Amo, A. *et al.* Exciton-polariton spin switches. *Nature Photonics* **4**, 361–366 (2010).

[26] Paraiso, T. K., Wouters, M., Leger, Y., Morier-GenoudF. & B., D.-P. Multistability of a coherent spin ensemble in a semiconductor microcavity. *Nature Materials* **9**, 655660 (2010).

[27] Liew, T. C. H. *et al.* Exciton-polariton integrated circuits. *Physical Review B* **82**, 033302 (2010).

[28] Liew, T. C. H., Shelykh, I. A. & Malpuech, G. Polaritonic devices. *Physica E: Low-dimensional Systems and Nanostructures* **43**, 1543–1568 (2011).

[29] Sich, M. *et al.* Observation of bright polariton solitons in a semiconductor microcavity. *Nature Photonics* **6**, 50–55 (2012).

[30] Ballarini, D. *et al.* All-optical polariton transistor. *arXiv:1201.4071v2* (2012).

[31] Tosi, G. *et al.* Sculpting oscillators with light within a nonlinear quantum fluid. *Nature Physics* **8**, 190–194 (2012).

[32] Tosi, G. *et al.* Geometrically-locked vortex lattices in semiconductor quantum fluids. *Nature Communications* **3**, 1243 (2012).

[33] Gao, T. *et al.* Polariton condensate transistor switch. *Physical Review B* **85**, 235102 (2012).

[34] Anton, C. *et al.* Dynamics of a polariton condensate transistor switch. *Applied Physics Letters* **101**, 261116 (2012).

[35] Tosi, G. *et al.* Vortex stability and permanent flow in nonequilibrium polariton condensates. *Journal of Applied Physics* **109**, 102406 (2011).

[36] Tosi, G. *et al.* Onset and dynamics of vortex-antivortex pairs in polariton optical parametric oscillator superfluids. *Physical Review Letters* **107**, 036401 (2011).

[37] Christmann, G. *et al.* Polariton ring condensates and sunflower ripples in an expanding quantum liquid. *Physical Review B* **85**, 235303 (2012).

[38] Yu, P. & Cardona, M. *Fundamentals of Semiconductors: Physics and Materials Properties*. Graduate Texts in Physics (Springer, 2010).

[39] Kavokin, A., Baumberg, J., Malpuech, G. & Laussy, F. *Microcavities* (Oxford University Press, 2007).

[40] Jackson, J. *Classical Electrodynamics* (Wiley, 1999).

[41] Boyd, R. *Nonlinear Optics* (Academic Press, 2008).

[42] Vahala, K. J. Optical microcavities. *Nature* **424**, 839–846 (2003).

[43] Goppl, M. *et al.* Coplanar waveguide resonators for circuit quantum electrodynamics. *Journal of Applied Physics* **104**, 113904 (2008).

[44] Hopfield, J. J. Theory of the contribution of excitons to the complex dielectric constant of crystals. *Physical Review* **112**, 1555–1567 (1958).

[45] Deveaud, B. *et al.* Enhanced radiative recombination of free excitons in GaAs quantum wells. *Physical Review Letters* **67**, 2355–2358 (1991).

[46] Novotny, L. Strong coupling, energy splitting, and level crossings: A classical perspective. *American Journal of Physics* **78**, 1199–1202 (2010).

[47] Norris, T. B. *et al.* Time-resolved vacuum Rabi oscillations in a semiconductor quantum microcavity. *Physical Review B* **50**, 14663–14666 (1994).

[48] Kaluzny, Y., Goy, P., Gross, M., Raimond, J. M. & Haroche, S. Observation of self-induced rabi oscillations in two-level atoms excited inside a resonant cavity: The ringing regime of superradiance. *Physical Review Letters* **51**, 1175–1178 (1983).

[49] Jaynes, E. & Cummings, F. Comparison of quantum and semiclassical radiation theories with application to the beam maser. *Proceedings of the IEEE* **51**, 89–109 (1963).

[50] Thompson, R. J., Rempe, G. & Kimble, H. J. Observation of normal-mode splitting for an atom in an optical cavity. *Physical Review Letters* **68**, 1132–1135 (1992).

[51] Wallraff, A. *et al.* Strong coupling of a single photon to a superconducting qubit using circuit quantum electrodynamics. *Nature* **431**, 162–167 (2004).

[52] Streater, R. & Wightman, A. *PCT, Spin and Statistics, and All That.* Landmarks in Physics (Princeton University Press, 1964).

[53] Leggett, A. J. Quantum liquids. *Science* **319**, 1203–1205 (2008).

[54] Einstein, A. *Abh. Preuss. Akad. Wiss.* **3**, 18 (1925).

[55] Pitaevskii, L. P. & Stringari, S. *Bose-Einstein Condensation* (Oxford University Press, 2003).

[56] Klaers, J., Vewinger, F. & Weitz, M. Thermalization of a two-dimensional photonic gas in a white wall photon box. *Nature Physics* **6**, 512–515 (2010).

[57] Klaers, J., Schmitt, J., Vewinger, F. & Weitz, M. Bose-Einstein condensation of photons in an optical microcavity. *Nature* **468**, 545–548 (2010).

[58] Weitz, M., Klaers, J. & Vewinger, F. Optomechanical generation of a photon Bose-Einstein condensate. *arXiv:1211.4793* (2012).

[59] Bogoliubov, N. N. *Journal of Phys. USSR* **11**, 23 (1947).

[60] Landau, L. D. & Lifshitz, E. M. *Quantum Mechanics* (Pergamon, Oxford, 1987).

[61] Lee, T. D. & Yang, C. N. Many-body problem in quantum mechanics and quantum statistical mechanics. *Physical Review* **105**, 1119–1120 (1957).

[62] Lee, T. D., Huang, K. & Yang, C. N. Eigenvalues and eigenfunctions of a Bose system of hard spheres and its low-temperature properties. *Physical Review* **106**, 1135–1145 (1957).

[63] Steinhauer, J., Ozeri, R., Katz, N. & Davidson, N. Excitation spectrum of a Bose-Einstein condensate. *Physical Review Letters* **88**, 120407 (2002).

[64] Kapitza, P. Viscosity of liquid helium below the l-point. *Nature* **141**, 74 (1938).

[65] Allen, J. F. & Misener, A. D. Flow of liquid Helium II. *Nature* **141**, 75 (1938).

[66] Leitner, A. Superfluid liquid helium (isotope 4) (1963). URL `http://alfredleitner.com/superfluid.html`.

[67] Donnelly, R. J. The discovery of superfluidity. *Physics Today* **48**, 30–36 (1995).

[68] Landau, L. Theory of the superfluidity of Helium II. *Physical Review* **60**, 356–358 (1941).

[69] Landau, L. D. The theory of superfluity of Helium III. *Journal of Physics USSR* **5**, 7190 (1941).

[70] Jelley, J. *Čerenkov radiation, and its applications* (Pergamon Press, 1958).

[71] Carusotto, I., Hu, S. X., Collins, L. A. & Smerzi, A. Bogoliubov-Čerenkov radiation in a Bose-Einstein condensate flowing against an obstacle. *Physical Review Letters* **97**, 260403 (2006).

[72] Cornell, E. Experiments in rotating, spinning, and shocked BECs (talk at the KITP conference on quantum gases) (2004). URL `http://online.itp.ucsb.edu/online/gases_c04/cornell/oh/107.html`.

[73] Weiner, A. *Ultrafast Optics* (John Wiley & Sons, 2011).

[74] Laussy, F. P., del Valle, E. & Tejedor, C. Luminescence spectra of quantum dots in microcavities. i. bosons. *Physical Review B* **79**, 235325 (2009).

[75] Manni, F., Lagoudakis, K. G., Andre, R., Wouters, M. & Deveaud, B. Penrose-onsager criterion validation in a one-dimensional polariton condensate. *Physical Review Letters* **109**, 150409 (2012).

[76] Dalfovo, F., Giorgini, S., Pitaevskii, L. P. & Stringari, S. Theory of Bose-Einstein condensation in trapped gases. *Reviews of Modern Physics* **71**, 463–512 (1999).

[77] Bloch, I., Hansch, T. W. & Esslinger, T. Measurement of the spatial coherence of a trapped bose gas at the phase transition. *Nature* **403**, 166–170 (2000).

[78] Mermin, N. D. & Wagner, H. Absence of ferromagnetism or antiferromagnetism in one- or two-dimensional isotropic heisenberg models. *Physical Review Letters* **17**, 1133–1136 (1966).

[79] Hohenberg, P. C. Existence of long-range order in one and two dimensions. *Physical Review* **158**, 383–386 (1967).

[80] Berezinskii, V. L. Destruction of long-range order in one-dimensional and two-dimensional systems possessing a continuous symmetry group. II. Quantum systems. *Soviet Journal of Experimental and Theoretical Physics* **34**, 610 (1972).

[81] Kosterlitz, J. M. & Thouless, D. J. Ordering, metastability and phase transitions in two-dimensional systems. *Journal of Physics C: Solid State Physics* **6**, 1181–1203 (1973).

[82] Hadzibabic, Z., Kruger, P., Cheneau, M., Battelier, B. & Dalibard, J. Berezinskii-Kosterlitz-Thouless crossover in a trapped atomic gas. *Nature* **441**, 1118–1121 (2006).

[83] Gross, E. Structure of a quantized vortex in boson systems. *Il Nuovo Cimento Series 10* **20**, 454–477 (1961).

[84] Pitaevskii, L. P. Vortex lines in an imperfect Bose gas. *Soviet Physics JETP-USSR* **13**, 451 (1961).

[85] Onsager, L. Statistical hydrodynamics. *Nuovo Cimento* **6**, 279 (1949).

[86] Feynman, R. Chapter II Application of quantum mechanics to liquid helium. In Gorter, C. (ed.) *Progress in Low Temperature Physics*, vol. 1 of *Progress in Low Temperature Physics*, 17–53 (Elsevier, 1955).

[87] Nye, J. F. & Berry, M. V. Dislocations in wave trains. *Proceedings of the Royal Society of London. A. Mathematical and Physical Sciences* **336**, 165–190 (1974).

[88] Staliunas, K. & Morcillo, V. *Transverse Patterns in Nonlinear Optical Resonators.* Springer Tracts in Modern Physics (Springer, 2003).

[89] Desyatnikov, A. S., Kivshar, Y. S. & Torner, L. Optical vortices and vortex solitons **47**, 291–391 (2005).

[90] Hess, G. B. & Fairbank, W. M. Measurements of angular momentum in superfluid Helium. *Physical Review Letters* **19**, 216–218 (1967).

[91] Packard, R. E. & Sanders, T. M. Observations on single vortex lines in rotating superfluid helium. *Physical Review A* **6**, 799–807 (1972).

[92] Yarmchuk, E. J., Gordon, M. J. V. & Packard, R. E. Observation of stationary vortex arrays in rotating superfluid helium. *Physical Review Letters* **43**, 214–217 (1979).

[93] Madison, K. W., Chevy, F., Wohlleben, W. & Dalibard, J. Vortex formation in a stirred Bose-Einstein condensate. *Physical Review Letters* **84**, 806–809 (2000).

[94] Abo-Shaeer, J. R., Raman, C., Vogels, J. M. & Ketterle, W. Observation of vortex lattices in Bose-Einstein condensates. *Science* **292**, 476–479 (2001).

[95] Abrikosov, A. A. On the magnetic properties of superconductors of the second group. *Soviet Physics JETP* **5**, 1174 (1957).

[96] Chevy, F. Ph.D. thesis, Laboratoire Kastler Brossel, Ecole Normale Superieure, Paris (2001).

[97] Ryu, C. *et al.* Observation of persistent flow of a Bose-Einstein condensate in a toroidal trap. *Physical Review Letters* **99**, 260401 (2007).

[98] Moskalenko, S. & Snoke, D. *Bose-Einstein Condensation of Excitons and Biexcitons: And Coherent Nonlinear Optics with Excitons* (Cambridge University Press, 2005).

[99] Eisenstein, J. P. & MacDonald, A. H. Bose-Einstein condensation of excitons in bilayer electron systems. *Nature* **432**, 691–694 (2004).

[100] High, A. A. *et al.* Spontaneous coherence in a cold exciton gas. *Nature* **483**, 584–588 (2012).

[101] Imamoglu, A., Ram, R. J., Pau, S. & Yamamoto, Y. Nonequilibrium condensates and lasers without inversion: Exciton-polariton lasers. *Physical Review A* **53**, 4250–4253 (1996).

[102] Dang, L. S., Heger, D., Andre, R., Boeuf, F. & Romestain, R. Stimulation of polariton photoluminescence in semiconductor microcavity. *Physical Review Letters* **81**, 3920–3923 (1998).

[103] Stevenson, R. M. *et al.* Continuous wave observation of massive polariton redistribution by stimulated scattering in semiconductor microcavities. *Physical Review Letters* **85**, 3680–3683 (2000).

[104] Baumberg, J. J. *et al.* Parametric oscillation in a vertical microcavity: A polariton condensate or micro-optical parametric oscillation. *Physical Review B* **62**, R16247–R16250 (2000).

[105] Richard, M., Kasprzak, J., Romestain, R., Andre, R. & Dang, L. S. Spontaneous coherent phase transition of polaritons in CdTe microcavities. *Physical Review Letters* **94**, 187401 (2005).

[106] Kasprzak, J., Solnyshkov, D. D., Andre, R., Dang, L. S. & Malpuech, G. Formation of an exciton polariton condensate: Thermodynamic versus kinetic regimes. *Physical Review Letters* **101**, 146404 (2008).

[107] Christmann, G., Butte, R., Feltin, E., Carlin, J.-F. & Grandjean, N. Room temperature polariton lasing in a GaN/AlGaN multiple quantum well microcavity. *Applied Physics Letters* **93**, 051102 (2008).

[108] Love, A. P. D. *et al.* Intrinsic decoherence mechanisms in the microcavity polariton condensate. *Physical Review Letters* **101**, 067404 (2008).

[109] Wertz, E. *et al.* Spontaneous formation of a polariton condensate in a planar GaAs microcavity. *Applied Physics Letters* **95**, 051108 (2009).

[110] Wertz, E. *et al.* Spontaneous formation and optical manipulation of extended polariton condensates. *Nature Physics* **6**, 860–864 (2010).

[111] Assmann, M. *et al.* From polariton condensates to highly photonic quantum degenerate states of bosonic matter. *Proceedings of the National Academy of Sciences* **108**, 1804–1809 (2011).

[112] Spano, R. *et al.* Build up of off-diagonal long-range order in microcavity exciton-polaritons across the parametric threshold. *arXiv:1111.4894* (2011).

[113] Spano, R. *et al.* Coherence properties of exciton polariton OPO condensates in one and two dimensions. *New Journal of Physics* **14**, 075018 (2012).

[114] Lagoudakis, K. G. *et al.* Quantized vortices in an exciton-polariton condensate. *Nature Physics* **4**, 706–710 (2008).

[115] Lagoudakis, K. G. *et al.* Observation of half-quantum vortices in an exciton-polariton condensate. *Science* **326**, 974–976 (2009).

[116] Roumpos, G. *et al.* Single vortex-antivortex pair in an exciton-polariton condensate. *Nature Physics* **7**, 129–133 (2011).

[117] Roumpos, G. *et al.* Power-law decay of the spatial correlation function in exciton-polariton condensates. *Proceedings of the National Academy of Sciences* **109**, 64676472 (2012).

[118] Sanvitto, D. *et al.* All-optical control of the quantum flow of a polariton condensate. *Nature Photonics* **5**, 610–614 (2011).

[119] Nardin, G. *et al.* Hydrodynamic nucleation of quantized vortex pairs in a polariton quantum fluid. *Nature Physics* **7**, 635–641 (2011).

[120] Grosso, G., Nardin, G., Morier-Genoud, F., Leger, Y. & Deveaud-Pledran, B. Soliton instabilities and vortex street formation in a polariton quantum fluid. *Physical Review Letters* **107**, 245301 (2011).

[121] Amo, A. *et al.* Polariton superfluids reveal quantum hydrodynamic solitons. *Science* **332**, 1167–1170 (2011).

[122] Hivet, R. *et al.* Half-solitons in a polariton quantum fluid behave like magnetic monopoles. *Nature Physics* **8**, 724–728 (2012).

[123] Butov, L. V. & Kavokin, A. V. The behaviour of exciton-polaritons. *Nature Photonics* **6**, 2 (2012).

[124] Deveaud-Pledran, B. The behaviour of exciton-polaritons. *Nature Photonics* **6**, 205 (2012).

[125] Umlauff, M. *et al.* Direct observation of free-exciton thermalization in quantum-well structures. *Physical Review B* **57**, 1390–1393 (1998).

[126] Tartakovskii, A. I. *et al.* Relaxation bottleneck and its suppression in semiconductor microcavities. *Physical Review B* **62**, R2283–R2286 (2000).

[127] Muller, M., Bleuse, J. & Andre, R. Dynamics of the cavity polariton in CdTe-based semiconductor microcavities: Evidence for a relaxation edge. *Physical Review B* **62**, 16886–16892 (2000).

[128] Tassone, F., Piermarocchi, C., Savona, V., Quattropani, A. & Schwendimann, P. Bottleneck effects in the relaxation and photoluminescence of microcavity polaritons. *Physical Review B* **56**, 7554–7563 (1997).

[129] Porras, D., Ciuti, C., Baumberg, J. J. & Tejedor, C. Polariton dynamics and Bose-Einstein condensation in semiconductor microcavities. *Physical Review B* **66**, 085304 (2002).

[130] Malpuech, G., Rubo, Y. G., Laussy, F. P., Bigenwald, P. & Kavokin, A. V. Polariton laser: thermodynamics and quantum kinetic theory. *Semiconductor Science and Technology* **18**, S395 (2003).

[131] Richard, M. *et al.* Experimental evidence for nonequilibrium Bose condensation of exciton polaritons. *Physical Review B* **72**, 201301 (2005).

[132] Baas, A. *et al.* Synchronized and desynchronized phases of exciton-polariton condensates in the presence of disorder. *Physical Review Letters* **100**, 170401 (2008).

[133] Guillet, T. *et al.* Polariton lasing in a hybrid bulk ZnO microcavity. *Applied Physics Letters* **99**, 161104 (2011).

[134] Franke, H., Sturm, C., Schmidt-Grund, R., Wagner, G. & Grundmann, M. Ballistic propagation of excitonpolariton condensates in a ZnO-based microcavity. *New Journal of Physics* **14**, 013037 (2012).

[135] Xie, W. *et al.* Room-temperature polariton parametric scattering driven by a one-dimensional polariton condensate. *Physical Review Letters* **108**, 166401 (2012).

[136] Das, A. *et al.* Room temperature strong coupling effects from single ZnO nanowire microcavity. *Optics Express* **20**, 11830–11837 (2012).

[137] Sun, L. *et al.* Room temperature one-dimensional polariton condensate in a ZnO microwire. *arXiv:1007.4686* (2010).

[138] Li, F. *et al.* ZnO-based polariton laser operating at room temperature: From excitonic to photonic condensate. *arXiv:1207.7172* (2012).

[139] Savvidis, P. G. *et al.* Angle-resonant stimulated polariton amplifier. *Physical Review Letters* **84**, 1547–1550 (2000).

[140] Ballarini, D. *et al.* Observation of long-lived polariton states in semiconductor microcavities across the parametric threshold. *Physical Review Letters* **102**, 056402 (2009).

[141] Wouters, M. & Carusotto, I. Goldstone mode of optical parametric oscillators in planar semiconductor microcavities in the strong-coupling regime. *Physical Review A* **76**, 043807 (2007).

[142] Krizhanovskii, D. N. *et al.* Effect of interactions on vortices in a nonequilibrium polariton condensate. *Physical Review Letters* **104**, 126402 (2010).

[143] Carusotto, I. & Ciuti, C. Spontaneous microcavity-polariton coherence across the parametric threshold: Quantum Monte Carlo studies. *Physical Review B* **72**, 125335 (2005).

[144] Carusotto, I. & Ciuti, C. Probing microcavity polariton superfluidity through resonant Rayleigh scattering. *Physical Review Letters* **93**, 166401 (2004).

[145] Keeling, J. & Berloff, N. G. Spontaneous rotating vortex lattices in a pumped decaying condensate. *Physical Review Letters* **100**, 250401 (2008).

[146] Aranson, I. S. & Kramer, L. The world of the complex Ginzburg-Landau equation. *Reviews of Modern Physics* **74**, 99–143 (2002).

[147] Keeling, J. & Berloff, N. G. Condensed-matter physics: Going with the flow. *Nature* **457**, 273–274 (2009).

[148] Ciuti, C. & Carusotto, I. Quantum fluid effects and parametric instabilities in microcavities. *physica status solidi (b)* **242**, 2224–2245 (2005).

[149] Pigeon, S., Carusotto, I. & Ciuti, C. Hydrodynamic nucleation of vortices and solitons in a resonantly excited polariton superfluid. *Physical Review B* **83**, 144513 (2011).

[150] Astrakharchik, G. E. & Pitaevskii, L. P. Motion of a heavy impurity through a Bose-Einstein condensate. *Physical Review A* **70**, 013608 (2004).

[151] Wouters, M. & Carusotto, I. Superfluidity and critical velocities in nonequilibrium Bose-Einstein condensates. *Physical Review Letters* **105**, 020602 (2010).

[152] Cancellieri, E., Marchetti, F. M., Szymanska, M. H. & Tejedor, C. Superflow of resonantly driven polaritons against a defect. *Physical Review B* **82**, 224512 (2010).

[153] Berceanu, A. C., Cancellieri, E. & Marchetti, F. M. Drag in a resonantly driven polariton fluid. *Journal of Physics: Condensed Matter* **24**, 235802 (2012).

[154] Wouters, M. & Carusotto, I. Excitations in a nonequilibrium Bose-Einstein condensate of exciton polaritons. *Physical Review Letters* **99**, 140402 (2007).

[155] Utsunomiya, S. *et al.* Observation of Bogoliubov excitations in exciton-polariton condensates. *Nature Physics* **4**, 673 (2008).

[156] Wouters, M. & Savona, V. Superfluidity of a nonequilibrium Bose-Einstein condensate of polaritons. *Physical Review B* **81**, 054508 (2010).

[157] Marchetti, F. M. & Szymanska, M. H. Vortices in polariton OPO superfluids. In Timofeev, V. & Sanvitto, D. (eds.) *Exciton Polaritons in Microcavities*, Springer Series in Solid-State Sciences, 173–213 (Springer, 2012).

[158] Huang, K. *Statistical mechanics* (Wiley, 1987).

[159] Cancellieri, E., Marchetti, F. M., Szymanska, M. H., Sanvitto, D. & Tejedor, C. Frictionless flow in a binary polariton superfluid. *Physical Review Letters* **108**, 065301 (2012).

[160] Marchetti, F. M., Szymanska, M. H., Tejedor, C. & Whittaker, D. M. Spontaneous and triggered vortices in polariton optical-parametric-oscillator superfluids. *Physical Review Letters* **105**, 063902 (2010).

[161] Tsintzos, S. I., Pelekanos, N. T., Konstantinidis, G., Hatzopoulos, Z. & Savvidis, P. G. A GaAs polariton light-emitting diode operating near room temperature. *Nature* **453**, 372–375 (2008).

[162] Khalifa, A. A., Love, A. P. D., Krizhanovskii, D. N., Skolnick, M. S. & Roberts, J. S. Electroluminescence emission from polariton states in GaAs-based semiconductor microcavities. *Applied Physics Letters* **92**, 061107 (2008).

[163] Tsintzos, S. I., Savvidis, P. G., Deligeorgis, G., Hatzopoulos, Z. & Pelekanos, N. T. Room temperature GaAs exciton-polariton light emitting diode. *Applied Physics Letters* **94**, 071109 (2009).

[164] Cristofolini, P. *et al.* Coupling quantum tunneling with cavity photons. *Science* **336**, 704–707 (2012).

[165] Cho, A. & Arthur, J. Molecular beam epitaxy. *Progress in Solid State Chemistry* **10, Part 3**, 157 – 191 (1975).

[166] Perrin, M., Bloch, J., Lemaitre, A. & Senellart, P. Enhanced polariton relaxation by electron-polariton scattering. *physica status solidi (c)* **2**, 759–762 (2005).

[167] Perrin, M., Senellart, P., Lemaitre, A. & Bloch, J. Polariton relaxation in semiconductor microcavities: Efficiency of electron-polariton scattering. *Physical Review B* **72**, 075340 (2005).

[168] Bajoni, D. *et al.* Dynamics of microcavity polaritons in the presence of an electron gas. *Physical Review B* **73**, 205344 (2006).

[169] Tsotsis, P. *et al.* Lasing threshold doubling at the crossover from strong to weak coupling regime in GaAs microcavity. *New Journal of Physics* **14**, 023060 (2012).

[170] Interactive Java tutorials - streak lifetime imaging (FLIM) camera. URL `http://learn.hamamatsu.com/tutorials/java/streakcamera/`.

[171] Born, M. & Wolf, E. *Principles of Optics: Electromagnetic Theory of Propagation, Interference and Diffraction of Light* (Cambridge University Press, 2000).

[172] Raman, C. *et al.* Evidence for a critical velocity in a Bose-Einstein condensed gas. *Physical Review Letters* **83**, 2502–2505 (1999).

[173] Andersen, M. F. *et al.* Quantized rotation of atoms from photons with orbital angular momentum. *Physical Review Letters* **97**, 170406 (2006).

[174] Ramanathan, A. *et al.* Superflow in a toroidal Bose-Einstein condensate: An atom circuit with a tunable weak link. *Physical Review Letters* **106**, 130401 (2011).

[175] Molina-Terriza, G., Torres, J. P. & Torner, L. Twisted photons. *Nature Physics* **3**, 305–310 (2007).

[176] Dholakia, K., Simpson, N. B., Padgett, M. J. & Allen, L. Second-harmonic generation and the orbital angular momentum of light. *Physical Review A* **54**, R3742–R3745 (1996).

[177] Martinelli, M., Huguenin, J. A. O., Nussenzveig, P. & Khoury, A. Z. Orbital angular momentum exchange in an optical parametric oscillator. *Physical Review A* **70**, 013812 (2004).

[178] Sakurai, J. & Tuan, S. *Modern Quantum Mechanics* (Addison-Wesley Publishing Company, 1994).

[179] Leggett, A. *Quantum Liquids: Bose Condensation And Cooper Pairing in Condensed-matter Systems.* Oxford graduate texts in mathematics (Oxford University Press, 2006).

[180] Lagoudakis, K. G. *et al.* Probing the dynamics of spontaneous quantum vortices in polariton superfluids. *Physical Review Letters* **106**, 115301 (2011).

[181] Shin, Y. *et al.* Dynamical instability of a doubly quantized vortex in a Bose-Einstein condensate. *Physical Review Letters* **93**, 160406 (2004).

[182] Baert, M., Metlushko, V. V., Jonckheere, R., Moshchalkov, V. V. & Bruynseraede, Y. Composite flux-line lattices stabilized in superconducting films by a regular array of artificial defects. *Physical Review Letters* **74**, 3269–3272 (1995).

[183] Blaauwgeers, R. *et al.* Double-quantum vortex in superfluid ^{3}He-A. *Nature* **404**, 471–473 (2000).

[184] Pu, H., Law, C. K., Eberly, J. H. & Bigelow, N. P. Coherent disintegration and stability of vortices in trapped Bose condensates. *Physical Review A* **59**, 1533–1537 (1999).

[185] Mottonen, M., Mizushima, T., Isoshima, T., Salomaa, M. M. & Machida, K. Splitting of a doubly quantized vortex through intertwining in Bose-Einstein condensates. *Physical Review A* **68**, 023611 (2003).

[186] Szymanska, M. H., M. H., Marchetti, F. M. & Sanvitto, D. Propagating wave packets and quantized currents in coherently driven polariton superfluids. *Physical Review Letters* **105**, 236402 (2010).

[187] Garcia-Ripoll, J. J., Molina-Terriza, G., Perez-Garcia, V. M. & Torner, L. Structural instability of vortices in Bose-Einstein condensates. *Physical Review Letters* **87**, 140403 (2001).

[188] Lai, C. W. *et al.* Coherent zero-state and π-state in an exciton-polariton condensate array. *Nature* **450**, 529–532 (2007).

[189] Lagoudakis, K. G., Pietka, B., Wouters, M., Andre, R. & Deveaud-Pledran, B. Coherent oscillations in an exciton-polariton Josephson junction. *Physical Review Letters* **105**, 120403 (2010).

[190] Abbarchi, M. *et al.* Macroscopic quantum self-trapping and Josephson oscillations of exciton-polaritons. *arXiv:1212.5467* (2012).

[191] Galbiati, M. *et al.* Polariton condensation in photonic molecules. *Physical Review Letters* **108**, 126403 (2012).

[192] Tikhonenko, V., Christou, J., Luther-Davies, B. & Kivshar, Y. S. Observation of vortex solitons created by the instability of dark soliton stripes. *Optics Letters* **21**, 1129–1131 (1996).

[193] Kivshar, Y. S. & Luther-Davies, B. Dark optical solitons: physics and applications. *Physics Reports* **298**, 81–197 (1998).

[194] Feder, D. L., Pindzola, M. S., Collins, L. A., Schneider, B. I. & Clark, C. W. Dark-soliton states of Bose-Einstein condensates in anisotropic traps. *Physical Review A* **62**, 053606 (2000).

[195] Brand, J. & Reinhardt, W. P. Solitonic vortices and the fundamental modes of the snake instability: Possibility of observation in the gaseous Bose-Einstein condensate. *Physical Review A* **65**, 043612 (2002).

[196] Mewes, M.-O. *et al.* Output coupler for Bose-Einstein condensed atoms. *Physical Review Letters* **78**, 582–585 (1997).

[197] Ladd, T. D. *et al.* Quantum computers. *Nature* **464**, 45–53 (2010).

[198] Kammann, E. *et al.* Nonlinear optical spin hall effect and long-range spin transport in polariton lasers. *Physical Review Letters* **109**, 036404 (2012).

[199] Wouters, M., Carusotto, I. & Ciuti, C. Spatial and spectral shape of inhomogeneous nonequilibrium exciton-polariton condensates. *Physical Review B* **77**, 115340 (2008).

[200] Tempel, J.-S. *et al.* Characterization of two-threshold behavior of the emission from a GaAs microcavity. *Physical Review B* **85**, 075318 (2012).

[201] Wouters, M. Synchronized and desynchronized phases of coupled nonequilibrium exciton-polariton condensates. *Physical Review B* **77**, 121302 (2008).

[202] Ruben, G., Paganin, D. M. & Morgan, M. J. Vortex-lattice formation and melting in a nonrotating Bose-Einstein condensate. *Physical Review A* **78**, 013631 (2008).

[203] Keeling, J. & Berloff, N. G. Controllable half-vortex lattices in an incoherently pumped polariton condensate. *arXiv:1102.5302* (2011).

[204] Essmann, U. & Trauble, H. The direct observation of individual flux lines in type II superconductors. *Physics Letters A* **24**, 526–527 (1967).

[205] Fetter, A. L. Rotating trapped Bose-Einstein condensates. *Reviews of Modern Physics* **81**, 647–691 (2009).

[206] Ruben, G., Morgan, M. J. & Paganin, D. M. Texture control in a pseudospin Bose-Einstein condensate. *Physical Review Letters* **105**, 220402 (2010).

[207] Scherer, D. R., Weiler, C. N., Neely, T. W. & Anderson, B. P. Vortex formation by merging of multiple trapped Bose-Einstein condensates. *Physical Review Letters* **98**, 110402 (2007).

[208] Swartzlander, J., G. A. & Law, C. T. Optical vortex solitons observed in Kerr nonlinear media. *Physical Review Letters* **69**, 2503–2506 (1992).

[209] Fleischer, J. W., Segev, M., Efremidis, N. K. & Christodoulides, D. N. Observation of two-dimensional discrete solitons in optically induced nonlinear photonic lattices. *Nature* **422**, 147–150 (2003).

[210] Liew, T. C. H., Rubo, Y. G. & Kavokin, A. V. Generation and dynamics of vortex lattices in coherent exciton-polariton fields. *Physical Review Letters* **101**, 187401 (2008).

[211] Gorbach, A. V., Hartley, R. & Skryabin, D. V. Vortex lattices in coherently pumped polariton microcavities. *Physical Review Letters* **104**, 213903 (2010).

[212] Wouters, M., Liew, T. C. H. & Savona, V. Energy relaxation in one-dimensional polariton condensates. *Physical Review B* **82**, 245315 (2010).

[213] Elbio, D. Experiments on ladders reveal a complex interplay between a spin-gapped normal state and superconductivity. *Reports on Progress in Physics* **62**, 1525 (1999).

[214] Kim, N. Y. *et al.* Dynamical d-wave condensation of exciton-polaritons in a two-dimensional square-lattice potential. *Nature Physics* **7**, 681–686 (2011).

[215] Penckwitt, A. A., Ballagh, R. J. & Gardiner, C. W. Nucleation, growth, and stabilization of bose-einstein condensate vortex lattices. *Phys. Rev. Lett.* **89**, 260402 (2002).

[216] Gardiner, C. W., Zoller, P., Ballagh, R. J. & Davis, M. J. Kinetics of Bose-Einstein condensation in a trap. *Physical Review Letters* **79**, 1793–1796 (1997).

[217] Burger, S. *et al.* Dark solitons in Bose-Einstein condensates. *Physical Review Letters* **83**, 5198–5201 (1999).

[218] Strecker, K. E., Partridge, G. B., Truscott, A. G. & Hulet, R. G. Formation and propagation of matter-wave soliton trains. *Nature* **417**, 150–153 (2002).

[219] Becker, C. *et al.* Oscillations and interactions of dark and dark-bright solitons in Bose-Einstein condensates. *Nature Physics* **4**, 496–501 (2008).

[220] Pelinovsky, D. E., Frantzeskakis, D. J. & Kevrekidis, P. G. Oscillations of dark solitons in trapped Bose-Einstein condensates. *Physical Review E* **72**, 016615 (2005).

[221] Christmann, G. et.al. Private communication (2013).

[222] Saleh, B. & Teich, M. *Fundamentals of photonics.* Wiley series in pure and applied optics (Wiley-InterScience, 2007).

[223] Kippenberg, T. J., Holzwarth, R. & Diddams, S. A. Microresonator-based optical frequency combs. *Science* **332**, 555–559 (2011).

[224] Josephson, B. D. The discovery of tunnelling supercurrents. *Reviews of Modern Physics* **46**, 251–254 (1974).

[225] Mohideen, U., Slusher, R. E., Jahnke, F. & Koch, S. W. Semiconductor microlaser linewidths. *Physical Review Letters* **73**, 1785–1788 (1994).

[226] Bajoni, D., Senellart, P., Lemaître, A. & Bloch, J. Photon lasing in GaAs microcavity: Similarities with a polariton condensate. *Physical Review B* **76**, 201305 (2007).

[227] Ctistis, G. *et al.* Ultimate fast optical switching of a planar microcavity in the telecom wavelength range. *Applied Physics Letters* **98**, 161114 (2011).

[228] Harding, P. J. *et al.* Observation of a stronger-than-adiabatic change of light trapped in an ultrafast switched GaAs-AlAs microcavity. *J. Opt. Soc. Am. B* **29**, A1–A5 (2012).

[229] El, G. & Kamchatnov, A. Spatial dispersive shock waves generated in supersonic flow of Bose-Einstein condensate past slender body. *Physics Letters A* **350**, 192–196 (2006).

[230] Bajoni, D. *et al.* Polariton laser using single micropillar GaAs-GaAlAs semiconductor cavities. *Physical Review Letters* **100**, 047401 (2008).

Nomenclature

χ and ς ..... page 28
Hopfield coefficients, see equation (1.48).

δ_{Ph-HH} ..... page 68
photon-heavy-hole-exciton detuning.

Γ ..... page 55
polariton decay rate, see equation (2.36).

Γ_x ..... page 23
exciton radiative broadening, see equation (1.35).

γ_x ..... page 22
exciton non-radiative damping, see equation (1.31).

$\hat{a}_{\mathbf{p}}$ ..... page 34
annihilation operator, see equation (2.8).

$\hat{a}^{\dagger}_{\mathbf{p}}$ ..... page 34
creation operator, see equation (2.8).

$\hat{C}$ ..... page 27
photon annihilation operator, see equation (1.42).

$\hat{C}^{\dagger}$ ..... page 27
photon creation operator, see equation (1.42).

$\hat{X}$ ..... page 27
exciton annihilation operator, see equation (1.42).

$\hat{X}^{\dagger}$ ..... page 27
exciton creation operator, see equation (1.42).

λ_T ..... page 32
de Broglie wavelength.

ϖ ..... page 45
vorticity, see equation (2.34).

$\mathbf{B}$ ..... page 13
magnetic flux, see equation (1.8).

$\mathbf{D}$ ..... page 13
electric flux, see equation (1.8).

E ..... page 12
electric field, see equation (1.7).

H ..... page 12
magnetic field, see equation (1.7).

J ..... page 12
charge current density, see equation (1.7).

j ..... page 44
fluid current density, see equation (2.30).

M ..... page 12
magnetization density, see equation (1.7).

P ..... page 12
polarization density, see equation (1.7).

$\mathbf{v}_s$ ..... page 45
condensate flow velocity, see equation (2.31).

$\mathcal{F}$ ..... page 18
finesse, see equation (1.27).

$\mathcal{H}_{e-h}$ ..... page 11
Hamiltonian accounting for electron–hole coulomb interactions, see equation (1.3).

$\mathcal{H}_{e-ions}$ ..... page 9
Hamiltonian describing vchanges in the electronic energy as a result of the displacements of the ions from their equilibrium positions, see equation (1.1).

$\mathcal{H}_{e-ph}$ ..... page 22
Hamiltonian accounting for electron-photon interaction, see equation (1.30).

$\mathcal{H}_e$ ..... page 8
Hamiltonian describing valence electrons with the ions frozen in their equilibrium positions, see equation (1.1).

$\mathcal{H}_{ions}$ ..... page 7
Hamiltonian describing interactions between atomic nuclei and cores electrons, see equation (1.1).

$\mathcal{H}_{ph}$ ..... page 22
Hamiltonian accounting for photonic dispersion, see equation (1.30).

μ ..... page 13
permeability, see equation (1.8).

μ_c ..... page 31
chemical potential, see equation (2.1).

μ_{eh} ..... page 11
electron-hole reduced effetive mass, see equation (1.5).

Ω ..... page 92
correlation-weighted vorticity, see equation (5.4).

ω ..... page 16
wave frequency multiplied by 2π.

Ω_R ..... page 26
Rabi frequency, see equation (1.41).

ω_{LT} ..... page 22
longitudinal-transverse splitting, see equation (1.33).

ρ ..... page 42
density matrix, see equation (2.25).

ρ_e ..... page 12
charge density, see equation (1.7).

ε ..... page 13
permittivity, see equation (1.8).

ξ ..... page 36
healing length, see equation (2.21).

a ..... page 35
scattering length, see equation (2.9).

A^+ ..... page 13
positive-propagating electric field, see equation (1.11).

A^- ..... page 13
negative-propagating electric field, see equation (1.11).

a_B ..... page 11
Bohr radius, see equation (1.5).

Al ..... page 52
Aluminium.

As ..... page 52
Arsenic.

c ..... page 13
light speed, see equation (1.10).

c_s ..... page 35
sound speed, see equation (2.13).

Cd ..... page 52
Cadmium.

CR ..... page 92
coherent rotation, see equation (5.5).

D ..... page 59
reservoir spatial diffusion coefficient, see equation (2.40).

e ..... page 11
elementary electron charge.

E_B ..... page 12
binding energy of the ground exciton state, see equation (1.6).

g ..... page 35
interaction coupling constant, see equation (2.9).

$g^{(1)}$ ..... page 76
complex degree of coherence, also known as 1^{st} order correlation function, see equation (4.3).

Ga ..... page 52
Gallium.

k_0 ..... page 13
wavevector in vacuum, see equation (1.11).

k_B ..... page 31
Boltzmann constant.

L_c ..... page 16
cavity thickness.

L_z ..... page 92
third component of angular momentum, see equation (5.3).

M ..... page 45
topological charge of a vortex, see equation (2.32).

m^* ..... page 10
effective mass.

m_e ..... page 11
effective electron mass.

m_h ..... page 11
effective hole mass.

n ..... page 13
refractive index, see equation (1.10).

Q ..... page 18
quality factor, see equation (1.28).

R ..... page 14
reflectivity, see equation (1.17).

r ..... page 14
Fresnel amplitude reflection, see equation (1.16).

R_R ..... page 59
polaritons scattering from the reservoir into the condensate.

T ..... page 14
transmittance, see equation (1.17).

t ..... page 14
Fresnel amplitude transmission, see equation (1.16).

Te ..... page 52
Tellurium.

AF ..... page 131
anti-ferromagnetism.

BEC ..... page 32
Bose-Einstein condensation.

BKT ..... page 44
Berezinskii-Kosterlitz-Thouless.

cGLE ..... page 55
complex Ginzburg-Landau equation.

CW ..... page 54
Continuous wave.

DBR ..... page 18
distributed Bragg reflector.

F ..... page 131
ferromagnetism.

FP ..... page 15
Fabry-Perrot interferometer.

FWHM ..... page 24
full width of half maximum.

GPE ..... page 44
Gross-Pitaevskii equation.

LG ..... page 94
Laguerre-Gaussian.

LPB ..... page 28
lower polariton branch.

MBE ..... page 67
molecular beam epitaxy.

MPB ..... page 68
middle polariton branch.

OPA ..... page 54
optical parametric amplification.

OPO ..... page 53
optical parametric oscillator.

QW ..... page 10
quantum well.

RRS ..... page 56
resonant Rayleigh scattering.

TOPO ..... page 54
triggered optical parametric oscillator.

UPB ..... page 28
upper polariton branch.

VCSEL ..... page 1
vertical-cavity surface emitting laser.